POLITECNICO DI TORINO

Applied Science and Technology Department

PhD in Physics XXVI cycle

New insights in Dye-sensitized Solar Cells: novel nanostructured photoanodes, metal-free dye, quasi-solid electrolytes and physics-based modeling

Supervisor

Prof. Elena Tresso

Candidate

Diego Pugliese

Learn from yesterday,

live for today,

hope for tomorrow.

The important thing

is not to stop questioning.

[Albert Einstein]

Outline

Chapter 1: Introduction

In this introductive Chapter an overview of the worldwide energy demand is reported, with the aim of clarifying the importance of seeking renewable energy sources. Between all the alternative energy sources, a special interest is devoted to the Photovoltaics, and in particular the current situation of PV, the principles of the solar radiation and the solar cell technologies will be thoroughly presented. Finally, the last Section of the Chapter is dedicated to the description of the structure and the targets of the thesis' work.

1.1 Worldwide energy demand

The global energy problem is raised from the ever-growing need to satisfy the energy demand of developed countries and from the necessity to provide energy through methods with low environmental impact, as well illustrated by Michael Grätzel with the following sentence:

"Perhaps the largest challenge for our global society is to find ways to replace the slowly but inevitably vanishing fossil fuel supplies by renewable resources and, at the same time, avoid negative effects from the current energy system on climate, environment, and health" [1].

As the world is becoming more advanced in technology and economy, more energy is being consumed to keep up with the development and the demand on energy boomed over the past years. Presently the annual world primary energy consumption increases by 1.6% per year and it is estimated to be about to 25.8 TW by the year 2035 [2].

At the moment, the energy economy is still highly dependent on three forms of fossil fuels - oil, natural gases and coal - which cover more than 85% of the total energy production. However, it is expected that world demand for fossil fuels will soon exceed annual production and shortages of fossil fuel may cause international economic and political crises and conflicts. Moreover, it is known that combustion of fossil fuels releases harmful emissions to the environment and the combustion products have not only local but also global effects. The use of fossil energy is, in fact, responsible of the so-called *greenhouse effect*. The increase of the amount of CO_2 produced in the combustion of fossil energy and then released in the air, together with other gasses called greenhouse gasses, generate a reduction of the airflow with the consequent isolation of the warm air inside the atmosphere, thus generating an overall increase of the temperature on the Earth. It has been predicted that the average global temperature will increase between 0.6 and 4.0 °C in the coming 100 years, depending on model parameters such as world population growth, primary energy source, and economic growth [3]. In Fig. 1.1 the global energy demand in 2011 and the prediction for 2040 is reported. From this graph it is possible to see that stored energies will continue to dominate the market (even if the coal is predicted to decrease a little bit), but the demand of renewable energies will increase drastically.

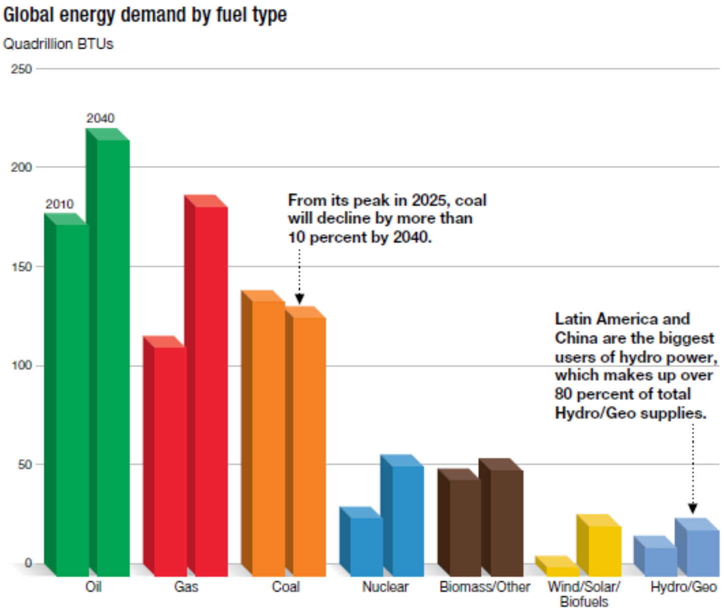

Fig. 1.1 Global energy demand by fuel type [4].

The term “renewable energy” stands for energy derived from a broad spectrum of resources, all of which are based on self-renewing energy sources such as sunlight, wind, flowing water, the earth’s internal heat, biomass such as energy crops, agricultural and industrial waste, and municipal waste. These resources can be used to produce electricity for all economic sectors, fuels for transportation, and heat for buildings and industrial processes.

To be economically competitive, alternative energy sources have to be efficient, inexpensive and environmentally friendly, i.e. they have to be sustainable. For example, nuclear power is an alternative energy source that cannot be defined sustainable because the use of nuclear plants is associated to a number of well-known environmental problems and public safety related to the use of radioactive nuclei and production of radioactive waste.

Between all the available technologies producing renewable energy, photovoltaic energy is a hot topic in current research. One simple reason is that the Earth receives $1.2 \cdot 10^{17}$ W insolation or $3 \cdot 10^{24}$ Joule of energy per year from the Sun and this means covering only 0.13% of the Earth's surface with solar cells with an efficiency of 10% would satisfy our present needs [5]. Apart from the abundance of potentially exploitable solar energy, photovoltaic cells have also other competitive advantages such as little need for maintenance, off-grid operation and silence, which are ideal for usage in remote sites or mobile applications. According to the Solar Generation 6 report, written by the EPIA (European Photovoltaic Industry Association) and Greenpeace International, the photovoltaic power generation will cover the 9% of the world demand in 2030 [6].

1.2 Photovoltaics

1.2.1 Photovoltaic market and the current situation of PV

After the development of the first silicon cell in 1954, photovoltaic devices were used primarily in space applications. It is only in the second half of the last decade that grid connected photovoltaic systems entered in the terrestrial market with significant contribution. Photovoltaic has a lot of advantages: the most important one is that it is a clean source of energy, thus allowing a reduction of atmosphere pollution.

Over the last decade, PV technology has shown the potential to become a major source of power generation for the world, with vigorous and incessant growth even during times of financial and economic crisis. That growth is expected to last in the years ahead as worldwide awareness of the advantages of PV increases. At the end of 2009, the world's PV cumulative installed capacity was approaching 23 GW. One year later it was 40 GW and in 2011 more than 69 GW were installed globally and could produce 85 TWh of electricity every year, as shown in Fig. 1.2 [7]. This energy volume is sufficient to cover the annual power supply needs of over 20 million households. PV is now, after hydro and wind power, the third most important renewable energy source in terms of globally installed capacity. The growth rate of PV during 2011 reached almost 70%, an exceptional level among all renewable technologies.

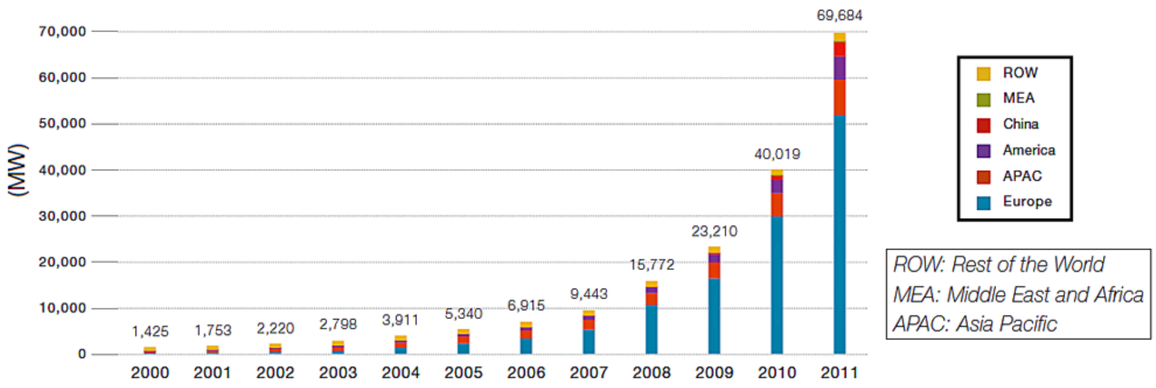

ROW: Rest of the World
MEA: Middle East and Africa
APAC: Asia Pacific

Fig. 1.2 Evolution of the World annual PV market (2000-2011) [7].

In terms of global cumulative installed capacity, Europe still holds the record with more than 51 GW installed in 2011. This represents about 75% of the world's total PV cumulative capacity. Next in the ranking are Japan (5 GW) and the USA (4.4 GW), followed by China (3.1 GW) which reached its first GW in 2011. Europe has developed from an annual market of less than 1 GW in 2003 to a market of over 13 GW in 2010 and 21.9 GW in 2011. For the first time, Italy in 2011 became the top PV market, with 9.3 GW of newly connected systems; Germany was second with 7.5 GW reported by authorities, after having been either first or second in each of the last eight years. Together, Italy and Germany accounted for nearly 60% of global market growth during last year. These two markets were followed by France (1.7 GW) and the United Kingdom (784 MW), which showed surprisingly robust growth in 2011. Many other markets have started to show significant development.

As it has for several years, Europe leads the way in the global PV market, with four countries that have markets close to or above 1 GW. Outside Europe, China has joined Japan and the USA in the group of countries with more than 1 GW of newly PV installed capacity. India could also reach that threshold quickly, but other medium sized markets will take several years to reach the same level of development.

1.2.2 The solar radiation

The efficiency of a solar cell is sensitive to variations of the intensity and the energy distribution of the incident light.

Solar radiation reaching the Earth's surface strictly depends on the location, atmospheric conditions, time of the day, Earth/Sun distance and solar rotation and activity. Since the solar spectrum depends on so many variables, it is fundamental to define a standard spectrum and power density, thus allowing an accurate comparison among different solar devices.

The Sun emission wavelength range covers the ultraviolet (UV), visible and infrared (IR) regions of electromagnetic spectrum, with a maximum peak at around 500 nm. Its spectrum is similar to that of a blackbody at 5670 K and it is influenced by the absorption of some molecules present in the atmosphere, such as O_3, CO_2, H_2O (see Fig. 1.3).

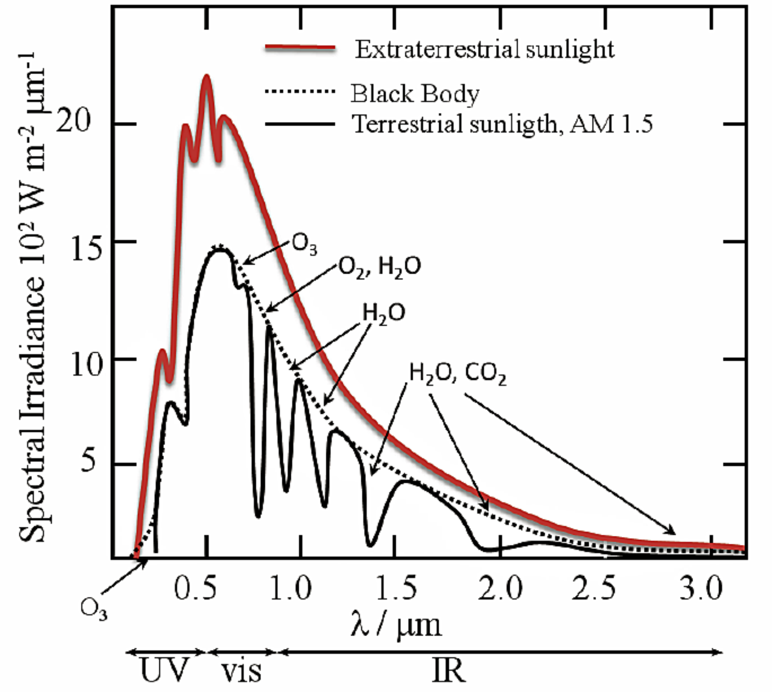

Fig. 1.3 Spectra of a black body at 5670 K, extraterrestrial sunlight and terrestrial sunlight (AM1.5) [8].

The power density at the surface of the Sun is 62 MW/m^2 and it is reduced to 1353 W/m^2 at the point just above the Earth's atmosphere [9]. The latter value is the so-called *solar constant,* which describes the amount of incoming perpendicular solar radiation measured on the outer surface of Earth's atmosphere. Before reaching the ground, the radiation passes through the atmosphere, which modifies the solar spectrum (see Fig. 1.3) due to the following factors: clouds (that absorb a high amount of radiation), angle of incidence of sunrays (the higher is the tilt of sunrays, the lower is the energy that arrives to the soil) and atmospheric mass. The radiation that finally impings on the ground will depend on the path length it has to pass through. This optical path, which takes into account the attenuation suffered by the solar radiation due to the atmospheric absorption and depends on the position of the Sun, is called Air Mass and it is expressed through the formula

$$AM = \frac{1}{\cos{(\theta)}} \tag{1.1}$$

where θ is the elevation angle of the Sun (see Fig. 1.4).

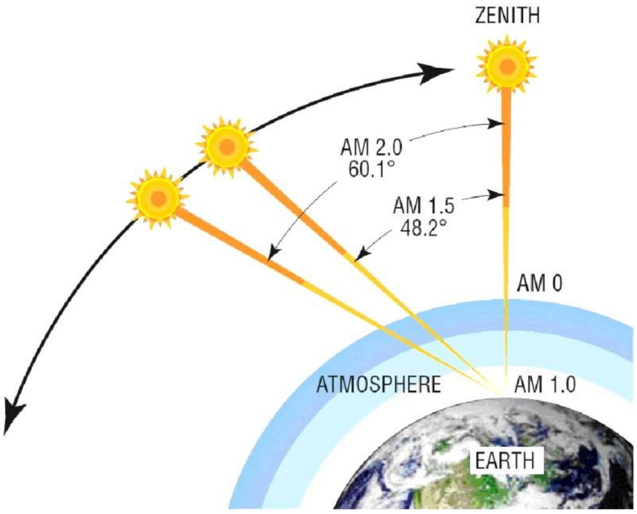

Fig. 1.4 Illustration of various Air Mass (AM) positions and of the zenith point [10].

When the Sun is directly overhead, the Air Mass is 1 (AM 1) and the irradiance reaching the Earth's surface is maximum. The standard spectral distribution of the light used for testing photovoltaic devices is AM 1.5 G [11] (elevation angle equal to θ = 48.2 ºC and optical path 1.5 times longer than in the case of AM 1 light). This atmosphere thickness should attenuate the solar spectrum to a mean irradiance of around 900 W/m^2 [9]. However, for convenience, the standard spectrum is normalized so that the integrated irradiance of this spectrum per unit area and unit time is 1000 W/m^2 (known as 1 sun illumination). This light intensity is used for standard testing conditions under simulated sunlight. The “G” in AM 1.5 G stands for Global, that is the sum of direct and diffuse light.

In Fig. 1.3 a comparison between the spectrum of a black body at 5670 K and the AM 1.5 spectrum is shown.

1.2.3 Solar cell technologies

Currently the photovoltaic market for terrestrial applications is dominated by mono- and poly-crystalline bulk silicon (see Fig. 1.5), which offer the best compromise between costs and performances. These devices are the main exponents of a group named as the *first generation* of photovoltaic cells and they comprise more than 86% of the solar cell market.

Fig. 1.5 Mono-crystalline and poly-crystalline solar cells [12].

The Si cell fabrication technology is based on the formation of a *p-n* junction, depicted in Fig. 1.6. This junction is created by doping different regions of the same semiconductor with different impurities. In this way, an interface between p-type and n-type materials is obtained, which creates a *built-in* electric field as a consequence of the different chemical potentials that electrons and holes have across the interface. This intrinsic electric field favors charge separation in the so-called *depletion layer* when a photon of energy larger than the band gap creates an electron-hole pair near the interface (see Fig. 1.6). There have been several theoretical calculations on the maximum conversion efficiency obtainable from a solar harvester based on the *p-n* junction. In particular, Shockley and Queisser in 1961 [13] established an upper limit of the efficiency of 33.7% for a *p-n* junction with a band gap energy (E_g) of 1.4 eV under AM 1.5 illumination. There are two main reasons explaining such a low maximum efficiency. On the one hand, photons with an energy $E < E_g$ are not absorbed by the solar cell. On the other hand, even electrons excited by photons with an energy $E > E_g$ can only deliver the band gap energy to the electric circuit, whereas the rest (E - E_g) is lost by thermal dissipation [14]. Based on this theoretical maximum conversion efficiency and on the nature of the materials, photovoltaic cells can be divided in three major categories or *generations*. The first group includes cells that make use of materials with high purity and containing low concentrations of structural defects. These are the most efficient cells up to date. To this group belong crystalline silicon, single-junction GaAs and multijunction solar cells, with confirmed record efficiencies of 25%, 30% and 43%, respectively [15].

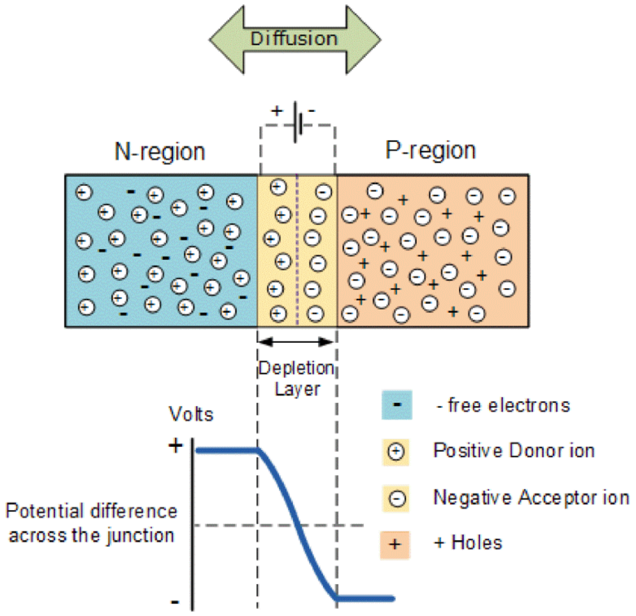

Fig. 1.6 *p*-*n* junction at equilibrium [16].

Although it has been the material most frequently employed and studied, silicon is not an ideal semiconductor for photovoltaic conversion. Its optical absorption coefficient is low due to the fact that it is an indirect semiconductor. Accordingly, Si wafers with a thickness of more than hundred microns are needed to efficiently absorb most of the incident light. This, together with costly purification and crystallization processes of silicon, make the production of silicon cells very expensive. Therefore, Si-based *first generation* photovoltaics is a robust and proven PV technology, but its cost reduction potential seems to be limited. In addition, even if there is still room for improvement, efficiencies of silicon solar cells are yet close to the theoretical Shockley-Queisser limit for a single-junction cell [17].

Two different approaches have been considered to face the problems associated with *first generation* photovoltaics: (a) to work on reducing the manufacturing costs and (b) to increase the energy conversion efficiency beyond the Shockley-Queisser limit. The greater incentive to the first approach has been the development of thin film solar cells. These devices are usually referred to as *second generation* photovoltaics. On the other hand, approaches focused on devices which could theoretically overcome the Shockley-Queisser limit are at the origin of *third generation* PV technologies.

Photovoltaic cells belonging to the *second generation* are known as thin film solar cells, because the thickness of their constituent material is less than 1 μm, i.e. 100-1000 times lower with respect to *first generation* devices. This is due to the fact that, being direct band gap semiconductors, the thin film materials have much higher absorption coefficient than silicon. These cells are based on a single-*p-n* junction and, therefore, share with *first generation* photovoltaics the theoretical efficiency limit. The driving force for the development of thin film solar cells has been their potential for the reduction of manufacturing costs. While silicon solar panels are assembled from individual cells processed from about 100 cm^2 silicon wafers, thin film semiconductor materials can be deposited onto large surfaces, which is beneficial for volume production.

Among the exploited materials, the most consolidated technology is that of amorphous silicon (a-Si), which is often used in the so-called double- or triple-junction cells: these devices are fabricated superimposing various cells based on materials with different band gap, that absorb in distinct wavelength regions [18].

Other used materials are: cadmium telluride (CdTe), whose photovoltaic performances are quite similar to crystalline Si, but with the advantages of diffuse light absorption and immunity to increasing temperature issues [19]; copper indium selenide (CIS), that presents high long-term stability and interesting application as *building-integrated photovoltaics* [19]; copper indium gallium (di)selenide (CIGS), that holds the record efficiency (up to 19.4%) between the thin film solar cells [18]. The CIGS and CdTe solar cell structures are shown in Fig. 1.7.

The efficiencies of *second generation* devices, however, are typically lower than efficiencies of *first generation* cells. In contrast to PV devices based on Si wafers, which are already very close to the theoretical efficiency limit, thin film solar cells are still well below their potential. Thin film technologies are in the early manufacturing phase, and efficiencies of small-area laboratory devices do not easily translate into efficiencies of large modules. The main issues associated with this kind of technology are the use of toxic materials as, i.e., cadmium and rare elements as telluride and indium. The implementation of a technology marketed as environmentally friendly that uses hazardous metals is quite controversial.

During the past decades, several examples of *third generation* solar cells have been proposed. The main difference from previous *generations* is that, here, the basic structure of the device is no more the *p-n* junction, but a multilayer structure in which carriers are exchanged. The term *third generation* includes various technologies and, commonly, is used to describe systems which do not fall into the *first* or *second generation* and/or which try to elude the 33.7% Shockley-Queisser limit [13]. Various approaches to achieve efficiencies above 30% have been explored. Tandems of cells provide the best known example of how such high efficiency might be reached: in this case, conversion efficiency can be enhanced by stacking cells of different band gaps, thus increasing the spectral sensitivity [20]. In principle, by stacking a large number of suitably tailored and designed cells, efficiencies as high as 67% and 86% for un-concentrated and maximally concentrated solar illumination are theoretically possible [17].

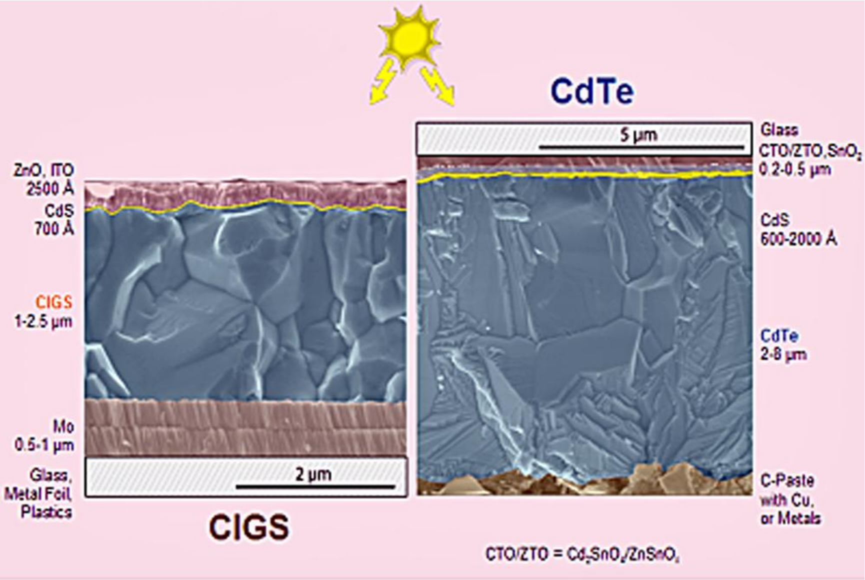

Fig. 1.7 CIGS and CdTe device structures [21].

In the 1990s, new concepts of solar cells based on nanostructured and organic materials were conceived as a new approach to low cost photovoltaics. Compared with the inorganic counterpart, recently discovered organic and polymeric conjugated semiconducting materials appear very promising for photovoltaics for several reasons, such as: lightweightness, low consumption of materials, flexibility, low cost for large scale production. These new solar cells have a big potential of development since molecular and nanostructural engineering approaches can be exploited for further improvement. The most active research fields comprise organic heterojunctions [22], extremely thin absorber (ETA) cells [23, 24, 25], hybrid solar cells [26, 27] and Dye-sensitized Solar Cells [28]. In an organic heterojunction the active layer is made up of a heterogeneous mixture (*polymer blend*) of two immiscible polymers: a donor (n-type) and an acceptor (p-type). Poly-phenylene vinylene derivatives and poly-alkylthiophenes are common donors; fullerene and its derivatives are common acceptors. The best confirmed photoconversion efficiency for this class of devices is 5.15% [29], obtained when employing P3HT/PCMB as donor-acceptor couple (see Fig. 1.8).

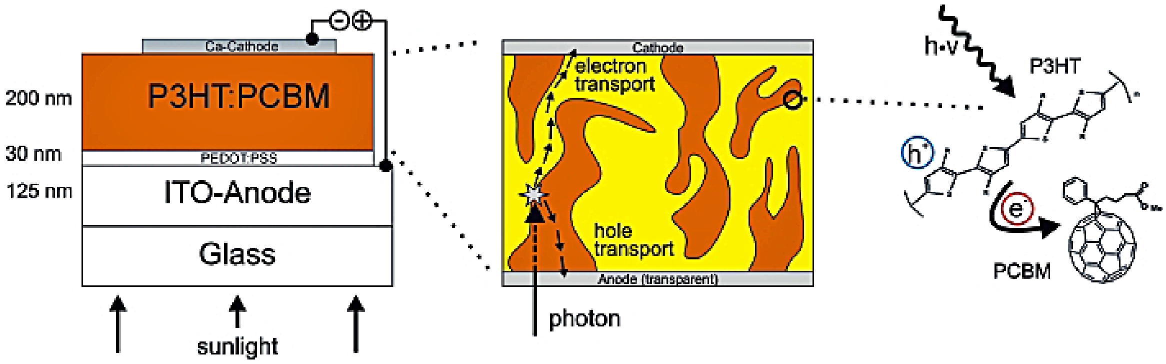

Fig. 1.8 Structure of a bulk heterojunction organic solar cell based on the P3HT/PCBM donor-acceptor couple [30].

The three-phase ETA cells are completely made up of solid inorganic materials. In these cells, a thin light absorbing semiconductor is sandwiched between two transparent, highly interpenetrated nanostructured semiconductors which act as electron and hole conductors [24, 31, 32]. Usually, wide band gap semiconductors as TiO_2 and ZnO are employed as electron conductors and CuSCN as hole conductor. A wide variety of inorganic absorbers can be exploited and the best efficiencies (3.5-4% [23, 33]) up to now for completely inorganic ETA cells have been obtained using In_2S_3.

In hybrid solar cells, in contrast to the previous two kinds of cells, both organic and inorganic materials are combined. They are usually composed of a conjugated polymer, which absorbs light and transports holes, and an inorganic electron conductor, both assembled together in a heterojunction. Power conversion efficiencies above 5% have been achieved with this kind of cells [34].

Finally, Dye-sensitized Solar Cells (DSCs) [28] are based on nanostructured wide band gap semiconductor films photosensitized with a dye. In 1991, M. Grätzel and B. O'Regan reported on a device made of sensitized nanoporous TiO_2 with a conversion efficiency of 7.1% [28]. This discovery opened a new field of scientific research and since then many research groups have worked on the improvement of the efficiency and the stability of this kind of solar cells. This field has experienced a boom in the last decade, with two or three research articles published every day [14]. At the time of writing, the record AM 1.5 efficiency for a DSC stood at 12.3% [35]. These devices are characterized by low fabrication costs and present some peculiar features like the transparency and the possibility of been fabricated in different colors (thanks to the usage of different dyes), thus being interesting for *building-integrated photovoltaics* (BIPV) applications. The major issue lays in a limited stability over time, mainly due to the presence of the liquid electrolyte, whose evaporation and/or leakage is still an unsolved drawback. A picture of a typical Dye-sensitized Solar Cell is reported in Fig. 1.9, while a detailed description of the structure and operating principle of this kind of cell will be provided in details in Chapter 2.

It is still not clear which one of all the technologies described above will determine the future of photovoltaics. Most probably the optimum solution will depend on the respective application and on other factors as, for example, the location. In that case, a major diversification of the photovoltaic market will be the most likely scenario in the near future.

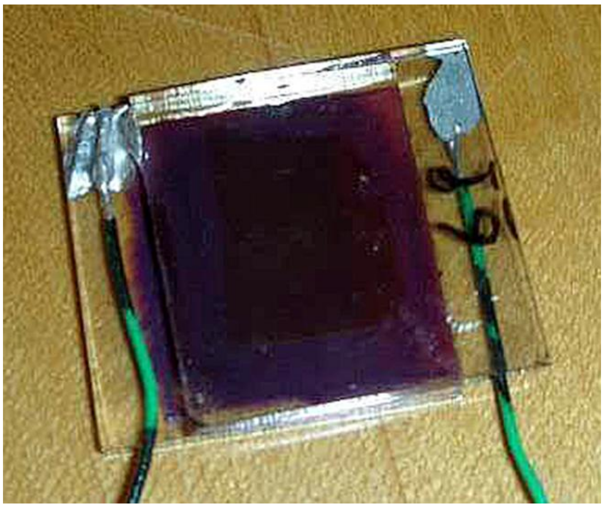

Fig. 1.9 Picture of a typical Dye-sensitized Solar Cell [36].

In Fig. 1.10 the efficiency trend of all the *generations* of solar cells is summarized. It can be seen that for *first generation* devices (blue points in the graph) the state-of-the-art efficiency was reached almost ten years ago, while research on *second* and *third* *generations* (green and orange points, respectively) is presently in progress, thus demonstrating the interest in finding some possible low cost competitors to Si-based solar cells.

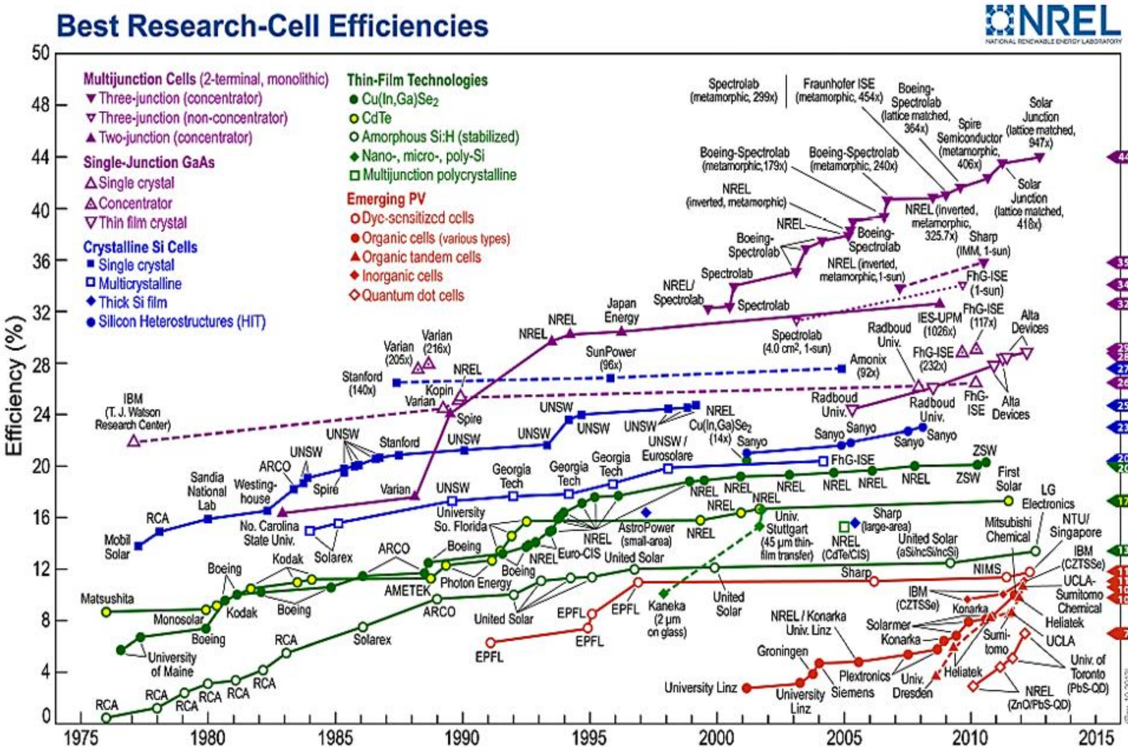

Fig. 1.10 Best Research-Cell Efficiencies chart [37].

1.3 Objectives and thesis structure

The main objective of this thesis is to develop and optimize innovative materials for Dye-sensitized Solar Cells application, with the aim of overcoming the drawbacks highlighted by the conventional ones. In particular, it is well known from the literature that TiO_2 presents the disadvantage of a reduced charge transport due to a long pathway for the electron diffusion within the semiconductor network; Ru-based sensitizers exhibit the important limits of expensive synthesis process, relatively low molar extinction coefficient in the visible region, limited availability of precursors and waste disposal troubles; finally, the main issues when exploiting liquid solvent-based electrolytes are their limited long-term stability, difficulty in sealing and leakage, which prevent the realization of devices having a high and constant-over-time efficiency. Within this framework, sponge-like and flower-like

ZnO nanostructures have been employed as alternative photoanode materials, hemi-squaraine organic sensitizer (CT1) has been exploited in substitution of Ru-based N719 dye, and UV-crosslinked polymer membrane and cellulose-based gel have been proposed in quality of quasi-solid electrolytes. In the fascinating but at the same time complex Dye-sensitized Solar Cells' research world, a theoretical support often reveals necessary to clarify and corroborate some experimental evidences. In this context, a physical model able to explain the aggregation phenomenon typically shown by organic dye molecules and an opto-electronic model applied to build a consistent picture of the static and dynamic small-signal performances of nanocrystalline TiO_2-based DSCs under different incident illumination intensities and directions will be presented.

The thesis is arranged into seven Chapters, the first one giving a brief introduction to the renewable energy sources focusing on the status of the today photovoltaic market. To introduce the backgrounds of the photovoltaic energy conversion and to define the right context of this study, a description of the current photovoltaic technologies with their basic operating principle and architecture is reported. This is preceded by a short consideration about the solar radiation and is followed by the purpose of the study as well as the outline of the thesis.

Chapter 2 introduces the Dye-sensitized nanostructured Solar Cells beginning with a description of the structure and the materials: the components of the cell are treated one by one at each time making a cut-through to the literature by examining the used materials, their key properties and the related preparation methods. The second part concentrates to the discussion of the fundamental physical and chemical processes of the cell operation and illustrates the main parameters of a solar cell.

Chapter 3 presents the experimental techniques exploited for the device characterization.

Chapter 4 is devoted to the description of materials and instrumentations used through the work, together with the device fabrication procedures.

Chapter 5 provides the theoretical support to the experimental activity, in particular a physical model able to explain the aggregation phenomenon of organic dye molecules and an opto-electronic model applied to describe the DSC performances under different operating conditions will be presented.

Chapter 6 discusses the experimental and theoretical results of the work.

Chapter 7 presents the general conclusions on the basis of the previous Sections, together with a brief discussion of future work to be done.

Almost all the experiments and characterizations were performed at the Center for Space Human Robotics @ PoliTO of the Istituto Italiano di Tecnologia (IIT) and in the Applied Science and Technology Department (DISAT) of the Politecnico di Torino, with the technological support of the Material and Microsystems Laboratory (χ-lab) of the Politecnico di Torino, in Chivasso.

This work is the result of a collaboration among the Center for Space Human Robotics @ PoliTO of the Istituto Italiano di Tecnologia (IIT), the Applied Science and Technology Department (DISAT) of the Politecnico di Torino, the Electronics and Telecommunications Department of Politecnico di Torino, the Chemistry Department of the Università degli Studi di Torino and the companies Cyanine Technologies S.p.A and Pianeta s.r.l..

References

---

[1] M. Grätzel, *Acc. Chem. Res.* **42**, 1788 (2009).

[2] U.S. Energy Information Administration, International Energy Outlook 2011, September 2011, http://www.eia.gov/forecasts/ieo/index.cfm.

[3] Intergovernmental Panel on Climate Change, http://www.ipcc.ch/index.htm.

[4] http:// www.exxonmobil.com.

[5] M. Grätzel, *Nature* **414**, 338 (2001).

[6] www.greenpeace.org/international/global/international/publications/climate/2011.

[7] www.epia.org/fileadmin/user_upload/Publications/Global-Market-Outlook-2016.pdf.

[8] E. Guillén Rodríguez, Photoelectrochemical characterization of dye solar cells based on nanostructured zinc oxide substrates, “PhD thesis” (2011).

[9] J. Nelson, “The Physics of Solar Cells”, (2003) Imperial College Press.

[10] http://cnx.org/content/m41217/1.1/.

[11] Solar Spectral Irradiance: Air Mass 1.5 http://rredc.nrel.gov/solar/spectra/am1.5/.

[12] www.tre-energia.com.

[13] W. Shockley, and H. J. Queisser, *J. Appl. Phys.* **32**, 510 (1961).

[14] A. Hagfeldt, G. Boschloo, L. Sun, L. Kloo, and H. Pettersson, *Chem. Rev.* **110**, 6595 (2010).

[15] M. A. Green, K. Emery, Y. Hishikawa, W. Warta, and E. D. Dunlop, *Prog. Photovoltaics Res. Appl.* **20**, 12 (2012).

[16] http://www.electronics-tutorials.ws/diode/diode_2.html.

[17] V. Avrutin, N. Izyumskaya, and H. Morkoç, *Superlattices Microstruct.* **49**, 337 (2011).

[18] S. J. Fonash, "Solar cell devices physics", (2010) Academic Press, Oxford.

[19] M. Pagliaro, G. Palmisano, and R. Ciriminna, "Il nuovo fotovoltaico", (2008) Dario Flaccovio Editore, Palermo.

[20] M. A. Green, “Third Generation Photovoltaics - Advanced Solar Energy Conversion”, (2006) Springer.

[21] http://newenergynews.blogspot.it/2008/06/thin-film-more-building-integratable.html.

[22] L. Travis, *Photosynth. Res.* **87**, 73 (2006).

[23] A. Belaidi, T. Dittrich, D. Kieven, J. Tornow, K. Schwarzburg, and M. Lux-Steiner, *Phys. Status Solidi RRL* **2**, 172 (2008).

[24] Y. Itzhaik, O. Niitsoo, M. Page, and G. Hodes, *J. Phys. Chem. C* **113**, 4254 (2009).

[25] K. Ernst, A. Belaidi, and R. Konenkamp, *Semicond. Sci. Technol.* **18**, 475 (2003).

[26] L. E. Greene, M. Law, B. D. Yuhas, and P. Yang, *J. Phys. Chem. C* **111**, 18451 (2007).

[27] M. Lira-Cantu, and F. C. Krebs, *Sol. Energy Mater. Sol. Cells* **90**, 2076 (2006).

[28] B. O'Regan, and M. Grätzel, *Nature* **353**, 737 (1991).

[29] M. A. Green, K. Emery, Y. Hishikawa, and W. Warta, *Prog. Photovoltaics Res. Appl.* **18**, 346 (2010).

[30] http://www.tft.kit.edu/21_152.php.

[31] C. Lèvy-Clèment, “Nanostructured Materials for Solar Energy Conversion”, 447 (2006) Elsevier.

[32] C. Lèvy-Clèment, R. Tena-Zaera, M. A. Ryan, A. Katty, and G. Hodes, *Adv. Mater.* **17**, 1512 (2005).

[33] M. Krunks, E. Kärber, A. Katersi, K. Otto, I. Oka Acik, Y. Dedova, and A. Mere, *Sol. Energy Mater. Sol. Cells* **94**, 1191 (2010).

[34] J. Chandrasekaran, D. Nithyaprakash, K. B. Ajjan, S. Maruthamuthu, D. Manoharan, and S. Kumar, *Ren. Sust. Energy Rev.* **15**, 1228 (2011).

[35] A. Yella, H. W. Lee, H. N. Tsao, C. Yi, A. K. Chandiran, M. K. Nazeeruddin, E. W. G. Diau, C. Y. Yeh, S. M. Zakeeruddin, and M. Grätzel, *Science* **334**, 629 (2011).

[36] www.cornellcollege.edu/physics/courses/phy312/Student-Projects/Solar-Cell/Solar-Cell.html.

[37] www.nrel.gov/ncpv/images/efficiency_chart.jpg.

Chapter 2: Dye-sensitized Solar Cells

This Chapter is fully devoted to the description of the Dye-sensitized Solar Cells. These devices belong to the *third generation* of photovoltaics, and are based on the use of organic and low cost materials and of cheap fabrication processes. In Section 2.1 a detailed overview of DSC architecture and components will be presented, while in Sections 2.2 and 2.3 the cell operating principle, with particular care dedicated to the charge transfer processes occurring inside the device, and the main parameters of a solar cell will be respectively described.

2.1 DSC structure and components

The standard architecture of a DSC, made up of a photoanode, a counter electrode and a liquid electrolyte solution [1], is reported in Fig. 2.1.

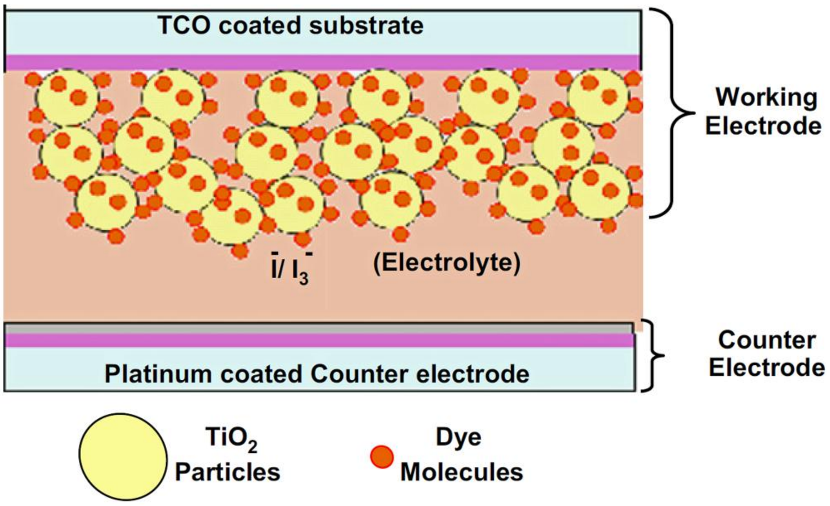

Fig. 2.1 Basic structure of a DSC [2].

The photoanode is constituted by a porous wide band gap semiconductor deposited onto a glass slice covered by a thin transparent conductive oxide (TCO) film. The photoanode is sensitized by a monolayer of dye molecules, responsible for light absorption and photoelectron generation. A nanostructured layer with a high specific surface area (SSA) is employed as photoanode material instead of a flat semiconductor [3] in order to ensure the attachment of a greater number of dye molecules to the surface, and thus achieving a relatively high light absorption and a higher photoconversion efficiency in the final device.

A TCO-covered glass, on which a thin film of catalyst is deposited, plays the role of the counter electrode. The catalyst allows speeding up the charge transfer between the electrode and the liquid solution.

Finally, an electrolytic solution, which penetrates the pores of the nanostructured photoanode to have a close proximity with the molecules of the sensitizer, is able to conduct holes through a redox couple and regenerate the oxidized dye molecules, thus closing the electrical circuit. In order to close the structure and to prevent electrolyte leakage, a thermoplastic material is placed between the electrodes and defines the electrolyte volume. In the following Sections the cell components and their main features will be thoroughly described.

2.1.1 Transparent conducting oxide-coated glass substrates

The electrodes of the standard DSC are prepared onto transparent conducting oxide (TCO)-coated glass substrates, between which the cell is assembled. The conducting coating of the substrate works as a current collector and the substrate material itself both as a support structure to the cell and as a sealing layer between the cell and the ambient air.

TCO can be opportunely deposited by sputtering or by low pressure chemical vapor deposition (LP-CVD). Sputtered TCO is basically flat and thus does not possess, as deposited, the light scattering properties required by the solar cells. However, surface nanotexturing can be achieved in a second step by chemical wet etching. TCO deposited by LP-CVD presents several advantages: it is basically a very simple process and easily upscalable up to 1 m, with deposition rates over 2 mm/s and the oxide grown has a high texturing with crystallographic preferential columnar growth.

A lot of TCOs were developed and studied in the last thirty years and, among them, Fluorine-doped Tin Oxide (FTO) and Indium Tin Oxide (ITO) are mostly used because they are considered the best compromise in terms of fabrication process, optical and electrical properties. Despite of the lower optical transparency and electrical conductivity (if compared with ITO), FTO is the preferred solution in DSC field, because of the high cost and the limited supply of indium, and the weak flexibility of ITO layers.

2.1.2 Photoanodes

The materials used to fabricate photoanodes are nanostructured oxide semiconductors, preferred in photoelectrochemistry because of their exceptional stability against photo-corrosion on optical excitation in the band gap [4]. Furthermore, the large band gap (> 3 eV) of the oxide semiconductors is needed in DSCs for the transparency of the semiconductor electrode for the large part of the solar spectrum.

Titanium dioxide has been, and still is, the cornerstone semiconductor for dye-sensitized nanostructured electrodes for DSCs [5]. In addition to TiO_2, other semiconductors have been studied and tested, like ZnO, CdSe, CdS, WO_3, Fe_2O_3, SnO_2, Nb_2O_5, and Ta_2O_5 [6].

Fig. 2.2 shows the two most important and used crystalline forms of TiO_2, i.e. anatase and rutile. Anatase appears as pyramid-like crystals and is stable at low temperatures, whereas needle-like rutile crystals are dominantly formed at high temperature processes. Single crystals of TiO_2 also have rutile structure. The densities are 3.89 g/cm^3 and 4.26 g/cm^3 for anatase and rutile respectively. Rutile absorbs about 4% of the incoming light in the near-UV region, and band gap excitation generates holes that act as strong oxidants reducing the long-term stability of the Dye-sensitized Solar Cells. The third crystalline form of TiO_2, brookite, is difficult to produce and it is therefore not of practical interest for the Dye-sensitized Solar Cells. The band gaps of the crystalline forms are 3.2 eV (the absorption edge at 388 nm) for anatase and 3.0 eV (the absorption edge at 413 nm) for rutile [4].

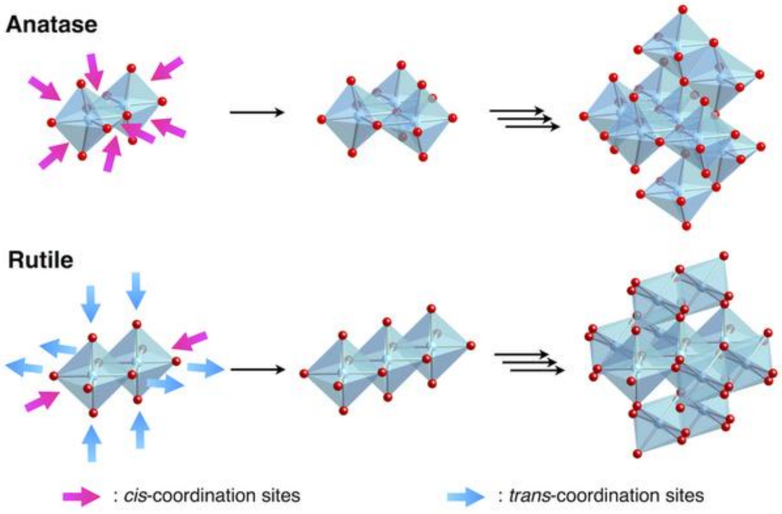

Fig. 2.2 Anatase and rutile crystalline forms of TiO_2 [7].

Titanium dioxide has some unique properties making it the preferred semiconductor for DSC. Its conduction band edge lies slightly below the excited state energy level of many dyes, that is one condition for efficient electron injection. Another positive aspect is the high dielectric constant of TiO_2 (ε = 80 for anatase) that provides good electrostatic shielding of the injected electron from the oxidized dye molecules attached on the TiO_2 surface, thus preventing their recombination before reduction of the dye by the electrolyte. Moreover, its refractive index has a suitable value (n = 2.5 for anatase) resulting in an efficient diffused scattering of the impinging light enhancing the light absorption. Some important and practical aspect of TiO_2 are that it is cheap, easily available and non toxic, in fact it is already employed as white pigment in paints and tooth pastes.

The TiO_2 film generally employed in a DSC is fabricated starting from a paste in which anatase nanoparticles (NPs), with a mean dimension of 20 nm, are dispersed. The oxide paste is deposited onto TCO substrates by tape casting or screen printing techniques and then it is subjected to a sintering process in order to enhance the electronic interconnection between the nanoparticles and the charge transfer towards the substrate. The NP-based photoanode presents at the same time the great advantage of a high SSA value (in the range 50 - 250 m^2/g), which permits the anchoring of a great number of dye molecules, and the disadvantage of a reduced charge transport due to a long pathway for the electron diffusion within the semiconductor network. In order to overcome this important drawback, thus ensuring enhanced transport properties, photoanode materials alternative to NPs, like 1-D nanostructures (nanorods [8], nanotubes [9], nanowires [10]), are becoming increasingly popular.

A promising alternative to Titanium dioxide for the fabrication of Dye-sensitized Solar Cells photoanode is Zinc oxide (ZnO) [11]. ZnO is a wide band gap semiconductor (energy gap 3.37 eV), with a conduction band edge positioned approximately at the same level as for TiO_2. With respect to Titanium dioxide, ZnO presents higher electron mobility and carrier lifetime, these parameters being very important to improve the performances of DSCs. Moreover, Zinc oxide is well known for its ability to easily grow in a wide variety of nanostructures, like for instance nanoparticles [12], nanowires or nanorods [13], nanotubes [14], nanosheets [15], nanoplants [16] and nanotetrapods [17]. At present, the photoconversion efficiencies of ZnO-based DSCs are below 8% [12, 18, 19], so the suggestion of new structures and/or architectures aimed at the improvement of the cell performances is an exciting challenge for the future research.

2.1.3 Sensitizers

The sensitizer can be regarded as the heart of a DSC: its role is to absorb photons and to generate electrons, which are subsequently injected into the conduction band of the semiconductor on which it is chemisorbed. The properties of the dye strictly affect the light harvesting efficiency and the overall photoelectric conversion efficiency of the solar cell.

Upon absorption of a photon, an electron is promoted from the fundamental state, the Highest Occupied Molecular Orbital (HOMO), to the excited one, the Lowest Unoccupied Molecular Orbital (LUMO). From the highest energetic orbital, if the energetic levels of the LUMO and the semiconductor conduction band (CB) are in favorable positions, the electron can pass into the oxide material. In fact, as will be explained in details in Section 2.2, the excited state of the dye must have a slightly higher energy with respect to the semiconductor conduction band of the oxide, in order to allow the injection of the excited electrons (the so-called staggered or type II heterojunction [20]); similarly, the HOMO level of the dye should be at lower energy with respect to the redox potential of the electrolyte to permit the dye regeneration [20]. For the mentioned reasons, an appropriate choice of the dye/semiconductor and dye/electrolyte pairs is of fundamental importance in order to have efficient DSCs. Another important property of the sensitizer is its absorption range: longer is the range, higher will be the cell efficiency. The light absorption spectrum of the dye must range from UV region to IR region, having an absorption peak in the visible range. Moreover the dye should be strongly anchored to the oxide surface in order to obtain a low charge transfer resistance and a stable chemical bond [21]. Finally, the dye should not incur in aggregation: often dye molecules tend to aggregate each other on the oxide surface, thus increasing the decay from the excited state to the fundamental one and consequently reducing the electron injection into the semiconductor CB. With the aim of decreasing the dye aggregation phenomenon, some additives are usually employed as co-adsorbent together with the sensitizer, such as the chenodeoxycholic acid (CDCA) [22].

The sensitizers typically used in DSC can be divided in two main families: metal-organic and organic dyes. Metal-based sensitizers exhibit some important limits: expensive synthesis process, relatively low molar extinction coefficient in the visible region, limited availability of precursors and waste disposal issues. In this context metal-free organic dyes could present several advantages, being obtainable with simple, fast and cost effective synthetic approach and characterized by high molar extinction coefficients [23, 24]. In comparison to the Ru-based sensitizers, however, organic dyes exhibit lower conversion efficiencies, due to the formation of dye aggregates on the semiconductor surface and to their narrow light absorption bands in the visible region.

Between metal-organic dyes, the most used ones are ruthenium or osmium derivates, which are characterized by prolonged long-term stability. In particular, the polypyridyl ruthenium sensitizer family allows fabricating DSCs with high conversion efficiency values: in Fig. 2.3 the molecular structures of most common ruthenium-based sensitizers are reported.

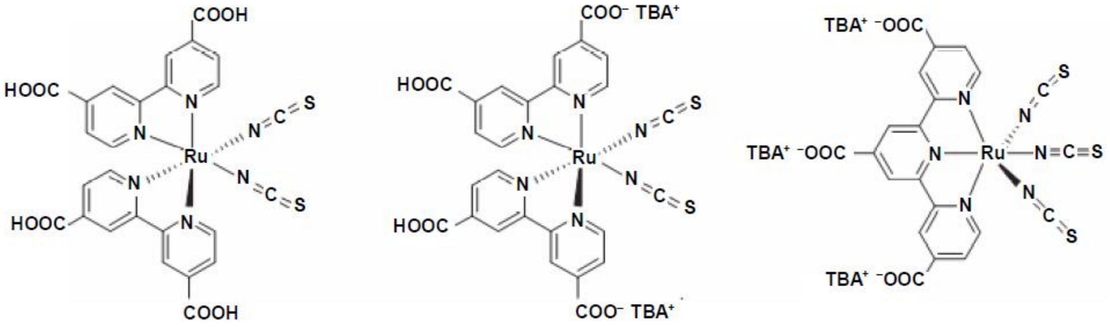

N3 **N719** **BLACK DYE**

Fig. 2.3 Molecular structure of N3, N719 and N749 (“black dye”) sensitizers [25].

The first developed sensitizer belonging to this group was the RuL_2 $(NCS)_2$ (L = 2,2’-bipyridyl-4,4’-dicarboxylic acid), known as N3 dye, which allows achieving a photoconversion efficiency as high as 10% [26]. Starting from this dye and substituting two protons with a tetra-n-butylammonium (TBA) cation group, the so-called N719 dye, $[RuL_2$ $(NCS)_2]$: 2 TBA, was obtained. The effect of the deprotonation is to change the polarity at the interface, thus shifting the semiconductor conduction band and increasing the V_{oc} of the cell. These Ru complexes are able to anchor to the TiO_2 surface by means of carboxyl groups. Anchoring causes a large electronic interaction between the ligand and the conduction band of the semiconductor, resulting in effective electron injection from the Ru complex into the oxide material.

The main disadvantage of these dyes lays in the reduced capability to absorb light with wavelengths greater than 600 nm: both N3 and N719 exhibit an absorption spectrum in the visible region, with an onset at about 700 nm. In order to overcome this important drawback, several dyes have been examined and proposed. It has been found that substituting some molecules of the dye, the LUMO level of the sensitizer raises and the

HOMO one decreases, leading to the absorption of higher wavelength light. For example, substituting a terpyridine group and a cyanide group with two bipyridine groups in the [RuL'(NCS)$_3$]: 3 TBA (L' = 2,2':6',2"-terpyridyl-4,4',4"-tricarboxylic acid) sensitizer (known as N749 or "black dye"), the absorption edge of the dye is shifted of approximately 100 nm towards IR region. This is confirmed by looking Fig. 2.4, where the *IPCE* (Incident Photon-to-electron Conversion Efficiency) spectrum of a DSC fabricated with black dye is compared with a N3-based one: it can be clearly seen that the black dye can absorb wavelengths up to 900 nm, so that the total photocurrent produced can be as high as 20.5 mA/cm^2 [27].

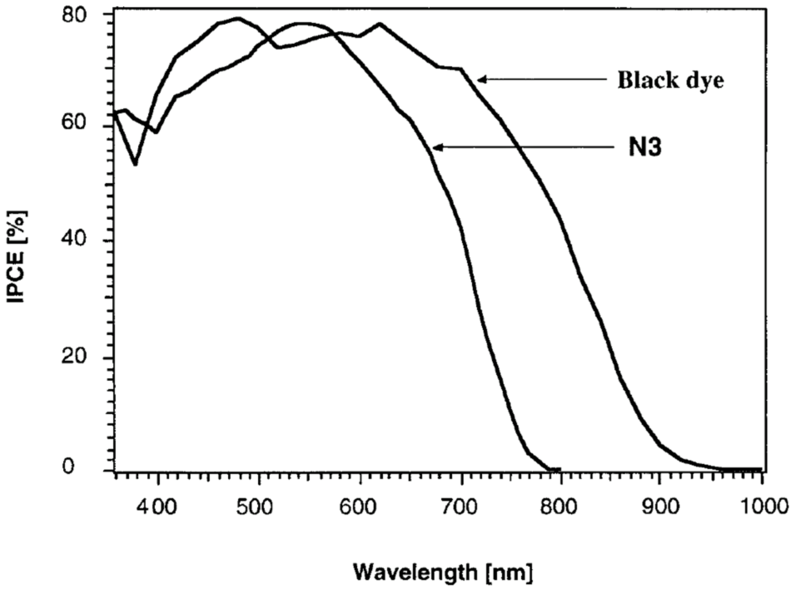

Fig. 2.4 Incident Photon-to-electron Conversion Efficiency of DSCs sensitized by N3 and N749 ("black dye") dyes [28].

Different families of organic sensitizers have been proposed in the last decade. In recent years, the development of DSCs based on organic dyes has been very rapid and the conversion efficiency of these cells has become comparable to the one of cells based on polypyridyl ruthenium dyes. Among the most commonly used organic dyes, it's important to mention the coumarin, the indoline, the cyanine and the squaraine dyes. Fig. 2.5 reports examples of sensitizers belonging to these families. Hara *et al.* proposed a series of coumarin derivatives and an efficiency of 7.7% [29], which is comparable with that for N719, was obtained. Indoline dyes, known for their reduced photodegradation that permits a high long-term stability of the cell, were synthesized for the first time by Uchida and co-workers [30] and a 9.5% photoconversion efficiency was achieved with the so-called D205 dye. Cyanine dyes are known for their high molar extinction coefficient values and the capability to absorb the near-IR radiation [31]. However the photovoltaic performances of DSCs based on these dyes are quite low: for example using the Cy3 dye, a 4.8% of PCE under 75 mW/cm^2 illumination has been obtained [32]. Representative sensitizers of the squaraine family are SQ1 and SQ2 dyes, proposed by Grätzel and co-workers [33, 34], which are characterized by relatively high conversion efficiencies (4.5% and 5.4% respectively), high molar extinction coefficient values and strong electronic coupling with the TiO_2 surface.

Sensitization with one single dye molecule is often poorly performing, since its absorption spectrum is hardly matched with the solar emission spectrum. In order to overcome this limit, co-sensitization of several dyes with different spectral response reveals to be a quite common strategy employed to increase the DSC performances. Zhang *et al.* [35, 36] used a series of squaraine dyes as co-sensitizer of ruthenium polypyridyl complexes and improved of 13% the efficiency for Dye-sensitized Solar Cells than those sensitized with simple ruthenium polypyridyl complexes.

An alternative to the use of molecules chemisorbed on the surface of the oxide material is the application of semiconductor quantum dots. They are particles made by a small number of atoms coming from II-VI or III-V groups with very small dimensions. They have a very wide absorption spectrum and it can be modified changing the dimension of the particles. A drawback of quantum dots is their easy corrosion when put in contact with a liquid electrolyte.

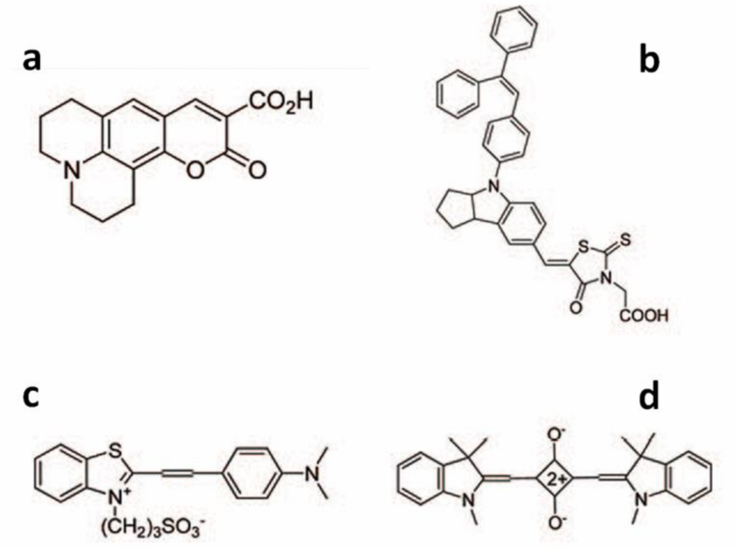

Fig. 2.5 Molecular structures of dyes belonging to different families of organic sensitizers: a) coumarin, b) indoline, c) cyanine and d) squaraine [5].

2.1.4 Counter electrodes

Like the photoanode, also the counter electrode is fabricated starting from a glass covered with a film of conductive oxide. In order to ensure a sufficiently fast reduction reaction kinetics at the TCO-coated cathode, a catalyst coating is needed [5].

The most employed catalysts in DSCs are platinum and carbon-based materials. The use of Pt assures high values both of current and voltage, and it is characterized by low counter electrode resistance [37]; platinum catalyst coating can be easily performed for example electrochemically [6, 38], by sputtering [26], pyrolytically or by spin coating [39]. Electrochemically and vapor deposited [40] Pt has been however found unstable in presence of the iodide-based electrolyte. An alternative Pt catalyst coating method called "platinum thermal cluster catalyst" has been developed. This catalyst provided superior kinetic performances with respect to conventional platinum deposition methods, chemical and electrochemical stability in practical cells and low platinum loading of 5 - 10 mg/cm^2, thus leading to costs reduction, mechanical stability of the counter electrode surface and optical transparency of the counter electrode due to the low platinum content.

While showing excellent catalytic action, platinum has the disadvantage of being very expensive. A low cost solution for counter electrode fabrication is represented by graphite [41]. The main problems related to this material are the low homogeneity and adhesion to the substrate, so the performances of the cells based on this catalyst are lower with respect to the Pt-based ones [42]. An interesting alternative material is graphene, which in principle could act as transparent conductive film and catalyst at the same time, thus reducing the counter electrode fabrication costs [43]. Finally, another promising design utilizes a porous carbon counter electrode as a catalyst layer. This carbon electrode is made from a mixture of carbon black, graphite powder and nanocrystalline TiO_2 particles. A high conductivity (sheet resistance of 5 Ω/sq for a 50 μm-thick layer) is obtained due to the carbon black particles connecting together separate graphite flakes, while the TiO_2 particles are used as a binder to the structure.

2.1.5 Electrolytes

The electrolyte plays one of the most relevant roles in the process of light-to-electricity conversion, since it works as an electron transfer mediator with the function of regenerating the dye sensitizer from the oxidized state. The requirements that must be met for any electrolyte employed in a Dye-sensitized Solar Cell are listed here below:

1. The electrolyte must have long-term stability, including chemical, thermal, optical and electrochemical stability, to prevent the degradation of the dye from the oxide surface.

2. The electrolyte must be able to transport the carriers between the working electrode and the back electrode. After the injection of the electrons into the conduction band of the oxide material, the oxidized dye must be regenerated and reported to its ground state. That is why the electrolyte must be chosen in a proper way in order to take into account the redox potential and the recombination properties of the dye.

3. The electrolyte must ensure the fast diffusion of the charge carriers into the device and produce good contact with the porous nanocrystalline oxide layer and the counter electrode. For liquid electrolytes it is necessary to prevent the loss of the solution by leakage or evaporation.

4. The electrolyte should not exhibit a significant absorption in the range of visible light. For electrolytes containing I^-/I_3^- couple, since I_3^- has its own color and reduces the visible light absorption by the dye, and I_3^- ions can react with the injected electrons, the dark current should be increased; that is why the concentration of I^-/I_3^- must be optimized.

Electrolytes for DSCs can be classified as liquid, quasi-solid, or solid, depending on their viscosity. The most common class of electrolytes used in DSCs is the liquid organic solvent-based one. They are usually constituted by a redox couple dissolved in a high dielectric constant organic solvent; moreover some additives can be inserted in order to increase the device performances [5].

The highly employed redox couple is iodide/triiodide (I^-/I_3^-), mainly because of the slow recombination reaction; electrolytes based on this couple are commonly prepared by dissolving iodide salts with different cations (Li^+, Na^+, Mg^+) in the liquid solvent. However the corrosive properties of iodine have led to the investigation of alternative redox couples, like Br^-/Br_3^- [44], $SCN^-/(SCN)_3^-$ [45] and $SeCN^-/(SeCN)_3^-$ [46], which have promising electrochemical and noncorrosive properties, but suffer for chemical instability [5]. Also some coordination compounds such as copper and cobalt complexes can act as redox mediators [47, 48]. Currently, Co complexes are the most promising redox couples, since they are noncorrosive, nonvolatile, and relatively transparent to the visible light. Moreover, it has been recently shown that $Co^{(II/III)}$tris(bipyridyl)-based redox electrolyte can exceed 12% efficiency [49].

Concerning the solvent, it must have low volatility in the operating DSC temperature range, low viscosity in order to allow the fast diffusion of charges, and a high dielectric constant to make the redox couple dissolution easier [5]. Between all the solvents used in DSC research field, acetonitrile (ACN) can be regarded as the most performing, due to its excellent stability, low viscosity and capability to dissolve a lot of salts and organic molecules. Unfortunately ACN boiling point is low (78 °C), so for long-term stability tests of the DSCs the preferred choice falls on 3-methoxypropionitrile (MPN), characterized by 164 °C boiling point and low toxicity: an efficiency of 7.6% after 1000 h of continuous irradiance has been achieved using MPN as solvent [50]. Less used solvents are water, ethanol, ethylene carbonate and propylene carbonate [51].

Regarding the additives, a lot of cations and compounds have been introduced and tested in liquid electrolytes in order to enhance the photovoltaic performances of the cell. Between them, the most employed one is the 4-tert-butylpyridine (TBP), whose effect is to suppress the dark current and increase Fill Factor and efficiency values, by inducing the coordination between N atoms and Ti ions on the TiO_2 surface, thus limiting the electron recombination [52]. The addition of guanidinium thiocyanate (GuSCN) in the liquid electrolyte leads to an increase of both current and voltage, due to a positive shift of the TiO_2 CB and a reduction of charge recombination [53]. Also Li cations are commonly used as additives: they can be adsorbed on the TiO_2 nanoparticles surface, leading to an important increase in photocurrent density values. This effect is due to the ability of Li ions to lower the acceptor states of TiO_2, changing the flat band on the photoanode surface and making the electron injection more energetically favorable [54].

The main issues when exploiting liquid solvent-based electrolytes are their limited long-term stability, difficulty in sealing and leakage, which prevent the realization of devices having a high and constant-over-time efficiency. To overcome these drawbacks, different alternative solutions have been proposed and are currently under study. Between them, a special consideration has to be deserved to the solvent-free liquid electrolytes, the quasi-solid electrolytes and the solid electrolytes.

The former are based on the so-called room temperature ionic liquids (RTIL) and are characterized by reduced volatility, good chemical and thermal stability and high ionic conductivity. Widely used RTILs for DSCs are alkyl imidazolium salt, trialkyl methylsufonium salt and alkylpyridinium salt. The only drawback of RTILs is their high viscosity, which makes the diffusion of the charge carriers rather slow [55].

Quasi-solid electrolyte can be obtained starting from organic solvent-based or ionic liquid electrolytes that can be gelled, polymerized, dispersed in polymeric matrix, or in which nanoparticles are dispersed [5].

Solid state electrolytes are represented by conductive polymers, hole-conducting molecular solids or organic p-type conductors, like polypyrrole [56], poly(3,4-ethylenedioxythiophene) (PEDOT) [57], poly(3-hexylthiophene) (P3HT) [58], polyaniline (PANI) [59] and 2,2′7,7′-tetranis-(N,N-di-p-methoxyphenyl-amine)9,9′-spirobifluorene (spiro-OMeTAD) [60]. However, the photovoltaic performances of DSCs based on all these alternative electrolytes are currently lower with respect to the liquid solvent-based ones, so further work is required.

2.1.6 Sealing

Sealing the DSCs has long been a difficult issue because of the corrosive and volatile liquid iodide electrolyte employed in the cells. Being directly related to the long-term stability of the cells, it seems to be one of the main technological challenges of the DSC technology. A suitable sealing material should at least:

1. Be leak-proof to the electrolyte components and impermeable to both ambient oxygen and water vapor.

2. Be chemically inert towards the electrolyte and the other cell components.

3. Adhere well to the glass substrate and the TCO coating.

Several sealing materials have been used, such as epoxy glue, water glass (sodium silicate) [41], an ionomer resin Surlyn® (grade 1702) from Du Pont, aluminum foil laminated with polymer foil [41], a vacuum sealant Torr Seal®, or a combination of these. When employing a sealing material, the cell assembly process becomes more time consuming. In fact, after the structure sealing, the electrolyte has to be inserted by means of a vacuum procedure, which consists in pouring an electrolyte droplet on the top of a hole drilled on the counter electrode and evacuating the free space between the electrodes, thus allowing the complete electrolyte filling into the volume [61]. One important question when selecting the sealant is the tolerance of the sealing material towards iodide and triiodide in the electrolyte. Interestingly, despite the fact that the most used sealant, the Surlyn® ionomer resin from Du Pont, has been classified by the manufacturer as not resistant towards iodine in long-term exposure, stable long-term operation has been demonstrated for DSCs utilizing Surlyn® sealing with iodide-based electrolytes.

2.2 Principle of operation

Dye-sensitized Solar Cells are photoelectrochemical devices where several electron transfer processes run in parallel and in competition. In contrast to the semiconductor *p-n* junction solar cells, where light absorption and charge transport occur in the same material, the DSC separates these functions: photons are absorbed by the dye molecules and transport of charges is carried out in the TiO_2 electrode and in the electrolyte.

In DSCs, the photoanode is a mesoporous oxide layer composed of nanometer-sized particles which have been sintered together to allow the electronic conduction. Attached to the surface of the oxide is a monolayer of dye molecules, which upon light absorption are promoted into an excited state. As a result, electrons from the valence band (VB) are injected into the conduction band (CB) of the semiconductor, giving rise to the formation of excitons and to the subsequent charge separation. The free electrons in the conduction band diffuse across the semiconductor towards the external circuit, performing electrical work. Once the electrons reach the counter electrode (CE), they react with the electrolyte that fills the space between the two electrodes. The original state of the oxidized dye is subsequently restored by electron donation from the electrolyte, which is itself regenerated at the platinum counter electrode by reduction of triiodide [21, 62, 63, 64]. The redox electrolyte therefore allows the transport of electrical charge between the two electrodes of the DSC, closing the cycle.

The efficiency of a DSC is strongly related to the electronic energy levels of the excited state (LUMO) and the ground state (HOMO) of the dye, by the electron Fermi level of the semiconductor and by the redox potential of the electrolyte. In particular, the dye LUMO must have an energy higher than the oxide CB and the HOMO should be lower with respect to the redox potential: for the above reasons the sensitizers have to be designed and synthesized in the appropriate way, to match the energy requirements of semiconductor and redox couple. The cell itself is able to produce a voltage drop between the two electrodes on the external load. The maximum photoelectric voltage that can be reached in open circuit condition is called V_{oc} and it is defined as the difference between the TiO_2 Fermi energy, E_F, and the redox potential of the electrolyte, E_{redox}. The cell can be defined as a “closed system” because when the structure has been assembled, during the operation, any chemical substance is destroyed or produced. However, some unwanted reactions resulting in losses in the cell efficiency can occur. The most important loss mechanisms are the direct recombination of the excited dye and the recombination of the injected electrons in the TiO_2 with the oxidized dye or with the holes in the electrolyte.

Fig. 2.6 shows the sequence of the charge transfer processes responsible for the operation of a DSC [65]:

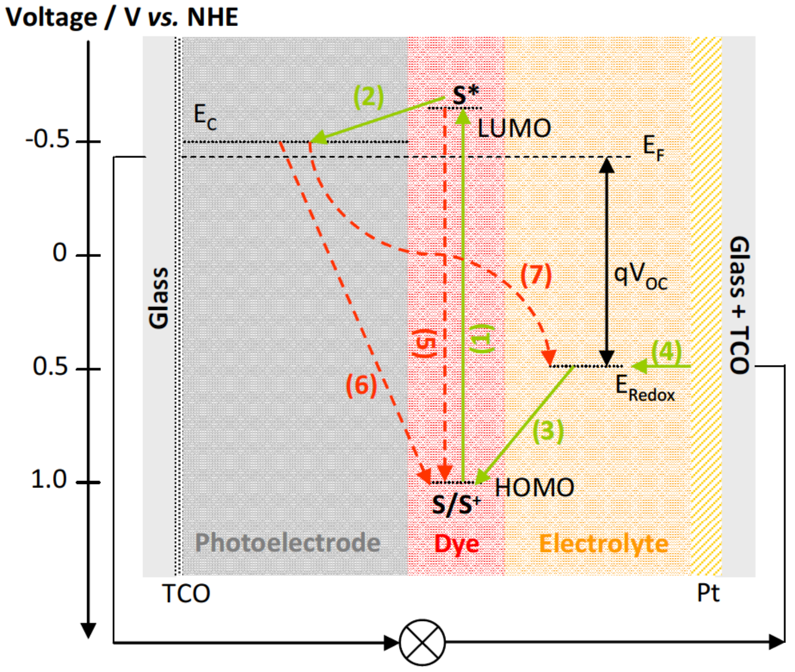

Fig. 2.6 Schematic diagram of the operation kinetics of a DSC: forward electron transfer (→) and electron loss pathways (– – →) [66].

1. The photosensitizer, adsorbed on the surface of the semiconductor, absorbs the incident sunlight and becomes excited from the ground state (S) to the excited state (S^*)

$$S + h\nu \rightarrow S^* \tag{2.1}$$

2. The excited electrons are injected into the conduction band of the semiconductor, resulting in the oxidation of the sensitizer (S^+)

$$S^* \rightarrow S^+ + e^-_{CB} \tag{2.2}$$

3. The oxidized sensitizer (S^+) is regenerated by accepting electrons from the iodide ion

$$S^+ + \frac{3}{2}I^- \rightarrow \frac{1}{2}I_3^- + S \tag{2.3}$$

4. The triiodide redox mediator diffuses towards the counter electrode and is reduced to iodide

$$I_3^- + 2e^-_{CE} \rightarrow 3I^- \tag{2.4}$$

Additionally to the forward electron transfer and ionic transport processes, several competing electron loss pathways should be considered:

5. Decay of the dye excited state to the ground state

$$S^* \rightarrow S \tag{2.5}$$

6. Recombination of the injected electrons with the dye cations

$$S^+ + e^-_{CB} \rightarrow S \tag{2.6}$$

7. Recombination of the injected electrons with the triiodide redox mediator

$$I_3^- + 2e_{CB}^- \rightarrow 3I^- \tag{2.7}$$

The charge transfer processes and the unwanted loss mechanisms presented above will be discussed in details in the following Sections.

2.2.1 Absorption of light

The high efficiency of the Dye-sensitized Solar Cell is due to a series of effects of numerous well-tuned physical and chemical properties. The most important one is the use of large band gap semiconductor material as electrode. Its properties are enhanced by the coating of the internal surface of the porous semiconductor with special dye molecules tuned to absorb the incoming light. The dye is adsorbed on the TiO_2 surface thanks to special anchoring groups attached to the dye molecule. The absorption of an impinging photon happens via an excitation between the electronic states of the molecule: in Ru complexes- based dyes, the excitation is of metal-to-ligand charge-transfer (MLCT) type, as reported in Fig. 2.7.

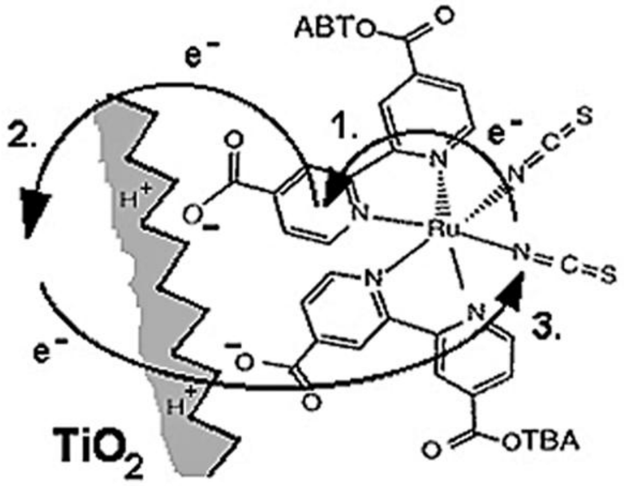

Fig. 2.7 Charge transfer processes between the dye and the TiO_2 lattice: 1. MLCT excitation; 2. Electron injection; 3. Charge recombination [67].

The highest occupied molecular orbital (HOMO) is placed near the Ru metal atom, whereas the lowest unoccupied molecular orbital (LUMO) is localized at the ligand species. When an excitation occurs, an electron is transferred from the HOMO to the LUMO level and, since there is a partial overlapping between the electron wavefunctions of the LUMO level of the dye with the conduction band of the oxide material, the electron is subsequently fast injected into the TiO_2 conduction band.

The injection process for Ru complex-based sensitizers attached to an oxide surface occurs in the femtosecond time scale [68]. In order to achieve good device performances, the duration of the injection process should be compared with the decay of the excited state of the dye to the ground state (process (5) reported in Fig. 2.6). This is given by the excited state lifetime of the dye, which for typical Ru complexes employed in DSCs is 20 - 60 ns [62]: by looking at these values, it can be stated that for this kind of dye the injection is an ultrafast process. However, for an efficient device, it is fundamental that also the quantum efficiency for injection is high. The electron injection efficiency is defined as follows

$$\eta_{inj} = \frac{k_{inj}}{k_{inj}+k_d}, \tag{2.8}$$

where k_{inj} and k_d are the rate constants for electron injection and decay of the excited dye, respectively; for efficient injection, k_{inj} should be about 100 times larger than k_d.

2.2.2 Charge separation

The charge separation in DSCs is based on the electron transfer from the dye molecule to the TiO_2 and on the movement of the holes from the oxidized dye to the electrolyte. The electron transfer mechanism is strongly related to the electronic structure of the adsorbed dye molecule and the energy level matching between the excited state of the sensitizer and the conduction band of the oxide semiconductor.

The main difference between the typical *p-n* junction cell and the one based on nanoparticle electrode/electrolyte interface is that the charge separation in silicon-based cell occurs thanks to an electric field across the junction region; instead in a DSC it is slightly different, because the small dimensions of the particles of the nanostructured electrode does not allow the generation of a field. The electrolyte surrounding all the nanoparticles decouples them and screens any electric field in a range of about a nanometer [69]. Even if the band bending inside the particles is denied, an electric field is otherwise created at the oxide/electrolyte interface thanks to the adsorbed dye molecules. In particular, the latter usually employ acid anchoring groups (COOH) as attachment units and, during the binding with the TiO_2, a proton (H^+) is released, leaving the dye molecule negatively charged. The generated potential difference is estimated to be approximately 0.3 eV and it is the responsible for the charge separation. The most important mechanism for the separation of charges is however the relative position of the energetic levels: the excited level of the dye must be higher with respect to the conduction band of the oxide, and the HOMO level of the sensitizer must be below the redox potential of the electrolyte.

2.2.3 Charge transport

In a Dye-sensitized Solar Cell, the charge transport occurs thanks to the electron transport in the nanostructured TiO_2 photoelectrode and to the hole transport in the electrolyte: both these mechanisms equally affect the overall performances of the cell.

The semiconductor nanoparticle network works not only as a large surface area substrate for the dye molecules but also as a transport media for the electrons injected from the dye molecules. Because of the porous structure of the electrode and of the screening effect of the electrolyte, the electrode can be viewed as an ensemble of individual particles through which electrons percolate by hopping from one particle to the next [62]. As mentioned above, the small size of the particles prevents the formation of a space charge layer and a *built-in* electric field inside the particles, and therefore the electrons cannot be drifted by an electric field. The collection of the electrons in the conduction band of the TiO_2 particles under illumination results in an electron concentration gradient in the electrode, and the electrons are transferred to the TCO back contact layer by diffusion. The movement of the electrons is characterized by a distribution of diffusion coefficients, related to the hopping of the electrons via surface traps of different depths [62]. These electron traps are localized energy states just below the conduction band edge of the semiconductor oxide and play a significant role in the electron transport. The diffusion coefficient of the electrons is strictly related with the position of the electron quasi-Fermi level under illumination. If the cell is exposed to a low illumination condition, only deep traps contribute to the electron transport, leading to a low diffusion coefficient. If the light intensity increases, the quasi-Fermi level raises and the number of traps contributing to the transport of electron increases, allowing a higher diffusion coefficient and so a higher photocurrent. The electron, together with its screening charge in the electrolyte side of the particle surface, can be viewed as a polaron moving by the electron diffusion towards the back contact where the electron is subsequently separated.

On the other side, considering positive charges, the electrolyte in a DSC works as a hole-conducting medium. At the photoelectrode the oxidized dye, left behind by the electron injected to the conduction band of the TiO_2, is regenerated by the I^- present in the electrolyte in the reaction reported by Eq. (2.3), while at the counter electrode I_3^- is reduced to I^- in the reaction reported by Eq. (2.4). In other words, I_3^- is produced at the TiO_2 electrode, it diffuses into the electrolyte and at the end it is consumed at the counter electrode. In the same way, I^- is produced at the counter electrode, it diffuses into the electrolyte in the opposite direction with respect to I_3^- and finally it is consumed at the TiO_2 interface. Summarizing, the electrolyte can be regarded as essentially a neutral sink of I^- and I_3^- feeding the reactions (2.3) and (2.4) at the electrodes and maintaining the redox potential in the bulk of the electrolyte via the fast redox reaction of the I^-/I_3^-. This redox reaction in the electrolyte is a two-electron reaction [70]

$$3I^- \Leftrightarrow I_3^- + 2e^- \tag{2.9}$$

which is composed of a series of successive reactions

$$(I^- \Leftrightarrow I + e^-)\ x2 \qquad \textit{charge transfer reaction,} \tag{2.10}$$

$$2I \Leftrightarrow I_2 \qquad \textit{fast chemical reaction,} \tag{2.11}$$

$$I_2 + I^- \Leftrightarrow I_3^- \qquad \textit{fast chemical reaction.} \tag{2.12}$$

2.2.4 Recombination

The recombination of the generated electrons with the holes in the dye-sensitized nanostructured TiO_2 electrode can in principle occur both after the electron injection or during its migration in the TiO_2 electrode on its way to the electrical back contact. The recombination of the injected electrons in the photoelectrode with the oxidized dye or with the holes in the electrolyte, which are two of the most important loss mechanisms in a DSC, will be thoroughly discussed here below.

The kinetics of the back electron transfer reaction from the semiconductor CB to the oxidized sensitizer (process (6) reported in Fig. 2.6 and in Eq. (2.6)) follows a multi exponential time law, occurring on a microsecond to millisecond time scale (depending on the electron concentration in the semiconductor and thus on the light intensity). The recombination of the electrons in TiO_2 with the acceptors in the electrolyte (process (7) reported in Fig. 2.6 and in Eq. (2.7)) is usually regarded as the electron lifetime (τ_n). Lifetimes observed with the I^-/I_3^- are very long (1 - 20 ms under 1 sun light intensity) compared with other redox systems employed in a DSC, thus clarifying why this redox couple is the commonly used one.

These two recombination mechanisms are possible in a DSC since the electrons are always within only a few nanometers distance from the semiconductor/electrolyte interface during their transport through the mesoporous TiO_2 film. In particular, taking place on the same time scale, the recombination of the electrons with the oxidized dye molecules can be in competition with the regeneration process. In fact, when the electron concentration in the TiO_2 nanoparticles increases, a strong enhancement in the recombination kinetics is evidenced [71]. In this case, it is useful to define the regeneration efficiency, η_{reg}, which gives the probability that an oxidized dye molecule is regenerated by an electron donor in the electrolyte rather than by the recombination with an electron in the TiO_2

$$\eta_{reg} = \frac{k_{reg}}{k_{reg}+k_{rec}}, \tag{2.13}$$

where k_{reg} is the rate constant for the regeneration process and k_{rec} is the first-order rate constant for the recombination of the electrons with the oxidized dye molecules. On the other side, regarding the recombination of the electrons in the TiO_2 with the acceptors in the electrolyte, this phenomenon can compete with the transport through the oxide, being in same time range. In order to have an efficient energy production, the oxide transport time τ_t should be lower than the electron lifetime: in this case the electrons are able to reach the front electrode before the recombination occurs. Often the transport properties are described with the diffusion length L_n, which is the square root of the product of the electron lifetime and the diffusion coefficient

$$L_n = \sqrt{\tau_n D_n}. \tag{2.14}$$

If this parameter is greater than the film thickness, all the photogenerated electrons will be statistically collected [3].

2.3 Main parameters of a solar cell

A photovoltaic cell is a device able to convert the incident sunlight to electrical energy, exploiting the photoelectric effect. The generation of the electrical power under illumination is achieved by the capability of the photovoltaic device to produce voltage over an external load and current through the load at the same time.

Fig. 2.8 shows the typical Current-Voltage (*I*-*V*) characteristic of a generic solar cell, together with some important figures of merit: the open circuit voltage V_{oc}, the short circuit current I_{sc} and the maximum power point P_{max}.

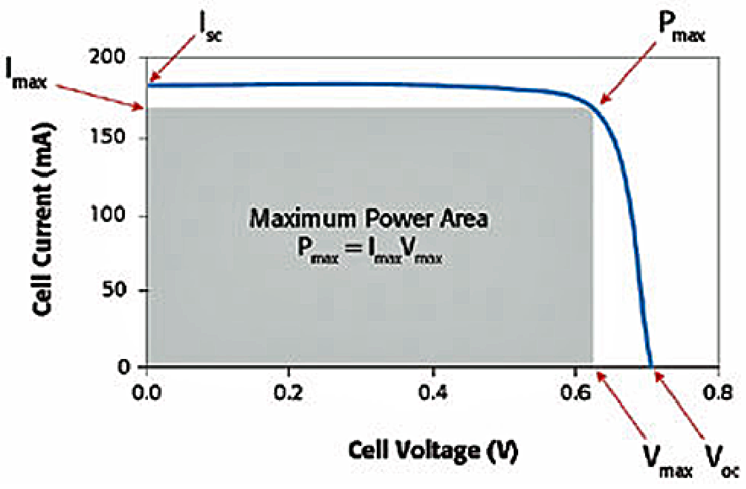

Fig. 2.8 Typical *I*-*V* characteristic of a solar cell [72].

The open circuit voltage V_{oc} is the maximum voltage generated by the solar device when it is connected to an infinite resistance (i.e. when no current flows) and it is defined as the difference between the potential of the conduction band of the TiO_2 and the redox potential of the electrolyte. The short circuit current I_{sc} represents the maximum current when the electrodes are short circuited, while the maximum power point P_{max} is the point in which the product of the current and the voltage is maximum. The current flowing in the device is dependent on the area illuminated by the sun radiation, so it is preferable to refer to the short circuit current density J_{sc} and the maximum current density J_{max} instead of the short circuit current and maximum current, simply dividing the currents for the exposed area A of the cell. Another important parameter obtainable from the *I*-*V* characteristic is the Fill Factor FF, which is a measure of the cell quality and is defined as the ratio between the theoretical maximum power obtainable (J_{max} V_{max}) and the measured power (J_{sc} V_{oc})

$$FF = \frac{J_{max}\,V_{max}}{J_{sc}\,V_{oc}}. \tag{2.15}$$

Finally, the most important parameter derived from the *I-V* characteristic is the PhotoConversion Efficiency (*PCE*), defined as the ratio between the maximum power developed by the cell and the power density of the incoming solar radiation in the cell P_{inc}

$$PCE = \frac{P_{max}}{P_{inc}} = \frac{J_{sc}\,V_{oc}\,FF}{W_{inc}}, \tag{2.16}$$

where W_{inc} is the optical incident power density (equal to 100 mW/cm^2, also called 1 sun, under standard AM 1.5 G condition, see Section 1.2.2).

Another crucial parameter necessary to evaluate the performances of a solar cell, and in particular to determine the maximum current obtainable from the device, is the Quantum Efficiency (*QE*), which represents the number of electrons photogenerated by an incident photon for a given wavelength λ. Two QEs, differing only in terms of the reflected light, can be defined: the Internal Quantum Efficiency (*IQE*), where only the photons not reflected by the cell surface are taken into account, and the External Quantum Efficiency (*EQE*), which accounts for all the impinging photons. These two quantities are linked by the following relation

$$EQE(\lambda) = [1 - R(\lambda)] \cdot IQE(\lambda), \tag{2.17}$$

where $R(\lambda)$ represents the reflectivity of the surface.

Using the external quantum efficiency, also known as Incident Photon-to-electron Conversion Efficiency (*IPCE*), the short circuit current density J_{sc} can be evaluated as

$$J_{sc} = q \int \Phi(\lambda)\, IPCE\,(\lambda) d\lambda, \tag{2.18}$$

where q is the elementary charge value, $\Phi(\lambda) = E(\lambda)/(hc/\lambda)$ is the incident photon flux for a given wavelength λ, $E(\lambda)$ is the solar spectral irradiance, h is the Planck constant and c is the speed of the light.

References

[1] M. K. Nazeeruddin, E. Baranoff, and M. Grätzel, *Sol. Energy* **85**, 1172 (2011).

[2] H. C. Weerasinghe, F. Huang, and Y.-B. Cheng, *Nano Energy* **2**, 174 (2013).

[3] M. Grätzel, *Inorg. Chem.* **44**, 6841 (2005).

[4] H. G. Agrell, G. Boschloo, and A. Hagfeldt, *Phys. Chem. B* **108**, 12388 (2004).

[5] A. Hagfeldt, G. Boschloo, L. Sun, L. Kloo, and H. Pettersson, *Chem. Rev.* **110**, 6595 (2010).

[6] A. Hagfeldt, and M. Grätzel, *Chem. Rev.* **95**, 49 (1995).

[7] N. Satoh, T. Nakashima, and K. Yamamoto, *Sci. Rep.* **3**, 1959 (2013).

[8] K. Fujihara, A. Kumar, R. Jose, S. Ramakrishna, and S. Uchida, *Nanotechnology* **18**, 365709 (2007).

[9] G. K. Mor, O. K. Varghese, M. Paulose, K. Shankar, and C. A. Grimes, *Sol. Energy Mater. Sol. Cells* **90**, 2011 (2006).

[10] X. Feng, K. Shankar, O. K. Varghese, M. Paulose, T. J. Latempa, and C. A. Grimes, *Nano Lett.* **8**, 3781 (2008).

[11] Q. Zhang, C. S. Dandeneau, X. Zhou, and G. Cao, *Adv. Mater.* **21**, 4087 (2009).

[12] K. Keis, E. Magnusson, H. Lindstrom, S.-E. Lindquist, and A. Hagfeldt, *Sol. Energy Mater. Sol. Cells* **73**, 51 (2002).

[13] D. Calestani, M. Zha, L. Zanotti, M. Villani, and A. Zappettini, *Cryst. Eng. Comm.* **13**, 1707 (2011).

[14] Q. C. Li, V. Kumar, Y. Li, H. T. Zhang, T. J. Marks, and R. P. H. Chang, *Chem. Mater.* **17**, 2001 (2005).

[15] J. H. Xiang, P. X. Zhu, Y. Masuda, M. Okuya, S. Kaneko, and K. Koumoto, *J. Nanosci. Nanotechnol.* **6**, 1797 (2006).

[16] A. Tiwari, and M. Snure, *J. Nanosci. Nanotechnol.* **8**, 3981 (2008).

[17] D. Calestani, M. Zha, R. Mosca, A. Zappettini, M. C. Carotta, V. Di Natale, and L. Zanotti, *Sens. Actuat. B* **144**, 472 (2010).

[18] I. Gonzalez-Valls, and M. Lira-Cantu, *Energy Environ. Sci.* **2**, 19 (2009).

[19] N. Memarian, I. Concina, A. Braga, S. M. Rozati, A. Vomiero, and G. Sberveglieri, *Angew. Chem. Int. Ed.* **50**, 1 (2011).

[20] A. Calzolari, A. Ruini, and A. Catellani, *J. Am. Chem. Soc.* **133**, 5893 (2011).

[21] F.-T. Kong, S.-Y. Dai, and K.-J. Wang, *Adv. OptoElectron.* **2007**, 75384 (2007).

[22] A. Mishra, M. K. R. Fischer, and P. Bäuerle, *Angew. Chem. Int. Ed.* **48**, 2474 (2009).

[23] J. Park, C. Barolo, F. Sauvage, N. Barbero, C. Benzi, P. Quagliotto, S. Coluccia, D. Di Censo, M. Grätzel, M. K. Nazeeruddin, and G. Viscardi, *Chem. Commun.* **48**, 2782 (2012).

[24] J. Park, G. Viscardi, C. Barolo, and N. Barbero, *Chimia* **67**, 129 (2013).

[25] A. Jena, S. P. Mohanty, P. Kumar, J. Naduvath, V. Gondane, P. Lekha, J. Das, H. K. Narula, S. Mallick, and P. Bhargava, *Trans. Ind. Ceram. Soc.* **71**, 1 (2012).

[26] M. K. Nazeeruddin, A. Kay, I. Rodicio, R. Humphrey-Baker, E. Muller, P. Liska, N. Vlachopoulos, and M. Grätzel, *J. Am. Chem. Soc.* **115**, 6382 (1993).

[27] M. K. Nazeeruddin, P. Péchy, and M. Grätzel, *Chem. Commun.* **18**, 1705 (1997).

[28] M. Grätzel, *Prog. Photovolt. Res. Appl.* **8**, 171 (2000).

[29] K. Hara, Z.-S. Wang, T. Sato, A. Furube, R. Katoh, H. Sugihara, Y. Dan-oh, C. Kasada, A. Shinpo, and S. Suga, *J. Phys. Chem. B* **109**, 15476 (2005).

[30] T. Horiuchi, H. Miura, and S. Uchida, *Chem. Commun.* **24**, 3036 (2003).

[31] X. Ma, J. Hua, W. Wu, Y. Jin, F. Meng, and H. Tian, *Tetrahedron* **64**, 345 (2008).

[32] W. Wu, J. Hua, Y. Jin, W. Zhan, and H. Tian, *Photochem. Photobiol. Sci.* **7**, 63 (2008).

[33] J.-H. Yum, P. Walter, S. Huber, D. Rentsch, T. Geiger, F. Nüesch, F. De Angelis, M. Grätzel, and M. K. Nazeeruddin, *J. Am. Chem. Soc.* **129**, 10320 (2007).

[34] T. Geiger, S. Kuster, J.-H. Yum, S.-J. Moon, M. K. Nazeeruddin, M. Grätzel, and F. Nüesch, *Adv. Funct. Mater.* **19**, 2720 (2009).

[35] W. Zhao, B. W. Zhang, Y. Cao, X. Xiao, and R. Yang, *J. Funct. Mater.* **30**, 304 (1999).

[36] W. Zhao, Y. J. Hou, X. S. Wang, B. W. Zhang, Y. Cao, R. Yang, W. B. Wang, and X. R. Xiao, *Sol. Energy Mater. Sol. Cells* **58**, 173 (1999).

[37] A. Hauch, and A. Georg, *Electrochim. Acta* **46**, 3457 (2001).

[38] G. Smestad, C. Bignozzi, and R. Argazzi, *Sol. Energy Mater. Sol. Cells* **32**, 259 (1994).

[39] S. Lee, Y. Jun, K.-J. Kim, and D. Kim, *Sol. Energy Mater. Sol. Cells* **65**, 193 (2001).

[40] E. Olsen, G. Hagen, and S.-E. Lindquist, *Sol. Energy Mater. Sol. Cells* **63**, 267 (2000).

[41] A. Kay, and M. Grätzel, *Sol. Energy Mater. Sol. Cells* **44**, 99 (1996).

[42] M. Pagliaro, G. Palmisano, and R. Ciriminna, "Il nuovo fotovoltaico", (2008) Dario Flaccovio Editore, Palermo.

[43] H. Wang, and Y. H. Hu, *Energy Environ. Sci.* **5**, 8182 (2012).

[44] S. Ferrere, A. Zaban, and B. A. Gregg, *J. Phys. Chem. B* **101**, 4490 (1997).

[45] G. Oskam, B. V. Bergeron, G. J. Meyer, and P. C. Searson, *J. Phys. Chem. B* **105**, 6867 (2001).

[46] P. Wang, S. M. Zakeeruddin, J. E. Moser, R. Humphry-Baker, and M. Grätzel, *J. Am. Chem. Soc.* **126**, 7164 (2004).

[47] S. A. Sapp, C. M. Elliott, C. Contado, S. Caramori, and C. A. Bignozzi, *J. Am. Chem. Soc.* **124**, 11215 (2002).

[48] S. Hattori, Y. Wada, S. Yanagida, and S. Fukuzumi, *J. Am. Chem. Soc.* **127**, 9648 (2005).

[49] A. Yella, H. W. Lee, H. N. Tsao, C. Yi, A. K. Chandiran, M. K. Nazeeruddin, E. W. G. Diau, C. Y. Yeh, S. M. Zakeeruddin, and M. Grätzel, *Science* **334**, 629 (2011).

[50] L. Andrade, S. M. Zakeeruddin, M. K. Nazeeruddin, H. Aguilar Ribeiro, A. Mendes, and M. Grätzel, *ChemPhysChem* **10**, 1117 (2009).

[51] Z. Yu, N. Vlachopoulos, M. Gorlov, and L. Kloo, *Dalton Trans.* **40**, 10289 (2011).

[52] S. C. Hao, J. H. Wu, L. Q. Fan, Y. F. Huang, J. M. Lin, and Y. L. Wei, *Sol. Energy* **76**, 745 (2004).

[53] C. Zhang, Y. Huang, Z. Huo, S. Chen, and S. Dai, *J. Phys. Chem. C* **113**, 21779 (2009).

[54] C. A. Kelly, F. Farzad, D. W. Thompson, J. M. Stipkala, and G. J. Meyer, *Langmuir* **15**, 7047 (1999).

[55] F. Fabregat-Santiago, J. Bisquert, E. Palomares, L. Otero, D. Kuang, S. M. Zakeeruddin, and M. Grätzel, *J. Phys. Chem. C* **111**, 6550 (2007).

[56] K. Murakoshi, R. Kogure, and S. Yanagida, *Chem. Lett.* **5**, 471 (1997).

[57] Y. Saito, T. Kitamura, Y. Wada, and S. Yanagida, *Synth. Met.* **131**, 185 (2002).

[58] P. Ravirajan, A. M. Peiró, M. K. Nazeeruddin, M. Grätzel, D. D. C. Bradley, J. R. Durrant, and J. Nelson, *J. Phys. Chem. B* **110**, 7635 (2006).

[59] P. R. Somani, and S. Radhakrishnan, *J. Solid State Electrochem.* **7**, 166 (2003).

[60] N. Cai, S. J. Moon, L. Cevey-Ha, T. Moehl, R. Humphry-Baker, P. Wang, S. M. Zakeeruddin, and M. Grätzel, *Nano Lett.* **11**, 1452 (2011).

[61] S. Ito, T. N. Murakami, P. Comte, P. Liska, C. Grätzel, M. K. Nazeeruddin, and M. Grätzel, *Thin Solid Films* **516**, 4613 (2008).

[62] A. Hagfeldt, and M. Grätzel, *Acc. Chem. Res.* **33**, 269 (2000).

[63] M. Grätzel, *C. R. Chim.* **9**, 578 (2006).

[64] M. Grätzel, *J. Photochem. Photobiol., A* **164**, 3 (2004).

[65] L. Peter, *J. Electroanal. Chem.* **599**, 233 (2007).

[66] L. Andrade, Study and characterization of Grätzel solar cells, "*PhD thesis*" (2010).

[67] J. Halme, Dye-sensitized nanostructured and organic photovoltaic cells: technical review and preliminary tests, "*Master Thesis"* (2002).

[68] D. Kuang, S. Ito, B. Wenger, C. Klein, J. E. Moser, R. Humphry-Baker, S. M. Zakeeruddin, and M. Grätzel, *J. Am. Chem. Soc.* **128**, 4146 (2006).

[69] F. Pichot, and B. A. Gregg, *J. Phys. Chem. B* **104**, 6 (2000).

[70] J. Ferber, R. Stangl, and J. Luther, *Sol. Energy Mater. Sol. Cells* **53**, 29 (1998).

[71] B. O'Regan, J. E. Moser, M. Anderson, and M. Grätzel, *J. Phys. Chem.* **94**, 8720 (1990).

[72] http://www.keithley.com/solar_cell.

Chapter 3: DSC characterization techniques

The purpose of this Chapter is to describe the different techniques commonly exploited to characterize the photovoltaic performances and the charge transport and recombination properties of DSCs. Current-Voltage and Incident Photon-to-electron Conversion Efficiency measurements, usually adopted to evaluate the photovoltaic response of the device and already introduced in Chapter 2, will be presented in the first two Sections of the Chapter. In Sections 3.3 and 3.4 Open Circuit Voltage Decay and Electrochemical Impedance Spectroscopy techniques, generally aimed at evaluating the charge transfer properties, will be respectively discussed.

3.1 Current-Voltage measurements

As already reported in Section 2.3, Current-Voltage (*I-V*) characteristic is the standard technique used to assess the photovoltaic behavior of a solar cell. With the goal of making the results achieved by the different research groups in the world comparable, the *I-V* measurements are usually performed under the standard AM 1.5 G condition (see Section 1.2.2).

The standard set-up is constituted by a solar simulator and a Source Measure Unit (SMU). The solar simulator provides the illumination by means of a Xe lamp and an AM 1.5 G optical filter able to modify the spectrum for a better match to the standard solar spectrum, while the SMU applies a bias voltage to the cell and acquires the corresponding current value. Starting from the *I-V* characteristics, the photovoltaic figures of merit can be evaluated by using Eqs. (2.15) and (2.16). The measurement conditions, i.e. the direction of the voltage scan, the delay time between two consecutive bias voltages and the use of a mask [1], have to be taken in great consideration during the characterization of a Dye-sensitized Solar Cell, differently for what happens with standard Si-based solar devices.

3.2 Incident Photon-to-electron Conversion Efficiency

Incident Photon-to-electron Conversion Efficiency is a powerful technique generally adopted to estimate the electrical response of a cell at different incident wavelengths.

One of the advantages that this characterization technique offers is the possibility to investigate the wavelength range in which a particular dye molecule is able to absorb the light and efficiently inject electrons into the conduction band of nanostructured TiO_2 film.

The set-up normally utilized to perform this kind of measurement on common silicon-based solar devices is constituted by two different lamps. The output beam provided by the first one passes through a chopper, then it is sent to a monochromator, and finally impinges on the cell under test; the second lamp, instead, illuminates the device with a constant output, thus keeping it under normal working conditions.

The short circuit current density yielded by the cell in response to the sum of monochromatic and constant illumination is acquired through a lock-in amplifier which selects only the AC component related to the monochromatic beam $J_{sc}(\lambda)$. If the incident light power density at each wavelength $\phi(\lambda)$ is known, the *IPCE* value at a given wavelength can be calculated by using the formula [2]

$$IPCE = 1240\frac{J_{sc}(\lambda)}{\lambda\phi(\lambda)} = \eta_{lh}(\lambda)\eta_{inj}(\lambda)\eta_{coll}(\lambda) \tag{3.1}$$

where J_{sc} is measured in mA/cm^2, ϕ in mW/cm^2, λ in nm, and η_{lh}, η_{inj} and η_{coll} are the light harvesting efficiency, the charge injection efficiency and the charge collection efficiency, respectively. This chopper-based method to evaluate the *IPCE* generally adopts a chopping frequency of the order of different tens of Hz, so it is suitable for *p-n* junction-based devices whose response time is of about 1 ms, while it can create problems when exploited to measure the *IPCE* spectrum of a DSC (whose response time can be as long as 1 s).

Recently an alternative set-up to perform the *IPCE* measurement exploiting continuous monochromatic irradiation without chopping and additional bias light has been proposed [2, 3, 4]. This method, in which the current is simply acquired by means of a SMU, has revealed to be reliable for the *IPCE* measurements of DSCs, with the only shrewdness to evaluate the current for a fixed wavelength after a sufficient long time (3 s) to be sure that the J_{sc} had reached a steady-state value before acquiring it [3, 5].

3.3 Open Circuit Voltage Decay

Open Circuit Voltage Decay (*OCVD*) is a well known technique used to study the recombination kinetics in DSCs [6].

The cells are kept under constant illumination at open circuit condition until they reach a steady-state photovoltage value. Then, the light is suddenly switched off and the subsequent voltage decay is monitored as a function of the time. Since under open circuit voltage condition the photogenerated electrons cannot be collected by the electrode, they recombine with an approximately constant rate, thus reducing the photovoltage. Therefore, the decrease of the V_{oc} depends only on the charge recombination, and can be associated to the electron lifetime through the formula [6]

$$\tau_n = -\frac{k_B T}{q}\left(\frac{dV_{oc}}{dt}\right)^{-1} = -V_{th}\left(\frac{dV_{oc}}{dt}\right)^{-1} \qquad (3.2)$$

where k_B is the Boltzmann constant, T the absolute temperature and q is the elementary charge value. The quantity $V_{th} = k_B T/q$ is called thermal voltage and it is approximately equal to 25 mV at room temperature. The advantage of this technique with respect to alternative methods based on small perturbations in the time or frequency domain is that the lifetime can be determined in a wide potential range with one single measurement.

3.4 Electrochemical Impedance Spectroscopy

Electrochemical Impedance Spectroscopy (*EIS*) is a technique widely exploited for characterizing the electrical behavior of systems in which the overall performances is determined by a number of strongly coupled processes, each proceeding at a different rate. This technique is based on the analysis of the electric response of a cell to an applied periodic voltage of variable frequency superimposed to a constant bias voltage [7]. Even if the transport and charge transfer processes occurring in real systems are commonly described by nonlinear equations, in the particular case of applied voltages with amplitude comparable with the thermal voltage (i.e. under small-signal condition), it is possible to describe all the processes by linear equations in which the coefficient between the potential and the current is the electric impedance [8].

For a Dye-sensitized Solar Cell, since the different transport and recombination processes taking place in the device are characterized by quite different time constants, this technique is able to distinguish all these mechanisms: the diffusion-recombination electronic processes in the TiO_2 layer and at the semiconductor/electrolyte interface, the diffusion mechanism of the redox species in the electrolyte, and also the charge transfer at the counter electrode [9].

In this context, the electrochemical cell behavior can be described by an equivalent electric circuit. Usually, the shape of the *I-V* curve of a DSC can be carefully fitted using the simple diode circuit model, reported in Fig. 3.1 and corresponding to the following equation [10]

$$I = I_{ph} - I_0 \left(e^{-\frac{V + I\,R_S}{m\,V_{th}}} - 1 \right) + \frac{V + I\,R_S}{R_{sh}} \tag{3.3}$$

where I_{ph} is the photocurrent modeled as an ideal current generator, I_0 the diode reverse saturation current (the so-called dark current), V_{th} the thermal voltage, m the diode ideality factor, and R_s and R_{sh} the series and shunt resistances of the cell respectively. All these parameters can be evaluated by fitting the model to a measured solar cell *I-V* curve. However, in the fitting process R_s needs to be assumed constant, and this is not possible in the case of the DSCs because the series resistance takes into account also the contributions from the current-dependent resistances of charge transfer and mass transport at the counter electrode [11]. For this reason, a more complicated modeling circuit, i.e. the transmission line model, TLM, is usually adopted to fit the *EIS* data and it will be presented in the next Section.

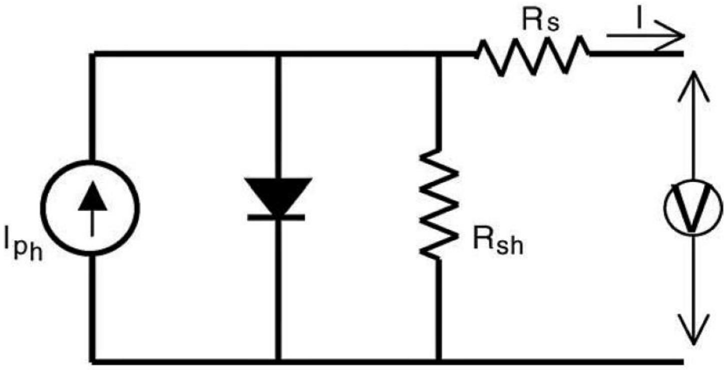

Fig. 3.1 Basic diode equivalent circuit model of a solar cell [10].

In Section 3.4.2, instead, the two typical *EIS* plot of a DSC will be discussed.

3.4.1 The transmission line model

Fig. 3.2 shows the widely used equivalent circuit model of a DSC, in the simplified case in which the potentials considered are near the V_{oc}.

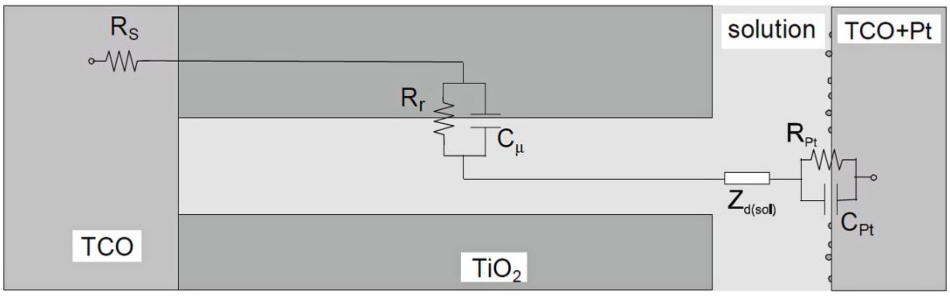

Fig. 3.2 Simplified equivalent circuit of a DSC for the TiO_2 in a conductive state [12].

In this picture, the nanostructured oxide representation has been simplified to a columnar model that represents the mesoporous layer in which the electrolyte solution interpenetrates. The circuit components and their units are:

- R_r *(Ω)*: charge transfer resistance related to the recombination of the electrons at the TiO_2+dye/electrolyte interface.
- C_μ *(F)*: capacitance at the TiO_2+dye/electrolyte interface.
- $Z_{d(sol)}$ *(Ω)*: impedance of the redox species diffusion into the electrolyte, generally called Nernst impedance Z_N.
- R_{Pt} *(Ω)*: charge transfer resistance at the counter electrode.
- C_{Pt} *(F)*: capacitance at the electrolyte/counter electrode interface.
- R_s (*Ω*): sheet resistance of the TCO layer and contact resistances.

The Nernst impedance Z_N, describing the diffusion of the triiodide in the electrolyte, is expressed by the following equation

$$Z_N = \frac{W}{\sqrt{j\omega}} tanh\left(\sqrt{\frac{j\omega}{k_N}}\right) \tag{3.4}$$

where the Warburg parameter W and the Nernst constant k_N are respectively defined as

$$W = \frac{k_B T}{n^2 e^2 C A \sqrt{D}} \tag{3.5}$$

and

$$k_N = \frac{D}{\delta^2}. \tag{3.6}$$

k_B is the Boltzmann constant, T the absolute temperature, n the number of electrons transferred in the reaction, e the elementary charge, C the concentration of triiodide, A the area of the electrode, D the diffusion coefficient of triiodide and δ the thickness of the diffusion layer [13].

Each interface (photoanode/electrolyte and counter electrode/electrolyte) is schematized with a *RC* circuit, representing an impedance: the resistance is related to the ability to oppose to the charge transfer, while the capacitance is related to the charge accumulated at the interface. The three impedances are associated to the main parts of a cell.

The total impedance at the nodes is:

$$Z_{tot} = \frac{R_r}{1 + j\omega R_r C_\mu} + Z_N + \frac{R_{Pt}}{1 + j\omega R_{Pt} C_{Pt}} + R_s. \tag{3.7}$$

3.4.2 Impedance plot of a DSC

The impedance is a measure of the ability of a circuit to resist the flow of electrical current [14]. Unlike the resistance, the impedance includes not only the relative amplitudes of the voltage and the current, but also the relative phases.

Taking into account the Euler's relationship, it is possible to express the impedance in terms of a magnitude Z_0 (ratio of the voltage amplitude to the current amplitude) and a phase shift ϕ by means of the following equation

$$Z = \frac{V_0}{I_0} e^{-j\phi} = Z_0 e^{-j\phi} = Z_0 \cos(\phi) - jZ_0 \sin(\phi) = Z' - j\, Z'' \tag{3.8}$$

By varying the frequency of the applied signal, one can get the impedance of the system as a function of the frequency. The recorded data can either be represented as magnitude and phase *vs.* frequency (i.e. Bode plot) or on a complex plane (Nyquist plot), as reported in Fig. 3.3. In Nyquist plot the real part of the impedance (Z') is plotted on the X-axis and the imaginary part (Z'') is plotted on the Y-axis.

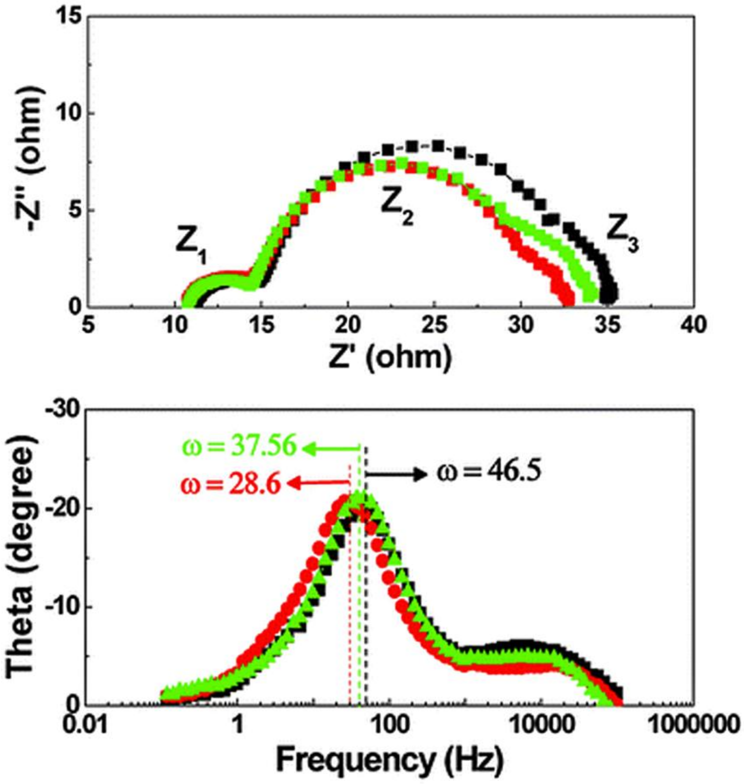

Fig. 3.3 Typical Nyquist and Bode plots of a DSC [15].

Analyzing the Nyquist diagram, that is the main output of the AC Impedance measurement, for voltages near the V_{oc}, it is possible to see three main semicircles (see Fig. 3.3) [16]: the first one at high frequency (above 100 Hz) describes the charge transfer at the Pt/electrolyte interface, the second one at intermediate frequency (1-100 Hz) is related to the recombination at the photoanode/electrolyte interface and to the charge transport into the semiconductor, and the third one at low frequency (below 1 Hz) represents the diffusion in the electrolyte and it is attributed to the Nernst contribution. If the voltage is reduced, the two external semicircles are incorporated into the biggest one.

Each parallel between a resistance and a capacitance of the circuit in Fig. 3.2 corresponds to a semicircle in the Nyquist diagram. The diameter of each section is given by the resistance of the associated *RC* circuit, that is the real part of the associated impedance (Z'). The series resistance R_s determines the shift of the entire diagram towards right.

References

---

[1] X. Yang, M. Yanagida, and L. Han, *Energy Environ. Sci.* **6**, 54 (2013).

[2] P. R. F. Barnes, A. Y. Anderson, S. E. Koops, J. R. Durrant, and B. O'Regan, *J. Phys. Chem. C* **113**, 1126 (2008).

[3] X.-Z. Guo, Y.-H. Luo, Y.-D. Zhang, X.-C. Huang, D.-M. Li, and Q.-B. Meng, *Rev. Sci. Instrum.* **81**, 103106 (2010).

[4] G. G. Xue, Y. Guo, T. Yu, J. Guan, X. R. Yu, J. Y. Zhang, J. G. Liu, and Z.G. Zou, *Int. J. Electrochem. Sci.* **7**, 1496 (2012).

[5] X. Guogang, Y. Xirui, Y. Tao, B. Chunxiong, Z. Jiyuan, G. Jie, H. Huan, T. Zekun, and Z. Zhigang, *J. Phys. D: Appl. Phys.* **45**, 425104 (2012).

[6] A. Zaban, M. Greenshtein, and J. Bisquert, *ChemPhysChem* **4**, 859 (2003).

[7] F. Fabregat-Santiago, J. Bisquert, E. Palomares, L. Otero, D. Kuang, S. M. Zakeeruddin, and M. Grätzel, *J. Phys. Chem. C* **111**, 6550 (2007).

[8] J. R. Macdonald, *Ann. Biomed. Eng.* **20**, 289 (1992).

[9] Q. Wang, J. E. Moser, and M. Grätzel, *J. Phys. Chem. B* **109**, 14945 (2005).

[10] N. Koide, A. Islam, Y. Chiba, and L. Han, *J. Photochem. Photobiol., A* **182**, 296 (2006).

[11] J. Halme, P. Vahermaa, K. Miettunen, and P. Lund, *Adv. Mater.* **22**, E210 (2010).

[12] F. Fabregat-Santiago, J. Bisquert, G. Garcia-Belmonte, G. Boschloo, and A. Hagfeldt, *Sol. Energy Mater. Sol. Cells* **87**, 117 (2005).

[13] M. Wu, Y. Wang, X. Lin, N. Yu, L. Wang, A. Hagfeldt, and T. Ma, *Phys. Chem. Chem. Phys.* **13**, 19298 (2011).

[14] Basics of Electrochemical Impedance Spectroscopy. Application Note. Gamry Instruments. http://www.gamry.com.

[15] B. Ding, M. Yang, B. J. Lee, and J.-K. Lee, *RSC Adv.* **3**, 9690 (2013).

[16] A. Sacco, A. Lamberti, M. Quaglio, S. Bianco, E. Tresso, A. L. Alexe-Ionescu, and C. F. Pirri, *Int. J. Photoenergy* **2012**, 216780 (2012).

Chapter 4: Experimental

The purpose of this Chapter is to introduce the different materials and instruments involved in the thesis work. Firstly the materials used for the DSC fabrication and the device assembly procedures will be analyzed, subsequently the instruments exploited for the characterization of both the materials and the solar cells will be presented.

4.1 Materials and methods

In this Section all the materials used for the DSC fabrication, divided on the basis of the different cell components, and the device assembly procedures will be reported.

4.1.1 Photoanodes

In this Section the different materials and procedures exploited for the fabrication of the photoanodes will be described.

For all the photoelectrodes, FTO-covered glasses (0.22 cm-thick, 7 Ω/sq, Solaronix) 2 cm x 2 cm were used as transparent substrates. Before usage, they were immersed in acetone in an ultrasonic bath for 10 min, then rinsed with isopropanol and dried under nitrogen flow. The substrates were then cleaned for 10 min in a 3:1 (sulfuric acid:hydrogen peroxide) *piranha* solution in order to remove the organic residues, abundantly rinsed with deionized water, dried with N_2 flow and finally placed on a hot plate for 2 min at 100 °C just to remove residual moistures on the surface.

This cleaning procedure has undergone some small variations only in the case where the TiO_2 paste purchased from DyeSol Co. was employed in substitution of the one bought from Solaronix. In particular, an ultrasonic bath in ethanol for 10 min was performed between the ultrasonic bath in acetone and the rinsing with isopropanol, the cleaning in *piranha* solution was replaced by a rapid firing for 5 min at 540 °C, and the step of heating for 2 min at 100 °C was skipped.

The choice of changing the supplier of the Titanium dioxide paste during the last months of the PhD, in particular when cellulose-based gel electrolyte was tested in a DSC (see Section 6.3.2), was due to the fact that the paste purchased from Solaronix was much more liquid, thus giving rise to cracked and no more reproducible photoanodes.

TiO_2 nanoparticles were used as standard material for the photoanodes, but they suffer for reduced charge transport due to a long pathway for the electron diffusion within the semiconductor network. With the aim of overcoming this disadvantage, two different ZnO nanostructures (i.e. sponge-like and flower-like particles) were successfully employed as alternative DSCs photoanode materials.

4.1.1.1 TiO_2 nanoparticles

A circular shaped (diameter of 10 mm) TiO_2 layer, employing Ti-Nanoxide D37 paste, Solaronix (DLS 18NR-AO paste, DyeSol Co.), was deposited onto FTO-covered glasses with tape casting technique [1]. After deposition, the layer was dried at room temperature for 30 min (10 min) and then baked at 50 °C for 10 min (100 °C for 10 min) on a hot plate. Finally, a sintering process in a muffle furnace (Nabertherm series L/LT - B180) at 450 °C for 30 min (525 °C for 30 min) enabled the formation of a nanoporous TiO_2 film with a mean thickness of (8.0±0.5) μm. In order to obtain an increase of the photovoltaic conversion efficiency of TiO_2 NPs-based devices, a $TiCl_4$ post-treatment was performed by dipping the freshly sintered TiO_2 films into a 50 mM $TiCl_4$ solution at 70 °C for 30 min, then rinsing in abundant deionized water and drying under nitrogen flow. After the post-treatment, the TiO_2 films were again sintered at 450 °C for 30 min [2]. The $TiCl_4$ treatment was performed only on Solaronix TiO_2 samples, since its beneficial effect was not observed on DyeSol TiO_2 photoanodes. The expected effect of the treatment is a downward shift of the oxide CB that enhances the electron injection efficiency, thus resulting in an increase of the short circuit current density [3].

4.1.1.2 Sponge-like ZnO

Zinc nanostructured layers with different thicknesses (12.5 μm and 15 μm) were deposited by radio-frequency (RF) magnetron sputtering technique onto FTO-covered glass slices. The vacuum chamber was pumped down to a pressure ranging from about $8 \cdot 10^{-6}$ Pa to about $6 \cdot 10^{-5}$ Pa. A zinc target, with a purity of 99.99% and a diameter of 101.6 mm (Goodfellow) was fixed on the cathode, placed at about 8 cm from the substrate holder. Argon (5.0 purity) was used as sputtering gas. The plasma discharge was created by applying a RF voltage at a frequency of 13.56 MHz between the target and the grounded substrate holder. Each film was grown at a deposition power of 100 W and at room temperature, i.e. no intentional heating was supplied to the substrates. After the deposition by sputtering, the films were placed on a hot plate at 380 °C for 60 min in ambient air, in order to oxidize the zinc and obtain high-density branched ZnO films.

4.1.1.3 Flower-like ZnO microstructures

Flower-like ZnO particles were prepared dissolving separately, in 50 mL bidistilled water (from Direct-Q System, Millipore), 2.8 g potassium hydroxide (KOH, 1 M, Merck) and 7.4 g zinc nitrate hexahydrate ($ZnNO_3 \cdot 6H_2O$, 0.5 M, Sigma). The zinc nitrate solution was dropped into KOH under vigorous stirring, thus the total volume was 100 mL. The obtained white gel was transferred in a closed Teflon bottle at 70 °C for 4 h. At the end of this time, the ZnO particles were separated from the solution by filtration, washed repetitively with deionized water until the pH neutralization, and dried at 60 °C overnight in air. ZnO flower-like particles thus obtained were dispersed in a solution containing acetic acid (1 vol.%), ethanol (67 vol.%) and water (33 vol.%) in a weight ratio of 1:2 (ZnO:solution) [4] and then sonicated for 4 h in order to obtain a homogeneous paste. Subsequently, a circular shaped ZnO layer was deposited with tape casting technique on FTO-covered glasses. The coated films were initially dried at 90 °C for 30 min and then thermally treated at 450 °C for 10 min in air, thus obtaining a ~14 μm-thick ZnO layer.

4.1.2 Sensitizers

In this Section the different materials and procedures exploited for the sensitization of the TiO_2 and ZnO photoanodes will be described.

Ru-based N719 dye has been chosen as standard sensitizer, while the hemi-squaraine organic dye CT1 has been proposed as promising alternative, with the purpose of overcoming the important limits exhibited by Ru-based sensitizers: i.e. expensive synthesis process, relatively low molar extinction coefficient in the visible region, limited availability of precursors and waste disposal issues.

All the photoanodes were heated at 70 °C for 5 min before the impregnation, and then soaked in the sensitizing solution at room temperature. After the sensitization, the dyed photoanodes were rinsed in the same solvent in which the dye powder has been dissolved, in order to remove the unabsorbed dye molecules.

4.1.2.1 Metal-organic dye

The metal-organic sensitizer used in this thesis is the N719 dye, purchased from Solaronix (Ruthenizer535bis-TBA). The absorption spectrum and the molecular structure of this sensitizer are depicted in Fig. 4.1. The UV-Vis absorption spectrum of the N719 sample in ethanol solution reveals four broad bands. The two broad visible bands at 531 and 390 nm are assigned to metal-to-ligand charge-transfer (MLCT) origin. The bands in the UV region at 313 and 215 nm with a shoulder at 253 nm, instead, are specified to intraligand (π-π^*) charge transfer transitions [5].

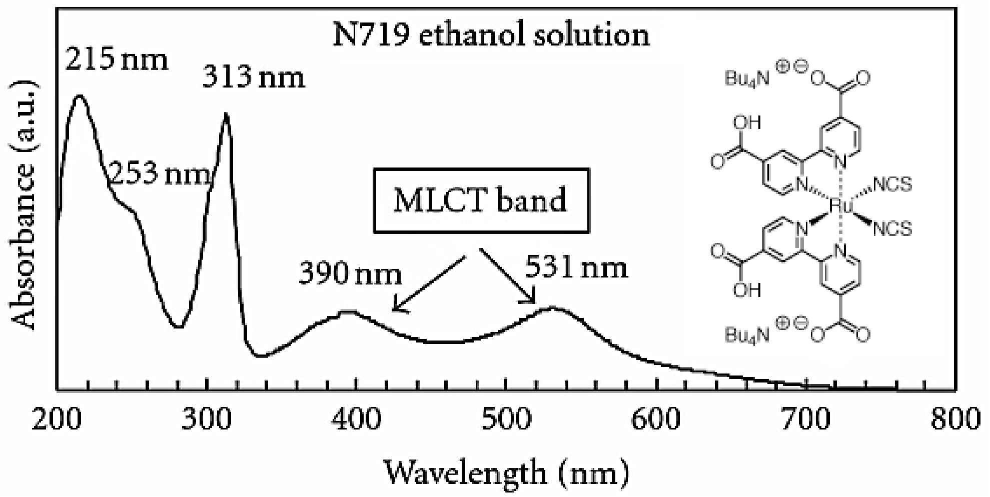

Fig. 4.1 UV-Vis absorption spectrum of N719 in ethanol [5]. The inset shows the molecular structure of N719 Ruthenizer535bis-TBA, Solaronix [6].

The standard solution, employed for the impregnation of TiO_2 samples, was constituted by a fixed concentration of 0.35 mM of dye dissolved in ethanol, and the loading time was fixed to 18 h.

For devices based on sponge-like ZnO photoanodes (see Section 6.1.1), the concentration of dye in solution was fixed to 0.25 mM and impregnation times of 1, 2 and 3 h were considered.

Finally, for devices based on flower-like ZnO photoanodes (see Section 6.1.2), three different concentrations of dye in solution and impregnation times were chosen, namely

0.05, 0.4 and 0.75 mM and 2 min, 6.5 h and 13 h, respectively. Moreover in some cases 0.3 or 0.6 mM NaOH was added to the solution in order to increase its pH (thus moving its value from 6.5 without the base to 8.6 or 10.7 when 0.3 or 0.6 mM NaOH was employed, respectively).

4.1.2.2 Organic dye: hemi-squaraine CT1

Hemi-squaraine CT1 dye was produced by Cyanine Technologies s.r.l. following a simple, easy and not expensive three steps synthesis: quaternarization (a), coupling (b), hydrolysis (c) (see Fig. 4.2), according to the classical procedure for hemi-squaraine dyes (see the Supporting Information of [7]).

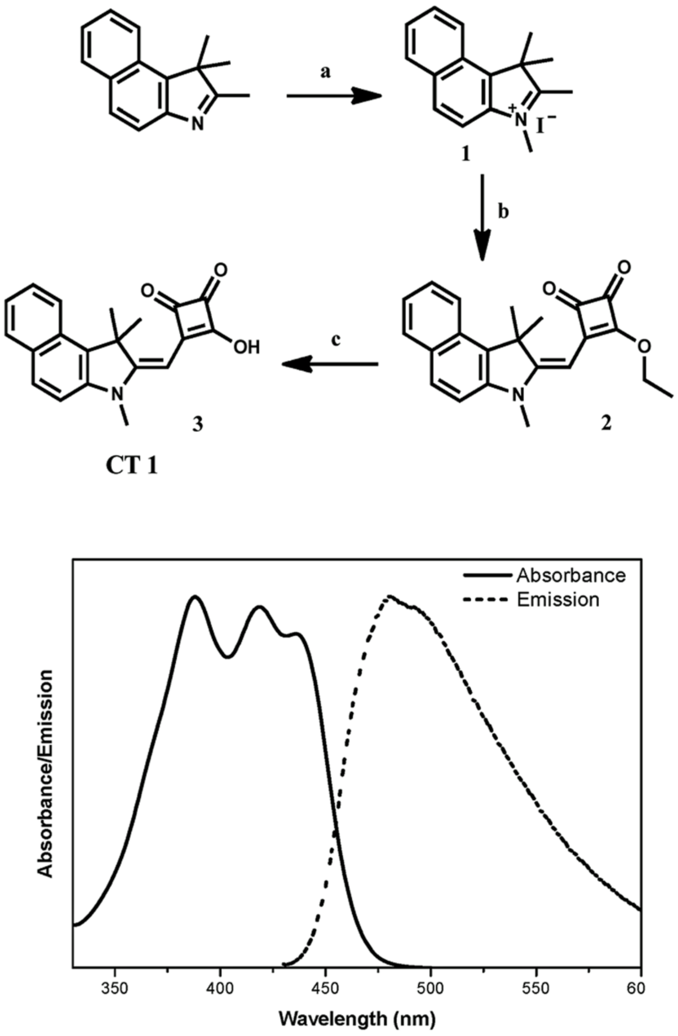

Fig. 4.2 Top panel: synthesis of CT1. Reagent and conditions: a) CH_3I, acetonitrile anhydrous, reflux, 85 °C, 3 h; b) diethyl squarate, tryethylamine (TEA), ethanol, reflux, 85 °C, 19 h; c) 40% NaOH solution, ethanol, reflux, 85 °C, 10 min. Bottom panel: absorbance and emission spectra of CT1 dye in acetonitrile.

CT1 can be considered as the prototype of a wide class of functionalized molecules with a common basic structure, where the squaric acid moiety functions as linker (see structure 3 in Fig. 4.2). CT1 absorbance and emission spectra in acetonitrile solution are reported in the bottom panel of Fig. 4.2. They exhibit a wide band composed of three neighboring peaks centered at 388 nm, 419 nm and 434 nm (optical gap 2.83 eV), with an average molar extinction coefficient of 15220 M^{-1} cm^{-1} and an emission peak at 480 nm (ΔE_{00} = 2.73 eV).

In a first phase of combined experimental and theoretical investigation of the hemi-squaraine/TiO_2 interface (see Section 6.2.1), the sensitizer solution was prepared by mixing 0.25 mM CT1 dye in acetonitrile, and chenodeoxycholic acid (CDCA) at different concentrations (0, 1 and 10 mM) was employed as a co-adsorbent, to reduce the dye aggregation at the TiO_2 surface [8]. CDCA has also a strong influence on the quantity of the adsorbed dye since it competitively saturates the anchoring sites present at the surface. The impregnation time was fixed to 5 h.

Subsequently, a detailed study aimed at optimize the performances of CT1-based DSCs was carried out. In this case (see Section 6.2.2), the concentration of the sensitizer in solution was reduced down to 0.17 mM, in order to make the dissolution process of the dye powder in acetonitrile easier and more reproducible, and different impregnation times were chosen, namely 5 min, 30 min, 1 h, 3 h and 5 h. In a second phase of the optimization process, chenodeoxycholic acid in different concentrations (1, 10, 14 and 18 mM) was added as co-adsorbent in the dye solution. Firstly, the sensitization time was fixed to 1 h. Then, it was extended to 3 h for the three most promising CDCA concentrations (0, 1 and 10 mM) in order to verify if a longer loading time could lead to an improvement of the photoconversion efficiency of the solar cells.

Finally, the dye loading time influence on the electrical impedance of a CT1-based Dye-sensitized Solar Cell was analyzed by means of a physical model which takes into account the possibility of the dye molecules aggregation. In the present case (see Section 6.2.3), the same impregnation times previously considered, i.e. 5 min, 30 min, 1 h, 3 h and 5 h, were chosen and the CDCA was not added in the dye solution.

4.1.3 Counter electrode

In order to ensure a sufficiently fast reduction reaction kinetics at the TCO-coated cathode, Pt was chosen as catalyst.

For counter electrode fabrication, the same transparent substrates used for the photoanode were employed. Two small pin-holes for electrolyte inlet/outlet were drilled in the FTO-covered glasses through powder blasting technology and then the substrates were cleaned with the same process described in Section 4.1.1. A thin layer of platinum (5 nm) was deposited on TCO by thermal evaporation. A 0.125 mm Pt wire (99.99% purity, Goodfellow) was put in a W crucible (ME5.005W, Testbourne) and connected with a high current circuit controlled by a variac. The evaporation current was in the range 90 - 110 A and the deposition rate was kept constant at 0.01 nm/s. The distance between the metal source and the substrate was 10 cm. The deposition occurred in high vacuum conditions (pressure lower than $5 \cdot 10^{-7}$ mbar), obtained by means of a series of a mechanical and a turbo-molecular pump.

In some cases, for the fabrication of irreversible sealed DSC (see Section 4.1.5.2), one hole-drilled or even non-drilled Pt-covered counter electrodes were employed.

4.1.4 Electrolytes

In this Section all the electrolytes employed in the thesis work will be introduced and thoroughly described.

A commercial liquid organic solvent-based electrolyte was used as standard material. The liquid solvent-based electrolytes, however, suffer for their limited long-term stability, difficulty in sealing and leakage, thus preventing the realization of devices having a high and constant-over-time efficiency. To overcome these issues, UV-crosslinked polymer membrane and cellulose-based gel quasi-solid electrolytes have been proposed as two promising alternative solutions.

4.1.4.1 Liquid electrolyte

The used liquid electrolyte solution was the Iodolyte AN 50, Solaronix, an iodide-based low viscosity electrolyte with 50 mM triiodide in acetonitrile. This electrolyte is intended for high performance cells, due to the excellent stability, low viscosity and capability to dissolve a lot of salts and organic molecules typical of acetonitrile. In the only one case of DSCs assembled with the optimized ZnO flower-like microparticles-based photoanode (see Section 6.1.2.2), N-methylbenzimidazole (NMBI) at different concentrations (0.25, 0.5 and 0.75 M) was employed as liquid electrolyte additive.

4.1.4.2 Quasi-solid electrolytes

4.1.4.2.1 UV-crosslinked polymer membrane

UV-crosslinked membranes were prepared using bisphenol A ethoxylate dimethacrylate (BEMA, average M_n = 1700, Aldrich) and poly(ethylene glycol) methyl ether methacrylate (PEGMA, average M_n = 475, Aldrich). 2-hydroxy-2-methyl-1-phenyl-propan-1-one (4 wt%, Darocur 1173, Ciba Specialty Chemicals) was added as free-radical photo-initiator.

The polymerization mixture was sandwiched between two UV-transparent glasses, separated by a 100 µm-thick tape. Self standing membranes were obtained by UV irradiating the mixtures for 4 min using a medium vapor pressure Hg lamp (Helios Italquartz, Italy), with an irradiation intensity on the surface of 30 mW/cm^2.

The membranes were free-standing 100 µm-thick films, transparent, highly thermally stable and highly insoluble in chloroform, meaning that they were highly crosslinked. Then, the membranes were swelled for 5 min by a liquid electrolyte composed of NaI and I_2 dissolved in acetonitrile (all purchased from Aldrich). The obtained quasi-solid polymer electrolytes were still free-standing, non-tacky, although extremely flexible and easy to handle.

The overall experimental procedure followed to prepare the UV-crosslinked polymer membrane is depicted in Fig. 4.3.

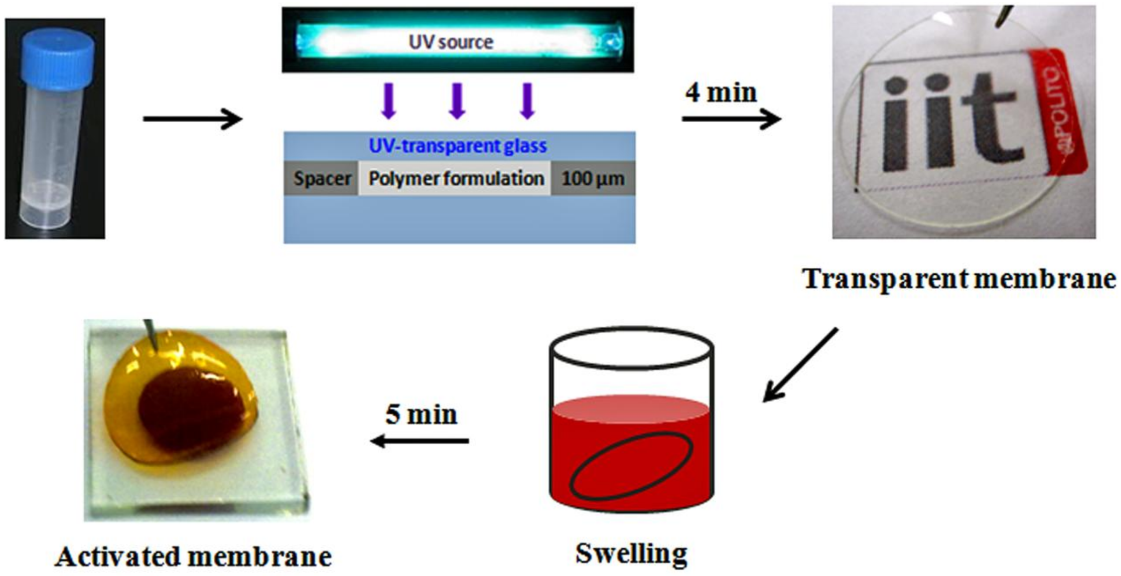

Fig. 4.3 Experimental procedure followed to prepare the UV-crosslinked polymer membrane.

4.1.4.2.2 Cellulose-based gel

The quasi-solid cellulose-based gel electrolytes tested in the Dye-sensitized Solar Cells were all composed by:

1. Two ionic liquids (the former with iodide as anion and the latter without iodide as anion).
2. A lithium salt (lithium iodide).
3. Iodine.
4. Cellulose microcrystalline powder.
5. An additive to increase the V_{oc} (4-tert-butylpyridine (TBP)).

1-methyl-3-propylimidazolium iodide (MPII) and 1-ethyl-3methylimidazolium thiocyanate (EMISCN) were chosen as ionic liquids. MPII is a very well known source of iodide species for DSC electrolytes [9], but it presents a high viscosity (about 800 mPa·s); thus, in order to decrease the overall viscosity of the gel, a second ionic liquid (EMISCN) with a low viscosity (about 20 mPa·s) was employed. Different volume percentage ratios between the two ionic liquids were studied, as reported in Table 4.1.

Table 4.1 Volume percentage ratios utilized in the gel electrolyte preparation.

MPII (vol%)	EMISCN (vol%)
50	50
60	40
70	30
80	20
90	10
100	0

A 2 wt% of lithium iodide respect with the MPII weight and a ratio 1/10 between iodine and iodide weights were applied for all the gel electrolytes prepared. The amount of the cellulose microcrystalline powder used as gelling agent was varied from 3 wt% to 6 wt% with respect to the total weight of the solution. The TBP weight percentage added to the gel electrolytes was changed from 10 up to 25.

Before starting the gel electrolyte preparation, the microcrystalline cellulose was put into an oven at 100 °C for at least 16 h, thus removing as much water as possible. This step is necessary, since the presence of water in the gel electrolytes causes a worsening in the DSC photovoltaic performances. Once the water had been removed and the cellulose had been cooled, lithium iodide, iodine, cellulose and the two ionic liquids were added into a 5 ml beaker. The recipient was sealed with an aluminium foil in order to avoid a direct contact with the ambient moisture and was stirred and heated at 90 °C for 24 h. After the 24 h, the beaker was taken out of the stirring and heating and let it cool down at room temperature; then, the solution was poured into a plastic Petri disc filled with several absorbing paper sheets, in order to remove the ionic liquid excess and let the solution becomes a gel.

Depending on the different amounts of the reagents used to prepare the gel electrolyte samples, it was necessary to change the absorbing paper after few hours. 24 h of "liquid ionic excess absorption" was usually the time needed for having a solid gel electrolyte.

A few hours before assembling the DSCs, the gel was mixed with the TBP. This adding was performed after the gelation, due to the fact that the temperature employed to dissolve the cellulose (90 °C) caused a partial evaporation of the additive, thus leading to a decrease in the photovoltaic DSC performances. The displacement of the gel onto the dyed photoanode was always performed with tape casting technique.

In Fig. 4.4 a pictorial scheme of the gel preparation is showed.

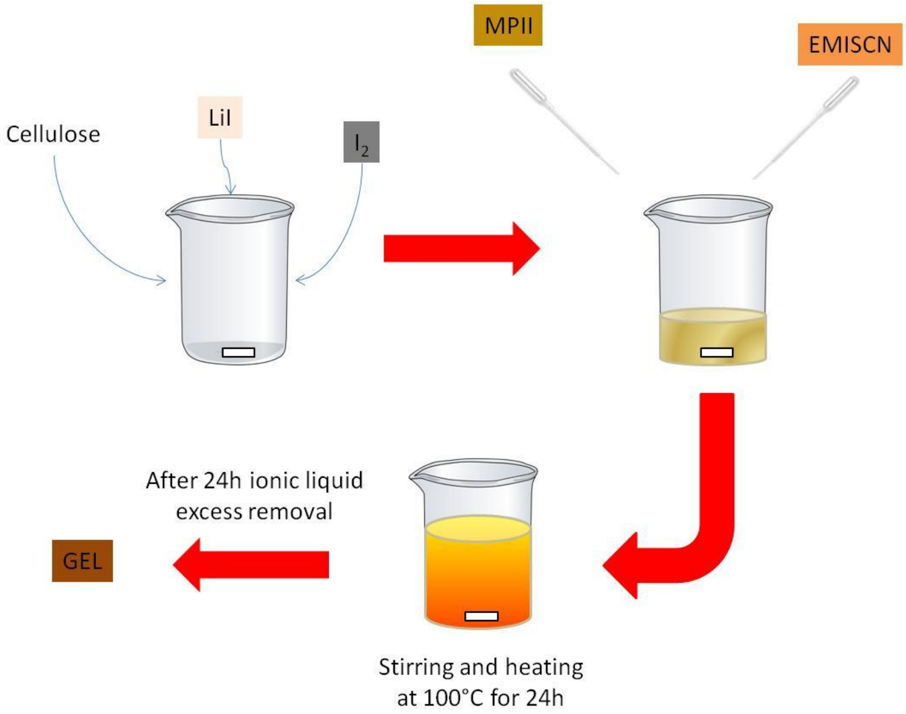

Fig. 4.4 A scheme of the cellulose-based gel electrolyte preparation.

4.1.5 Housing systems and cell assembly

In this Section the two housing systems employed to assemble the Dye-sensitized Solar Cells, i.e. microfluidic and irreversible sealed, will be described. Both these architectures present some advantages and disadvantages and their usage depends on whether the purpose is to perform (irreversible sealed) or less (microfluidic) repeated measures of stability over time.

The innovative microfluidic housing system, recently proposed by the “DSCs Research Group” of IIT @ PoliTo [10], is based on all the components of a traditional Grätzel device with the addition of a microfluidic chamber, designed by means of a PolyDiMethylSiloxane (PDMS) membrane, and an external clamping system closed by screws. The microfluidic structure allows to assemble the cell in an easy and reversible way, thus granting inspection and control of the components also after the experiments. Another advantage in using this kind of architecture is the possibility of inserting in a controlled way the electrolyte into the chamber, without losses and wastes. This modular device is really useful for laboratory studies and tests, in which a high number of samples have to be tested, but presents the important disadvantage of a short duration in time. The PDMS, in fact, is oxygen-permeable, thus allowing the partial evaporation of the electrolyte and, consequently, a degradation of the overall performances of the device. In order to overcome the drawback related to the time-stability of the microfluidic cell, a new structure, the irreversible sealed cell, was proposed and successfully implemented.

4.1.5.1 The microfluidic cell

The structure of the microfluidic DSC, together with a picture of the final device, is reported in Fig. 4.5.

Poly(methyl methacrylate) (PMMA) mechanical clamping system consisting in two identical frames with inlet/outlet ports was fabricated using a Benchman VMC4000 numerical control milling machine. The same instrument was used for the fabrication of the masters for polydimethylsiloxane (PDMS) membrane casting and O-ring interconnections.

The membranes were prepared by mixing and degassing at room temperature for 1 h the PDMS pre-polymer and the curing agent (Sylgard 184, Dow Corning) in a 5:1 weight ratio. The mixture was then poured into the double-drop shaped mould and cured in a convection oven for 1 h at 70 °C. Finally the membranes were peeled off from the mould.

The cells were assembled by sandwiching the membrane between the dyed photoanode and the counter electrode, and closing the structure with the PMMA clamping system through the use of screws. The electrolyte filling was done with a syringe connected to the housing ports (PDMS O-ring interconnections) via low-density polyethylene (LDPE) tubes. The ports were finally sealed employing homemade caps consisting in LDPE tubes obstructed with PDMS. Copper foils (50 μm-thick, area 1.5 cm^2) were used as electric connections at the electrodes, dielectrically isolated by the PDMS membrane.

Microfluidic housing system was employed for all the CT1- and ZnO-based DSCs considered in this thesis (see Sections 5.1, 6.1 and 6.2).

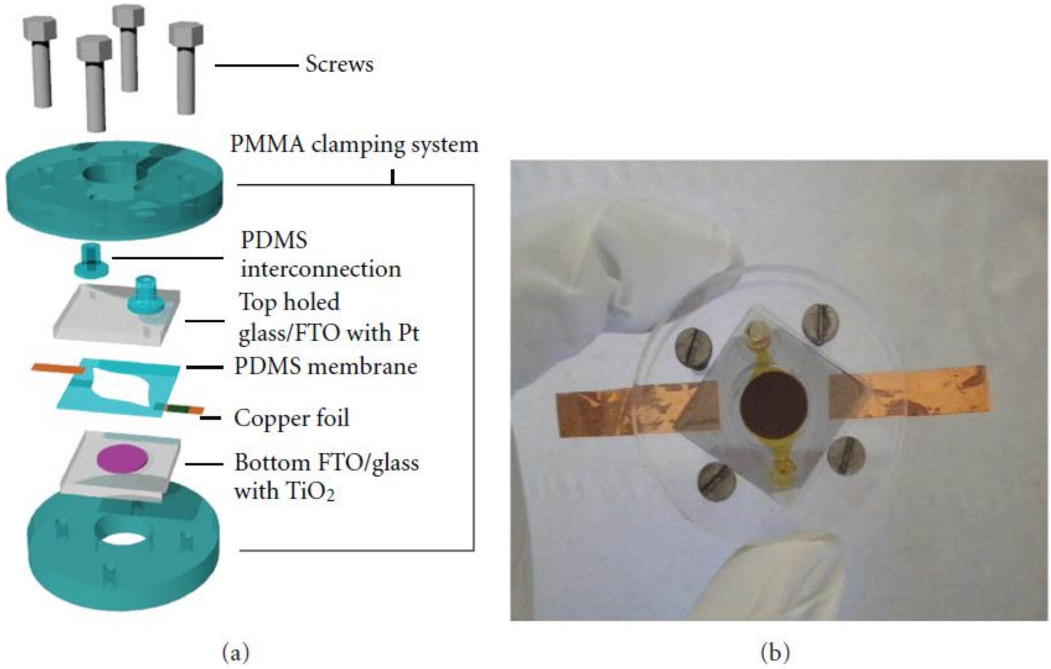

Fig. 4.5 Scheme of the microfluidic DSC with the detail of all the elements constituting the cell (a). A picture of the final device (b) [10].

4.1.5.2 The irreversible sealed cell

The scheme of the irreversible sealed DSC, together with a picture of the final device, is reported in Fig. 4.6.

The cells were assembled by sandwiching a 25 μm-thick thermoplast hot-melt sealing foil (Meltonix 1170-25, Solaronix) between the sensitized photoanode and the counter electrode. Sealing occurred in a hot-press by heating the two plates at 90 °C and applying a pressure of 1.3 bars for about 25 s.

The electrolyte filling was performed by putting a drop of electrolyte on the hole present in the counter electrode, and then air-evacuating with a small vacuum pump the circular region delimited by the melting film between the two electrodes. By generating the vacuum in the cell, the liquid solution could enter the active area and fill it completely. When the region was filled, the hole was closed by displacing on it a piece of the melting film used for sealing and a small piece of glass, and finally fluxing hot air at 100 °C for few seconds. The external electrical contacts were obtained by depositing a silver paint (Elecolit 340) onto the TCO layer, in order to reduce the contact resistance.

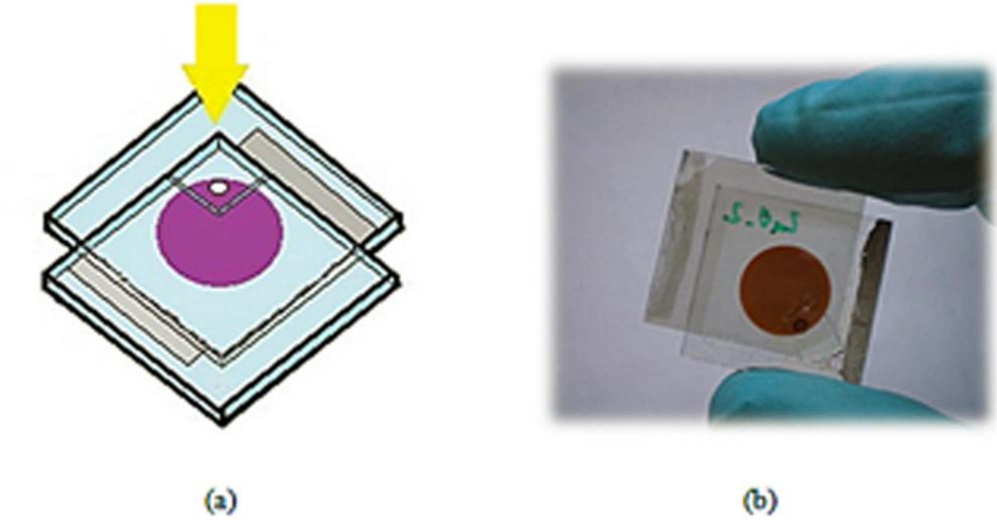
(a) (b)

Fig. 4.6 Scheme of the irreversible sealed DSC (a). A picture of the final device (b).

The irreversible sealed architecture depicted in Fig. 4.6 was employed to realize the DSCs able to validate the consistent static and small-signal physics-based modeling under different illumination conditions (see Sections 5.2 and 6.4). This housing system, instead, was not suitable for sealing the quasi-solid electrolytes-based DSCs (see Sections 4.1.4.2 and 6.3). The encountered issues were essentially two: the thermoplast hot-melt sealing foil thickness was not compatible with the sum of the thicknesses of the photoanode and the electrolyte and the direct contact of the quasi-solid electrolyte with the melting film prevented a good adhesion of the sealing foil with the FTO-covered glasses. Accordingly, in the quasi-solid state DSCs the thermoplastic polymer was substituted by a strip of cyano-acrylic glue (Super Attak, Loctite), applied on the lateral surface of the cathode. This sandwich-type cell, shown in Fig. 4.7, was pressed with two binder clips and a further strip of glue was placed on the external perimeter of contact between the electrodes in order to guarantee a better protection from the environment.

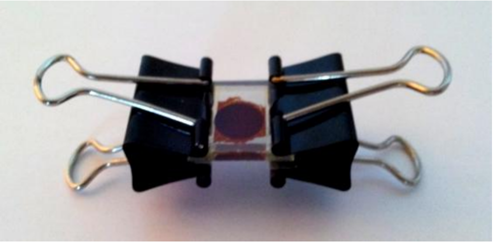

Fig. 4.7 Sandwich-type quasi-solid state DSC pressed with two binder clips.

4.2 Chemometric approach

Chemometrics is the mathematical approach which converts experimental data into useful information for decision-making in science [11]. Nowadays, the strong imbalance that exists between the technical ability to generate a large amount of excellent experimental data and the human ability to properly interpret it, is quite worrying. To overcome this, chemometric methods (in particular the Design of Experiments, DoE) were proposed: the main goal is to plan the type and the number of experiments required to obtain the maximum possible information from the investigated system, reducing concurrently the overall number of experiments.

In the thesis work this innovative approach has been proposed twice, in particular to optimize the remarkably critical sensitization procedure of ZnO flower-like microstructures with Ru-based N719 dye (see Sections 4.2.1 and 6.1.2.2) and to correlate the photovoltaic properties of the UV-crosslinked polymer electrolyte membranes to the polymer morphology (see Sections 4.2.2 and 6.3.1.2).

4.2.1 Multivariate optimization of ZnO flower-like microstructures sensitization procedure

ZnO is now considered as the second most used semiconductor for solar energy conversion by means of *third generation* devices [12], thanks to its higher electron mobility and similar electronic band structure with respect to those of TiO_2 [13]. However, despite the many efforts spent to improve the performances of ZnO-based Dye-sensitized Solar Cells, the light-to-electricity conversion efficiency remains lower than the one of TiO_2-based cells. Actually, the most efficient ZnO-based DSC was achieved by Memarian *et al.* [14], who obtained a 7.5% overall efficiency, around half of the maximum performances obtained for TiO_2 [15].

The main reason which prevents Zinc oxide from achieving photoconversion performances comparable to those obtained for TiO_2 is the remarkably critical sensitization procedure of this semiconductor with Ru-based dyes. In particular, the presence of carboxylic acid binding groups of Ru dyes can lead to the dissolution of ZnO and the precipitation of molecular Zn^{2+}/dye complexes, resulting in a reduced overall electron injection efficiency by the excited dye [16]. Several approaches were performed to overcome these sensitization problems. Keis *et al.* [17] obtained 5% of efficiency by adding KOH to the acidic dye loading solutions and shortening the loading time. Other researchers [4, 18] claimed that an improvement of the dye loading can be achieved by changing the microstructure of the ZnO films, thus avoiding complex formation without the need of basic dye solutions [19]. However, these works were focused on the investigation of specific aspects of the preparation and sensitization procedure of ZnO: a multivariate and comprehensive study of the critical points listed above has never been carried out.

This important lack has been fulfilled in the present thesis, where a multivariate optimization of the sensitization procedure for flower-like ZnO nanostructured microparticles for the fabrication of efficient DSC photoanodes was performed by means of a chemometric approach [20]. The chosen experimental variables were the dye loading time (x_1), the dye solution concentration (x_2) and its pH (x_3), and the selected ranks of the values associated with the variables were the followings: x_1 was between 2 and 780 min, x_2 ranged between 0.05 and 0.75 mM, x_3 from 6.5 to 10.7. In order to carry out a multivariate DoE, the software MODDE (version 7.0.0.1, Umetrics), widely used in chemistry [21] and materials science [22], was adopted. An experimental domain as the one considered here can be investigated by means of a factorial design, which has a cubical geometry and is able to study the influence of all the factors (experimental variables) on the selected response (efficiency of sunlight conversion). A particular factorial design, which is the one adopted here, is the Central Composite Face-centered (CCF): in this case, the experiments were carried out not only on the vertices, but the axial points on the faces of the factorial hypercube were added (see Fig. 4.8). Each factor was studied on 3 levels (-1, 0, +1), with a total of 17 experiments, as detailed in Section 6.1.2.2.

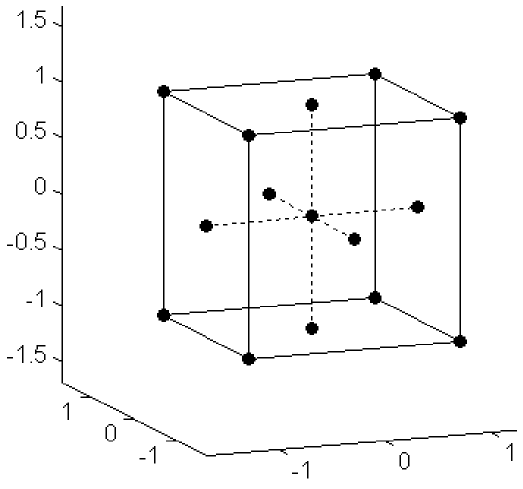

Fig. 4.8 Factorial hypercube of a Central Composite Face-centered (CCF) DoE in the presence of three factors. The black circles indicate the experimental domain points where the experiments were performed.

4.2.2 Chemometric optimization and fine tuning of morphological and photovoltaic properties of UV-crosslinked polymer electrolyte membranes

Polymer electrolyte membranes, in which the liquid electrolyte is trapped in the soft cages formed by the host polymer matrix, exhibit some advantages compared with other kinds of materials such as high ionic conductivity, intimate contact with the mesoporous TiO_2 layer, and easy handling of the system [23]. In this context free radical photo-polymerization (UV-curing) is an attractive method for building a tri-dimensional polymeric network as it is a very fast and environmentally friendly polymerization process, which requires low energy, no solvents and no catalysts, in addition to being transferable to industrial scale [24].

With the aim of correlating the photovoltaic properties of the UV-cured polymer electrolyte membranes (see Section 4.1.4.2.1) to the polymer morphology and, at the same time, of obtaining quasi-solid DSCs with excellent efficiency and durability, the optimization of the experimental conditions was carried out by exploiting a chemometric approach. In particular, two designs of experiments (DoE) were planned. At first, a two-level fractional factorial design (resolution V) with five factors was used to select the relevant ones. The five factors, carefully chosen according to our previous experience and bibliographic research [15, 25, 26], were: NaI (supplier of the I^-/I_3^- redox couple in the liquid electrolyte), propylene carbonate (membrane plasticizer) and $LiClO_4$ (liquid electrolyte additive) concentrations, BEMA:PEGMA ratio, and swelling duration. From the data analysis (see the Supporting Information of [20]), BEMA:PEGMA ratio and NaI concentration proved to be the significant factors. Then, a Central Composite Face-centered design (CCF-DoE) was employed to investigate their simultaneous effect on the performances of the DSCs: x_1 was defined as the weight percentage of BEMA (complementary to the PEGMA one) and x_2 as the molar concentration of NaI in acetonitrile (a 10:1 molar ratio NaI:I_2 was maintained [27]). The swelling time of 5 min was chosen as optimum as an extended swelling did not reflect on the ionic conductivity of the membrane. For the CCF-DoE, 12 experiments were performed, two variables were codified in three levels, and four central points were used to evaluate the experimental reproducibility. Experiments were carried out in random order to provide protection against the effects of lurking variables and also in this case experimental data were analyzed using the MODDE software (version 7.0.0.1, Umetrics).

4.3 Characterization

In this Section the instruments and the techniques exploited for the electrical, optical and physical-chemical characterization of the materials and of the Dye-sensitized Solar Cells will be presented.

4.3.1 Electrical characterization

I-V electrical characterization was carried out under AM 1.5 G illumination using a class A solar simulator (Newport 91195A) calibrated by means of a Si reference cell (VLSI SRC-1000-TC-QZ), and a Keithley 2440 SMU to apply the bias voltages and to measure the photocurrent. The measurements were performed using a black mask with a hole that allowed illuminating the cells with an area of 0.22 cm^2. In the particular case of the study devoted to the performance optimization of CT1-based DSCs (see Section 6.2.2), the sun simulator was calibrated by means of a pyranometer (CMP11, Kipp&Zonen), since at that time the Si reference cell was at the manufacturer for a recalibration. Finally, the *I-V* characteristics of the DSCs realized to validate the consistent static and small-signal physics-based modeling under different illumination conditions (see Sections 5.2 and 6.4) were measured for both photoelectrode (PE) and counter electrode (CE) side and, for the

PE-side illumination, were also performed at light intensities in the range 0.1 - 1 sun, by using neutral density filters.

The *IPCE* spectra were acquired in DC mode using a Newport 100-W QTH lamp as light source and a 150-mm Czerny Turner monochromator (Lot-Oriel Omni-l 150). The measured wavelength range was 400 - 800 nm (350 - 650 nm in case of CT1-based DSCs) with steps of 10 nm, and the current was measured by means of a Keithley 2440 SMU. The measurements were performed using a 0.22 cm^2 black mask. The *IPCE* spectra of the DSCs analyzed in the physics-based modeling study reported in Sections 5.2 and 6.4 were measured for both PE- and CE-side.

Electrochemical impedance spectra were collected through an electrochemical workstation (CH Instruments 760D) in the frequency range 10^{-1} - 10^5 Hz (10^{-2} - $2 \cdot 10^4$ Hz in case of quasi-solid DSCs based on UV-crosslinked polymer electrolyte membranes, see Section 6.3.1.2) with an amplitude of the sinusoidal signal of 10 mV. Sponge-like ZnO-based DSCs (see Section 6.1.1.2) and CT1-based DSCs exploited to investigate the hemi-squaraine/TiO_2 interface (see Section 6.2.1) and to model the dye loading time influence on the *EIS* (see Sections 5.1 and 6.2.3) were measured at open circuit voltage (0.5 V for the last mentioned cells) under 1 sun illumination using a solar simulator (Newport 91195A) and a 0.22 cm^2 black mask. *EIS* spectra of irreversible sealed DSCs employed to validate the consistent static and small-signal physics-based modeling under different illumination conditions (see Sections 5.2 and 6.4) were acquired in the same conditions at bias voltages ranging from 0 to 0.8 V and for the PE-side illumination were also performed at light intensities in the range 0.1 - 1 sun, by using neutral density filters. Finally, *EIS* spectra of flower-like ZnO-based DSCs (see Section 6.1.2.2), of UV-crosslinked polymer electrolyte membranes-based DSCs (see Section 6.3.1.2) and of CT1-based DSCs realized to optimize the photovoltaic performances of the hemi-squaraine (see Section 6.2.2) were collected in dark conditions at different bias voltages ($V_{oc} \pm 0.10$ V with steps of 0.05 V).

The experimental *EIS* data of flower-like ZnO-based DSCs were fitted using the equivalent circuit shown in Fig. 4.9, which includes a contact resistance (R_S), an equivalent impedance of the photoanode (Z_{ox}), and a charge transfer impedance (R_{CE} and C_{CE}) at the electrolyte/cathode interface [28]. The mass transport impedance due to the diffusion of the electrolyte species has been neglected since no significant contribution was evidenced in the measured frequency range. According to a purely diffusive transport model of the electrons across the photoanode, the small-signal impedance of the oxide is modeled by the input impedance of the distributed *RC* circuit, open load terminated, shown in Fig. 4.9 (bottom) [29]. The constant phase element Q_μ with equivalent impedance

$$Z = Q_\mu^{-1}(i\omega)^{-\beta} \tag{4.1}$$

is a generalization of the conventional electrochemical capacitance, included to account for the possible frequency dispersion observed in the *EIS* spectra. The electrochemical capacitance C_μ, corresponding to the constant phase element, results as

$$C_\mu = Q_\mu^{\frac{1}{\beta}} R_{CT}^{\frac{1}{\beta}-1}. \tag{4.2}$$

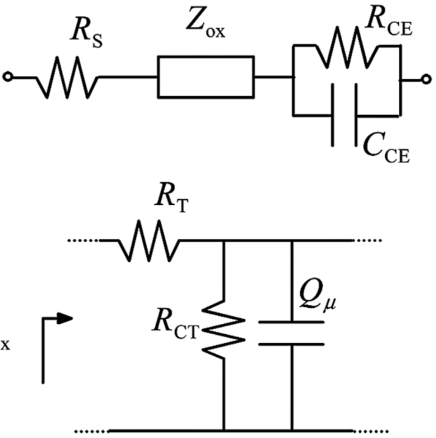

Fig. 4.9 Equivalent circuit exploited for the fitting of the *EIS* spectra of flower-like ZnO-based DSCs. Top: equivalent circuit of the overall cell. Bottom: transmission line model of the oxide film [30].

The *EIS* experimental data of all the other DSCs reported above were fitted using the equivalent circuit shown in Fig. 3.2, valid in the approximation of potentials close to the V_{oc}. In this modeling circuit [31], the parallel $R_1//Q_1$ represents the interface between the electrolyte and the counter electrode, while the interface between the oxide and the electrolyte was described through the parallel $R_2//Q_2$; in both cases R_i is a resistance and Q_i is a constant phase element (CPE). The use of a CPE instead of a capacitance led to a better description of interfaces involving a high-porosity medium. A resistance R_s was introduced to take into account all the series resistances. The charge diffusion within the electrolyte was described by a Warburg impedance [32].

4.3.2 Optical characterization

UV-Visible spectroscopy measurements were carried out by means of a Varian Cary 5000 spectrophotometer equipped with an integrating sphere for diffuse and specular reflectance. For all the absorbance measurements, the Kubelka-Munk function

$$F(R) = \frac{(1-R)^2}{2R} = \frac{k}{s} = \frac{aC}{s} \tag{4.3}$$

(where R stands for the reflectance, k for the absorption coefficient, s for the scattering coefficient, C for the concentration of the absorbing species and a for the absorbance) was evaluated, in order to correlate reflectance and absorbance [33].

4.3.3 Physical-chemical characterization

Field Emission Scanning Electron Microscopy (FESEM) was exploited for all the morphological characterizations performed in this work. In particular, the morphology of the coral-shaped Zn and ZnO films (see Section 6.1.1.1) was investigated, both in top and in cross view, by means of a Zeiss SUPRA 40, while the morphology of the flower-like ZnO microparticles and film (see Section 6.1.2.1) was analyzed only in top view by means of a Zeiss Dual Beam AURIGA. The electron energy employed was always equal to 5 keV.

X-ray diffraction technique was used to determine the crystalline structure of the coral-shaped Zn and ZnO films (Panalytical PW1140-PW3020, CuK_α X-ray source) (see Section 6.1.1.1) and of the flower-like ZnO powder (X′Pert diffractogram, CuK_α = 1.54 Å) (see Section 6.1.2.1). In the first case, the scans were performed in a parallel beam geometry with a fixed angle of incidence ω = 1.5°, in order to minimize the contribution of the substrate to the observed diffracted intensities, while a Bragg-Brentano configuration was used in the second case.

The BET (Brunauer-Emmett-Teller) specific surface area of the coral-shaped ZnO sample (see Section 6.1.1.1) and of the flower-like ZnO powder (see Section 6.1.2.1) were evaluated from N_2 sorption isotherms (Quantachrome Autosorb1 and Quadrasorb SI, Quantachrome, respectively) by multipoint method within the relative pressure range of 0.1 - 0.3 p/p_0.

Density Functional Theory (DFT) and Time Dependent DFT (TDDFT) were exploited to study the structural and electronic coupling between the hemi-squaraine and the

TiO_2 (see Section 6.2.1), while DFT model was applied to estimate the pore size distribution of the flower-like ZnO particles (see Section 6.1.2.1).

The kinetics of the photo-polymerization process (see Section 6.3.1.1) was investigated by using FT-IR spectroscopy (NICOLET-5700 FT-IR instrument by Thermo Fisher Scientific Inc., Illkirch, France), which collects the spectra in real time while the sample is irradiated by UV light, following the decrease in the area of the band attributable to the methacrylate groups at 1630 cm^{-1}. The tests were carried out at ambient temperature on a UV transparent SiC wafer. A medium pressure mercury lamp (Hamamatsu) equipped with an optical guide was used to induce the photo-polymerization (light intensity on the surface of the sample: 30 mW/cm^2).

The Thermo Gravimetric Analysis (TGA) was exploited with the aim of assessing the thermal stability of the different UV-crosslinked polymer membranes and of the cellulose-based gels (See Sections 6.3.1.1 and 6.3.2.1). The analysis were performed in the temperature range 25 - 500 °C using a TGA/SDTA-851 instrument (METTLER, Zurich, Switzerland) under N_2 flux at a heating rate of 10 °C/min and in the temperature range 25 - 600 °C using a Netzsch TG 209 F1 TGA instrument under N_2 flux at a heating rate of 10 °C/min, respectively.

Dynamic mechanical analysis (TTDMA, Triton Technology) was carried out to correlate the composition of the UV-cured polymer matrix and the DSCs photovoltaic performances (see Section 6.3.1.2).

The conductivity measurements of cellulose-based gels were performed by means of a Metrohm EC.AUT.MAC multipotentiostat equipped with a FRA32 module (see Section 6.3.2.1). Impedance tests were performed at room temperature in a frequency range between 1 and 100 Hz. The resistance of the electrolyte was given by the low frequency intercept determined by analyzing the impedance response using a fitting program provided with the Metrohm instrument NOVA software. Conductivity values (σ) were obtained by exploiting the following equation:

$$\sigma = \frac{l}{A\,R} \tag{4.4}$$

where l is the thickness of the sample, A the area and R the measured resistance.

The viscosity measurements of cellulose-based gels were carried out at room temperature and 60 °C using an Anton Paar MCR 302 Modular Compact Rheometer with a logarithmic sweep in the range 0.1 - 100 s^{-1} (see Section 6.3.2.1).

References

[1] M. K. Nazeeruddin, A. Kay, I. Rodicio, R. Humphry-Baker, E. Mueller, P. Liska, N. Vlachopoulos, and M. Grätzel, *J. Am. Chem. Soc.* **115**, 6382 (1993).

[2] L. Vesce, R. Riccitelli, G. Soscia, T. M. Brown, A. Di Carlo, and A. Reale, *J. Non-Cryst. Solids* **356**, 1958 (2010).

[3] P. M. Sommeling, B. O'Regan, R. R. Haswell, H. J. P. Smit, N. J. Bakker, J. J. T. Smits, J. M. Kroon, and J. A. M. van Roosmalen, *J. Phys. Chem. B* **110**, 19191 (2006).

[4] M. Saito, and S. Fujihara, *Energy Environ. Sci.* **1**, 280 (2008).

[5] P. Wen, Y. Han, and W. Zhao, *Int. J. Photoenergy* **2012**, 906198 (2012).

[6] www.solaronix.com/products/rutheniumdyes/ruthenizer535bistba/.

[7] G. Cicero, G. Musso, A. Lamberti, B. Camino, S. Bianco, D. Pugliese, F. Risplendi, A. Sacco, N. Shahzad, A. M. Ferrari, B. Ballarin, C. Barolo, E. Tresso, and G. Caputo, *Phys. Chem. Chem. Phys.* **15**, 7198 (2013).

[8] J. H. Yum, S. J. Moon, R. Humphry-Baker, I. Walter, T. Geiger, F. Nuesch, M. Grätzel, and M. K. Nazeeruddin, *Nanotechnology* **19**, 424005 (2008).

[9] Y. Cao, J. Zhang, Y. Bai, R. Li, S. Zakeeruddin, M. Grätzel, and P. Wang, *J. Phys. Chem. C.* **112**, 13775 (2008).

[10] A. Lamberti, A. Sacco, S. Bianco, E. Giuri, M. Quaglio, A. Chiodoni, and E. Tresso, *Microelectron. Eng.* **88**, 2308 (2011).

[11] K. R. Beebe, R. J. Pell, and M. B. Seasholtz, “Chemometrics: a practical guide”, (1998) John Wiley & Sons, Inc.

[12] A. Hagfeldt, G. Boschloo, L. Sun, L. Kloo, and H. Pettersson, *Chem. Rev.* **110**, 6595 (2010).

[13] C. Bauer, G. Boschloo, E. Mukhtar, and A. Hagfeldt, *J. Phys. Chem. B* **105**, 5585 (2001).

[14] N. Memarian, I. Concina, A. Braga, S. M. Rozati, A. Vomiero, and G. Sberveglieri, *Angew. Chem. Int. Ed.* **50**, 1 (2011).

[15] A. Yella, H. W. Lee, H. N. Tsao, C. Yi, A. K. Chandiran, M. K. Nazeeruddin, E. W. G. Diau, C. Y. Yeh, S. M. Zakeeruddin, and M. Grätzel, *Science* **334**, 629 (2011).

[16] T. P. Chou, Q. Zhang, and G. Cao, *J. Phys. Chem. C* **111**, 18804 (2007).

[17] K. Keis, E. Magnusson, H. Lindstrom, S.-E. Lindquist, and A. Hagfeldt, *Sol. Energy Mater. Sol. Cells* **73**, 51 (2002).

[18] K. Kakiuchi, E. Hosono, and S. Fujihara, *J. Photochem. Photobiol., A* **179**, 81 (2006).

[19] A. Lamberti, R. Gazia, A. Sacco, S. Bianco, M. Quaglio, A. Chiodoni, E. Tresso, and C. F. Pirri, *Prog. Photovoltaics Res. Appl.* **22**, 189 (2014).

[20] F. Bella, D. Pugliese, J. R. Nair, A. Sacco, S. Bianco, C. Gerbaldi, C. Barolo, and R. Bongiovanni, *Phys. Chem. Chem. Phys.* **15**, 3706 (2013).

[21] J. Fricke, K. Pohlmann, N. A. Jonescheit, A. Ellert, B. Joksch, and R. Luttmann, *Biotechnol. J.* **8**, 738 (2013).

[22] F. Bella, J. R. Nair, and C. Gerbaldi, *RSC Adv.* **3**, 9 (2013).

[23] Z. Lan, J. Wu, D. Wang, S. Hao, J. Lin, and Y. Huang, *Sol. Energy* **80**, 1483 (2006).

[24] C. Decker, *Prog. Polym. Sci.* **21**, 593 (1996).

[25] B. E. Hardin, H. J. Snaith, and M. D. McGehee, *Nat. Photonics* **6**, 162 (2012).

[26] J. Preat, D. Jacquemin, and E. A. Perpète, *Energy Environ. Sci.* **3**, 891 (2010).

[27] R. Kawano, H. Matsui, C. Matsuyama, A. Sato, M. A. Bin Hasan Susan, N. Tanabe, and M. Watanabe, *J. Photochem. Photobiol., A* **164**, 87 (2004).

[28] J. Halme, P. Vahermaa, K. Miettunen, and P. Lund, *Adv. Mater.* **22**, E210 (2010).

[29] J. Bisquert, G. Garcia-Belmonte, F. Fabregat-Santiago, N. S. Ferriols, P. Bogdanoff, and E. C. Pereira, *J. Phys. Chem. B* **104**, 2287 (2000).

[30] A. Sacco, A. Lamberti, R. Gazia, S. Bianco, D. Manfredi, N. Shahzad, F. Cappelluti, S. Ma, and E. Tresso, *Phys. Chem. Chem. Phys.* **14**, 16203 (2012).

[31] R. Harikisun, and H. Desilvestro, *Sol. Energy* **85**, 1179 (2011).

[32] J. R. Macdonald, *Ann. Biomed. Eng.* **20**, 289 (1992).

[33] D. J. Dahm, and K. D. Dahm, "Interpreting diffuse reflectance and transmittance", (2007) NIR Publications, Chichester.

Chapter 5: Modeling

This Chapter is dedicated to the description of two different models aimed at studying and deep understanding the many physical and opto-electronic mechanisms involved in the Dye-sensitized Solar Cells. The first one is a physical model built to investigate the influence of different dye loading conditions on the *EIS* response of a CT1-based DSC, while the second one is an opto-electronic model applied to build a consistent picture of the static and dynamic small-signal performances of nanocrystalline TiO_2-based DSCs under different incident illumination intensities and directions.

5.1 Influence of different dye loading conditions on the *EIS* response of a CT1-based DSC

5.1.1 Introduction

The dye sensitization of large band gap semiconductors is a fundamental aspect to be taken into account in order to develop efficient Dye-sensitized Solar Cells [1]. The device photovoltaic performances have often been observed to be directly dependent on the impregnation time used for the dye uptake by the porous photoanode. Moreover, for each combination of sensitizer-and-semiconductor film, an optimal loading time can be evaluated, beyond which the performances of the cell no longer change, or even get worse [2]. For traditional N719/TiO_2-based DSCs the influence of the impregnation time on the electric response has already been thoroughly discussed by several authors [3, 4, 5], and also our group recently suggested an electric model showing that the time dependence of the N719 coverage on TiO_2 nanostructured surface is in agreement with a square root dependence of the dipping time [6]. The optimal impregnation time for the usually employed 0.3 - 0.5 mM N719 ethanol solution revealed to be overnight, around 40% of the entire time [7, 8] spent to fabricate the solar cells. In order to overcome this drawback, thus assuring a great savings in terms of production costs and times, innovative dye molecules able to anchor to the semiconductor surface in shorter periods were synthesized by many research groups.

As an example, a simple hemi-squaraine organic dye molecule (CT1) acting as TiO_2 sensitizer has been proposed by our group and reported in Section 4.1.2.2. Even if the anchoring group (squaric acid moiety) of this sensitizer exhibits a quite fast attachment to the semiconductor surface, nevertheless this newly introduced organic dye molecule tends to aggregate, inducing a worsening of the electric performances of the DSCs [9].

The influence of the dye adsorption time on the electrical impedance of a CT1-based DSC has been studied. Differently from what was observed with N719-based DSCs [6], a non-monotonic effect of the impregnation time on the *EIS* has been found. This feature has been analyzed in terms of the dye molecules tendency to aggregate close to the TiO_2/electrolyte interface. A physical model that fits well the experimental data is here proposed [10], which also takes into account a correction related to the difference between the illuminated area of the cell and the total area available in the electrical measurements.

5.1.2 Consistent physical model

To better understand the electrical response of a CT1-based DSC, a cell schematically presented in Fig. 5.1a has to be considered.

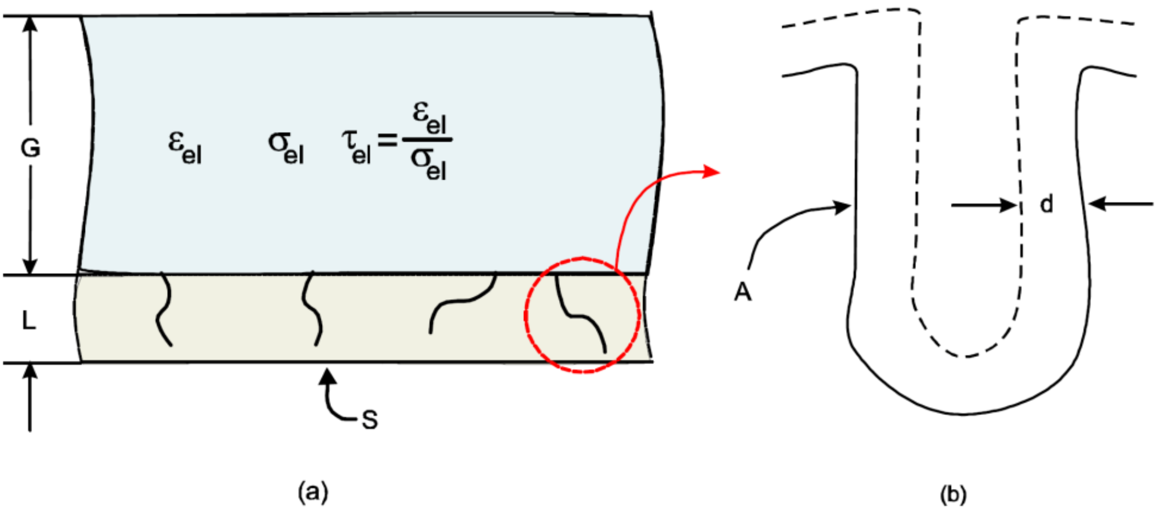

Fig. 5.1 Representation of the cell showing the TiO_2 electrode and the electrolyte (a) with the sketch of a pore (b). S is the surface area and L is the thickness of the porous electrode. G, ε_{el}, σ_{el}, τ_{el} are the thickness, the dielectric constant, the conductivity, and the characteristic time of the electrolyte, respectively. A is the total lateral area of the pores, while d is the thickness of the adsorbed dye layer [10].

The porous TiO_2 electrode covered with the organic dye is in contact with the electrolyte of thickness G, characterized by the material parameters ε_{el}, σ_{el} and $\tau_{el} = \varepsilon_{el}/\sigma_{el}$ standing for the dielectric constant, the conductivity and the characteristic time, respectively. In Fig. 5.1a some of the pores originating at the TiO_2/electrolyte interface are also presented. A model of a pore, showing the lateral area A and the limit d of the dye molecules adsorbed on the surface, is drawn in Fig. 5.1b. A is the area of all the pores that is in contact with the electrolyte. It may be estimated, in this case, knowing $\boldsymbol{A}$, the ratio between the area of the porous film and all its volume [11],

$$A = \boldsymbol{A} \cdot volume\ of\ the\ film = \boldsymbol{A} \cdot L \cdot S, \tag{5.1}$$

where L is the thickness of the TiO_2 layer and S the surface of the cell.

When the adsorption process begins, the lateral area A starts to be covered with a monomolecular layer of the sensitizer, forming patches of adsorbed dye that, summed up, represent a fraction θ of A. Due to the fact that the free ion density in the electrolyte is large enough, the potential in the bulk can be considered constant. On the contrary, the potential may vary within a thin layer delimited by the surface A and an equipotential surface parallel to it, a distance d apart.

Applying a small sinusoidal voltage to the CT1-based DSC, two types of currents are drawn: one across the area θA, characterized by the admittance Y_1, and another one across the free surface $(1 - \theta)A$ with the admittance Y_2, as shown in Fig. 5.2.

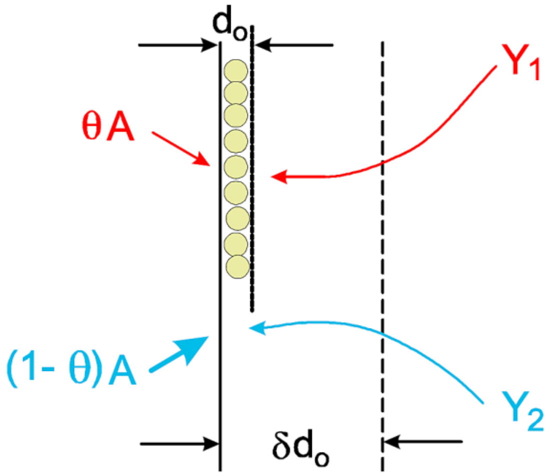

Fig. 5.2 Currents passing through the dye-adsorbed monolayer θA and through the free surface $(1 - \theta)A$. d_0 is the thickness of the dye monolayer, while δd_0 is the distance until the influence of the pore's wall is felt by the dye molecules [10].

The monolayer is described by the average molecular diameter d_0 (10^{-9} m [9]) and the equipotential surface of thickness δd_0, where δ is a rather small average number of molecular diameters. This is the physical limit within which a dye molecule feels the attraction force from the surface of the pore. The total admittance in the δd_0 layer is $Y = Y_1 + Y_2$.

The process of dye adsorption starts when the nanostructured TiO_2 photoanode is immersed into the sensitizer solution and saturates after a while as the parameter θ goes to 1. Since the dye loading technological step is mainly governed by the diffusion of dye molecules into the porous layer, one may consider the following time dependence of θ

$$\theta(t) = \sqrt{\frac{t}{t+\tau}} \tag{5.2}$$

where τ is a characteristic time corresponding to the moment when practically 70% of the total area A is covered with a monomolecular dye layer. This time dependence of θ is also valid in the case of N719-based DSCs [12]. Fig. 5.2 shows the situation when $t < \tau$. When $t > \tau$, the possibility that dye molecules can build up on top of already existing monomolecular layer, eventually filling the layer of thickness δd_0 [9], as shown in Fig. 5.3a, can be considered.

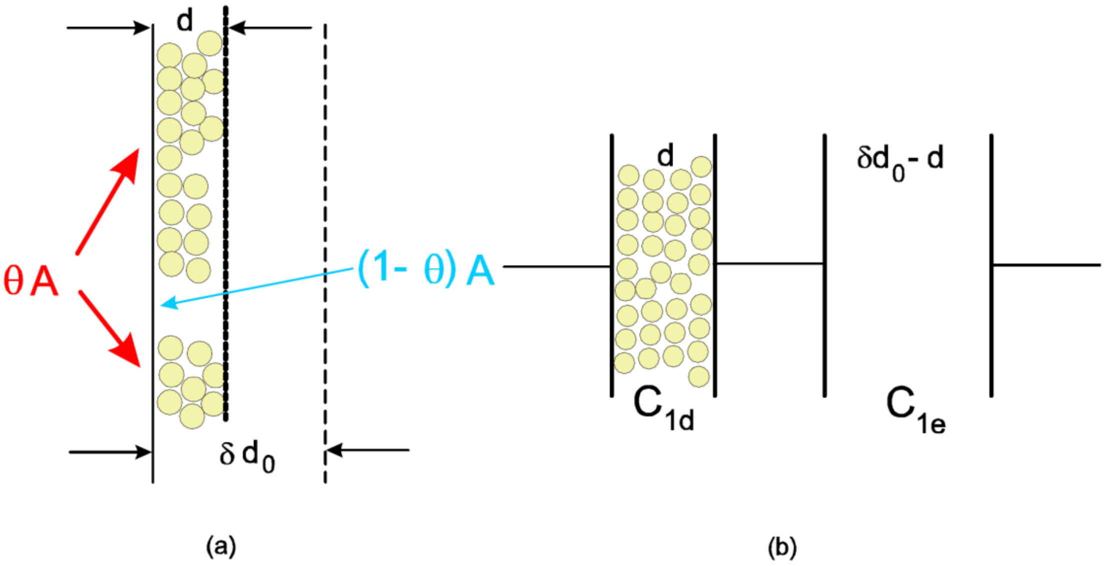

Fig. 5.3 A build-up of dye-molecules on TiO_2 surface for $d_0 < d < \delta d_0$ (a). Equivalent capacitances in series: C_{1d} filled with the CT1 dye and C_{1e} filled with the electrolyte (b) [10].

Since θ is quite large (≤ 1) and the free surface $(1 - \theta)A$ is quite small, one can define an average thickness d of the adsorbed dye layers ($d_0 < d < \delta d_0$). The growth of this layer decreases exponentially in time, the thickness d would go asymptotically to the value δd_0 and the whole process could be characterized by a decaying time, for convenience expressed as $k \cdot \tau$, where k is an arbitrary small number. The reason why one can imagine such a process is that the adsorption of the dye molecules originates from the interaction with the solid surface of the TiO_2 layer and the adsorption of the second or the third layer is screened by the other inner layers. The screening varies exponentially with the thickness of the adsorbed layers. A thicker adsorbed dye layer prevents the transfer of electrons, leading to a worsening in the electric performances of the device.

Dye molecules may not agglomerate in the bulk. The agglomeration mechanism is present only at the surfaces, due to the attraction forces between them and the dye molecules. These forces decrease when increasing the number of absorbed layers, until the thermal energy is larger than the absorption energy. For long impregnation time, the thickness of the dye layers will reach the value $\delta d_{0.}$

In *EIS* spectra a higher impedance of the δd_0 layer has to be expected in the regions marked with θA in Fig. 5.3a. In this region two capacitors in series, one related to the dye layer C_{1d} and the other one to the remaining electrolyte layer C_{1e}, as shown in Fig. 5.3b, can be considered.

The impedance Z of the cell, apart from the contribution Y^{-1}, includes the following series elements: Z_b, the bulk impedance of the electrolyte, and R_0, the transfer resistance of the electrodes and the connecting wires. In order to express the total impedance of the cell, for each film a parallel of resistance and capacitance can be considered, with the exception of the electrolyte bulk where the diffusion of free ions is not negligible and a Warburg type element [13] should be taken into account. The free surface $(1 - \theta)A$ presents the admittance Y_2

$$Y_2 = \frac{1}{R_2} + j\,\omega\,C_2 \quad \text{where} \quad R_2 = \frac{\delta d_0}{\sigma_{el}\,(1-\theta)\,A} \quad \text{and} \quad C_2 = \frac{\sigma_{el}\,\tau_{el}\,(1-\theta)A}{\delta d_0}. \tag{5.3}$$

The dye covered surface θA is described by two capacitors in series, one filled with CT1 dye molecules and another one with electrolyte, as shown in Fig. 5.3b. Considering the values σ_d and τ_d as the conductivity and the characteristic time of the dye layer respectively, the following equations can be written

$$Y_1 = \frac{1}{R_1} + j\ \omega\ C_1 \tag{5.4}$$

$$R_1 = \frac{\delta d_0 - d}{\sigma_{el}\ \theta\ A} + \frac{d}{\sigma_d\ \theta\ A} \tag{5.5}$$

$$C_{1d} = \frac{\sigma_d\ \tau_d\ \theta\ A}{d},\ C_{1e} = \frac{\sigma_{el}\ \tau_{el}\ \theta\ A}{\delta d_0 - d} \tag{5.6}$$

$$C_1 = \sigma_{el}\ \tau_{el}\ \theta\ A \left(\frac{\sigma_{el}\ \tau_{el}}{\sigma_d \tau_d} d + \delta d_0 - d\right)^{-1}. \tag{5.7}$$

Another important feature to be taken into account is that *d* starts to increase toward *δd₀* only after *θ* has got a certain value, for instance *θ* (*τ*) may be considered to be ≈ 0.707. One may use the step function *UnitStep* defined as

$$UnitStep(t) = \begin{cases} 0\ if\ t < 0 \\ 1\ if\ t \geq 1 \end{cases} \tag{5.8}$$

so that the following expression for *d* can be obtained

$$d = d_0 + (\delta - 1)d_0 \left[1 - exp\left(-\frac{t-\tau}{k\cdot\tau}\right)\right] UnitStep(t - \tau) \tag{5.9}$$

Finally, the bulk impedance of the electrolyte, written as a parallel *RC* element, turns out to be

$$Z_b = \frac{R_b}{(1 + j\ \omega\ \tau_{el})} = \frac{G}{\sigma_{el}\ S\ (1 + j\ \omega\ \tau_{el})} \tag{5.10}$$

where *G* is the thickness of the electrolyte layer.

5.2 Physical and electrical modeling of static and small-signal response in a Ru-based DSC

5.2.1 Introduction

The main purpose of the ongoing research on DSCs is to increase the cell efficiency improving, at the same time, its reliability and stability through material and structural optimization. Within this context, a physics-based model capable of consistently describing and understanding the device behavior and its relation with microscopic mechanism under different operating conditions may provide a significant support in the interpretation of the experimental results and in the advancement of DSC technology.

The modeling and simulation of DSCs have been dealt with by many researchers, focusing on device-level behavior or on some specific physical aspects. Models based on drift-diffusion approaches of charged species in the electrolyte permeated nanostructured TiO_2 film have been proposed [14, 15, 16, 17, 18] and applied to evaluate the *I-V* characteristic and to link the microscopic description of the cell to its photovoltaic behavior. Physics-based steady-state models exploiting a purely diffusive description of the charge transport have been used starting from the analytic model reported by Södergren *et al.* [19], then used to build an analytic device model [20] containing all the optical and electrical main features of the device, and to develop coupled optical and electrical models [21, 22]. The diffusion transport approach has been progressively enriched by novel recombination and transport models, in view of describing experimental observations arising from static but also dynamic characterization techniques [23, 24, 25].

A static (DC) and dynamic small-signal (SS) device-level model of DSCs is here presented [26], which self-consistently couples a physics-based description of the nanoporous photoactive layer to a compact circuit-level description of the passive parts of the cell. The opto-electronic model of the nanoporous dyed film includes a detailed description of photogeneration and trap-limited kinetics, and a phenomenological description of nonlinear recombination. Numerical simulations of the dynamic small-signal behavior of DSCs, accounting for trapping and nonlinear recombination mechanisms, are reported and validated against experiments. The model is applied to build a consistent picture of the static and dynamic small-signal performances of nanocrystalline TiO_2-based DSCs under different incident illumination intensities and directions, analyzed in terms of

Current-Voltage characteristic, Incident Photon-to-electron Conversion Efficiency, and Electrochemical Impedance Spectroscopy. This is achieved with a reliable extraction and validation of a unique set of model parameters against a large enough set of experimental data. Such a complete and validated description allows gaining a detailed view of the cell collection efficiency dependence on different operating conditions.

5.2.2 Coupled opto-electronic diffusion transport model

In view of modeling the DSC, a detailed physics-based model of the electrolyte permeated sensitized nanoporous TiO_2 film, approximated as an equivalent homogenous medium, is coupled with a compact equivalent circuit model accounting for the electrical loss induced by diffusion through the bulk electrolyte (described by a Warburg impedance, Z_W), the charge transfer at the electrolyte/counter electrode interface (R_{CE}, C_{CE}), and the contact series resistance, as depicted in Fig. 5.4.

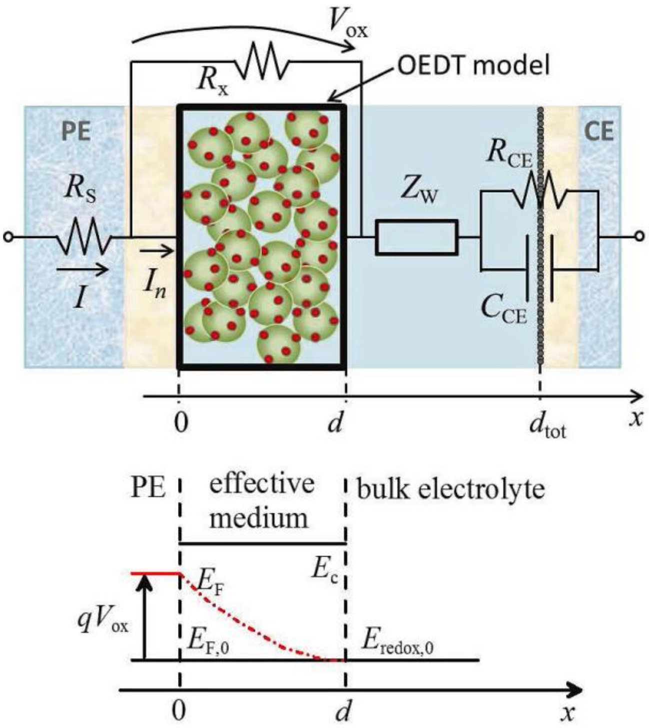

Fig. 5.4 Top: mixed circuit and physical description of the DSC. The intrinsic device is simulated through the Opto-Electronic Diffusion Transport (OEDT) model described in the text. Bottom: definition of the nanoporous film boundaries and a sketch of the energy band diagram at thermal equilibrium (solid lines) and out of equilibrium (dashed line) [26].

The photovoltaic *I-V* characteristics of the cell are described by the following nonlinear system

$$I = I_n(V_{ox}) - \frac{V_{ox}}{R_x} \tag{5.11}$$

$$V = V_{ox} - RI \tag{5.12}$$

where *I* and *V* are the total current flowing across the cell and the voltage drop between the counter electrode (CE) and the photoelectrode (PE), taken with the generator convention sign, $R = R_s + R_{CE} + R_W$ is the total parasitic resistance, and I_n and V_{ox} are the current and voltage across the photoelectrode, respectively. Additional efficiency losses related to the non-zero slope of the *I-V* characteristics under the short circuit conditions are empirically modeled by the parallel resistance R_x.

5.2.2.1 Diffusion transport model

According to the multiple trapping and release model [27], the electron transport across the nanocrystalline semiconductor oxide takes place through the extended states in the conduction band, whereas the localized states in the band gap just act as thermally activated capture or emission centers. The conduction band electrons are described by the Boltzmann statistics, with thermal equilibrium density given by

$$n_0 = N_c \, e^{\frac{E_{F,0} - E_C}{k_B T}} \, , \tag{5.13}$$

where N_c is the conduction band density of states, $E_{F,0}$ the Fermi level in thermal equilibrium and E_c the conduction band edge in the TiO_2, respectively. On the other hand, the density of the electrons trapped in the localized states is expressed as

$$n_T = \int_{E_v}^{E_c} g(E) f(E) dE, \tag{5.14}$$

where *g(E)* is the density of states of the traps, approximated as an exponential

$$g(E) = \alpha \frac{N_T}{k_B\,T}\, e^{\alpha \frac{E-E_C}{k_B\,T}} \tag{5.15}$$

where N_T is the concentration of trap levels per unit volume and $\alpha = T/T_0$ represents the depth of the states distribution below E_c. By approximating the Fermi-Dirac distribution with a step function

$$f(E) = \frac{1}{1+e^{\frac{E-E_F}{k_B\,T}}} \approx \begin{cases} 0 \;\; if \;\; E > E_F \\ 1 \;\; if \;\; E < E_F \end{cases}, \tag{5.16}$$

the trapped electron concentration finally reveals to be

$$n_T = \int_{E_v}^{E_C} g(E)dE \approx N_T\, e^{\alpha \frac{E_F-E_C}{k_B\,T}} \;. \tag{5.17}$$

Neutral conditions across the nanostructured TiO_2 layer and a concentration of the redox couple in the electrolyte close to the equilibrium value and much larger than the electron concentration are assumed. The Fermi energy in the electrolyte phase can thus be assumed constant and equal to the equilibrium energy of the I^-/I_3^- redox couple. Under these assumptions, the time dependent continuity equation for the conduction band electron density n can be written as

$$\frac{\partial n}{\partial t} = \frac{1}{q}\frac{\partial J_n}{\partial x} - U_n(n) + G_n^{op}(x) - \frac{\partial n_T}{\partial t}\,, \tag{5.18}$$

where U_n and G_n^{op} are the net recombination rate and the optical generation rate, respectively, and J_n is the diffusion current density, given by

$$J_n = qD_0 \frac{\partial n}{\partial x}\,, \tag{5.19}$$

where D_0 is the free electron diffusivity.

Under static (DC) conditions the cell behavior is fully described by Eq. (5.18), i.e. considering only the physical mechanisms involving the extended states, which share a common equilibrium Fermi level with the localized ones. On the other hand, under time-varying conditions, the dynamics of the electrons in the extended and in the localized states will evolve independently, so that a full description of the trap kinetics is generally required. However, as long as the frequency of interest is low with respect to the trap dynamics [27], an approximated quasi-static configuration can be adopted [28], assuming that even in non equilibrium conditions, the conduction band and trap populations share the same quasi-Fermi level. Under this assumption, the dynamics of the extended and the localized states occupation are related as

$$\frac{\partial n_T}{\partial t} \approx \frac{\partial n_T}{\partial n}\frac{\partial n}{\partial t}, \tag{5.20}$$

where the term $\partial n_T/\partial n$ does not explicitly depend on time; by exploiting Eq. (5.13) and (5.17), this results in

$$\frac{\partial n_T}{\partial t} \approx \alpha \frac{N_T}{N_c} e^{(\alpha-1)\frac{E_F-E_C}{k_B T}} = \alpha \frac{N_T}{N_c^{\alpha}} n^{\alpha-1} . \tag{5.21}$$

Introducing this expression in the continuity equation (5.18), a single equation taking into account the dynamics of both free and trapped electrons [23, 29] is obtained in the following form

$$k_T(n)\frac{\partial n}{\partial t} = \frac{1}{q}\frac{\partial J_n}{\partial x} - U_n(n) + G_n^{op}(x), \tag{5.22}$$

where the adiabatic factor k_T is defined as

$$k_T(n) = 1 + \alpha \frac{N_T}{N_c^{\alpha}} n^{\alpha-1}. \tag{5.23}$$

Despite the suppression of trap-assisted recombination, the electron lifetime is generally limited by recombination at the semiconductor/dye/electrolyte interface with the acceptor species in the electrolyte and with the excited dye molecules. The two recombination mechanisms are here modeled by means of an equivalent nonlinear net recombination rate [24]

$$U_n(n) = k_0 n^{\beta-1}(n - n_0) \tag{5.24}$$

aimed at describing the observed discrepancy between the photovoltaic performances under different illumination conditions through a carrier density dependent lifetime. It is worth noting that a zero net recombination rate is yielded under thermal equilibrium conditions ($n = n_0$). The conventional constant lifetime approximation is recovered when $\beta = 1$; on the other hand, $-1 < \beta < 1$ describes a sub-linear increase in the recombination rate with carrier density, and $\beta > 1$ a super-linear one. Using the definition of the electron diffusion current, the electron continuity equation can be finally written as

$$k_T(n)\frac{\partial n}{\partial t} = D_0 \frac{\partial^2 n}{\partial x^2} - k_0 n^{\beta-1}(n - n_0) + G_n^{op}(x). \tag{5.25}$$

The model is completed by a voltage-driven boundary condition at the FTO/TiO_2 interface ($x = 0$) and by a Neumann (or reflective) boundary condition at the interface between the nanostructured TiO_2 film and the bulk electrolyte ($x = d$, being d the nanostructured TiO_2 thickness). As depicted in Fig. 5.4, the thermal equilibrium condition is set by $E_{F,0} = E_{redox,0}$. A voltage drop V_{ox} across the semiconductor layer displaces the Fermi level in the TiO_2 (E_F) with respect to the redox energy potential in the electrolyte according to $qV_{ox} = E_F - E_{F,0}$. Under non-equilibrium conditions, using Eq. (5.13) and expressing N_c as a function of n_0, it results

$$n(x) = n_0\, e^{\frac{E_C - E_{F,0}}{k_B T}}\, e^{\frac{E_F(x) - E_C}{k_B T}}. \tag{5.26}$$

Thus, the following boundary conditions can be exploited

$$n(x = 0) = n_0\, e^{\frac{qV_{ox}}{k_B T}} \tag{5.27}$$

$$\left.\frac{\partial n}{\partial x}\right|_{x=d} = 0. \tag{5.28}$$

Once the continuity equation is solved, the total electron current density across the photoelectrode is evaluated from Eq. (5.19) at x = 0.

5.2.2.2 Optical model

Carrier photogeneration is simulated using measurement-based optical data of the sensitized TiO_2 film and other cell layers. The optical generation rate is calculated assuming a Lambert-Beer exponential attenuation of the light across the solar cell, which has been proven to be rather accurate in conventional DSCs. The optical absorption of the photoelectrode is evaluated according to an effective medium approximation as $\alpha = \alpha_D + P\varepsilon\alpha_{EL}$ [20]. α_D and α_{EL} are the optical absorption of the sensitized TiO_2 film and of the electrolyte, respectively; while P and ε model the porosity and the average mean path length of the light across the film. The optical generation rate is then evaluated as

$$G_n^{op} = \int_\lambda \Phi\,(\lambda)\ \eta_{inj}\,\eta_{ill}(\lambda)\alpha_D(\lambda)e^{-\alpha(\lambda)x}F(\lambda)d\lambda \tag{5.29}$$

where $\Phi(\lambda)$ is the spectral photon flux density and the function $F(\lambda)$ assumes different values depending on the simulated photovoltaic experiment (*I-V* or *IPCE*)

$$F(\lambda) = \begin{cases} 1 & \rightarrow G_n^{op}(x) \quad \rightarrow I\text{–}V \\ \lambda'\delta(\lambda-\lambda') & \rightarrow G_n^{op}(x,\lambda) \rightarrow IPCE. \end{cases} \tag{5.30}$$

The illumination efficiency $\eta_{ill}(\lambda)$, accounting for the optical loss, is calculated as [21, 30]

$$\eta_{ill,PE}(\lambda) = T_{PE}(\lambda)\,(1 - R_{PE}(\lambda)) \tag{5.31}$$

for illumination from the photoelectrode side, and as

$$\eta_{ill,CE}(\lambda) = T_{CE}(\lambda)\,T_{EL}(\lambda)(1 - R_{PE}(\lambda)) \tag{5.32}$$

for illumination from the counter electrode side. T_{PE} and R_{PE} are the transmittance and the reflectance of the photoelectrode, respectively; while T_{CE} and T_{EL} are the transmittance of the counter electrode and of the bulk electrolyte, respectively. Finally, η_{inj} is related to the electron injection efficiency from the excited state of the dye into the conduction band of the TiO_2 [31].

5.2.2.3 Small-signal model

Small-signal condition is a particular operation mode in which a small-amplitude electrically or optical driven time-varying signal perturbs the DC operating point, i.e. the static concentration n_{dc}. The case of electrical perturbation of the DC operating point (i.e. the case of *EIS* measurements) is here considered. Under a harmonic small-amplitude voltage with angular frequency ω, it can be written

$$v = V_{dc} + Re(\hat{v}e^{j\omega t}),\ \hat{v} \ll V_{dc} \tag{5.33}$$

$$n = n_{dc} + Re(\hat{n}e^{j\omega t}),\ \hat{n} \ll n_{dc}. \tag{5.34}$$

After the linearization and the Fourier transform of Eq. (5.25), it results

$$\frac{\partial^2 \hat{n}}{\partial x^2} = \frac{\hat{n}}{[L_n^{ss}(x)]^2}\,, \tag{5.35}$$

with the boundary condition in Eq. (5.28) at $x = d$, and the linearized boundary condition at $x = 0$,

$$\hat{n}(x = 0) = n_0 \frac{\hat{v}}{V_T}\,. \tag{5.36}$$

The small-signal complex diffusion length in Eq. (5.35) is

$$L_n^{ss}(x, \omega) = \left(\frac{\tau_n^{ss} D_n^{ss}}{1 + j\omega\tau_n^{ss}}\right)^{\frac{1}{2}}, \tag{5.37}$$

where the small-signal diffusivity D_n^{ss} and the small-signal lifetime τ_n^{ss} are defined as

$$D_n^{ss}(n_{dc}) = \frac{D_0}{k_T(n_{dc})} \tag{5.38}$$

$$\tau_n^{ss}(n_{dc}) = k_T(n_{dc})\tau_f, \tag{5.39}$$

τ_f being the static lifetime of conduction band electrons

$$\tau_f = \left(\frac{\partial U_n}{\partial n} \bigg|_{n_{dc}} \right)^{-1} . \tag{5.40}$$

Due to the space-dependence of the above parameters, induced by both trap states and nonlinear recombination, Eq. (5.35) is a second-order differential equation with non constant coefficients, thus generally requiring a numerical solution.

Once Eq. (5.35) is solved, the small-signal impedance of the sensitized oxide is calculated as

$$Z_{ox} = \frac{\hat{v}_{ox}}{\hat{J}_n} , \tag{5.41}$$

with $\hat{J}_n$ given by Eq. (5.19). It has to be noted that, in the particular case of constant n_{dc} throughout the photoelectrode, Eq. (5.35) reduces to a conventional diffusion equation with constant parameters, leading to the following analytic closed-form expression for the photoelectrode impedance

$$Z_{ox}(\omega) = \frac{L_n}{\sigma_n} (1 + j\omega\,\tau_n^{ss})^{-1/2} coth \left[\frac{d}{L_n} (1 + j\omega\,\tau_n^{ss})^{1/2} \right] , \tag{5.42}$$

where $\sigma_n = V_T/(qD_0 n_{dc})$ is the electrical conductivity associated to the DC electron concentration and $L_n = L_n^{ss}(\omega = 0) = (\tau_f D_0)^{1/2}$. In other words, the DC diffusion length depends only on the band transport properties and the recombination rates; thanks to the compensation of the adiabatic factor in Eqs. (5.38) - (5.39), it is not affected by the trap dynamics.

From the implementation point of view, SS simulations require a double numerical solution: a DC simulation allows to achieve the charge density distribution across the device, necessary in order to assess the density dependent parameters in the SS Eqs. (5.35) - (5.37); then, the SS behavior is simulated. A finite difference method is applied for the solution of the DC and SS partial differential equations, whose self-consistent solution with the circuit-level equations is get using a Newton-Raphson algorithm.

References

[1] B. O'Regan, and M. Grätzel, *Nature* **353**, 737 (1991).

[2] F. Hirose, K. Kuribayashi, M. Shikaku, Y. Narita, Y. Takahashi, Y. Kimura, and M. Niwano, *J. Electrochem. Soc.* **156**, B987 (2009).

[3] S. Nakade, Y. Saito, W. Kubo, T. Kanzaki, T. Kitamura, Y. Wada, and S. Yanagida, *Electrochem. Commun.* **5**, 804 (2003).

[4] S. Sakaguchi, H. Ueki, T. Kato, T. Kado, R. Shiratuchi, W. Takashima, K. Kaneto, and S. Hayase, *J. Photochem. Photobiol., A* **164**, 117 (2004).

[5] J. K. Kim, H. Seo, M. K. Son, I. Shin, J. Hong, and H. J. Kim, *Curr. Appl. Phys.* **10**, S418 (2010).

[6] A. L. Alexe-Ionescu, G. Barbero, C. F. Pirri, and E. Tresso, *J. Appl. Phys.* **112**, 024106 (2012).

[7] M. K. Nazeeruddin, C. Klein, P. Liska, and M. Grätzel, *Coord. Chem. Rev.* **249**, 1460 (2005).

[8] R. Katoh, K. Yaguchi, and A. Furube, *Chem. Phys. Lett.* **511**, 336 (2011).

[9] G. Cicero, G. Musso, A. Lamberti, B. Camino, S. Bianco, D. Pugliese, F. Risplendi, A. Sacco, N. Shahzad, A. M. Ferraris, B. Ballarin, C. Barolo, E. Tresso, and G. Caputo, *Phys. Chem. Chem. Phys.* **15**, 7198 (2013).

[10] D. Pugliese, N. Shahzad, A. Sacco, E. Tresso, and A. L. Alexe-Ionescu, *J. Appl. Phys.* **114**, 094901 (2013).

[11] M. K. Nazeeruddin, A. Kay, I. Rodicio, R. Humphry-Baker, E. Mueller, P. Liska, N. Vlachopoulos, and M. Grätzel, *J. Am. Chem. Soc.* **115**, 6382 (1993).

[12] N. Shahzad, A. L. Alexe-Ionescu, E. Tresso, and G. Barbero, *Phys. Lett. A* **377**, 915 (2013).

[13] J. O. M. Bockris, and A. K. N. Reddy, “Modern Electrochemistry”, (1998) Plenum Press, New York.

[14] J. Ferber, R. Stangl, and J. Luther, *Sol. Energy Mater. Sol. Cells* **53**, 29 (1998).

[15] A. Usami, and H. Ozaki, *J. Phys. Chem. B* **105**, 4577 (2001).

[16] T. Oda, S. Tanak, and S. Hayase, *Sol. Energy Mater. Sol. Cells* **90**, 2696 (2006).

[17] K. Nithyanandam, and R. Pitchumani, *Sol. Energy* **86**, 351 (2012).

[18] D. Gentilini, A. Gagliardi, M. A. der Maur, L. Vesce, D. D’Ercole, T. M. Brown, A. Reale, and A. Di Carlo, *J. Phys. Chem. C* **116**, 1151 (2011).

[19] S. Södergren, A. Hagfeldt, J. Olsson, and S.-E. Lindquist, *J. Phys. Chem.* **98**, 5552 (1994).

[20] J. Halme, P. Vahermaa, K. Miettunen, and P. Lund, *Adv. Mater.* **22**, E210 (2010).

[21] S. Wenger, M. Schmid, G. Rothenberger, A. Gentsch, M. Gratzel, and J. O. Schumacher, *J. Phys. Chem. C* **115**, 10218 (2011).

[22] M. Topic, A. Campa, M. Filipic, M. Berginc, U. O. Krasovec, and F. Smole, *Curr. Appl. Phys.* **10**, S425 (2010).

[23] P. R. F. Barnes, A. Y. Anderson, J. R. Durrant, and B. O'Regan, *Phys. Chem. Chem. Phys.* **13**, 5798 (2011).

[24] J. Bisquert, and I. Mora-Sero, *J. Phys. Chem. Lett.* **1**, 450 (2010).

[25] J. Villanueva-Cab, H. Wang, G. Oskam, and L. M. Peter, *J. Phys. Chem. Lett.* **1**, 748 (2010).

[26] F. Cappelluti, S. Ma, D. Pugliese, A. Sacco, A. Lamberti, G. Ghione, and E. Tresso, *Phys. Chem. Chem. Phys.* **15**, 14634 (2013).

[27] J. Bisquert, *Phys. Rev. B: Condens. Matter Mater. Phys.* **77**, 235203 (2008).

[28] J. Bisquert, and V. S. J. Vikhrenko, *J. Phys. Chem. B* **108**, 2313 (2004).

[29] J. A. Anta, J. Idigoras, E. Guillen, J. Villanueva-Cab, H. J. Mandujano-Ramirez, G. Oskam, L. Pelleja, and E. Palomares, *Phys. Chem. Chem. Phys.* **14**, 10285 (2012).

[30] J. Halme, G. Boschloo, A. Hagfeldt, and P. Lund, *J. Phys. Chem. C* **112**, 5623 (2008).

[31] S. Koops, B. O'Regan, P. F. Barnes, and J. R. Durrant, *J. Am. Chem. Soc.* **131**, 4808 (2009).

Chapter 6: Results and discussion

This Chapter aims to present and thoroughly discuss the different experimental and theoretical results obtained in the thesis work. A large part of the Chapter is devoted to the characterization and to the photovoltaic performances evaluation of innovative and low cost materials (ZnO photoanodes, metal-free dye and quasi-solid electrolytes) for DSCs application, able to overcome the issues exhibited by the conventional ones. With the purpose of supporting and corroborating the experimental analysis, a physical model built to interpret the aggregation phenomenon typically shown by organic dye molecules and an opto-electronic model applied to evaluate the static and dynamic small-signal performances of DSCs under different incident illumination intensities and directions will be also presented.

6.1 Innovative and low cost ZnO photoanodes for DSCs application

In this Section, a detailed description of the morphological and physical-chemical characterization of sponge-like and flower-like ZnO-based photoanodes will be provided, together with a deep investigation of their photovoltaic performances.

6.1.1 Sponge-like ZnO-based photoanodes

6.1.1.1 Photoanode characterization

In Fig. 6.1a the morphology of the deposited film as evaluated by FESEM is presented. The Zn film shows a sponge-like structure, compatible with the results proposed by Baker *et al.* for Zn-Al coatings [1]. The nanostructuring of a metallic film in a sponge-like structure occurs for growth processes performed with a substrate temperature T approximately equal to a half of the melting temperature T_m (i.e. $T/T_m \sim 0.5$) [2]. Being the melting temperature for zinc particularly low, it is possible to synthesize a porous nanostructured layer for $T \sim T_{amb}$. Films with thicknesses up to 15 µm were deposited.

As depicted in Fig. 6.1b, no significant morphological variation can be noticed after the high temperature oxidation procedure, resulting only in a moderate volume expansion.

Top view in Fig. 6.1c allows appreciating the porous morphology of the film and its similarity with the structure of natural coral. The specific exposed surface, as measured by BET, was equal to 14.1 m^2/g, in line with what measured for mesoporous ZnO layers deposited with other techniques [3].

On the magnified FESEM picture in Fig. 6.1d it is possible to observe the 3-dimensional coral-like nanostructure, formed by the superimposition of small branches able to grow in length along basically every direction. The typical dimension of the particulate is around 40 nm, with spacing between adjacent structures in the range 10 - 60 nm. Taking into account that the typical exciton length in ZnO is in the range 5 - 20 nm, such morphological feature presents all the desired characteristics for efficient dye loading and charge transport towards the electrode [4].

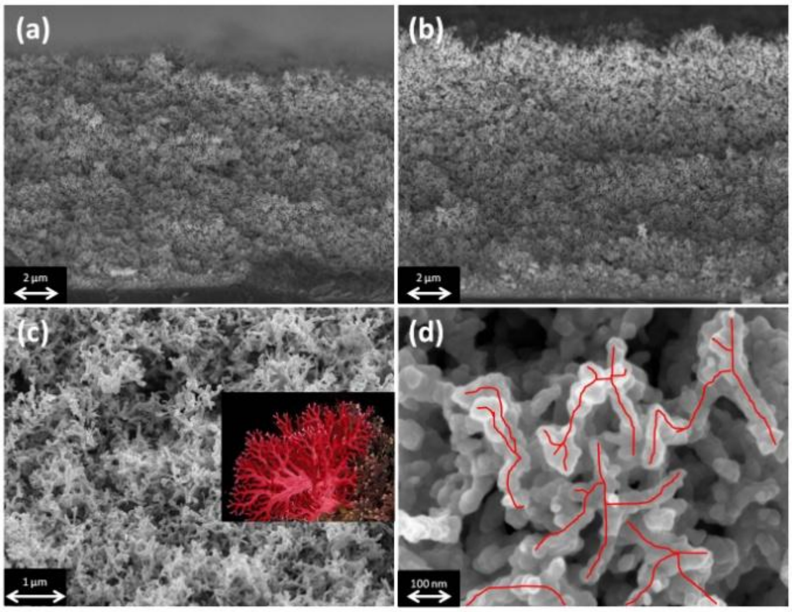

Fig. 6.1 FESEM characterization: Zn film, cross view (a); ZnO film, cross view (b); ZnO film, top view, and (inset) visual comparison with a natural coral (c); magnified image of the coral-like morphology, where the branched structure is evidenced (d).

The macroscopic appearance of the deposited film before and after the oxidation treatment drastically changes, moving from a black to a transparent feature, as shown in Fig. 6.2a. In Fig. 6.2b, the XRD characterization of the film before and after the oxidation procedure is reported. The diffraction pattern after the thermal treatment witnesses a complete oxidation of the film, without the formation of Zn residuals, which could be detrimental for charge transport in DSC photoelectrodes.

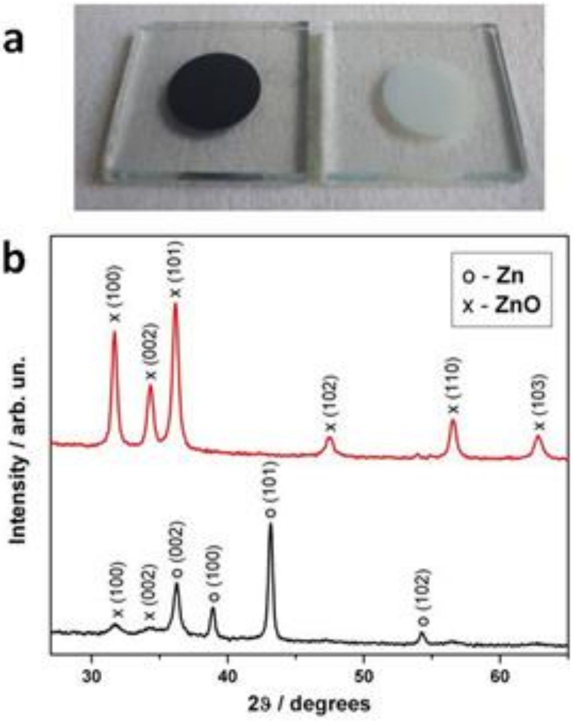

Fig. 6.2 Picture of the photoanode, before (left) and after (right) the oxidation treatment (a); XRD characterization, before (bottom) and after (top) the oxidation treatment (JCPDS cards: Zn 87-0713, ZnO 89-1397) (b).

6.1.1.2 Photovoltaic performances investigation

In Fig. 6.3 the *J-V* curves and the evaluation of the Photovoltaic Conversion Efficiency (*PCE*) as a function of the dye incubation time are reported.

Photoanodes with a ZnO film thickness equal to 15 µm were used. Several devices were tested and the relative error between different samples was within the 5%, meaning a very high reproducibility. An incubation time of two hours was found to be optimal for the sensitization of this material, in line with previously reported data [5] and with materials synthesized with other techniques [6]. In particular, an evident increase in the J_{sc} is noticed, while the *FF* reveals to be almost independent from the sensitization procedure.

The efficiency increase for short incubation times is related with the slow kinetics of dye adsorption on the surface of the semiconductor. When the number of chemisorbed dye molecules on the surface of ZnO is low, the *PCE* is reduced both because of the small number of photogenerated charges injected in the semiconductor and because of the higher recombination rate with the electrolyte, occurring at the semiconductor unoccupied sites. When the optimal incubation time is exceeded, the formation of molecular aggregates between the dissolved Zn^{2+} ions and the dye molecules occurs [7]. The aggregates are inactive in terms of charge generation and act as filters for the impinging light, decreasing the overall efficiency of the device.

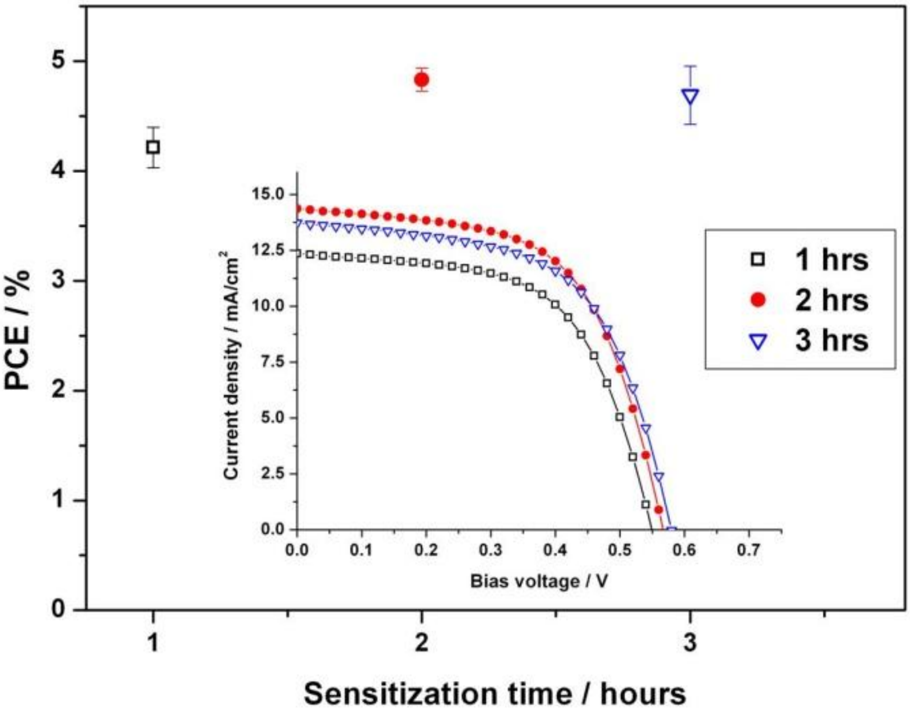

Fig. 6.3 Evaluation of the Photovoltaic Conversion Efficiency in microfluidic cells for different sensitization times, starting from the *J-V* curves (inset). The thickness of the ZnO film is 15 µm.

With the optimized sensitization time of two hours, the photovoltaic behavior of the device as a function of the ZnO film thickness was tested. The results of the *I-V* characterization and the Bode representation of the *EIS* phase are reported in Fig. 6.4. The increase in photoanode thickness from 12.5 µm up to 15 µm allowed obtaining a slightly higher efficiency, with an increase on the short circuit current, while the *FF* value remained unaffected. Thicker photoelectrodes are able to load a higher amount of dye, thus leading to the injection of a higher number of carriers in the conduction band of the semiconductor, and the charge transport is efficient enough to allow the collection of the electrons at the FTO electrode. More interestingly, the carrier lifetime shows a dependence on the photoanode thickness. The experimental curves of *EIS* were fitted using an equivalent circuit in order to obtain information about transport and recombination of charges [8]. In particular, the electron lifetimes at open circuit voltage can be estimated from the frequency f giving the maximum in the Bode plots reported in Fig. 6.4, as $\tau = 1/(2\pi f)$. The evaluated charge carrier lifetimes at V_{oc} were equal to 12 ms and 48 ms for the 12.5 µm- and the 15 μm-thick ZnO photoanodes, respectively. The dependence of the electron lifetime on the photoanode thickness is probably related to the contribution of the back transfer of electrons at the FTO/electrolyte interface [7]. For thicker photoanodes, this parasitic effect loses importance, giving as a macroscopic result a higher overall carrier lifetime, as reported previously for mesoporous TiO_2 films [9].

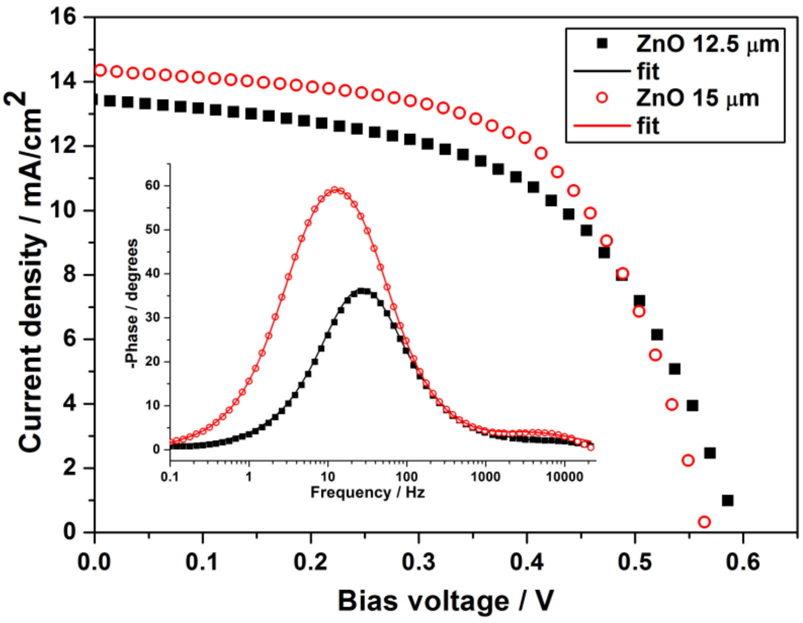

Fig. 6.4 *I-V* and *EIS* (Bode plots, inset) characterization of ZnO-based DSCs fabricated with different photoanode thicknesses, namely 12.5 μm (black) and 15 μm (red). The sensitization time was fixed to 2 h.

In conclusion, the solar energy conversion efficiency of DSCs based on coral-shaped ZnO photoanodes sensitized with Ru-based dyes was evaluated [10]. The sensitization procedure was refined, being the optimal sensitization time equal to 2 h. Using a 15 μm-thick photoanode assembled in a microfluidic architecture, a noticeable photovoltaic conversion efficiency of 4.83% was evaluated, with a charge carrier lifetime at the open circuit voltage equal to 48 ms.

6.1.2 ZnO flower-like microstructures as promising nanostructured photoanode

6.1.2.1 Photoanode characterization

X-Ray Diffraction (XRD) patterns of ZnO flower-like microparticles prepared at 70 °C are reported in Fig. 6.5. The diffraction peaks show a good crystalline quality of the sample, with the presence of a pure hexagonal wurtzite structure (JCPDS file, No. 80-0074).

Fig. 6.6a and b show the FESEM images of ZnO flower-like particles and of ZnO film after drying at 90 °C and subsequently heating at 450 °C, respectively. Zinc oxide powder is composed of nearly spherical particles with regular nanostructured prism-shaped planes as building blocks. The branched and nanostructured morphology of the ZnO is still well maintained after the preparation of the photoanode, with only a slight smoothing of the sharp edges due to the little dissolution effect of acetic acid-based solution. However, the XRD pattern after the photoanode preparation did not show any degradation of the crystalline wurtzite structure (data not reported).

The specific surface area, as measured by the BET approach, is 19.58 m^2/g, in line with the value measured for nanoporous ZnO electrodes [3]. Flower-like ZnO particles also show some degree of nanoporosity, evaluated by DFT model, with pore sized distribution peaking at about 4 nm. These pores, as well as the microparticle flower-like morphology, are responsible for the relatively high surface area and also act as preferential adsorption sites of Zn^{2+}/dye aggregates, generated by the dissolution of the ZnO by the Ru-based sensitizer during the DSC operation. The N_2 sorption isotherm and the DFT pore size distribution are reported in Fig. 6.7.

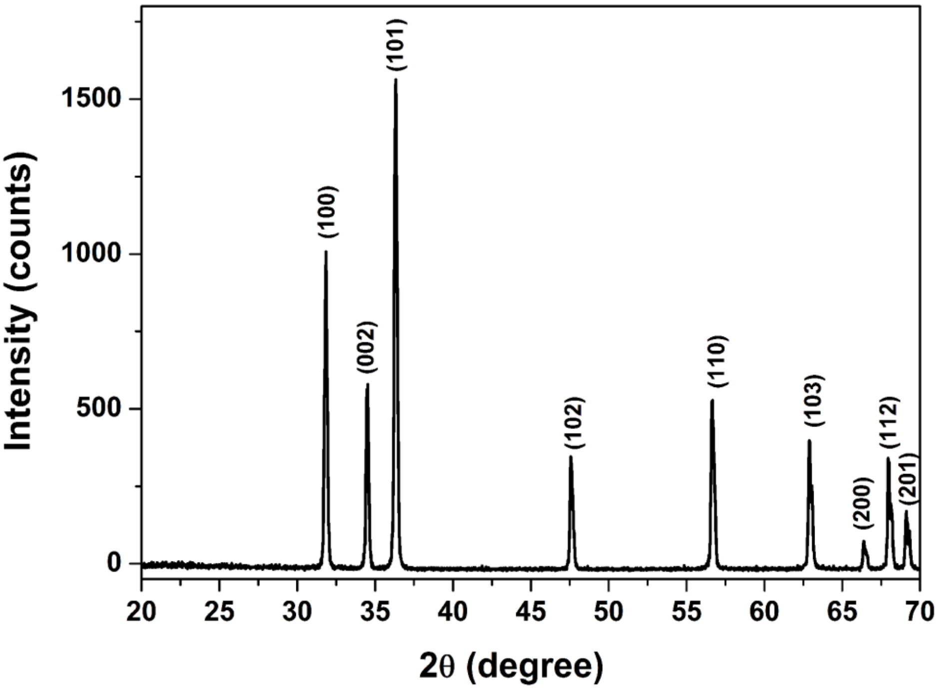

Fig. 6.5 XRD patterns of ZnO flower-like microparticles prepared at 70 °C.

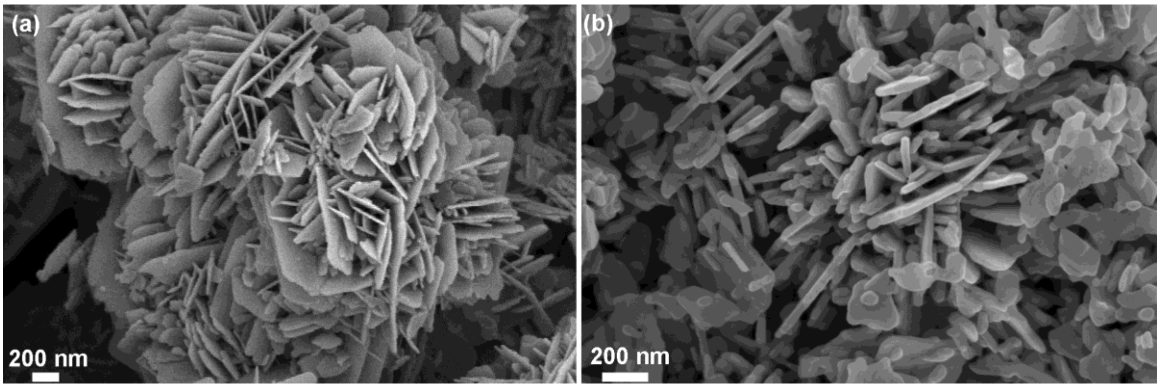

Fig. 6.6 FESEM image of ZnO flower-like microparticles prepared at 70 °C (a) and FESEM image of ZnO film after drying at 90 °C and subsequently heating at 450 °C (b).

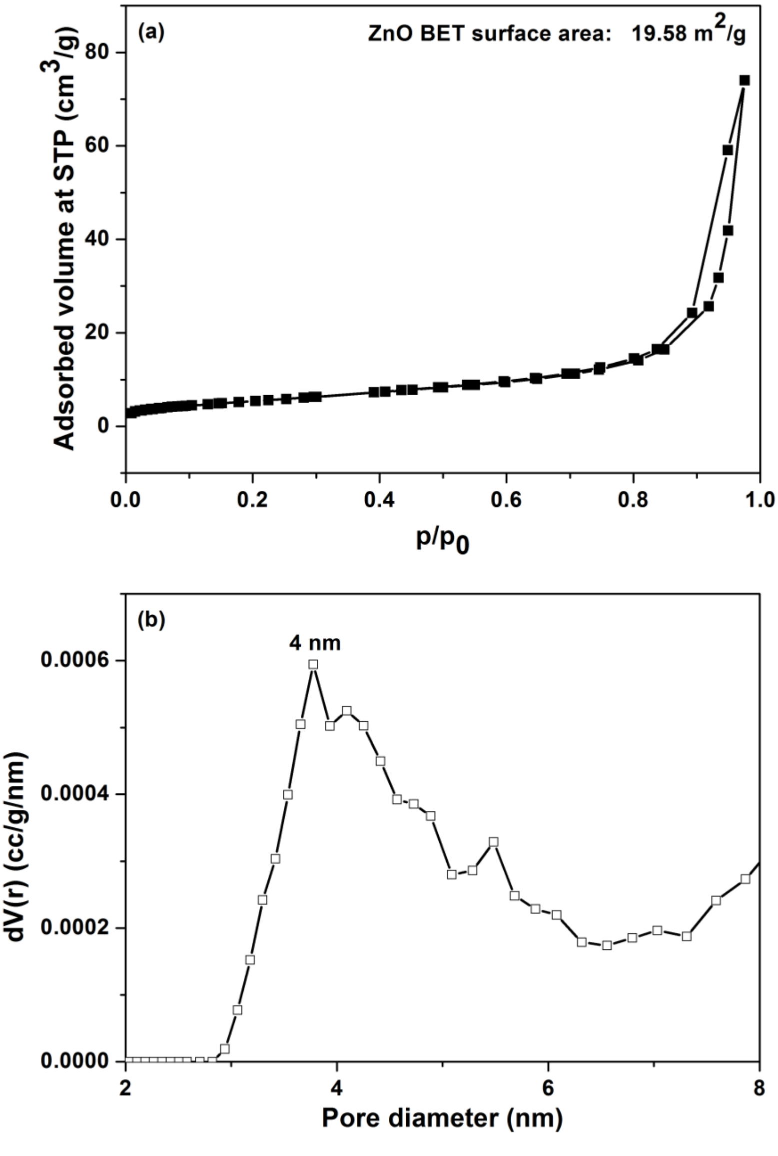

Fig. 6.7 Nitrogen sorption isotherm with the indication of the calculated BET surface area (a) and DFT pore size distribution of the ZnO nanostructured flower-like particles (b).

6.1.2.2 Chemometric investigation of the photovoltaic performances

The sensitization of the ZnO flower-like microparticles and the resulting performances on lab-scale DSCs were investigated by means of a CCF-DoE [11], a multivariate analysis method which permits the optimization of functional materials, simultaneously determining variables as others are modified. With this mathematical technique, the operational variables (dye loading time x_1, dye solution concentration x_2 and its pH x_3) can be simultaneously changed in order to identify the weight of each one and the relationship between them, indicating antagonisms and synergies. To the best of our knowledge, most of the investigations about DSCs consist of a monovariate analysis, even if this procedure leads to error when, at the very least, interactions between the variables occur. For all these reasons, an experimental design that simultaneously studies different variables is necessary to obtain an empirical mathematical equation for all the factors involved, as well as a response map that considers the influence of all the parameters.

Table 6.1 presents the experimental matrix generated by the software for the adopted CCF-DoE. As experimental response (y), it was decided to evaluate the light-to-electricity conversion efficiency (η) under 1 sun. In order to assess the experimental reproducibility, three replicas (F15, F16, F17) of the central point were carried out. In fact, the DoE reproducibility is usually evaluated on the experimental point with all the variables at their intermediate value. However, since the study of the reproducibility on a single experiment might seem insufficient, a second step of validation of the chemometric model will be introduced later.

The set of carried out experiments allowed to achieve a maximum light-to-electricity conversion efficiency of 3.16% (short circuit current density J_{sc} = 8.57 mA/cm^2, open circuit voltage V_{oc} = 0.56 V, Fill Factor FF = 0.65) for the ZnO photoelectrode sensitized with a 0.4 mM dye solution (pH 10.7) for 391 min (6.5 h). The current density-voltage curve and the corresponding *IPCE* curve of the DSC with the highest photoconversion efficiency, as mentioned above, are reported in Fig. 6.8. Multiple linear regression interpolation parameters were R^2 = 0.99 and Q^2 = 0.96. For the sake of completion, R^2 represents the fraction of the response variation explained by the model and Q^2 is the fraction of the response variation that can be predicted by the model. More broadly, R^2 and Q^2 provide the summary of the fit of the model: R^2 is an overestimated measure and Q^2 an underestimated value of the goodness of the fitting model. Both of these values are very close to 1, meaning that the regression model provides an excellent description of the relationship between the independent variables and the response, and therefore an optimal analysis of the investigated system. Furthermore, the average value of the sunlight conversion efficiency for the three replicated cells (from F15 to F17) was 2.88 (±0.13)%: this value is not only an excellent index of reproducibility, if compared to the repeatability typically observed in the literature for the DSC devices, but it also perfectly corresponds to the theoretical value predicted by the chemometric model (2.86%).

Table 6.1 Experimental matrix of variables and corresponding experimental and predicted responses to optimize the sunlight conversion efficiency. For completeness, short circuit current density (J_{sc}), open circuit voltage (V_{oc}), and Fill Factor (*FF*) values are also reported. Each variable was investigated at three levels (-1, 0, +1).

Exp. Name	**Dye loading time (x_1, min)**	**Dye concentration (x_2, mM)**	**Dye solution pH (x_3)**	**η observed (y, %)**	**η predicted (%)**	**J_{sc} (mA/cm^2)**	**V_{oc} (V)**	***FF***
F1	2 (-1)	0.05 (-1)	6.5 (-1)	0.24	0.19	0.82	0.46	0.62
F2	780 (+1)	0.05 (-1)	6.5 (-1)	2.85	2.92	8.96	0.55	0.58
F3	2 (-1)	0.05 (-1)	10.7 (+1)	0.22	0.25	0.79	0.46	0.61
F4	780 (+1)	0.05 (-1)	10.7 (+1)	2.68	2.66	7.54	0.54	0.66
F5	2 (-1)	0.75 (+1)	6.5 (-1)	1.12	1.13	3.08	0.53	0.69
F6	780 (+1)	0.75 (+1)	6.5 (-1)	2.22	2.19	6.04	0.58	0.64
F7	2 (-1)	0.75 (+1)	10.7 (+1)	1.77	1.69	4.64	0.55	0.69
F8	780 (+1)	0.75 (+1)	10.7 (+1)	2.37	2.42	7.11	0.57	0.59
F9	2 (-1)	0.4 (0)	8.6 (0)	0.92	1.01	2.57	0.53	0.68
F10	780 (+1)	0.4 (0)	8.6 (0)	2.81	2.74	7.31	0.59	0.66
F11	391 (0)	0.4 (0)	6.5 (-1)	3.04	3.04	7.98	0.58	0.65
F12	391 (0)	0.4 (0)	10.7 (+1)	3.16	3.18	8.57	0.56	0.65
F13	391 (0)	0.05 (-1)	8.6 (0)	2.28	2.25	7.31	0.52	0.60
F14	391 (0)	0.75 (+1)	8.6 (0)	2.55	2.60	7.58	0.57	0.59
F15	391 (0)	0.4 (0)	8.6 (0)	2.73	2.86	8.22	0.58	0.57
F16	391 (0)	0.4 (0)	8.6 (0)	2.87	2.86	8.46	0.58	0.59
F17	391 (0)	0.4 (0)	8.6 (0)	3.03	2.86	8.33	0.57	0.64

Fig. 6.9 shows the influence (with 95% confidence) of each experimental factor on the response y (sunlight conversion efficiency). This coefficient plot is useful to develop the final modeling equation, which is an empirical relationship between the response and the factors expressed in polynomial form. From the ANOVA statistical analysis, it results in the following equation:

$$
\begin{aligned}
y(\%) = {} & 2.86(\pm 0.11) + 0.87(\pm 0.08)x_1 + 0.18(\pm 0.08)x_2 \\
& + 0.07(\pm 0.08)x_3 - 0.99(\pm 0.16)x_1^2 - 0.44(\pm 0.16)x_2^2 \\
& + 0.25(\pm 0.16)x_3^2 - 0.42(\pm 0.09)x_1x_2 - 0.08(\pm 0.09)x_1x_3 \\
& + 0.12(\pm 0.09)x_2x_3
\end{aligned} \qquad (6.1)
$$

where $y(\%)$, x_1, x_2 and x_3 are the light-to-electricity conversion efficiency, the dye loading time, the dye solution concentration and the pH of the dye solution, respectively. The coefficients indicate the importance of each factor in the equation.

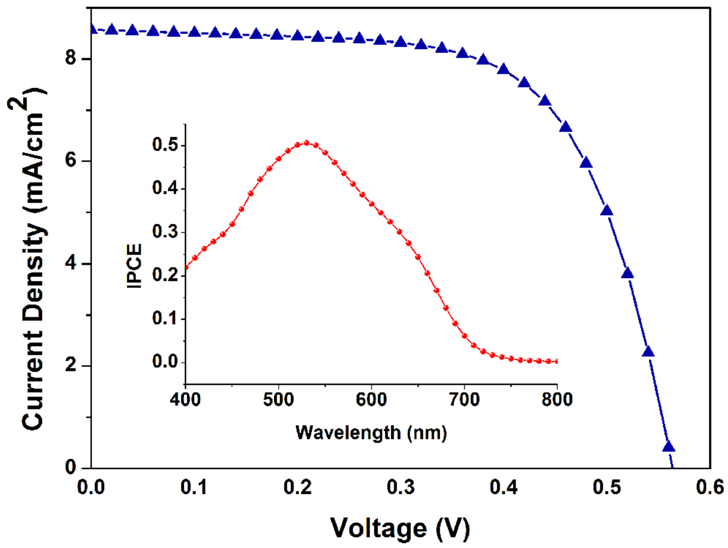

Fig. 6.8 Current density-voltage curve of the DSC (Experiment F12 in Table 6.1) with the highest photoconversion efficiency. The corresponding *IPCE* curve is shown in the inset.

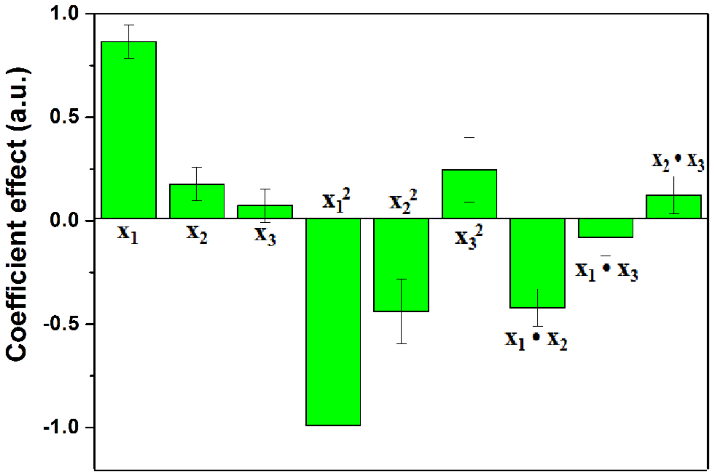

Fig. 6.9 Coefficient plot for the CCF-DoE. x_1: dye loading time; x_2: dye solution concentration; x_3: pH of the dye solution.

It is interesting to note that the coefficients of x_1 and x_2 are positive, while those of the quadratic effects are negative: this means that a slight increase in x_1 and x_2 leads to an increase of the DSC performances, but higher values of these factors lead to a reduction in the device efficiency. It can be assumed that beyond a certain value of dye impregnation time and dye concentration, protons derived from the Ru complexes make the dye loading solution relatively acidic and dissolve ZnO, generating Zn^{2+}/dye aggregates [12]. Such aggregates are harmful to the cell because they lower the electron injection efficiency and fill the nano-sized pores of the ZnO photoanode. On the other hand, the coefficient of x_3 is not very significant, while its quadratic term is positive, indicating that dye solutions with high pH values improve the photovoltaic performances. One possible reason why protons from the carboxyl groups of the dye initiate a dissolution process of the ZnO and form Zn^{2+}/dye complexes is related to the surface properties of the oxide. In particular, the protons adsorbed on the oxide surface dissolve the ZnO, since the pH of the dye solution is much lower than the point of zero charge (*pzc*) of the metal oxide, defined as the pH where the concentrations of protonated and deprotonated surface groups are equal [13]. The addition of a base to the dye loading solution, proposed by Keis *et al.* [3], makes the pH of the dye solution similar to the *pzc* of the ZnO, thus reducing the aggregation phenomenon and improving the photovoltaic performances of the cell. Lastly, as regards the interaction terms, only the coefficient of $x_1 \cdot x_2$ is significantly negative, indicating that soaking the flower-like microparticles with a concentrated solution of dye for a long time is counterproductive. Thus, the residence time of ZnO photoanode in the dye has to be shortened when using concentrated dye solution, in view of limiting the dissolution of ZnO during the dye loading.

The fitted response surfaces of the CCF-DoE are reported in Fig. 6.10, where the maximum response zone for sunlight conversion efficiency is observed at x_1 = 391 min, x_2 = 0.4 mM and x_3 = 10.7. In order to validate the experimental model, two hypotheses were analyzed:

- H_0: dependency between the variables does not exist.
- H_1: dependency between the variables exists.

The Student's *t*-test was applied using the quadratic differences between the results and their average, giving a probability of 5% for H_0 and a probability of 95% for H_1, thus corroborating H_1: dependency between the variables exists.

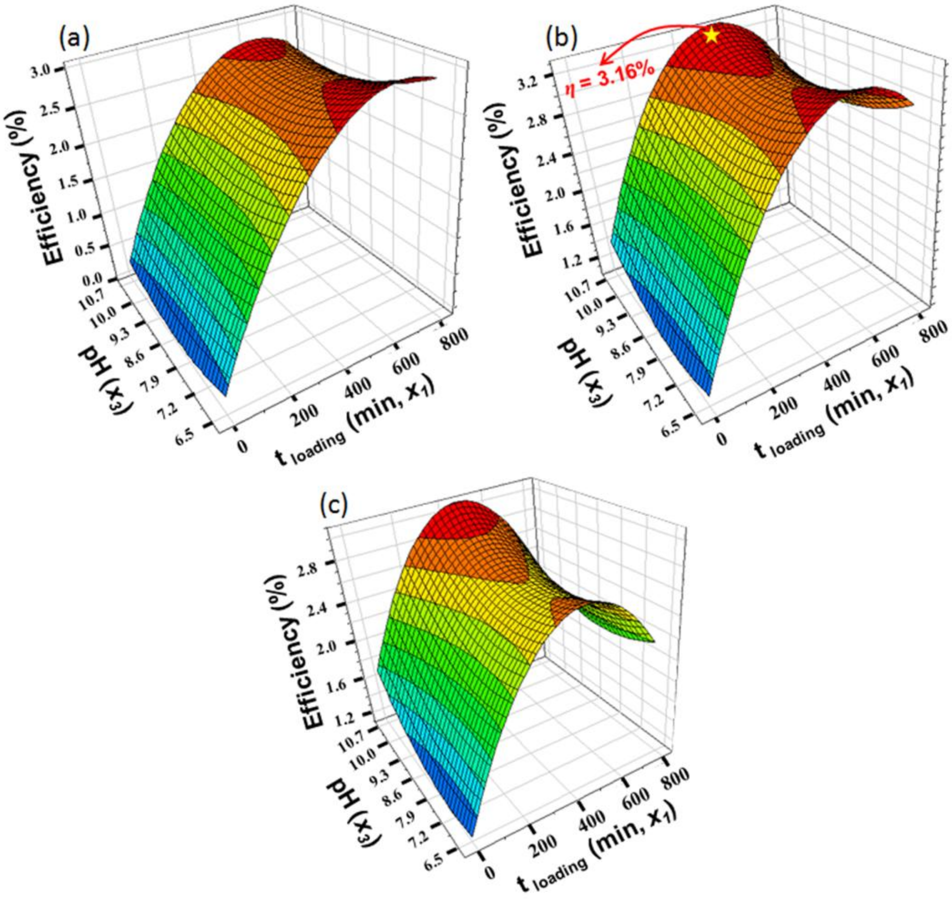

Fig. 6.10 Response surfaces showing the effect of the dye loading time (x_1) and the pH of the dye solution (x_3) on the light-to-electricity conversion efficiency of DSCs assembled with flower-like microparticle photoanodes, as a function of the dye solution concentration (x_2): 0.05 mM (a); 0.4 mM (b) and 0.75 mM (c).

Finally, in order to further support the statistical model, a cross-validation process was carried out: it is a model validation technique for assessing how the fitted results of a chemometric model will generalize to an independent data set. On a practical level, the software proposed some new experiments to be carried out, and also predicted the result to be experimentally obtained. The validation of the chemometric model is achieved if the obtained experimental results are - with 95% confidence - adherent to the predicted ones. This was actually the case, meaning that the chemometric model presented here is robust and valid.

Once identified the best conditions for the preparation procedure of the flower-like microparticle-based photoanodes, a further increase in photovoltaic performances can be accomplished by including additives to the commercial liquid electrolyte. While for TiO_2-based cells a large number of investigations on liquid electrolyte additives were reported in several reviews [14, 15], the effect of additives for ZnO-based cells has not been adequately addressed yet. In particular, the effect of N-methylbenzimidazole (NMBI), usually added to standard liquid electrolytes for TiO_2-based DSCs, but never tested in the presence of ZnO photoelectrodes, was investigated. Concerning TiO_2-based devices, NMBI was generally reported to increase the V_{oc} of a DSC, since it adsorbs onto the surface of TiO_2 [14, 15]. In addition, Yang *et al.* [16] found that this additive had a positive effect on ionic conductivity and apparent diffusion coefficient of triiodide, $D_{app}(I_3^-)$, weakening the Coulomb force between the cation and the anion, thus facilitating the ion dissociation.

In this specific case, the effect of NMBI was investigated for DSCs assembled with the photoanode prepared according to the optimal conditions (Experiment F12 in Table 6.1), and the results are reported in Table 6.2 and in Fig. 6.11.

Table 6.2 Photovoltaic performances of DSCs assembled with the optimized ZnO flower-like microparticle-based photoanode and with the addition of NMBI into the liquid electrolyte at different concentrations.

Electrolyte	**J_{sc} (mA/cm^2)**	**V_{oc} (V)**	***FF***	**η (%)**
AN 50	8.57	0.56	0.65	3.16
AN 50 + NMBI 0.25 M	8.75	0.58	0.65	3.26
AN 50 + NMBI 0.5 M	9.47	0.59	0.64	3.59
AN 50 + NMBI 0.75 M	9.18	0.59	0.62	3.35

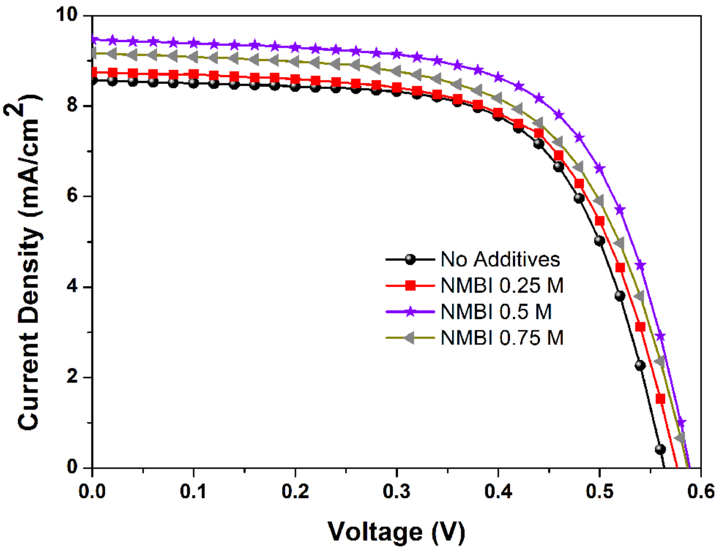

Fig. 6.11 Current density-voltage curves of DSCs assembled with the best ZnO flower-like microparticle-based photoanode (Experiment F12 in Table 6.1) and with the addition of NMBI into the liquid electrolyte at different concentrations.

As it can be noted, the addition of NMBI leads to an increase of both J_{sc} and V_{oc}. This result seems to confirm that the two effects observed by Yang *et al.* [16] for the TiO_2-based photoanode occur even in the presence of a ZnO-based one. In particular, in the presence of 0.5 M NMBI, the highest efficiency of the devices assembled with ZnO flower-like microparticle-based photoanodes was obtained: 3.59% (J_{sc} = 9.47 mA/cm^2, V_{oc} = 0.59 V, FF = 0.64). From the data reported in Table 6.2, it seems that the NMBI effect in reducing the electron recombination was maximized by using the concentration of 0.5 M.

In order to further confirm the above mentioned hypothesis, Electrochemical Impedance Spectroscopy measurements on the NMBI-based cells were performed and the results were compared with the reference cell (i.e. Experiment F12 in Table 6.1). In Fig. 6.12 examples of Nyquist plots of cell impedances are reported. The arcs related to the diffusion of charges in the electrolytic solution cannot be observed due to the lowest frequency value measured (usually the characteristic time constant of this process lies in the range 1 - 100 s [17]). In contrast, the high frequency arcs related to the charge transfer at the electrolyte/counter electrode interface are quite superimposed for the two kinds of devices, meaning that the presence of the additive has no influence on the charge transfer between the Pt and the solution. On the other hand, it can be noted that the main arc related to the recombination at the oxide/electrolyte interface exhibited by the NMBI-based cell is taller and wider than the one obtained from the device fabricated without additives: in accordance with the results of Yang *et al.* (despite of using a different semiconductor [16]), the presence of NMBI is effective in increasing the charge lifetime, witnessed by a larger recombination resistance (basically equal to the arc radius).

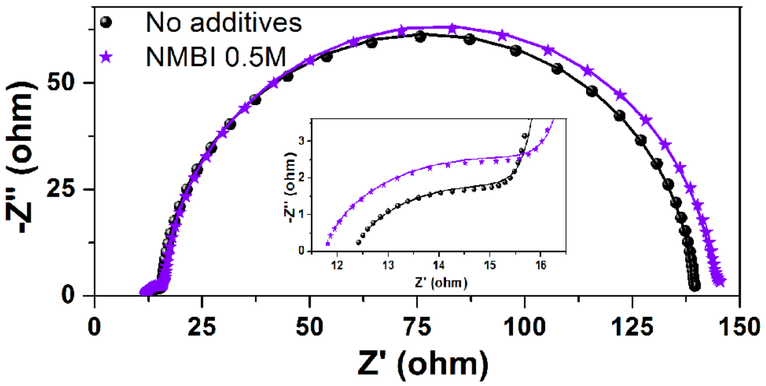

Fig. 6.12 Nyquist plots of DSCs assembled with the best ZnO flower-like microparticles-based photoanode (experiment F12 in Table 6.1) and with the addition of NMBI into the liquid electrolyte acquired at the open circuit voltage. The points are the experimental data while the continuous lines are the fitting curves.

To quantitatively evaluate the charge recombination and the transport properties in the flower-like ZnO-based photoanode, the experimental impedance spectra were fitted through the equivalent circuit reported in Fig. 4.9. The results of the fitting procedure are shown in Fig. 6.12 superimposed to the experimental curves, evidencing a good match between the measured and the calculated spectra. The electron lifetime τ_n and the diffusion coefficient D_n were evaluated from the fitting parameters [17], and in Fig. 6.13 they are reported as a function of the applied bias voltage. In agreement with what was observed from the Nyquist plots, the lifetime values of NMBI-based cells are larger with respect to those of the reference cell; the reduction of the charge recombination is therefore the reason for the higher photovoltage exhibited by the NMBI-containing devices [18]. In addition, the electron diffusion coefficient of these cells is higher than the reference one. Differently from what reported by Yang *et al.* [16], the triiodide apparent diffusion coefficient was not assessable due to frequency limitation. However, it was found that the inclusion of NMBI has a positive effect also on the oxide transport properties, thus further increasing the collection efficiency and, as a consequence, the short circuit current density [19]. Overall, it was shown that the addition of NMBI is a valuable means of increasing the performances of DSCs assembled with ZnO photoelectrodes.

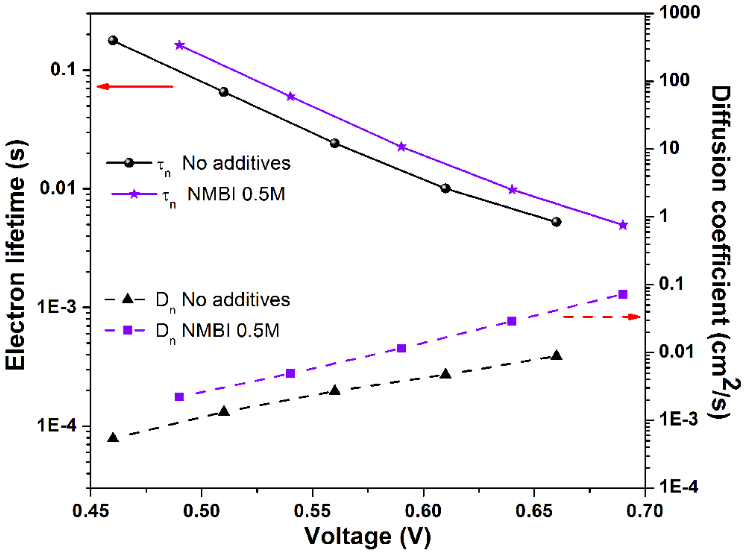

Fig. 6.13 Electron lifetime and diffusion coefficient dependence on the applied voltage for DSCs assembled with the optimized ZnO flower-like microparticle-based photoanode and with the addition of NMBI into the liquid electrolyte.

To sum up, promising photovoltaic properties of ZnO flower-like microstructures were demonstrated. A chemometric approach was employed, for the first time with ZnO-based DSCs, with the purpose of establishing the best sensitization conditions, thus avoiding Zn^{2+}/dye complexes formation. A maximum photoconversion efficiency value of 3.16% was achieved. The efficiency was enhanced up to 3.59% when adding, as unprecedently reported in the presence of a ZnO photoanode, N-methylbenzimidazole into the liquid electrolyte. This effect was attributed to the reduction of the charge recombination and to the enhancement of the diffusion coefficient, as evidenced by *EIS* analysis.

6.2 Metal-free hemi-squaraine CT1 sensitizer

This Section is entirely devoted to the study of a simple hemi-squaraine dye (CT1) as a TiO_2 sensitizer for application in Dye-sensitized Solar Cells. After a combined experimental and theoretical investigation of the hemi-squaraine/TiO_2 interface, a detailed study aimed at optimize the performances of CT1-based DSCs was carried out. Finally, the dye loading time influence on the electrical impedance of a CT1-based Dye-sensitized Solar Cell was analyzed by means of a physical model which takes into account the possibility of dye molecules aggregation close to the TiO_2/electrolyte interface.

6.2.1 Experimental and theoretical investigation of the hemi-squaraine/TiO_2 interface

In this Section the effectiveness of the CT1 dye, which belongs to a relatively new photosensitizers’ class, namely the hemi-squaraine molecule, will be studied. Although squaraine dyes are well known in DSCs [20], their hemi-squaraine intermediate has been rarely proposed [21] and never well studied as a TiO_2 sensitizer. Indeed this dye, beside its simplicity, its small dimension and its quite reduced absorption energy range, can be efficiently employed in DSCs. One of the peculiar features that makes hemi-squaraines a unique class of sensitizers is their anchoring group, the squaric acid moiety. The molecular structure of the hemi-squaraine dye is reported in Fig. 6.14.

The study of structural and electronic coupling between the hemi-squaraine and the TiO_2, focused on the role of the anchoring group, was performed by means of theoretical calculations based on the Density Functional Theory (DFT) and the Time Dependent DFT (TDDFT), and it is reported in details in ref. [18].

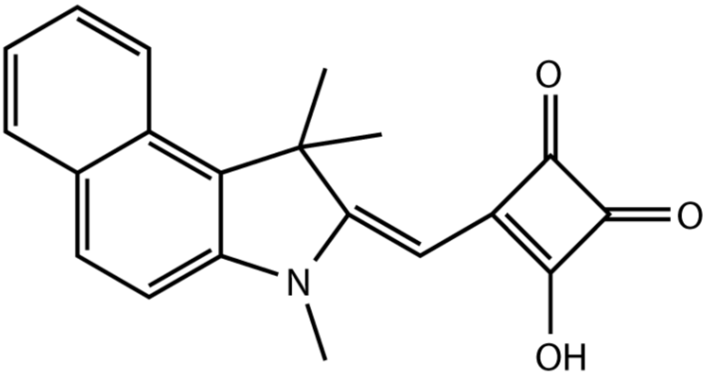

Fig. 6.14 Molecular structure of the hemi-squaraine sensitizer.

Briefly, the results showed that the relatively high efficiency of the hemi-squaraine dye could be ascribed to a large displacement of the electron charge towards the anchoring group in the excited state and to a strong chemical bonding between the squarate moiety of the dye and the anatase surface, which also induces hybridization between the unoccupied molecular states of the dye and the surface atoms of the oxide, revealing an adiabatic electron transfer mechanism. In order to verify if CT1 can work as a TiO_2 sensitizer, the alignment of the dye molecular levels with respect to the oxide band structure was determined experimentally by cyclic voltammetric analysis, also reported in ref. [18]. This analysis showed the formation of a staggered (or type II) interface (see Section 2.1.3), that is responsible for an efficient electron injection into the semiconductor CB.

Since the predictions of the *ab initio* calculations showed that the requirements for efficient application of CT1 in solar cells are satisfied, the sensitization of a TiO_2 nanoparticle network was experimentally characterized. Moreover the effect of the chenodeoxycholic acid (CDCA), employed as co-adsorbent in order to reduce the dye aggregation at the TiO_2 surface, was studied, by adding it in different concentrations (1 and 10 mM, corresponding to 4:1 and 40:1 concentration ratio between the CDCA and the dye, respectively) in the sensitizing solution. CDCA has also a strong influence of the quantity of the adsorbed dye since it competitively saturates the anchoring sites present at the surface. The impregnation time was fixed to 5 h. For comparison, a reference photoelectrode obtained with overnight impregnation of the oxide layer with a 0.35 mM N719 dye ethanol solution was fabricated and characterized. Fig. 6.15a and b compare the absorption spectrum of the dye in acetonitrile solution and those obtained for the TiO_2 photoanodes. The latter spectra exhibit an absorption range that is broader and red-shifted with respect to the dye in solution independently on the presence of CDCA.

These results are confirmed also by Incident Photon-to-electron Conversion Efficiency (*IPCE*) spectra reported in Fig. 6.15c, which show a surprisingly large red-shifted on-set (for a yellow dye having a maximum centered at 430 nm) around 600 nm.

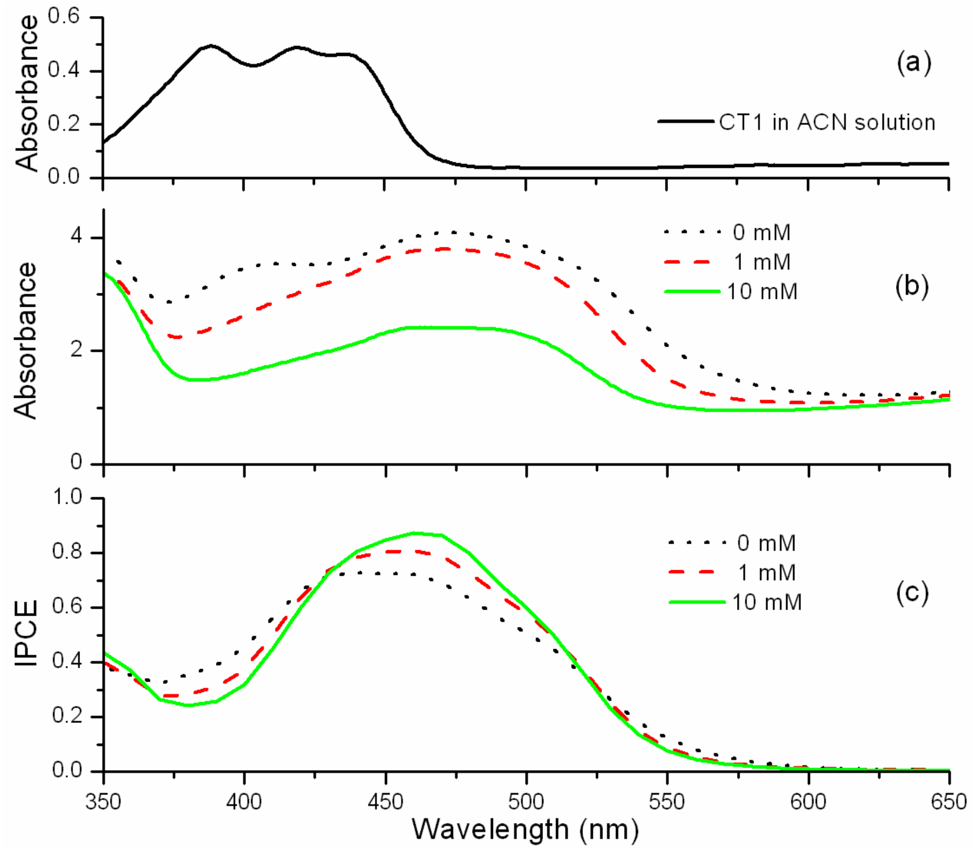

Fig. 6.15 UV-Visible absorbance spectra obtained for hemi-squaraine dye in acetonitrile solution (a) and for the dye attached to the nanocrystalline TiO_2 layer for different CDCA concentrations (b). *IPCE* curves of hemi-squaraine-based solar cells for different CDCA concentrations (c).

Both the broadening and the shift (blue or red depending on the dye characteristics) are commonly observed in spectral responses of organic dyes attached to the TiO_2 surface and they are generally attributed to the interaction of the anchoring group with the substrate surface, and/or to the formation of dye aggregates [22]. In this case, no strong dependence of the red shift on the presence of a co-adsorbent can be observed, thus it cannot be related with dye aggregation. Moreover the relatively high *IPCE* values demonstrate that the dye effectively injects electrons into the oxide conduction band as suggested by DFT electronic structure study. Fig. 6.15 also reveals the beneficial effects of the co-adsorbent, whose presence leads to higher, narrower and slightly red-shifted peaks in the *IPCE* spectra (Fig.

6.15c), reaching the maximum value of 87% at around 470 nm for a 10 mM CDCA concentration. CDCA molecules act as spacers among the hemi-squaraine molecules, avoiding the dye aggregation and thus facilitating the electron injection into the semiconductor CB. In the absorption spectra of Fig. 6.15b, a lower dye loading induced by CDCA presence is evident, together with the disappearance of a shoulder at about 395 nm. The shoulder, not present in the *IPCE* spectra, can be attributed to dye molecules aggregates which are not contributing to charge generation and whose formation is inhibited by CDCA.

The results obtained under AM 1.5 G illumination for the *I-V* and the Electrochemical Impedance Spectroscopy measurements at open circuit voltage are summarized in Table 6.3 and reported in Fig. 6.16; the Bode representation of impedance phase of the cells is also shown in the inset of Fig. 6.16.

Table 6.3 Photovoltaic performances of microfluidic DSCs sensitized by CT1 and N719 dyes for different CDCA concentrations evaluated from *I-V* characterization and *EIS* analysis.

Dye	CDCA (mM)	J_{sc} (mA/cm^2)	V_{oc} (V)	*FF*	η (%)	τ_n (ms)
CT1	0	7.68	0.55	0.64	2.74	10.68
CT1	1	7.82	0.61	0.69	3.32	15.25
CT1	10	7.89	0.64	0.70	3.54	21.74
N719	0	15.68	0.62	0.65	6.33	12.46

By fitting the *EIS* experimental data, the values of the electron lifetime τ_n were calculated and they are reported in the last column of Table 6.3. An analysis of the photovoltaic characterizations reveals a photoconversion efficiency of 2.74% without co-adsorbent, which becomes 3.54% when adding CDCA at 10 mM concentration. This efficiency is lower than the one obtained for the reference cell with N719 (6.33%), yet it has to be highlighted that one of the main technological steps that may require further optimization is the impregnation time of the nanostructured titania that was currently fixed to 5 h. This time interval is quite short if compared to those required by Ru-based dyes but already gives satisfactory cell performances. This result indicates that the attachment of the hemi-squaraine dye to the TiO_2 surface is fast, in agreement with the theoretical calculations predicting a strong interaction of the squaric acid group with anatase. This aspect is very important since reducing the soaking time would lead to important technological advantages during the cell fabrication.

In Table 6.3 it is also possible to note that both the open circuit voltage, V_{oc}, and the short circuit current density, J_{sc}, values increase when using the co-adsorbent acid. The current density increase can be attributed to the improved electron injection efficiency [23] following dye disaggregation. The increase of V_{oc} can be explained by examining the τ_n values reported in Table 6.3 and the Bode plots shown in the inset of Fig. 6.16. Upon CDCA adsorption, surface TiO_2 trap sites are occupied by the acid molecules and consequently the CDCA causes an increase of the lifetime (also witnessed by a corresponding shift of the middle frequency peak of the Bode plot towards lower frequency values). Considering that τ_n increases with CDCA, the V_{oc} increase has to be related to a decrease of back electron transfer recombination due to the fact that the TiO_2 trap sites are occupied by the acid molecules [24].

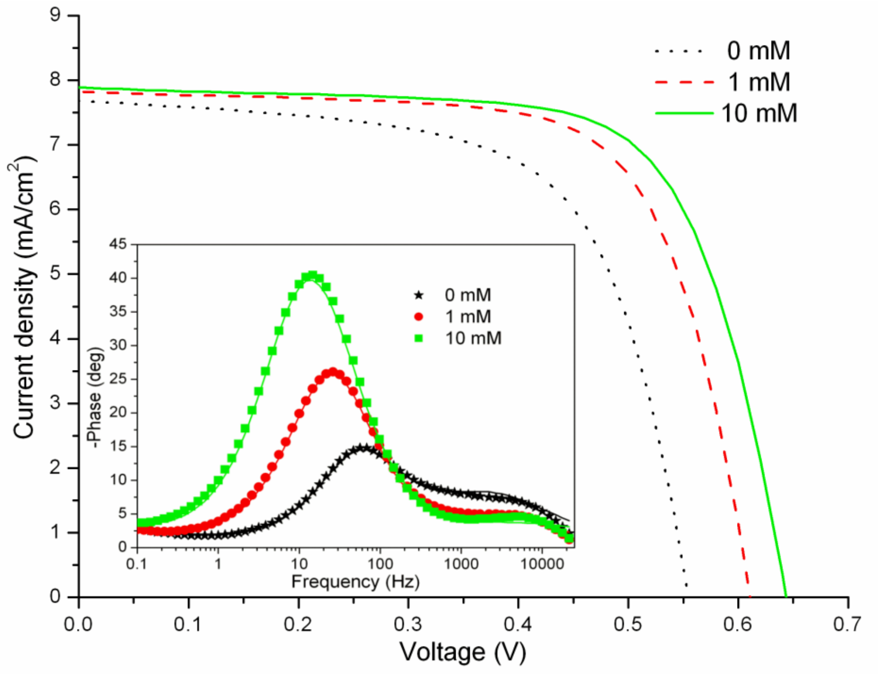

Fig. 6.16 Current density-voltage curves of hemi-squaraine-based solar cells for different CDCA concentrations. The corresponding Bode plots of *EIS* phase are shown in the inset (the points are the experimental data while the continuous lines are the fitting curves).

In conclusion, a combined experimental and theoretical investigation of the structural and electronic coupling between the hemi-squaraine and the anatase surface, focusing on the role of its anchoring group, was presented. *Ab initio* simulations revealed that the squarate moiety of the dye strongly interacts with the anatase surface giving rise to an optimal alignment of the electronic molecular levels with respect to the oxide energy bands, thus favoring an adiabatic electron transfer from the excited molecule to the semiconductor.

This resulted in an efficient electron injection with an observed maximum *IPCE* of 87% and a maximum photoconversion efficiency of 3.54% for a sensitization time of 5h and a CDCA concentration of 10 mM.

6.2.2 Optimization of the hemi-squaraine CT1 anchoring to the TiO_2 surface

Once the effectiveness of the hemi-squaraine CT1 as a sensitizer for TiO_2 had been assessed, an optimization of the photovoltaic performances of CT1-based DSCs was carried out by studying the effect of the sensitization time of the TiO_2 photoelectrode in the dye solution and investigating the addition of the chenodeoxycholic acid (CDCA) as co-adsorbent in the dye solution at different concentrations [25].

Fig. 6.17a compares the absorption spectrum of the CT1 in acetonitrile solution with the spectra of CT1-sensitized TiO_2 photoanodes at different dipping time intervals, while Fig. 6.17b shows the typical *IPCE* action spectra of CT1-based DSCs for the same sensitization times. Absorbance peaks of CT1-sensitized TiO_2 photoanodes show a monotonous heightening while increasing the sensitization time that can be ascribed to the enhancement of the number of adsorbed dye molecules on the TiO_2 film (see Fig. 6.17a). On the contrary, the maximum *IPCE* value (55% at 460 nm) was obtained for a short loading time of only 30 min (see Fig. 6.17b). This result shows that for impregnation times longer than 30 min not all the hemi-squaraine molecules attached on the TiO_2 surface effectively inject electrons in the TiO_2 conduction band. This fact can be ascribed to their spontaneous aggregation or to an ineffective anchorage of the dye on the TiO_2 surface. Since, as previously reported in Section 6.2.1, the anchoring of the hemi-squaraine molecule to the (101) anatase surface through the squarate moiety is based on a strong chemical bonding, it is most likely that the ineffective charge transfer for long incubation times is related to the formation of molecular aggregates. The photoanode absorption and the *IPCE* spectra are broadened and red-shifted with respect to the absorption spectrum of the hemi-squaraine in acetonitrile, extending approximately from 375 nm up to 600 nm (see Fig. 6.17a). The red-shift, which was also confirmed by DFT *ab-initio* calculations, is beneficial for photovoltaic applications [18, 22]. The absorption spectra of CT1-sensitized TiO_2 photoanodes exhibit two well distinguishable peaks: the first one at 414 nm, whose intensity strongly increases until 5 h of impregnation and the second one at 480 nm, which shows very small variations in intensity with increasing sensitization time. *IPCE* spectra, instead, show a blue-shift, with a lowering and broadening of the peak at 460 nm for loading times longer than 1 h. The peak at 414 nm is not mirrored in the *IPCE* spectra, suggesting that its origin is related to H aggregates formation [22], which are unable to inject photogenerated electrons to be collected at the photoanode.

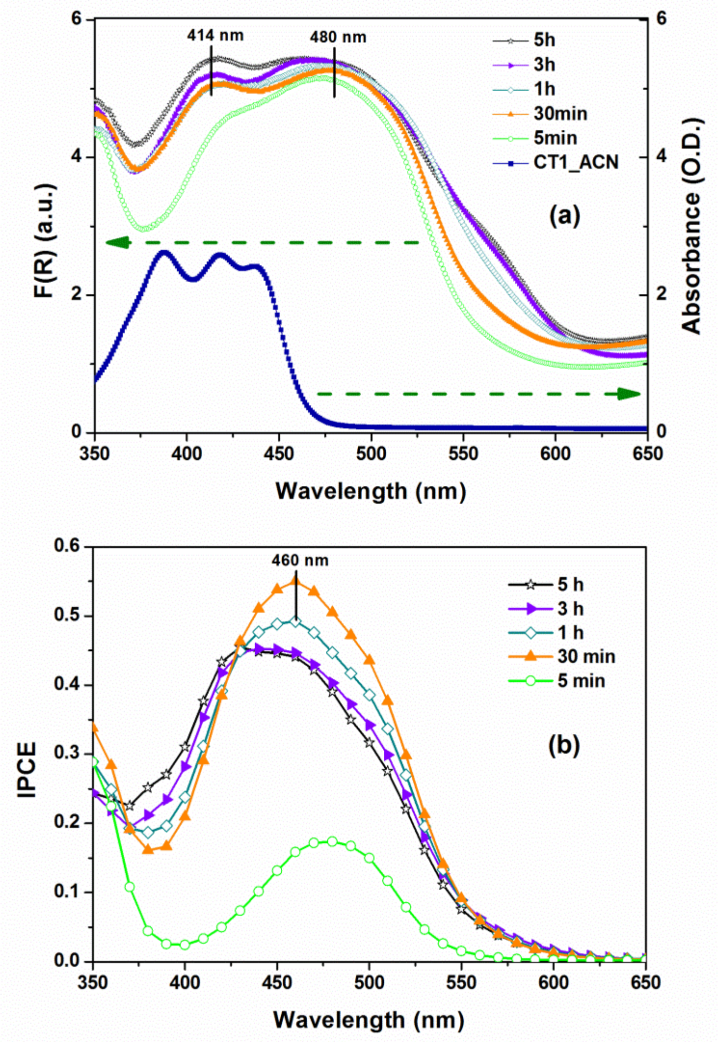

Fig. 6.17 UV-Visible absorbance spectra of the hemi-squaraine dye in acetonitrile solution and of the TiO_2 photoanodes sensitized in CT1 dye for different time intervals. The values for the CT1 in acetonitrile solution refer to the right-hand axis, whereas the other curves refer to the left-hand axis (a). *IPCE* action spectra of CT1-based DSCs for the same sensitization times (b).

The average photovoltaic parameters (mean values of five cells) obtained from the *I-V* measurements varying the sensitization time are summarized in Table 6.4. For comparison, the data obtained with a reference N719-based cell are also reported in the last row. It has to be noted that the same assembly and characterization procedures were employed, but the

N719 dye concentration in the ethanol solution and the impregnation time had to be fixed to 0.35 mM and to 18 h respectively in order to achieve the optimal conversion efficiency of 4.83%.

Table 6.4 Average cell parameters (mean values of five cells) evaluated from the *I-V* characterization. Last row reports the data obtained with a reference N719-based DSC.

Dye	**Sensitization time**	J_{sc} **(mA/cm^2)**	V_{oc} **(V)**	***FF***	η **(%)**
CT1	5 min	1.78	0.49	0.61	0.58
CT1	30 min	4.76	0.55	0.67	1.75
CT1	1 h	4.61	0.54	0.67	1.66
CT1	3 h	4.54	0.54	0.68	1.65
CT1	5 h	4.27	0.54	0.66	1.53
N719	18 h	11.56	0.63	0.66	4.83

Fig. 6.18 presents a typical current density-voltage curve of the microfluidic DSCs using the TiO_2/CT1 electrodes dipped in the dye solution for each sensitization time. The photoconversion efficiency reached the maximum value of 1.75% when the loading time was only 30 min long. Increasing the sensitization time up to 1, 3 and 5 h, the conversion efficiencies decreased down to 1.66, 1.65 and 1.53% respectively.

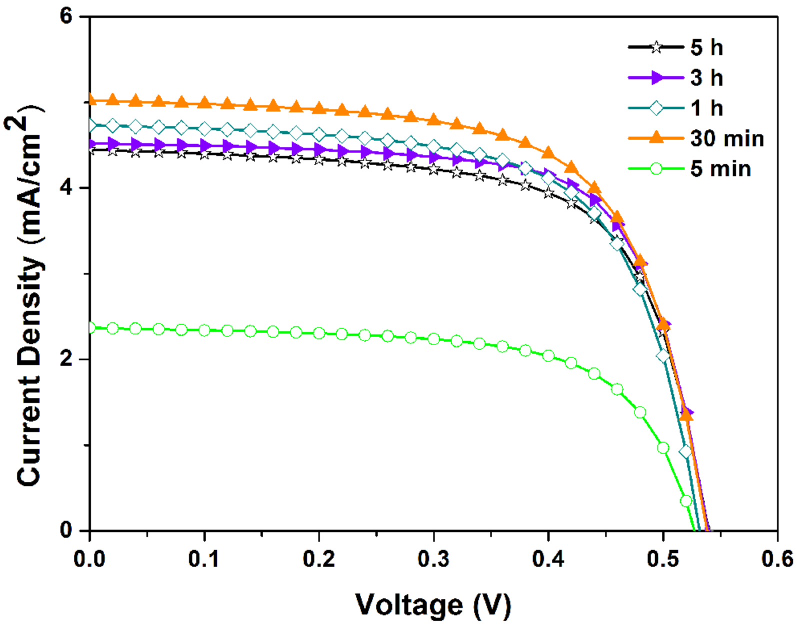

Fig. 6.18 Current density-voltage curves of hemi-squaraine-based DSCs for different sensitization times.

The worsening in the DSC performances with longer impregnation times is related to the decrement of the short circuit current density, while open circuit voltage and Fill Factor can be considered constant (see Table 6.4). This behavior, in agreement with the trend evidenced in the *IPCE* action spectra, can be ascribed to a spontaneous aggregation of the hemi-squaraine molecules (not effective at 30 min). It is particularly interesting to note that, even for a sensitization time as short as 5 min, a consistent number of molecules are already attached to the titania surface and are responsible for photocurrent generation. This observation further demonstrates the very efficient and fast linking obtained through the squarate moiety.

Fig. 6.19a shows a typical Bode representation of the impedance phase of the cells by increasing the sensitization time acquired at open circuit voltage condition. Analyzing the Bode plots of *EIS* (see Fig. 6.19a), it is possible to notice that the peak related to the electron recombination at the TiO_2+dye/electrolyte interface shifts to a lower frequency when the sensitization time increases from 5 up to 30 min and then it shifts back again to a higher frequency when the loading time further increases from 30 min up to 5 h.

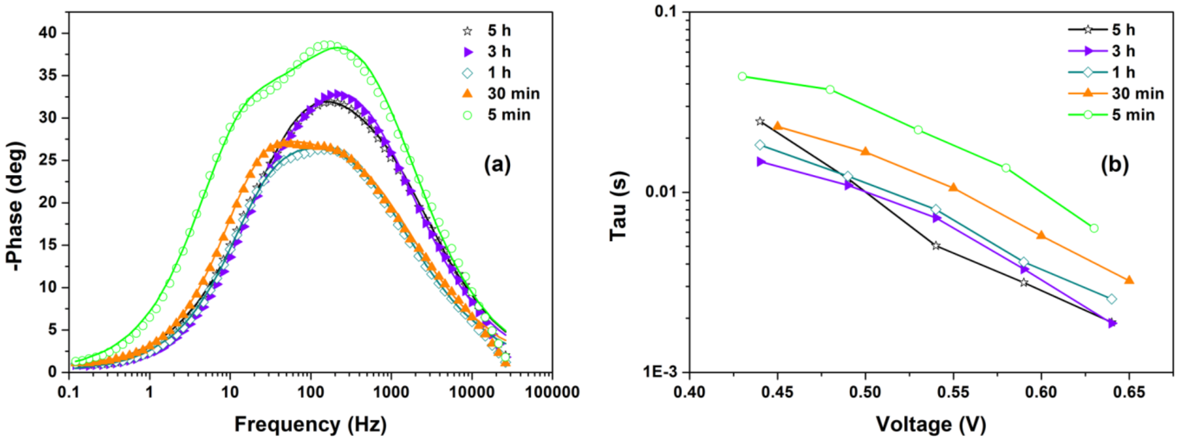

Fig. 6.19 Bode plots of hemi-squaraine-based solar cells for different sensitization times measured at open circuit voltage (the symbols represent the experimental data while the continuous lines correspond to the fitting curves) (a). Electron lifetimes evaluated by fitting *EIS* data (b).

These characteristic frequency peaks in the Bode plots are inversely proportional to the electron lifetime into the TiO_2 film [26, 27, 28]. Accordingly, the shift to higher (lower) frequency of the peaks in the Bode phase plots reveals an increase (decrease) of the recombination rate constant or equally a decrease (increase) of the electron lifetime τ. The recombination properties were evaluated by fitting the *EIS* experimental data using the equivalent circuit shown in Fig. 3.2. The electron lifetime values (reported in Fig. 6.19b for different applied bias voltages), calculated using the formula $\tau = (R_2Q_2)^{1/\beta_2}$, where β_2 is the exponent of the CPE Q_2, are in agreement with this theoretical prediction for all the sensitization times investigated. In particular, the electron lifetime experiences a monotonous drop while increasing the sensitization time (see Fig. 6.19b). This behavior can be ascribed to a spontaneous aggregation of the hemi-squaraine dye molecules, phenomenon which leaves a high number of TiO_2 trap site not occupied by the dye molecules, and so free for electron-hole recombination.

The effect of the chenodeoxycholic acid in different concentrations was studied in order to reduce the sensitizer aggregation at the semiconductor surface. The positive effect of the co-adsorbent is expected to be more evident for longer sensitization times: for this reason, 1 and 3 h were chosen as dye loading times. Fig. 6.20a and b compare the absorption spectra of TiO_2 photoanodes sensitized in hemi-squaraine (CT1) dye for 1 h at different CDCA concentrations with the typical *IPCE* action spectra of CT1-based DSCs for the same sensitization time and CDCA concentrations. In Fig. 6.20a, a lower dye loading induced by CDCA presence is evident; in particular the Kubelka Munk function of CT1-sensitized TiO_2 photoanodes experiences a monotonous decrease while enhancing the co-adsorbent concentration in the dye solution. This trend is also valid for 3 h sensitization time (results not reported). It has to be noted that the addition of CDCA in the hemi-squaraine acetonitrile solution is responsible for the disappearance of the shoulder at 414 nm (see Fig. 6.20a): this confirms the attribution of this absorption peak to the dye molecule aggregates in the semiconductor surface. CDCA molecules act as spacers among the CT1 molecules, avoiding the dye aggregation and thus facilitating the electron injection into the TiO_2 conduction band. In the *IPCE* action spectra of Fig. 6.20b**,** the beneficial effect of the co-adsorbent leads to a rise, narrowing and slight red-shift of the peak passing from 0 mM to 1 mM CDCA. Subsequently, further increasing the CDCA concentration, the peak width remains nearly constant, a slight red-shift is still present but a height reduction occurs. Maximum *IPCE* (71% at 460 nm) was obtained for a loading time of 1 h and a CDCA concentration of 1 mM (Fig. 6.20b).

The average photovoltaic parameters (mean values of the five cells) obtained from the *I-V* measurements varying the CDCA concentration are summarized in Table 6.5. The physical quantities in the columns are equal to those reported in Table 6.4.

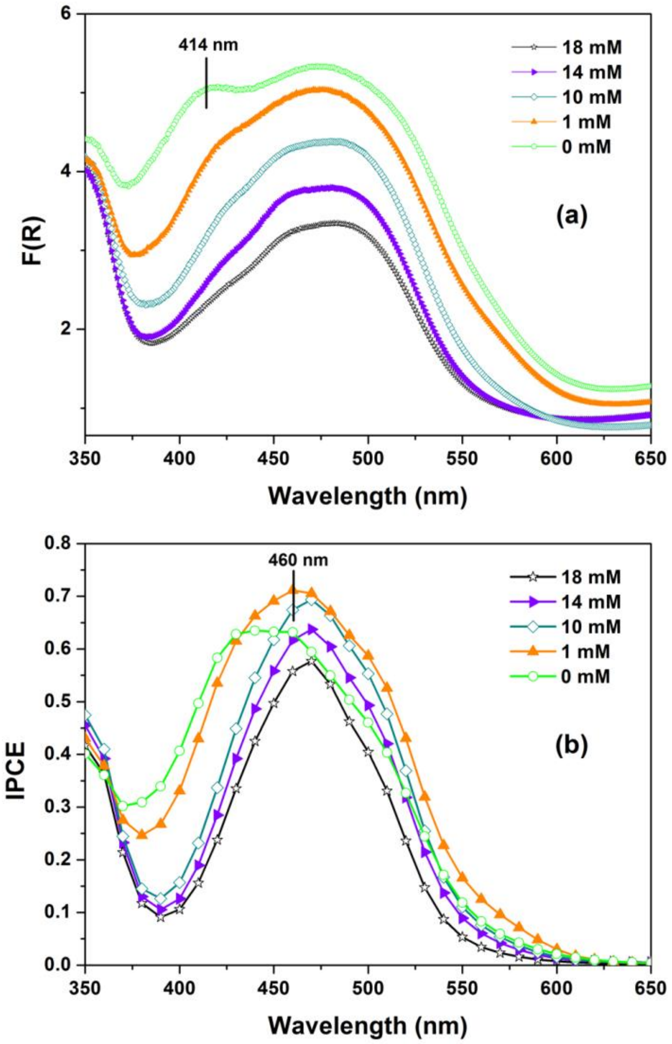

Fig. 6.20 UV-Visible absorbance spectra of TiO_2 photoanodes sensitized in CT1 dye for 1 h at different CDCA concentrations (a). *IPCE* action spectra of CT1-based DSCs for the same sensitization time and CDCA concentrations (b).

Table 6.5 Average cell parameters (mean values of five cells) evaluated from the *I*-*V* characterization.

Sensitization time	**CDCA (mM)**	**J_{sc} (mA/cm^2)**	**V_{oc} (V)**	***FF***	**η (%)**
1 h	0	5.33	0.54	0.65	1.88
1 h	1	5.90	0.61	0.70	2.50
1 h	10	4.58	0.65	0.69	2.10
1 h	14	3.98	0.65	0.68	1.76
1 h	18	3.76	0.64	0.69	1.65
3 h	0	4.57	0.55	0.66	1.67
3 h	1	4.79	0.60	0.75	2.16
3 h	10	3.96	0.65	0.74	1.89

It has to be pointed out that the differences in the photoconversion efficiency values reported in Table 6.4 and Table 6.5 and the ones presented in the Section 6.2.1 are first of all due to the different dye and CDCA concentrations and also to the different calibration of the solar simulator. In fact, as recently discussed in the literature [29], the measured DSC performances are influenced by the employed measurement conditions such as the usage of reference cells. Fig. 6.21 presents a typical current density-voltage curve of hemi-squaraine-based solar cells for different CDCA concentrations.

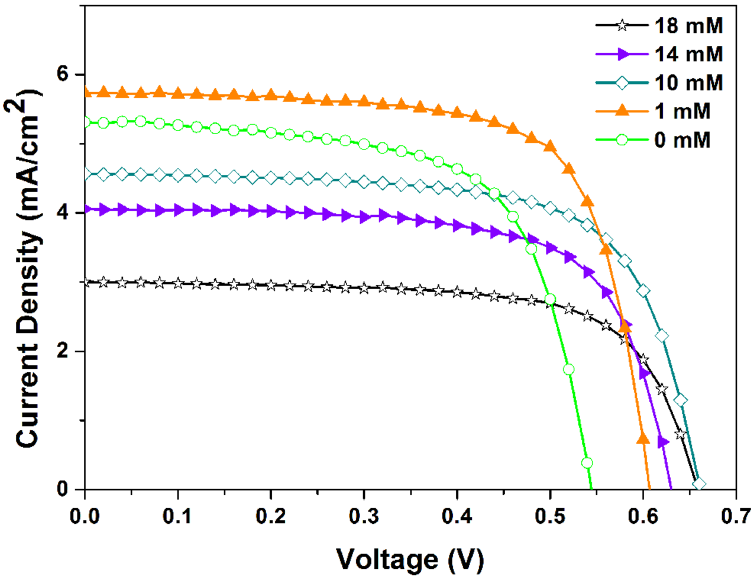

Fig. 6.21 Current density-voltage curves of hemi-squaraine-based DSCs for different CDCA concentrations at an impregnation time of 1 h.

Maximum photoconversion efficiency of 2.50% was obtained when adding 1 mM CDCA. Further increasing the co-adsorbent concentration up to 18 mM, the conversion efficiency decreased down to 1.65%. It is important to highlight that the photoconversion efficiency at 1 h without CDCA (1.88%) is higher than the one reported in Table 6.4 (1.66%) since a thicker TiO_2 layer was deposited onto FTO/glasses. The improvement in the DSC performances with a CDCA concentration of 1 mM is related to the enhancement of both the short circuit current density (J_{sc}) and the open circuit voltage (V_{oc}), while the reduction of the efficiency with higher co-adsorbent concentrations (10, 14 and 18 mM) is due to a net decrease of the J_{sc} originated from a lower dye loading not compensated by an equal increase of the V_{oc} (see Table 6.5). This trend is confirmed by using an impregnation time of 3 h. In fact, starting from a photoconversion efficiency of 1.67% without CDCA, it subsequently increases up to a value of 2.16% with a CDCA concentration of 1 mM and it finally experiences a decrease down to 1.89% further increasing the CDCA concentration up to 10 mM. The worsening in the DSC performances with a longer impregnation time of 3 h with respect to 1 h is due to the decrement of the short circuit current density, while open circuit voltage can be considered constant (see Table 6.5). Increasing the impregnation time, therefore, once the disaggregation has been completed, the acid becomes responsible for a “conflicting mechanism” that prevents the effective attachment of the sensitizer onto the semiconductor surface.

The short circuit current density increase when using the co-adsorbent acid for both the loading time of 1 h and 3 h can be attributed to the improved electron injection efficiency [30, 23] following the dye disaggregation. The enhancement of the open circuit voltage, instead, can be explained by analyzing either the τ values plotted in Fig. 6.22b and the Bode diagrams shown in Fig. 6.22a. The CDCA molecules dissolved in the dye solution cause an increase of the electron lifetime (see Fig. 6.22b) and a corresponding shift (and an increase) of the middle-frequency peak of the Bode plots toward lower frequency values (see Fig. 6.22a).

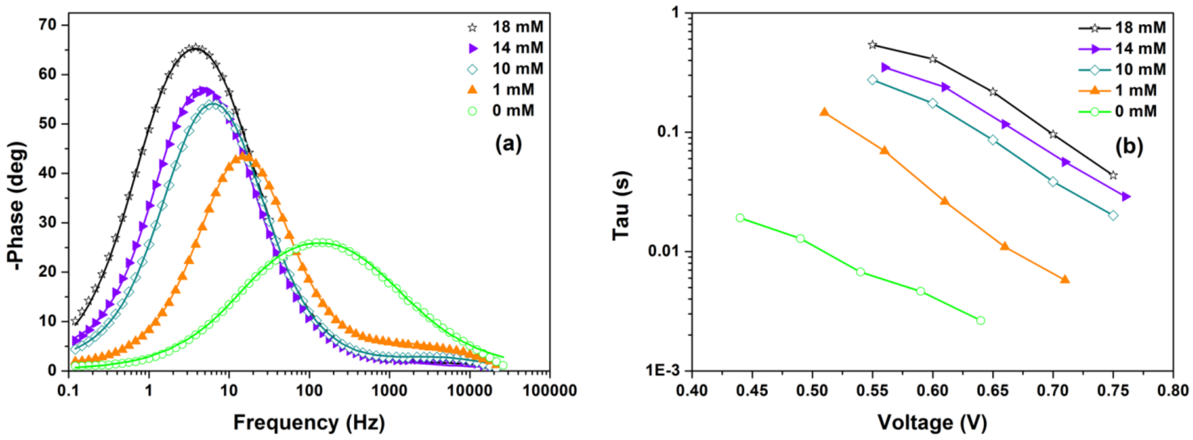

Fig. 6.22 Bode plots of CT1-based solar cells for different CDCA concentrations at an impregnation time of 1 h measured at open circuit voltage (the symbols represent the experimental data while the continuous lines correspond to the fitting curves) (a). Electron lifetimes evaluated by fitting the *EIS* data (b).

The enhancement of the open circuit voltage, which corresponds to the difference between the free energy of the TiO_2 electrons and the redox potential of the electrolyte [31], can be therefore linked to a decrease of the back electron transfer recombination due to the occupation of the TiO_2 trap sites by the acid molecules.

In conclusion, the hemi-squaraine anchoring to the TiO_2 surface was optimized and characterized by means of an electrical and optical study. The dye sensitization time and the CDCA co-adsorbent concentration in the dye solution were successfully monitored. A maximum photoconversion efficiency of 1.75% for a sensitization time of only 30 min without co-adsorbent was obtained, and this value was enhanced up to 2.50% when adding 1 mM CDCA in the dye solution and fixing the loading time to 1 h. The very fast kinetics in the dye adsorption, with optimal sensitization time intervals almost 15 times lower than conventional Ru-based sensitizers, confirms the theoretical predictions and indicates a strong interaction of the semisquaric acid group with the anatase surface. This result suggests that this small molecule can be a promising sensitizer even in a continuous industrial process.

6.2.3 Modeling of the dye loading time influence on the *EIS* of a CT1-based DSC

In this Section the physical model introduced in Section 5.1, built taking into account the CT1 dye molecules spontaneous tendency to aggregate close to the TiO_2/electrolyte interface, will be exploited to fit the *EIS* experimental data of CT1-based DSCs fabricated with photoanodes impregnated in the dye solution at different time intervals (from 5 min up to 5 h) [32].

Fitting the data shows that a better impedance than the bulk impedance of the electrolyte written as a parallel *RC* element reported in Eq. (5.10) would be

$$Z = R_0 + Z_b + (Y_1 + Y_2)^{-1} \tag{6.2}$$

where $R_0 \approx 9.8\ \Omega$ and

$$Z_b = \frac{G}{\sigma_{el}\, S\left(1+(j\,\omega\,\tau_{el})^{\beta}\right)^{\alpha}} \tag{6.3}$$

with $\alpha \approx 0.65$ and $\beta \approx 0.85$, where α and β are well known fitting parameters for relaxation time distributions [33].

The fit can well interpolate 4 sets of data, the ones concerning the absorption times of

30 min, 1 h, 3 h, and 5 h. On the contrary, the agreement with the 5 min loading time data, within the same set of parameters, reveals not to be satisfactory. The reason why this happens is most probably due to the fact that the *EIS* measurements were done under illuminating conditions (at least for some part of the total area of the cell) and 5 min is a time too short to allow a reasonable absorption of dye into the TiO_2 pores. In other words, the cell behaves as if it was operating in dark conditions. An important point to be remarked is that, once a part (ξ) of the electrode area is illuminated, the electronic density within the conduction band of TiO_2 semiconductor increases and expands, almost instantaneously, over the entire volume of TiO_2. This electron density is also the source of the potential difference across the TiO_2/electrolyte interface. The transfer resistance decreases exponentially when enhancing this potential difference. Hence, a much larger real part of *Z*, for low frequencies, has to be expected for 5 min with respect to the other soaking times considered.

The above mentioned equations can be adjusted in order to take into consideration the fact that the cell is under light conditions for only a part of the total area.

Introducing

$$\xi = \frac{illuminated\ area}{total\ area} = \frac{2.2 \cdot 10^{-5} m^2}{7.8 \cdot 10^{-5} m^2} = 0.28, \tag{6.4}$$

and taking into account that under illumination the transfer resistance between the TiO_2 and the electrolyte is reduced, an average electrolyte conductivity within δd_0 enlarged by a factor of ζ can be considered.

Preliminary fittings with Eqs. (6.2) and (6.3) show that $\sigma_d/\sigma_{el} < 3 \cdot 10^{-9}$ so, in comparison to Y_2, Y_1 is practically negligible.

When the cell is under light conditions, the Eq. (5.3) preserves the form with the only difference that σ_{el} has to be replaced by an average σ_p (from pore) proportional to σ_{el} (i.e. σ_{el} in dark). The proportionality, ζ, should include the total area covered by dye ($\sim\theta$) as well as the number of dye layers ($\sim d/d_0$) and the illuminated fraction ($\sim\xi$), thus obtaining

$$\sigma_p = \zeta \sigma_{el} = p\theta\xi\sigma_{el} d/d_0, \tag{6.5}$$

p being a proportionality parameter.

Then

$$Y_2 = \frac{1}{R_2} + j\,\omega\,C_2 = \frac{1-\theta}{\delta\,d_0}\,\sigma_p\,A\,(1 + j\,\omega\,\tau_{el}) = \frac{\theta\,(1-\theta)\xi d}{\delta d_0^2}pA\,(1 + \\ +j\,\omega\,\tau_{el})\,\sigma_{el}. \tag{6.6}$$

As neither *p* nor *A* are known, a fitting parameter Σ may be introduced

$$\Sigma = \frac{pA}{S}. \tag{6.7}$$

The total impedance *Z* would be

$$Z = R_0 + Z_b + Y_2^{-1} = R_0 + \frac{G}{\sigma_{el}\,S\,(1+j\,\omega\,\tau_{el})} + \\ + \frac{\delta d_0^2}{\theta\,(1-\theta)\xi\Sigma d\,(1+j\,\omega\,\tau_{el})\,\sigma_{el}\,S}\,. \tag{6.8}$$

Introducing the fitting parameters α and β, the impedance to be fitted becomes

$$Z = R_0 + \frac{G + \frac{\delta d_0^2}{\theta\,(1-\theta)\xi\Sigma d}}{\sigma_{el}\,S} \cdot \frac{1}{\left(1+(\,j\,\omega\,\tau_{el})^{\beta}\right)^{\alpha}}. \tag{6.9}$$

Summarizing, the electrical impedance *Z* of hemi-squaraine-based DSCs is function of the following parameters: σ_{el}, τ_{el}, Σ, τ, k, δ, R_0, α and β.

Fig. 6.23 shows the parametric plots of the real and imaginary parts of the electrical impedance of the cell, for different dye absorption times. The theoretical curves obtained using Eq. (6.9) are plotted in the same figure. Even if the fits are not perfect, they follow the general trend of the experimental points.

In Fig. 6.24 the points represent the values of the fraction θ of the area *A* obtained from the best fits for each absorption time. The continuous line represents the function $\theta(t) = \sqrt{t/(t+\tau)}$. The good match may be a proof of the correctness of the fit.

In Fig. 6.25 it is plotted the variation in time of the average thickness *d* of the adsorbed dye layers. The points are the values of *d* for each absorption time obtained from the best fits and the full line shows that *d(t)* may be fitted with a simpler function

$$d(t) = d_0\left(\delta - \frac{\delta-1}{1+\left(\frac{t}{\tau}\right)^k}\right) \tag{6.10}$$

that avoids the threshold character of the Eq. (5.9).

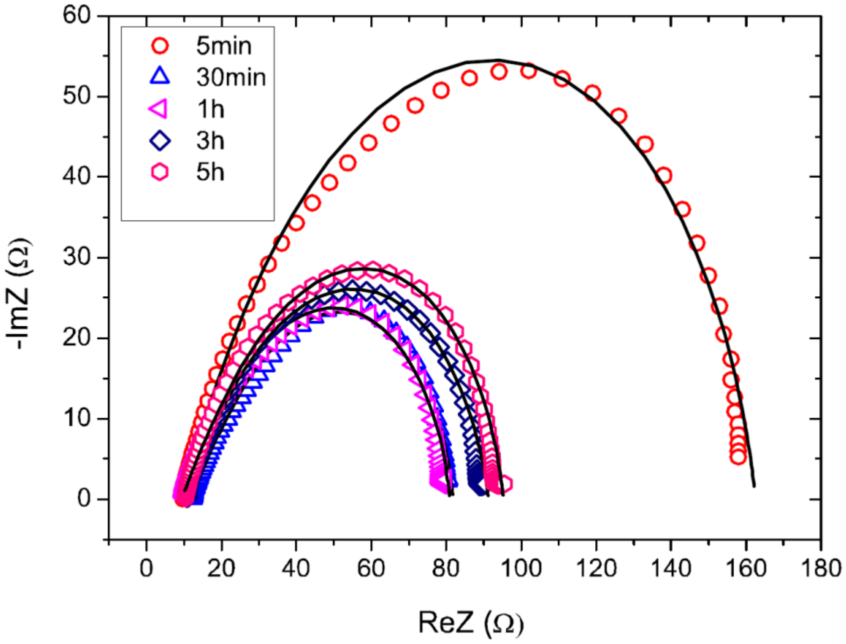

Fig. 6.23 Parametric plots (-ImZ *vs.* ReZ) for different dye absorption times. The fitting curves are in full black lines.

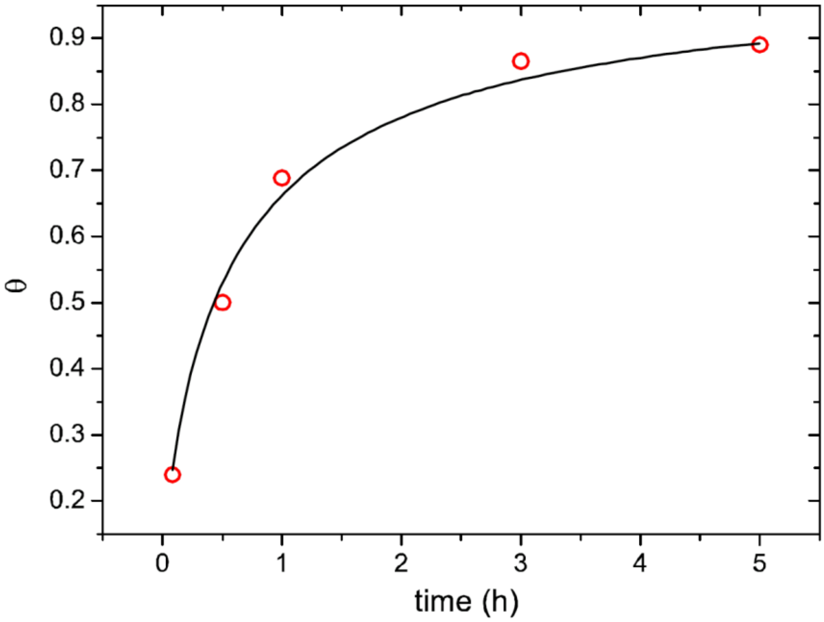

Fig. 6.24 Fraction θ of area A of the pores (fitting values). The continuous curve (Eq. (5.2)) confirms the validity of the fitting model.

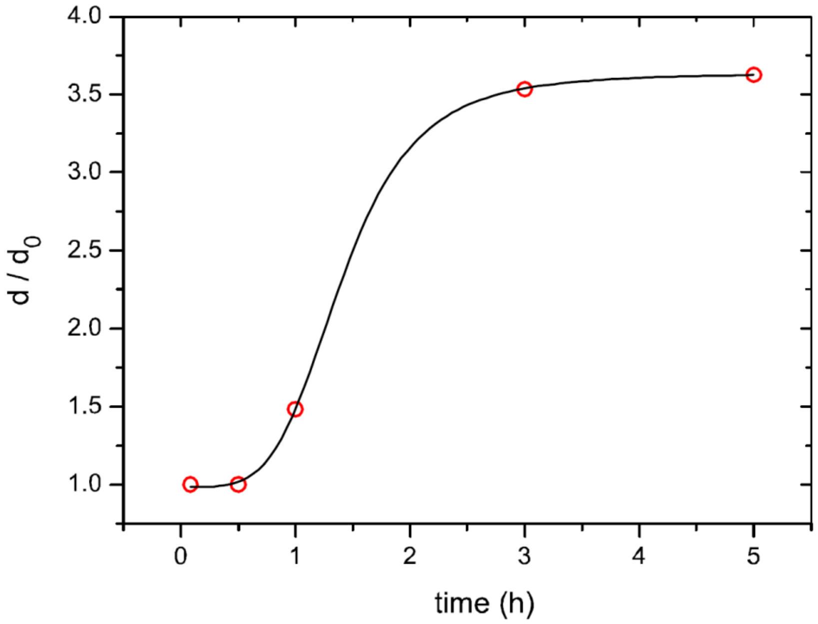

Fig. 6.25 Plot of the fitting values of *d* (circles) and the Eq. (6.10) (in full black line).

The important fitting parameters σ_{el}, Σ and δ are reported in Table 6.6. The value $\sigma_{el} \sim 0.030$ S/m = 0.30 mS/cm corresponds to a normal conductivity of the ionic solution (obviously, it depends on the concentration and the temperature).

Table 6.6 Parameters σ_{el}, δ and Σ resulted from the best fits, at different loading times.

Sensitization time	**σ_{el} (mS/cm)**	**δ**	**Σ**
5 min	0.26	3.97	$8.9 \cdot 10^{-4}$
30 min	0.36	4.12	1110
1 h	0.35	4.82	1043
3 h	0.31	4.98	1100
5 h	0.30	4.34	1093

δ, which is $d(max)/d_0$, represents the limiting distance over which the inner surface of the pores' walls manifests the attraction toward the dye molecules.

The only parameter that needs a thorough analysis is Σ. It has more or less the same value for t = 30 min, 1 h, 3 h and 5 h but a value six orders of magnitude smaller for t = 5 min. By looking the Eq. (6.7), it results that Σ, apart from the fixed value A/S, is actually representing p, that is the factor ζ normalized with respect to θ, ξ and $d(max)/d_0$. In other words, Σ gives an estimation of how many orders of magnitude the transfer resistance decreases when passing from dark to light conditions.

To conclude, a physical model, based on the hypothesis that dye molecules can aggregate on the electrode surface creating an adsorbed layer which prevents the charge transfer and thus worsens the electrical performances of the cell, was proposed. The changes in the electrical impedance spectra of a solar cell sensitized with hemi-squaraine organic dye molecules, when varying the dye absorption time, were analyzed and it was observed a non-monotonic behavior of the impedance of the cell, differently from the case of Ru-based DSCs [34]. The model fits well the experimental data if a correction is made regarding the difference between the illuminated area of the cell and the total area available in the electrical measurements.

6.3 Quasi-solid electrolytes for DSCs application

In this Section, an accurate description of the physical-chemical characterization of UV-crosslinked polymer electrolyte membranes and of cellulose-based gel electrolyte will be provided, together with a detailed investigation of their photovoltaic performances, both in terms of efficiency and durability.

6.3.1 UV-crosslinked novel polymer electrolyte membranes

6.3.1.1 Electrolyte characterization

Fig. 6.26 shows the percentage of conversion of the BEMA:PEGMA reactive mixture under UV light as a function of the irradiation time. The reactivity of all the monomers was very high in the initial stages of UV-curing, the rate of polymerization was very fast and the conversion was completed in less than 300 s.

TGA analysis under N_2 flux (temperature range 25 - 500 °C) of BEMA:PEGMA polymer membranes before swelling in the liquid electrolyte solution is reported in Fig. 6.27. The thermal stability of the BEMA:PEGMA membranes was found to be very high if one considers that, generally, the operating temperature of DSCs does not exceed 65 - 70 °C. The activated polymer membranes (after swelling in the liquid electrolyte) were also tested for their thermal stability. Even though the liquid electrolyte addition reduced the thermal stability up to approximately 82 °C, which is the temperature at which the solvents began to evaporate, this is well in the limit of application as electrolyte for DSC devices.

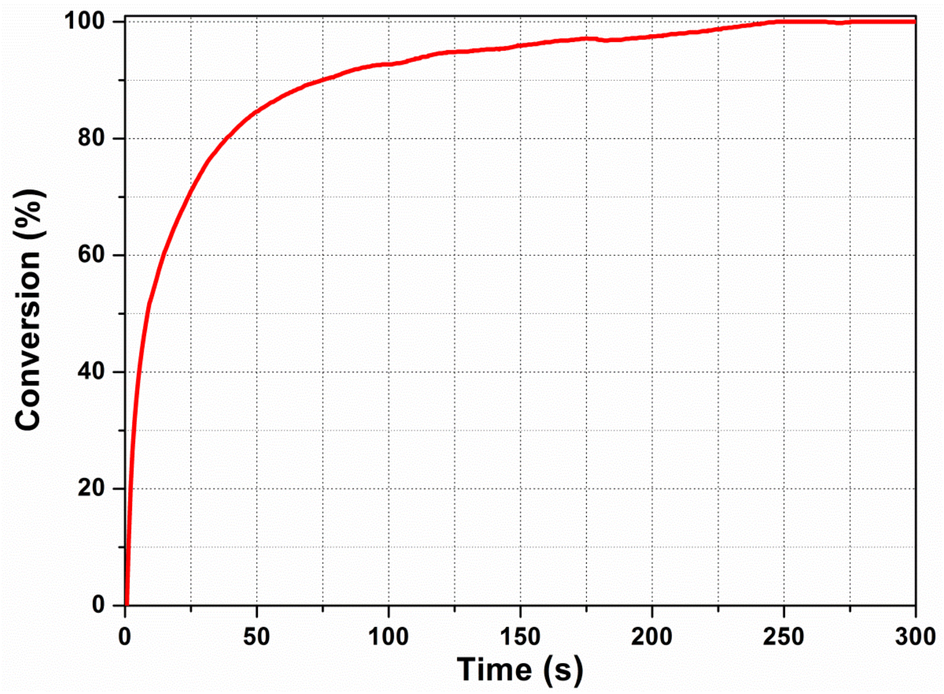

Fig. 6.26 Methacrylic double bonds conversion of the reactive monomer mixtures checked by real time FT-IR spectroscopy as a function of the irradiation time.

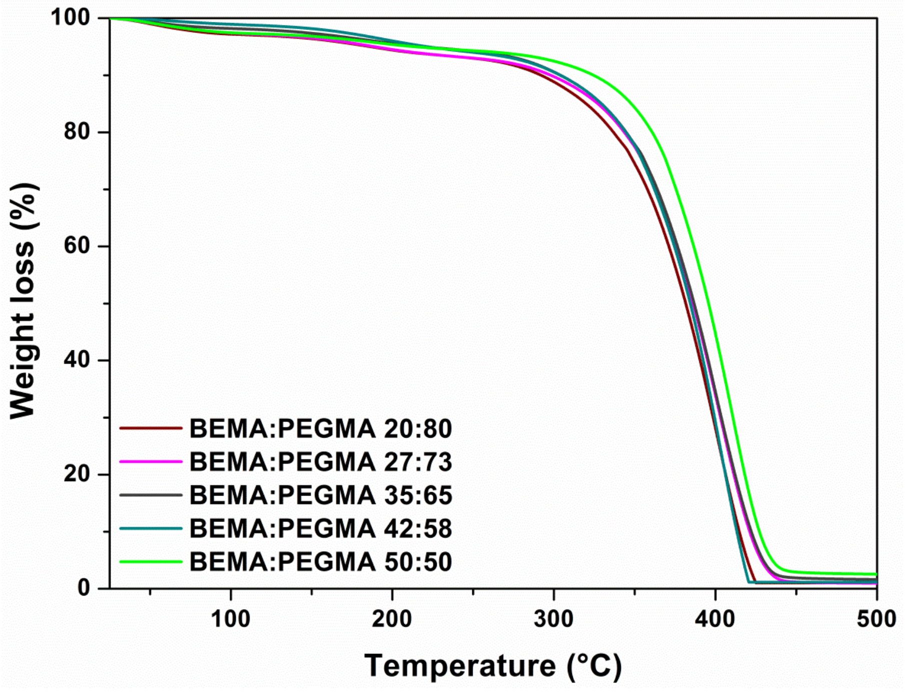

Fig. 6.27 TGA analysis under N_2 flux (temperature range 25 - 500 °C) of BEMA:PEGMA polymer membranes before swelling in the liquid electrolyte solution.

6.3.1.2 Chemometric investigation of photovoltaic performances

The complete CCF-DoE (see Section 4.2.2) matrix, ranges, levels of factors and the obtained results are summarized in Table 6.7.

Table 6.7 Composite Face-centered design matrix for two test variables in coded and natural units along with the observed and predicted responses (light-to-electricity conversion efficiency (η) values). Short circuit current density (J_{sc}), open circuit voltage (V_{oc}), and Fill Factor (*FF*) are also reported.

BEMA (x_1, wt%)	**NaI (x_2, mol/L)**	**η observed (%)**	**η predicted (%)**	**J_{sc} (mA/cm^2)**	**V_{oc} (V)**	***FF***
20 (-1)	0.150 (-1)	4.40	4.32	13.2	0.576	0.58
50 (+1)	0.150 (-1)	2.98	3.03	9.2	0.575	0.57
20 (-1)	0.600 (+1)	4.65	4.62	14.0	0.575	0.58
50 (+1)	0.600 (+1)	3.71	3.68	11.4	0.574	0.57
20 (-1)	0.375 (0)	4.73	4.80	14.8	0.574	0.56
50 (+1)	0.375 (0)	3.97	3.92	12.3	0.575	0.56
35 (0)	0.150 (-1)	4.70	4.66	14.2	0.575	0.57
35 (0)	0.600 (+1)	4.90	4.94	15.0	0.576	0.57
35 (0)	0.375 (0)	5.41	5.38	16.0	0.580	0.58
35 (0)	0.375 (0)	5.38	5.38	16.0	0.578	0.58
35 (0)	0.375 (0)	5.41	5.38	16.1	0.581	0.58
35 (0)	0.375 (0)	5.39	5.38	15.9	0.579	0.59

The model was evaluated through the analysis of the variance (ANOVA). Its regression coefficient (R^2) of 0.974 is in reasonable agreement with the experimental results, indicating that 97.4% of the variability can be revealed by the model and 2.6% residual variability remains. At the same time, the adjusted determination coefficient (R^2_{adj} = 0.960) is also very high to advocate for a high significance of the model. Finally, for validation, duplicate assenting experiments were conducted using the optimized parameters: the results are closely co-related with the data obtained using the CCF-DoE.

The set of experiments allowed achieving a maximum light-to-electricity conversion efficiency of 5.41% (short circuit current density J_{sc} = 16.0 mA/cm^2, open circuit voltage V_{oc} = 0.580 V, Fill Factor *FF* = 0.58) for a polymer electrolyte membrane obtained using a BEMA:PEGMA ratio equal to 35:65, swelled by a liquid electrolyte composed of 0.375

mol/L NaI and 0.0375 mol/L I_2 in acetonitrile. This polymer electrolyte membrane will be considered in the following Paragraphs. For comparison, a DSC in presence of only the liquid electrolyte described above was also assembled: it achieved an efficiency of 6.34% (J_{sc} = 16.5 mA/cm^2, V_{oc} = 0.680 V, FF = 0.57). Current density-voltage (J-V) curves of two cells, one containing the polymer electrolyte membrane and the other one with the liquid electrolyte, are reported in Fig. 6.28. As also shown in Table 6.8, J_{sc} and FF values of the two cells are quite similar, while the V_{oc} of the cell assembled with the polymer electrolyte membrane is 100 mV lower. For a polymer electrolyte, this difference in V_{oc} is typically attributable to the higher back transfer of injected electrons from the conduction band of the TiO_2 film to the I^-/I_3^- couple [35]. Overall, it is important to note that the difference between the light-to-electricity conversion efficiencies of the two cells is considerably small.

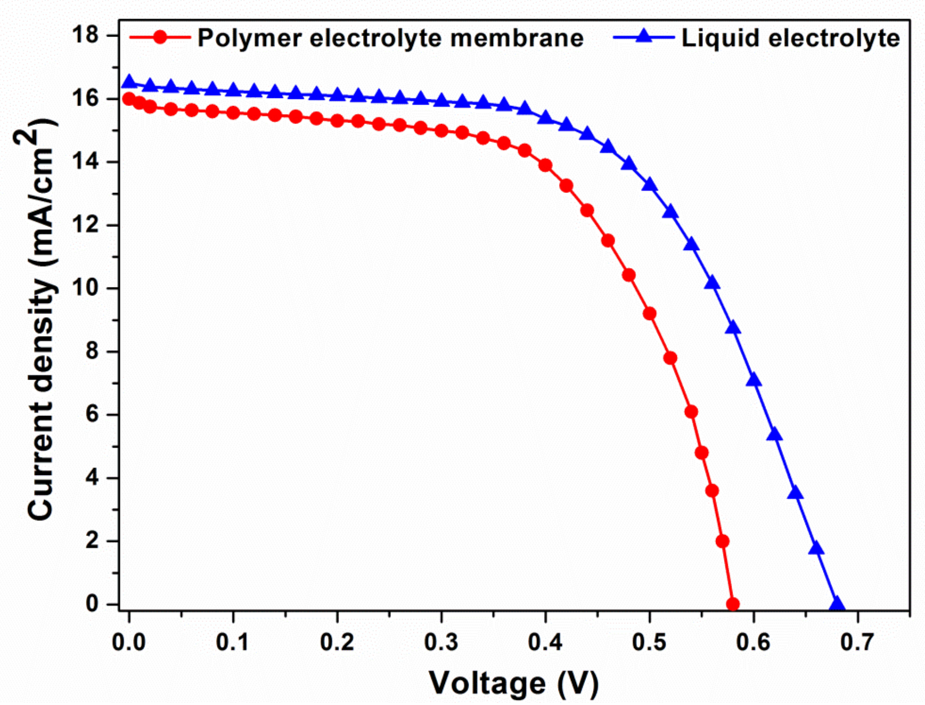

Fig. 6.28 *J-V* curves of DSCs assembled with the polymer electrolyte membrane (red circles) and with the liquid electrolyte (blue triangles).

Table 6.8 Photovoltaic parameters of the DSCs fabricated with different electrolytes and measured at 1 sun illumination condition at room temperature.

Electrolyte	**J_{sc} (mA/cm^2)**	**V_{oc} (V)**	**FF**	**η (%)**
Liquid	16.5	0.680	0.57	6.34
Polymer	16.0	0.580	0.58	5.41

The CCF-DoE response surface showing the effect of x_1 and x_2 on the cell efficiency is drawn in Fig. 6.29.

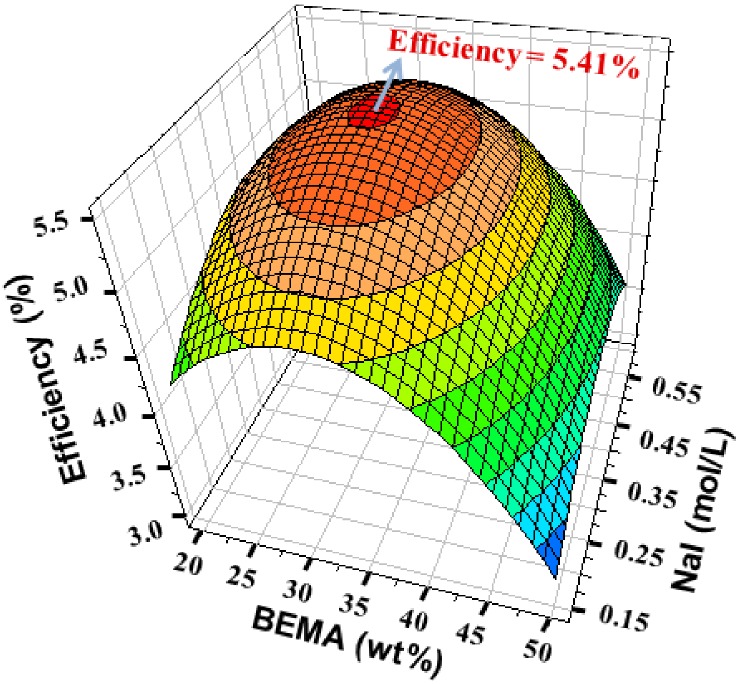

Fig. 6.29 Response surface showing the effect of BEMA:PEGMA ratio (x_1) and NaI concentration (x_2) on the light-to-electricity conversion efficiency of DSCs assembled with polymer electrolyte membranes.

The efficiency surface is hump-shaped as a function of both factors, BEMA:PEGMA ratio (x_1) and NaI concentration (x_2). Examining the effect induced by varying the amount of NaI (x_2), it can be observed that the increase of NaI concentration from 0.150 mol/L to 0.375 mol/L improves the cell performances. In fact, the regeneration of the dye cations (D^+) by means of reaction (6.11) is improved when the iodide amount increases. At the same time, the increase of the amount of NaI enhances the I_3^- concentration, according to the reaction (6.12). Finally, I_3^- ions promote the reactions (6.13) and (6.14), correlated with the rapid increase in efficiency, due to the increased J_{sc} [36]

$$2D^+ + 3I^- \rightarrow 2D + I_3^- \qquad (6.11)$$

$$I_2 + I^- \leftrightarrow I_3^- \qquad (6.12)$$

$$I_3^- + 2e^- \xrightarrow{dark\ cathode} 3I^- \qquad (6.13)$$

$$3I^- \xrightarrow{photoanode} I_3^- + 2e^- \tag{6.14}$$

A further increase in the NaI content from 0.375 mol/L to 0.600 mol/L diminishes the cell efficiency. As reported in the literature, at higher concentration the ions in the polymer electrolyte become contact ions and their mobility is restrained [37]. As a result, the effective ions in the polymer electrolyte become relatively lower, and J_{sc} values decrease [38]. This correlation between J_{sc} and NaI concentration is clearly evident in Fig. 6.30. Here, the curves obtained for different polymers have a similar trend, but are shifted among them as a function of the amount of BEMA introduced in the formulation (this factor, x_1, will be further discussed later).

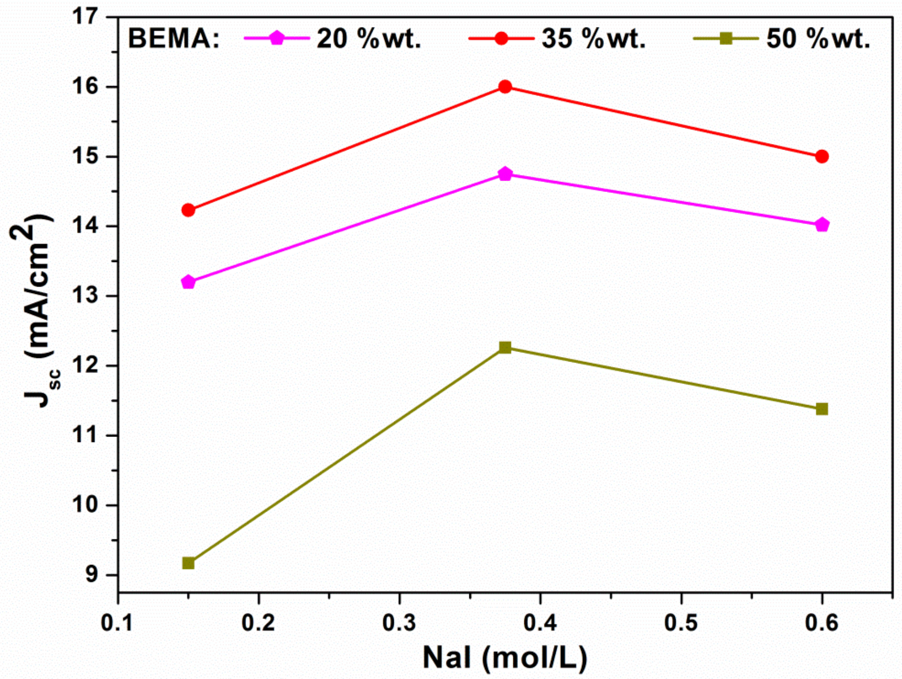

Fig. 6.30 Variation of J_{sc} as a function of NaI concentration for DSCs assembled with polymer electrolyte membranes prepared with different BEMA:PEGMA ratios.

On the basis of these results, it is important to choose carefully the concentration of iodine salts used for preparing the polymer electrolyte membranes: the standard concentrations adopted in many investigations (0.5 mol/L NaI and 0.05 mol/L I_2) [39], according to the data reported here, are not the optimal ones.

The second factor studied by means of the CCF-DoE is the BEMA:PEGMA ratio (x_1), i.e. the ratio between the difunctional oligomer and the monofunctional one. As reported elsewhere [40], BEMA forms a three-dimensional network and the addition of PEGMA as a comonomer influences the propagation reaction and change the architecture of the polymeric matrix, thus affecting its properties. As shown in Table 6.7, the amount of BEMA was varied from 20 to 50 wt%. Below 20 wt% the membranes were not self-standing, while above 50 wt% they were rigid and hard to manage in assembling the cells. Within this experimental domain explored by the CCF-DoE, the best cell efficiencies were obtained in the presence of 35 wt% of BEMA. To find a correlation between the composition of the polymer matrix and the device performances, dynamic mechanical analysis (TTDMA, Triton Technology) was performed and the storage modulus E' as a function of the temperature was measured [41]. In fact, by measuring the elastic modulus of the networks at the rubbery plateau (i.e. well above the glass transition temperature of the polymer), one can calculate the crosslinking density (υ_e) of the networks, according to the classical rubber theory equation:

$$\upsilon_e = \frac{E'}{3RT} \tag{6.15}$$

where T is the temperature (K) at which the storage modulus is evaluated, and R is the gas constant [42]. Here, T was 283 K, being the glass transition temperature of the samples in the range 230 - 235 K. In Fig. 6.31 υ_e as a function of the quantity of BEMA is reported.

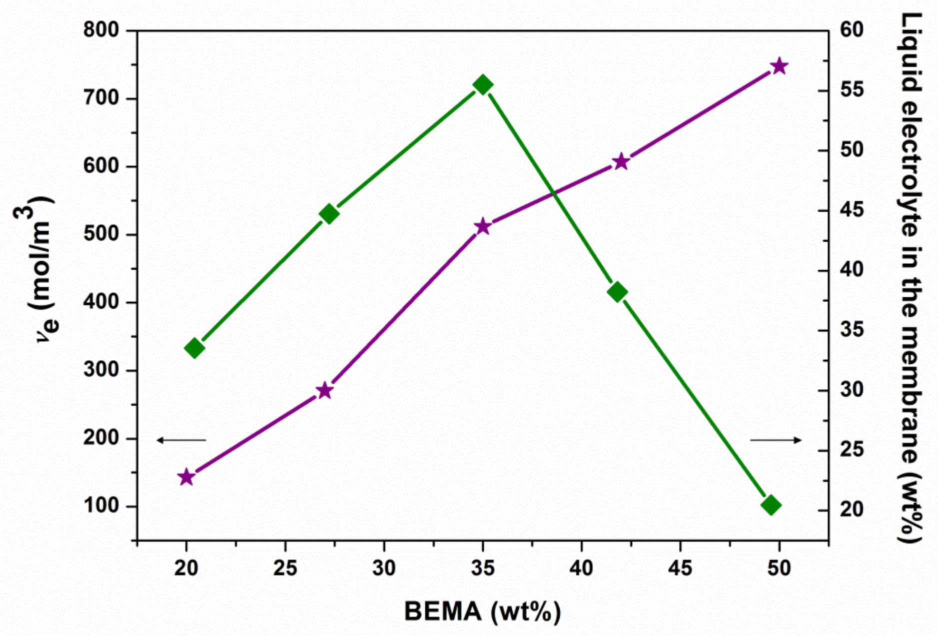

Fig. 6.31 Variation of the crosslinking density (υ_e) in polymer electrolyte membranes as a function of weight concentration of BEMA (violet line + stars) and relative amounts of liquid electrolyte trapped in the membranes (green line + squares).

It can be observed that, as expected, υ_e increases linearly with the amount of BEMA, i.e. when the difunctional monomer increases, the network obtained becomes tighter. Fig. 6.31 also shows how the BEMA:PEGMA ratio influences the amount of liquid electrolyte trapped in the membranes by swelling. Quite surprisingly, the weight concentration of the liquid electrolyte stored in the membranes first increases as a function of BEMA amount, and then decreases. This may be due to the fact that, increasing υ_e, the polymeric network is too crosslinked to store a fair amount of liquid electrolyte. On the other hand, below 35 wt% of BEMA the network is very loose and it is no longer able to trap the electrolyte.

The study of the long-term stability of a DSC containing the most performing polymer electrolyte membrane, maintained at 60 °C for 500 h and checked every 30 h, is reported in Fig. 6.32.

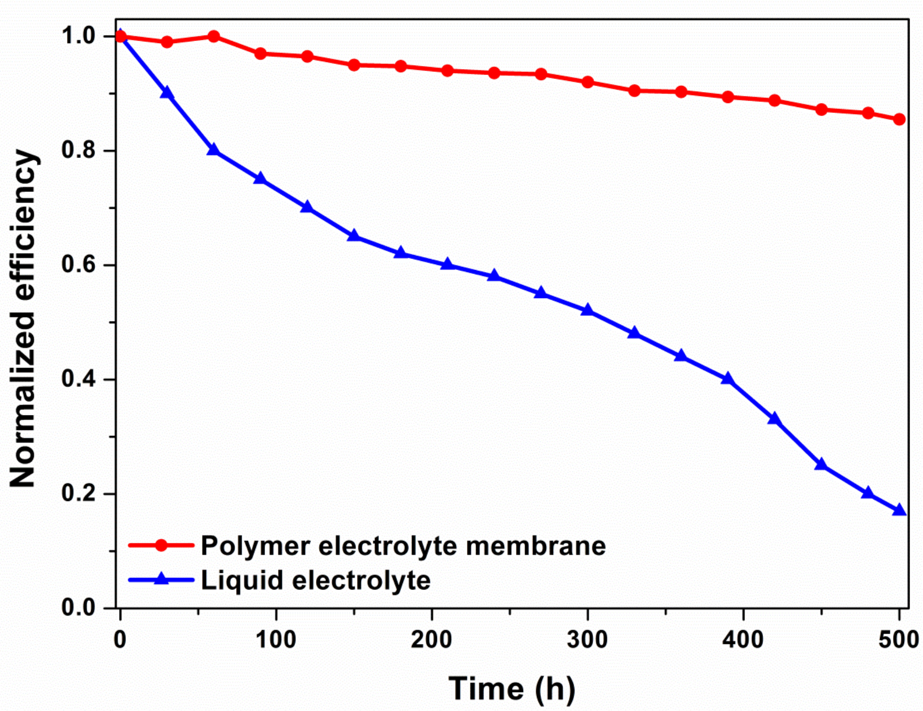

Fig. 6.32 Normalized light-to-electricity conversion efficiencies of DSCs assembled with the polymer electrolyte membrane (red circles) and with the liquid electrolyte (blue triangles) *vs.* conservation time under 60 °C.

The results are compared with those of a DSC based on a liquid electrolyte (see Table 6.8). It can be seen that after 120 h (5 days), the efficiency of the DSC with the quasi-solid electrolyte decreases only by 3.5%, while the DSC with the liquid electrolyte shows a marked 30% decay. After 500 h (20 days), the cell based on the polymer electrolyte membrane remarkably retains an efficiency of above 85% of its initial value, indicating that the cell exhibits very good stability upon prolonged storage/testing; on the contrary, the efficiency of the DSC with liquid electrolyte shows a rapid decay to below 17% of the initial value. In order to better understand the effect of the two different electrolytes on the charge transport mechanisms of the cells, the Electrochemical Impedance Spectroscopy (*EIS*) measurements were performed and the obtained spectra were modeled using the equivalent circuit shown in Fig. 3.2. The *EIS* curves measured at open circuit voltage for the two different cells immediately after fabrication and upon storage at 60 °C (for 90 h or 240 h) are reported in Fig. 6.33, together with the results of the fitting.

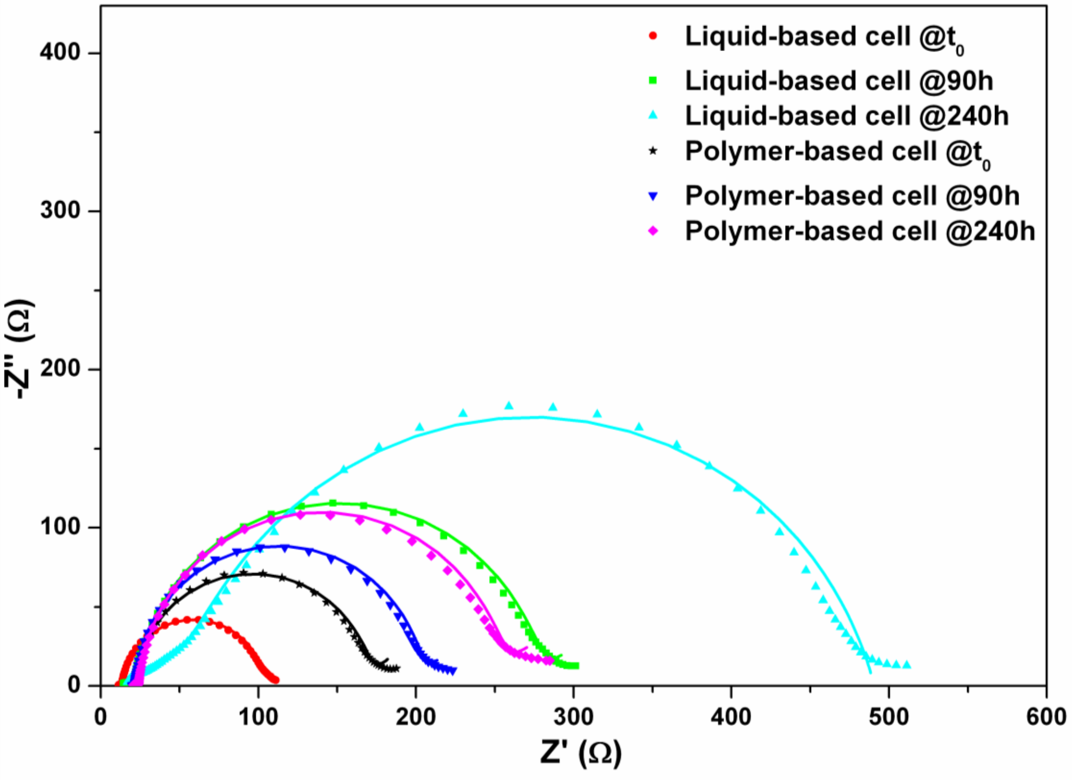

Fig. 6.33 Measured (symbols) and fitted (solid lines) impedance spectra at open circuit voltage of DSCs fabricated with the polymer electrolyte membrane and the liquid electrolyte. For each cell, the spectrum of the fresh-assembled device and the spectra measured after 90 h and 240 h of storage at 60 °C are reported.

From the fitting parameters, the chemical capacitance values C_μ were calculated by using the formula

$$C_\mu = Q_1^{\frac{1}{\beta_1}} R_1^{\frac{1}{\beta_1}-1} \tag{6.16}$$

where β_1 is the exponent of the CPE Q_1.

In Fig. 6.34 the chemical capacitance values as a function of the bias voltage are shown. The typical exponential dependence on the applied voltage is evident in the semi-logarithmic plots. It can clearly be seen that the liquid electrolyte-based cell presents chemical capacitance values that decrease upon time, while these values remain almost constant for the polymer-based cell, evidencing its remarkably increased long-term stability, due to a higher electron injection. The chemical capacitance is dependent on the conduction band energy, whose level is influenced by the electron injection from the dye molecules and by the presence of structural defects in the TiO_2 surface. The decrease in the electron injection in the aged liquid electrolyte-based cells (also deducted from the reduction of J_{sc} values) or the increase in the number of surface defects upon ageing can be therefore responsible for a reduction of the capacitance values [43].

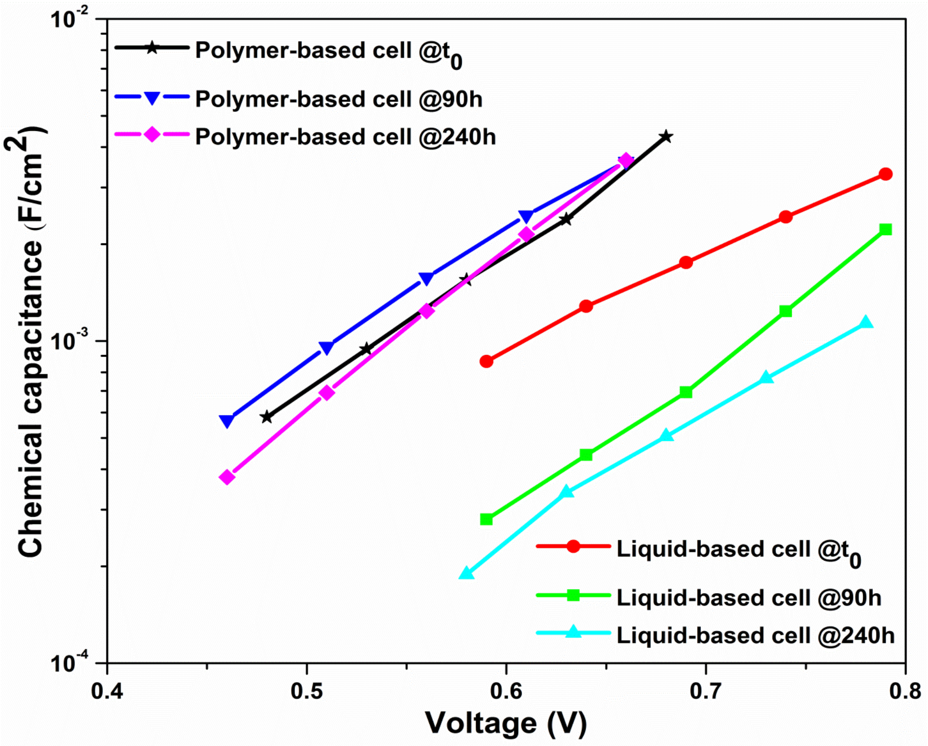

Fig. 6.34 Chemical capacitance dependence on the bias voltage for DSCs fabricated with the polymer electrolyte membrane and the liquid electrolyte. For each cell, the curves related to the fresh-assembled device and to the cells after 90 h and 240 h of storage at 60 °C are reported.

Compared to other UV-cured polymers presented in the literature (see Table 3 in ref. [44]), the performances of the DSC containing the optimized BEMA:PEGMA polymer electrolyte (i.e. 5.41% of efficiency) is very high. Qin *et al.* obtained a slightly higher efficiency (i.e. 5.83%) and similar durability, but introducing an expensive ionic liquid (1-hexyl-3-methylimidazolium iodide) instead of NaI as iodine salt [45]; Lee *et al.* reached 6.10% in the presence of an aliphatic urethane acrylate, however the durability was not reported [46].

In summary, a novel methacrylic-based crosslinked polymer electrolyte was obtained by a rapid, economic and environmentally friendly process of photo-curing, using low cost chemicals. Light-to-electricity conversion efficiency of the DSC assembled with this polymer electrolyte was admirably quite equal to that of the corresponding liquid cell, moreover a remarkably better long-term stability was obtained with BEMA:PEGMA membranes. The experimental conditions for the preparation of the polymer electrolyte were optimized by a design of experiments approach and an interesting correlation between the photoelectrochemical results and the structure of the polymeric network was presented.

6.3.2 Cellulose-based gel polymer electrolyte

6.3.2.1 Electrolyte characterization

The viscosity of the different micro-cellulose weight percentage gels was measured and the values obtained at 25 and 60 °C are summarized in Table 6.9. The tests at 60 °C were carried out with the aim of estimating the contribution of the heating step to the charge transport inside the gel network.

Table 6.9 Viscosity values for different micro-cellulose weight percentage gels.

Micro-cellulose weight percentage	**25 °C ν (mPa·s)**	**60 °C ν (mPa·s)**
3	700	964
4	517	706
5	119	160
6	234	315

The viscosity values are lower for gels with higher cellulose content, supporting the thesis of a material with more liquid inside the network (a possible explanation for this phenomenon is reported in pp. 142 - 143). The heating step, generally, leads to the fabrication of gels with higher viscosities than those measured at room temperature, because of the starting of liquid evaporation from the gel.

In order to evaluate the ion transport inside the gel network, conductivity measurements were carried out. The tests were performed on the 50/50 and 40/60 volume percentage ratio of the two ionic liquids (MPII and EMISCN) gel electrolytes, thus making possible the evaluation of how much the viscosity of the gel affects the ion transport. The results of the conductivity measurements are reported in Table 6.10.

Table 6.10 Conductivity values for different MPII/EMISCN volume percentage ratio gel electrolytes.

Gel sample	Conductivity (mS/cm)
50/50	0.76
40/60	0.77

The values obtained are similar in both gel electrolytes and this suggests that there is not a great influence of the MPII viscosity on the charge transport inside the gel network.

An important requirement that a DSC electrolyte must fulfill is the thermal stability, i.e the electrolyte components should not evaporate at the temperatures at which the cell operates during the sunlight exposure. With the purpose of verifying this feature, a Thermo Gravimetric Analysis of the gel electrolyte was performed and the relative graph is reported in Fig. 6.35.

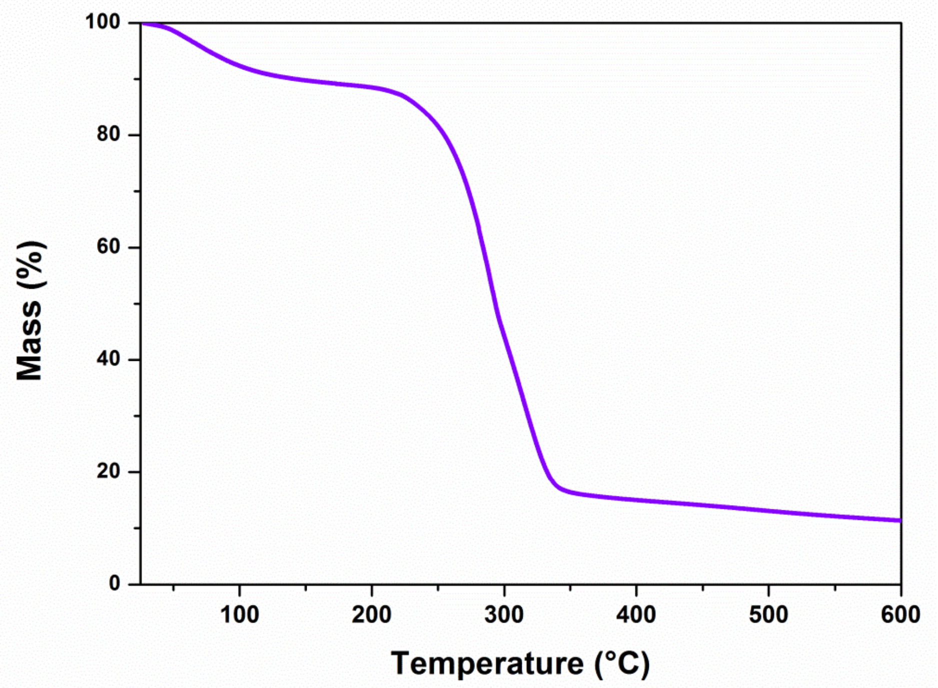

Fig. 6.35 TGA measurement of a gel electrolyte containing 5 wt% of micro-cellulose.

A first mass percentage loss is present at around 100 °C and it is due, most of all, to water evaporation. A small amount of 4-TBP can be responsible for this loss, as well. The main mass loss starts after 300 °C and it is related to the ionic liquid decomposition. Taking into account that DSCs usually work at temperatures not higher than 80 °C, it is possible to assert that the prepared gel electrolytes are stable under normal DSCs operating conditions.

6.3.2.2 Photovoltaic performances investigation

The gel electrolyte optimization process started with a series of samples prepared according to the volume percentage ratios between the two ionic liquids (MPII and EMISC) reported in Table 4.1. The weight percentages of the other reagents were 2 wt% of LiI, 5 wt% of micro-cellulose and 10 wt% of 4-TBP. In Table 6.11 the photovoltaic parameters obtained from the *I*-*V* characterization are summarized.

Table 6.11 Photovoltaic parameters, evaluated from *I*-*V* characterization, of DSCs fabricated with gel electrolytes containing different ionic liquid volume percentage ratios.

Volume percentage ratio (MPII/EMISCN)	J_{sc} **(mA/cm^2)**	V_{oc} **(V)**	***FF***	η **(%)**
50/50	7.87	0.43	0.54	1.86
60/40	7.39	0.42	0.55	1.72
70/30	6.17	0.42	0.46	1.18
80/20	5.64	0.41	0.48	1.10
90/10	3.98	0.41	0.47	0.76
100/0	5.83	0.38	0.46	1.03

All the cells were heated at 60 °C for 1 h in a vacuum oven before starting the *I*-*V* measurements, thus trying to obtain a better gel penetration into the porous matrix of the semiconductor layer. It is possible to note that the highest photoconversion efficiency was reached with a 50/50 volume percentage ratio of the two ionic liquids. A possible explanation for this result could be the lower viscosity of the gel, responsible for a faster movement of the ions inside the solid part of the material. Another interesting feature to be considered is that all the cells present low V_{oc} values; this experimental evidence can be ascribed to the 4-TBP partial evaporation during the cellulose dissolution at 100 °C.

Fig. 6.36 shows the *J*-*V* curves of the DSCs fabricated by employing gel electrolytes with different ionic liquid volume percentage ratios. The enhancement of the viscosity when increasing the MPII volume percentage ratio, evident just by a visual inspection of the samples, is the cause of the current density decrease. The gels with 90 and 100 vol% of MPII were so viscous that became fragile.

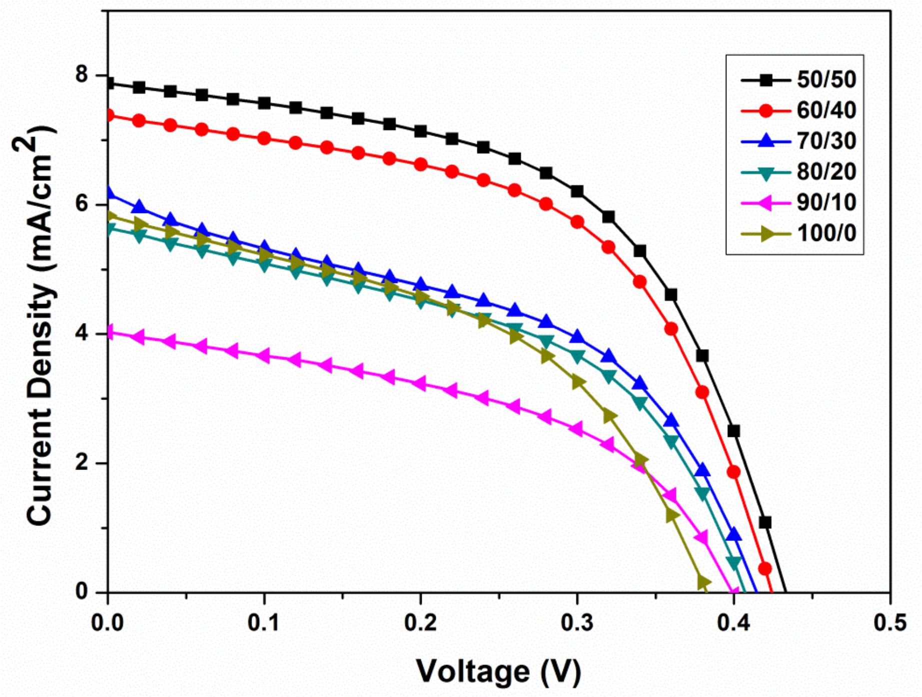

Fig. 6.36 *J-V* curves of the DSCs prepared with gel electrolytes containing different ionic liquid volume percentage ratios.

Once the better ionic liquid volume percentage ratio was fixed, a liquid electrolyte containing the same reagents (except for the cellulose) was prepared for a comparison purpose. Three cells with the liquid electrolyte were fabricated in order to ensure statistics for the results, and their photovoltaic parameters are reported in Table 6.12.

Table 6.12 Photovoltaic parameters of DSCs containing the liquid electrolyte.

Sample	**J_{sc} (mA/cm^2)**	**V_{oc} (V)**	***FF***	**η (%)**
1	13.27	0.68	0.63	5.65
2	13.52	0.68	0.65	6.02
3	13.37	0.68	0.64	5.77
Average	13.39	0.68	0.64	5.81

In order to avoid the 4-TBP evaporation, a variation in the gel preparation process revealed necessary: 4-TBP was added after the complete finalization of the gelation and the removal of the ionic liquid excess. The 50/50 ionic liquid volume ratio gel was re-prepared applying this modified procedure and it was employed to fabricate the DSCs. Subsequently, the devices were heated at various temperatures (45, 60 and 75 °C) for different time intervals (1, 2 and 3 h), with the aim of finding the better conditions for the gel penetration into the TiO_2 layer. The photovoltaic parameter values for the different DSCs are summarized in Table 6.13.

Table 6.13 Photovoltaic parameters, evaluated from the *I-V* characterization, of DSCs fabricated with 50/50 ionic liquid volume ratio gel electrolyte and heated at various temperatures for different time intervals.

Sample	**J_{sc} (mA/cm^2)**	**V_{oc} (V)**	***FF***	**η (%)**
25 °C	5.91	0.58	0.61	2.08
45 °C 1 h	6.54	0.54	0.58	2.07
45 °C 2 h	7.74	0.54	0.58	2.41
45 °C 3 h	6.85	0.54	0.60	2.20
60 °C 1 h	6.95	0.55	0.57	2.17
60 °C 2 h	6.64	0.54	0.58	2.10
60 °C 3 h	6.50	0.53	0.57	1.98
75 °C 1 h	5.09	0.55	0.65	1.81
75 °C 2 h	3.63	0.53	0.69	1.32
75 °C 3 h	1.41	0.51	0.64	0.46

From the data shown in Table 6.13 it is possible to infer that the heating step is beneficial to the DSC performances when performed at 45 °C and 60 °C, while it proved to be counterproductive when the temperature of the oven was fixed to 75 °C. In particular, the improvement in DSCs photoconversion efficiency values for the first two temperatures is related to an enhancement of the J_{sc} (due to a better mobility of the redox species into the gel network) not compensated by an equal decrease of the V_{oc} (due to the 4-TBP partial evaporation). For what concerns the heating time, an enhancement of the efficiency was observed at 45 °C by increasing the time interval from 1 h up to 2 h, while a decrement was witnessed when the temperature was set to 60 °C and 75 °C. The heating time interval of 3 h, instead, gave always worst results with respect to those obtained for 1 h and 2 h. The better photovoltaic performances were achieved by heating the cell at 45 °C for 2 h or at 60 °C for 1 h. From this point onwards all the cells were heated at 60 °C for 1 h before being measured. In general, it can be assessed that the cell performances got worse after few measurements when the heating step was not employed, contrary to what happened if the heating step was performed. It is worthwhile to underline that the DSC performances increased more and more rapidly during the first ten measurements reaching a quasi-steady-state. This phenomenon is well represented in Fig. 6.37, where the variation of the photovoltaic parameters during a campaign of 40 measurements for DSCs heated at 45 °C for 1, 2 and 3 h is reported.

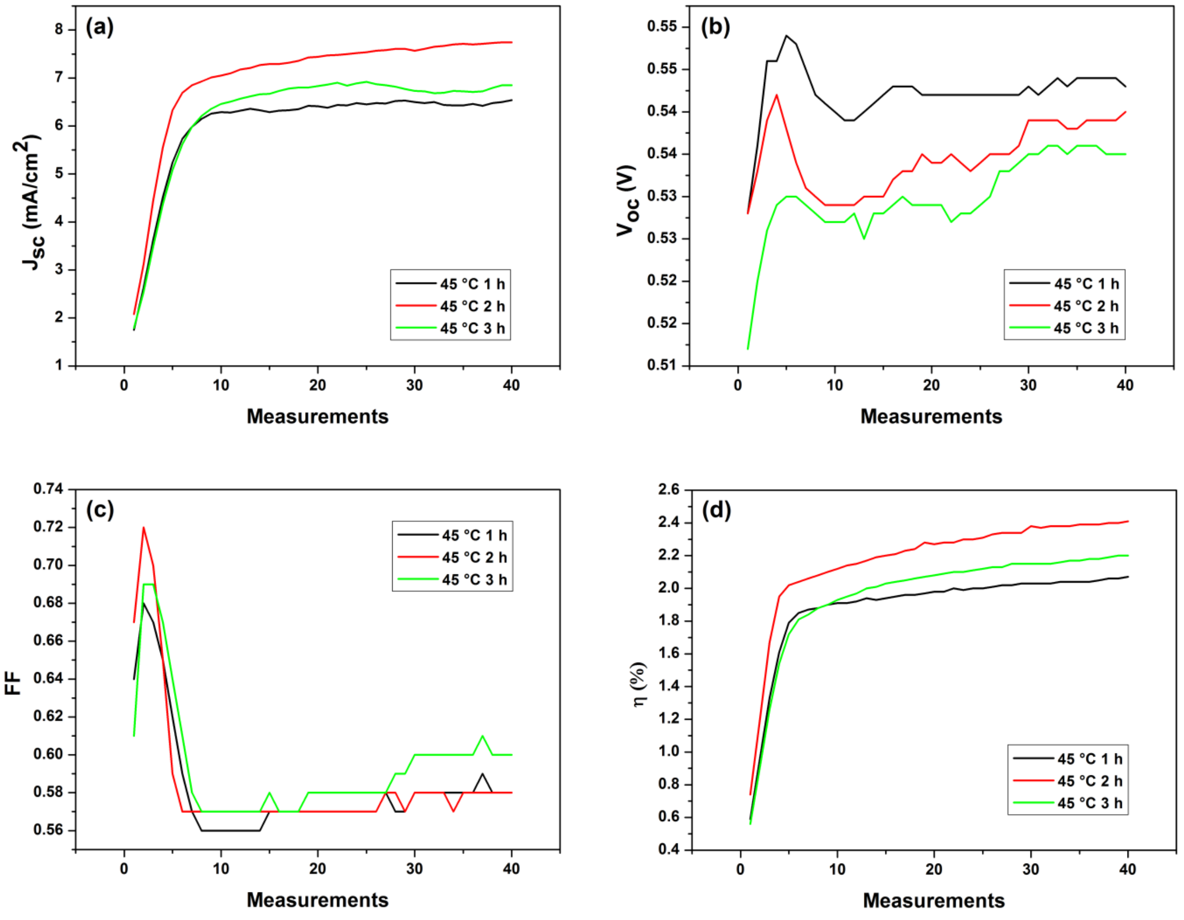

Fig. 6.37 Variation of the photovoltaic parameters during a campaign of 40 measurements for DSCs heated at 45 °C for 1, 2 and 3 h: J_{sc} (a), V_{oc} (b), *FF* (c) and efficiency (d).

The 4-TBP addition after the gelation had been completed allowed obtaining higher V_{oc} values, but they are still far from those measured for the liquid cells. With the purpose of further enhancing the open circuit voltage of the cells, the 4-TBP weight percentage added to the gel electrolyte was increased up to 15, 20 and 25%. The values of the photovoltaic parameters, evaluated from the *I-V* characterization, are listed in Table 6.14. Unfortunately, the V_{oc} values did not increase and the current density ones decreased dramatically, since probably the 4-TBP excess caused the detachment of the dye from the Titanium dioxide substrate [47].

Table 6.14 Photovoltaic parameters, evaluated from the *I-V* characterization, of DSCs fabricated with 50/50 ionic liquid volume ratio gel electrolyte in which 15, 20 and 25% 4-TBP was added.

4-TBP weight percentage	**J_{sc} (mA/cm^2)**	**V_{oc} (V)**	**FF**	**η (%)**
15	0.55	0.49	0.78	0.21
20	1.99	0.52	0.67	0.69
25	1.06	0.52	0.72	0.40

Another parameter that can influence the gel electrolyte behavior in a DSC is the micro-cellulose weight percentage; thus, gels with 3, 4, 5 and 6 wt% of micro-cellulose were prepared and their photovoltaic performances were tested. The obtained results are reported in Table 6.15 and the related *J-V* curves are shown in Fig. 6.38.

Table 6.15 Photovoltaic parameters, obtained from the *I-V* characterization, of DSCs fabricated with gels containing 3, 4, 5 and 6 wt% of micro-cellulose.

Micro-cellulose weight percentage	**J_{sc} (mA/cm^2)**	**V_{oc} (V)**	**FF**	**η (%)**
3	5.45	0.54	0.60	1.75
4	5.42	0.53	0.57	1.64
5	8.18	0.56	0.59	2.71
6	7.47	0.58	0.61	2.62

From both Table 6.15 and Fig. 6.38 it is possible to note that for low micro-cellulose weight percentages (3 and 4) the efficiencies are lower, while for higher micro-cellulose weight percentages (5 and 6) the cell performances considerably increase. At a first sight this trend seems to be unexpected, since the cellulose is an inert material and the increase of its amount into the gel should cause a decrement of the ion transport from the counter electrode to the photoanode, giving a worsening in the photovoltaic performances. One possible explanation for this phenomenon, supported by the viscosity values reported in Table 6.9, could be related to a higher amount of gelling material that can adsorb the other electrolyte reagents. In this way much more ionic species are present inside the gel, thus leading to an enhancement of the photoconversion efficiency of the cell.

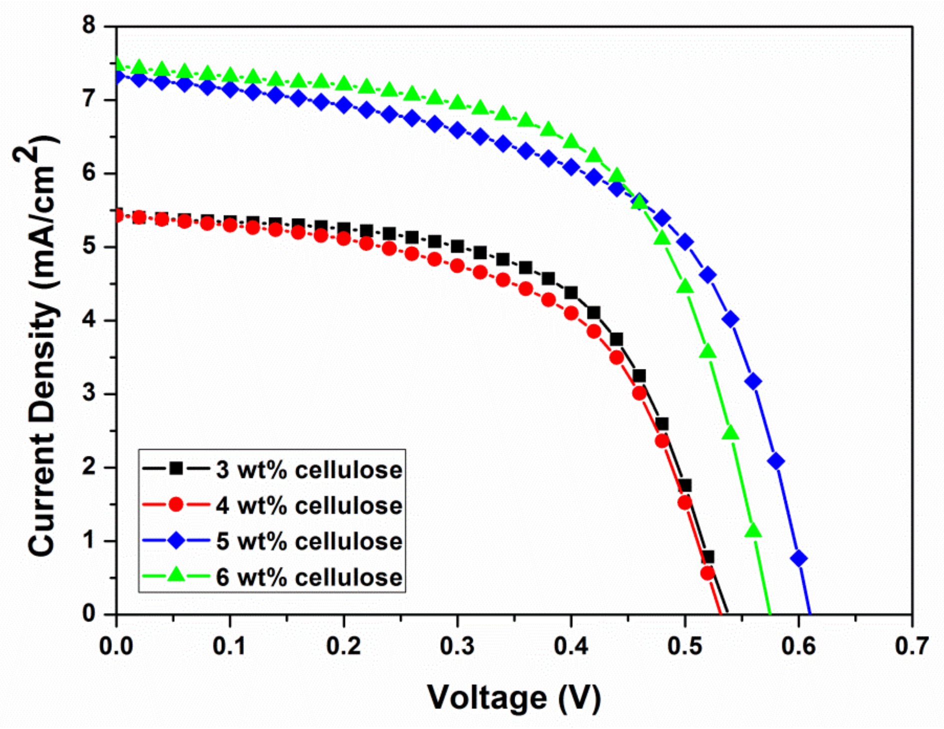

Fig. 6.38 *J-V* curves of the DSCs prepared with gel electrolytes containing different micro-cellulose weight percentages.

One of the most important requirements that gel electrolytes for DSCs application must satisfy is their stability regarding the photovoltaic measurements. In order to test this essential feature, two kinds of experiments were performed: (a) a gel stability test and (b) a stability test of the DSC photovoltaic performances. In the experiment (a), three DSCs were fabricated: in the first one the gel was just prepared, while in the second and in the third ones the gel was one week and two weeks old, respectively. The photovoltaic parameter values are summarized in Table 6.16, the evolution of the photovoltaic parameters during 80 measurements is reported in Fig. 6.39, and the *J-V* curves are shown in Fig. 6.40.

Table 6.16 Photovoltaic parameters, evaluated from *I-V* characterization, of DSCs fabricated with the fresh-prepared gel, with the gel after 1 week of storage and with the gel after 2 weeks of storage.

Gel ageing time	J_{sc} **(mA/cm^2)**	V_{oc} **(V)**	***FF***	η **(%)**
Just prepared	8.18	0.56	0.59	2.71
After 1 week	8.25	0.57	0.56	2.64
After 2 weeks	8.92	0.56	0.55	2.71

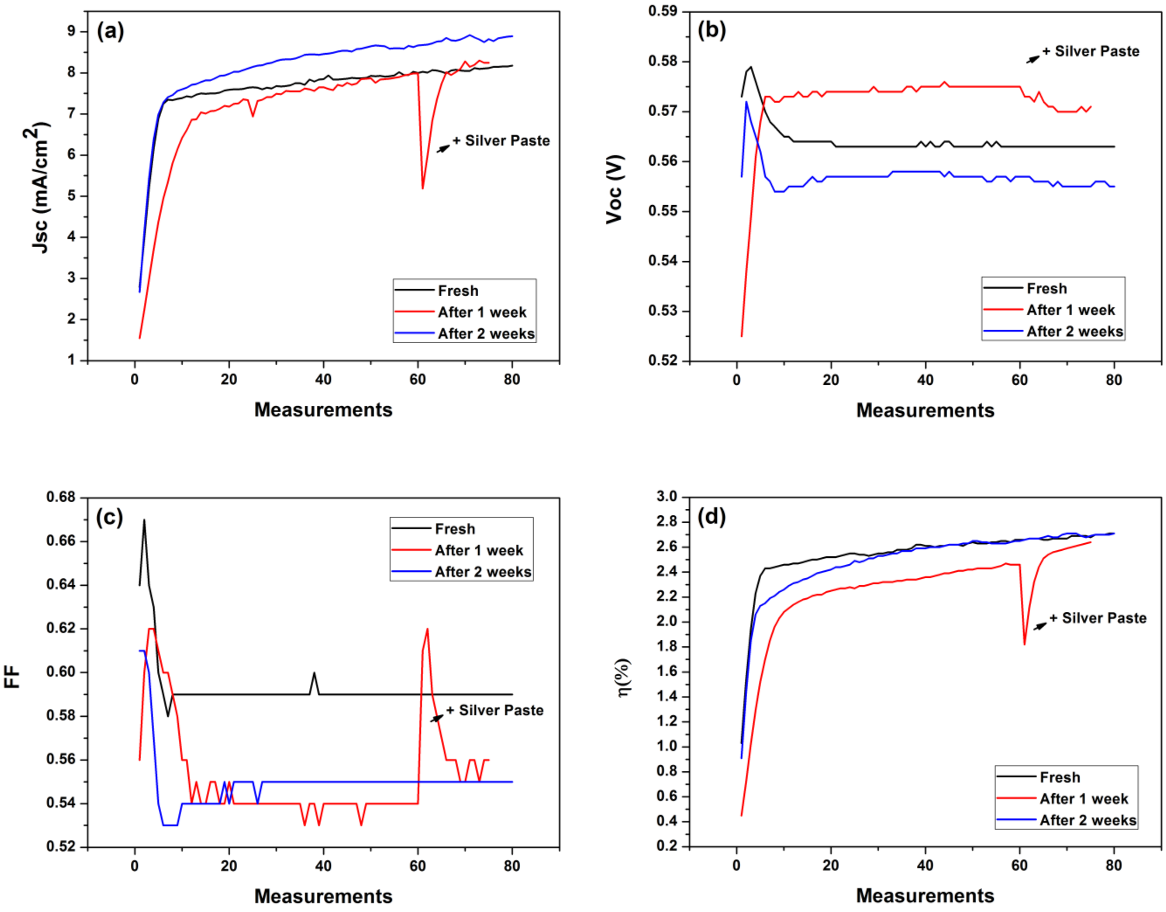

Fig. 6.39 Evolution of the photovoltaic parameters during 80 measurements for DSCs fabricated with the fresh-prepared gel, with the gel after 1 week of storage and with the gel after 2 weeks of storage: J_{sc} (a), V_{oc} (b), *FF* (c) and efficiency (d).

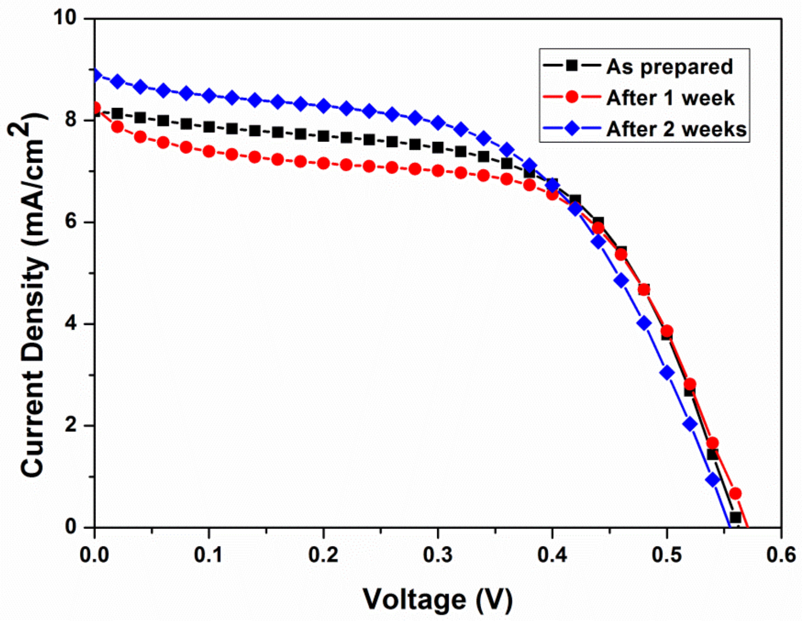

Fig. 6.40 *J-V* curves of DSCs fabricated with the fresh-prepared gel (black line), with the gel after 1 week of storage (red line) and with the gel after 2 weeks of storage (blue line).

From a comparison between all the graphs reported in Fig. 6.39, it is possible to note that there is a steep increase in efficiency and J_{sc} in the first measurements and even if the increment is lower with the measurement advancement, the values still increase after 80 measurements. The V_{oc} trend is quite different with respect to that shown by liquid electrolyte-based DSCs, where the values decrease steeply just after few measurements. In gel-based DSCs, the V_{oc} values, usually, decrease a little after few measurements and then remain constant. The *FF* values follow a trend similar to the V_{oc} one. As it can be seen in Fig. 6.39, starting from a certain measurement a silver paste was deposited onto the TCO layer of both the counter electrode and the photoanode of the DSCs, in order to reduce the contact resistance and try to enhance the photovoltaic performances of the devices.

In the experiment (b), a DSC was assembled by employing the best formulation of the gel electrolyte, according to the photovoltaic characterization results showed above. The cell was measured freshly-fabricated and after 3, 17 and 32 days. A cycle of 500 measures was performed for each test. This means that the DSC had to undergo more than 8 h of exposition to the simulated solar light. The results obtained from the *I-V* characterization are summarized in Table 6.17.

Table 6.17 Photovoltaic parameters, evaluated from the *I-V* characterization, of a quasi-solid DSC during the ageing test.

DSC ageing time	**Measure time**	J_{sc} **(mA/cm^2)**	V_{oc} **(V)**	***FF***	η **(%)**
Just prepared	8 h 1 min	8.07	0.53	0.62	2.68
After 3 days	8 h 9 min	7.98	0.49	0.61	2.40
After 17 days	8 h 6 min	8.17	0.47	0.60	2.31
After 32 days	2 h 35 min	7.22	0.48	0.51	1.75

The variation of the photovoltaic parameters during the ageing test and the *J-V* curves corresponding to the best efficiency for each ageing time considered are reported in Fig. 6.41 and Fig. 6.42, respectively.

From Fig. 6.41 it is evident how the V_{oc} values become lower and lower during the ageing test. This phenomenon could be ascribed to a not perfect sealing of the cell (see Section 4.1.5.2), which leads to a partial evaporation of the liquid part inside the gel during the prolonged solar light exposition as a consequence of the cell heating. From the same figure it’s also possible to note that the best values showed in Table 6.17 were obtained at the end of each cycle of measurement, save for the test performed after 32 days.

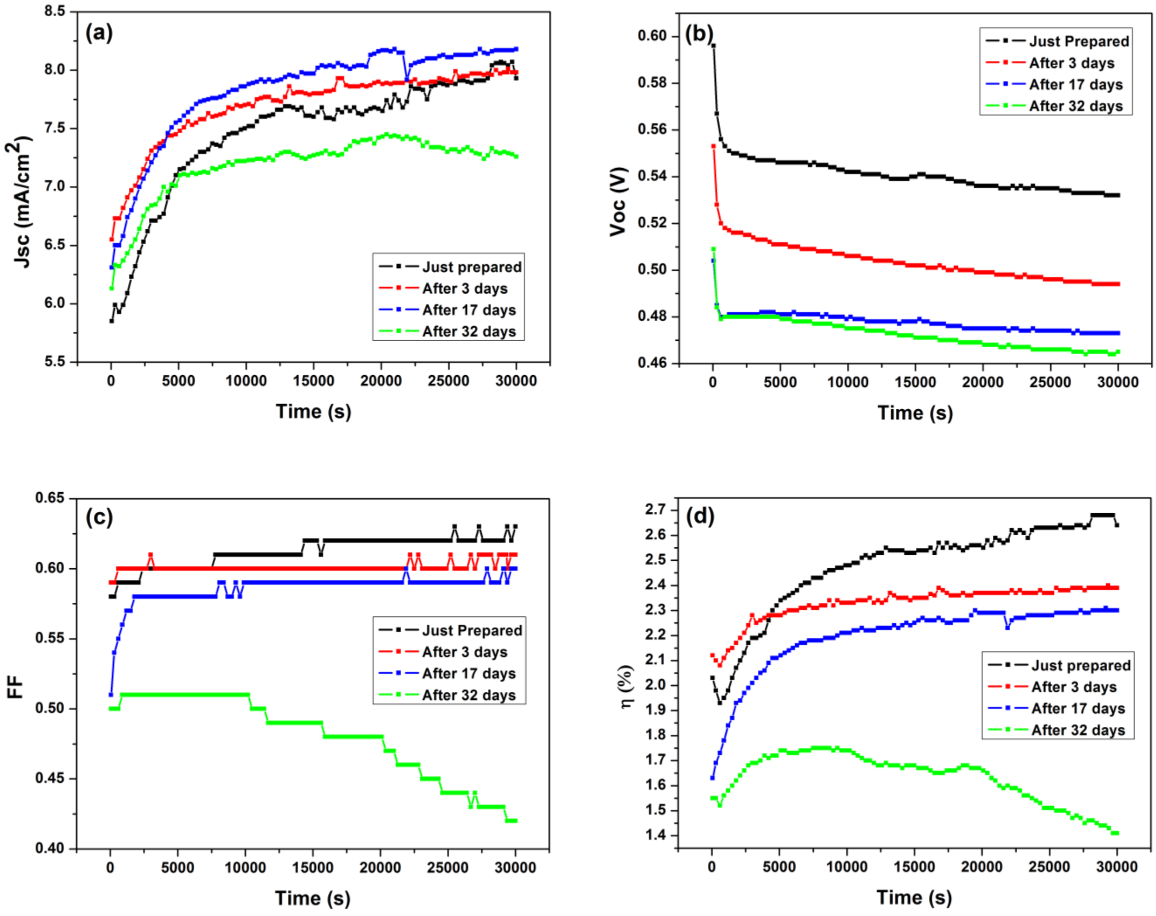

Fig. 6.41 Variation of the photovoltaic parameters during the ageing test: J_{sc} (a), V_{oc} (b), *FF* (c) and efficiency (d).

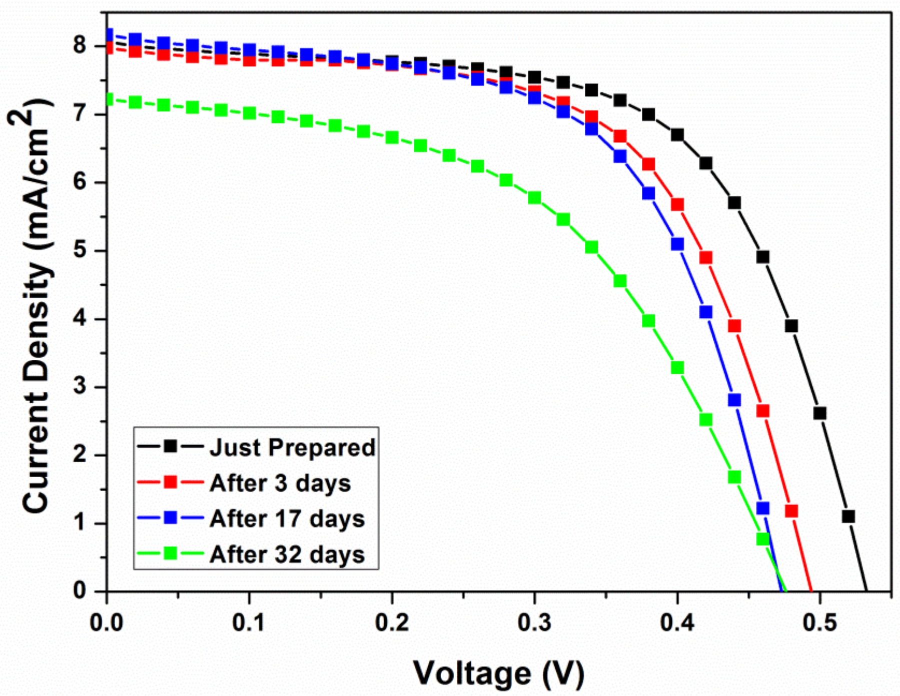

Fig. 6.42 *J-V* curves corresponding to the best efficiency for each ageing time considered.

A good stability was reached even in severe conditions, i.e. more the 8 h of measurements performed in a lapse time longer than one month. Only after 32 days the cell started giving a dramatic worsening in the photovoltaic performances.

In conclusion, a polymer gel electrolyte with the micro-cellulose as natural gelling agent was prepared and applied in Dye-sensitized Solar Cells. The volume percentage ratio between the two ionic liquids MPII and EMISC, the weight percentage of 4-TBP and micro-cellulose and the time and the temperature of the heating step necessary to improve the gel penetration into the TiO_2 layer, were successfully monitored. A maximum photoconversion efficiency of 2.71% was obtained by heating the cell at 60 °C for 1 h and by employing a gel prepared with 2 wt% of LiI, iodine (1/10th of the whole weight of iodide), 5 wt% of micro-cellulose, 10 wt% of 4-TBP and a MPII/EMISC volume percentage ratio of 50/50. An ageing test on the DSC photovoltaic performances was carried out and a good stability in severe conditions was reached.

6.4 Electrical and physical modeling of DSCs under different illumination conditions

In this Section the physics-based model introduced in Section 5.2 will be applied to build a consistent picture of the static and dynamic small-signal performances of nanocrystalline TiO_2-based DSCs under different incident illumination intensities and directions. This is achieved with a reliable extraction and validation of a unique set of model parameters against a large enough set of *I-V*, *IPCE* and *EIS* experimental data.

All the characterizations were carried out in the same day, following a schedule that includes repeated measures of *I-V*, *IPCE*, and *EIS*, designed to monitor the stability of the device performances during the whole characterization and to identify possible fluctuations due to the light intensity stability or to the change of the cell temperature. This enables to meaningfully and consistently compare the *I-V*, *IPCE* and *EIS* experimental data with the model results derived with a unique set of physical parameters. The maximum observed deviations of J_{sc} and V_{oc} under 1 sun, with respect to the first measure, were about 0.8 mA/cm^2 and 50 mV, respectively. Finally, the *I-V* and *IPCE* measurements were repeated after two weeks, and a substantial stability of the devices was verified.

For all the cells, a quite significant discrepancy between the short circuit current density value as directly measured from the photovoltaic characterization under AM 1.5 G illumination and the value predicted from the integration of the *IPCE* spectrum (see Eq. (2.18)) was observed. In particular, under PE-side and CE-side illumination, the *IPCE* evaluated values were respectively 20% and 15% lower than the measured ones. It has to be noted that similar or possibly larger discrepancies have been reported in the literature by exploiting the same *IPCE* measurement set-up [48, 49, 50].

6.4.1 Device numerical model

A consistent description of the device under DC and SS conditions and under different illumination implies to extract and verify a unique set of model parameters on the basis of a large enough set of experimental data, which should be able to accurately reproduce the measured behavior under conditions which are different from the ones exploited for the model extraction. Hereinafter, the extraction of the model parameters will be carried out on the *I-V* and *EIS* characterizations at 1 sun and on the *IPCE* spectra acquired under weak light intensity; the model is then successfully validated against the *I-V* and *EIS* measurements carried out at light intensities in the range 0.1 - 1 sun [51].

6.4.1.1 Extraction of the model parameters

As already mentioned, the J_{sc} extrapolated from the *IPCE* measurements at weak light intensities significantly underestimates the actual J_{sc} measured under 1 sun illumination, for both the illumination sides. Moreover, and coherently, an analysis of the ratio of the CE and PE *IPCE* spectra [48] suggests a diffusion length with non-negligible wavelength dependence and a peak value comparable to the film thickness, in contrast to the *EIS* measurements under 1 sun, at open circuit voltage, from which a diffusion length of about 30 μm was estimated.

To introduce the discussion, it can be useful to recall the definition of two widely used figures of merit of the cell efficiency. These are the light harvesting efficiency η_{LH}, which measures the number of collected photons with respect to the incident ones, thus providing an upper bound to the achievable photocurrent density for zero carrier recombination and full injection efficiency, and the collection efficiency η_{COLL}, which measures the fraction of collected electrons with respect to the generated ones. From Eq. (5.29), with $\eta_{inj} = 1$, it results

$$\eta_{LH,s}(\lambda) = \frac{\int_0^d G_{op}(x,\lambda)}{\lambda\Phi(\lambda)} = \eta_{ill,s}\frac{\alpha_D}{\alpha}(1 - e^{-\alpha d}), \tag{6.17}$$

where s = PE (or CE) depending on the illumination direction. The collection efficiency is then evaluated as

$$\eta_{COLL,s}(\lambda) = \frac{J_{sc,s}(\lambda)}{q\,\eta_{inj,s}\,\eta_{LH,s}\,\lambda\,\Phi(\lambda)}, \tag{6.18}$$

where J_{sc} *(λ)* is the short circuit photocurrent density. Thus, assuming that neither injection nor light harvesting is affected by the photogenerated electron density, the aforementioned discrepancy in the cell behavior under low and high light intensity can be described by the nonlinear recombination model in Eq. (5.24), yielding a collection efficiency significantly higher under 1 sun illumination with respect to the one detected during the unbiased *IPCE* measurement. This provides a way to estimate the optical and the electrical model parameters, as summarized in the rest of the Section.

Literature data were exploited to model the optical generation; in particular, the spectral dependence of transmittance and reflectance of the PE and CE and the optical attenuation of the bulk electrolyte were derived from Halme *et al.* [52], whereas the optical absorption spectrum of the sensitized TiO_2 film was derived from the absorbance measurements reported by Boschloo *et al.* [53]. The peak values of T_{PE}, T_{CE}, T_{EL} and α_D were tuned in order to match the measured short circuit current density under 1 sun, assuming almost ideal collection efficiency. The optical parameters used in the simulation reported hereinafter are shown in Fig. 6.43.

The analysis of the *I-V* characteristics requires also an estimation of the electrical circuit components in Fig. 5.4, which was carried out on the basis of the *EIS* characterization at 1 sun. At $V = V_{oc}$, the electron density across the photoelectrode film turns to be almost constant, thus allowing to use the analytical impedance expression in Eq. (5.41). As well known, such equation admits for an equivalent circuit representation of the photoactive film in terms of a uniform distributed *RC* circuit [54], terminated by an open load (see the inset in Fig. 6.44), whose circuit elements are directly linked to the small-signal transport and recombination parameters in Eqs. (5.37) - (5.39) according to

$$R_{CT}C_{\mu} = \tau_n^{ss} \tag{6.19}$$

$$R_T C_\mu = \frac{d^2}{D_n^{ss}} \tag{6.20}$$

$$\frac{R_{CT}}{R_T} = \left(\frac{L_n}{d}\right)^2 \tag{6.21}$$

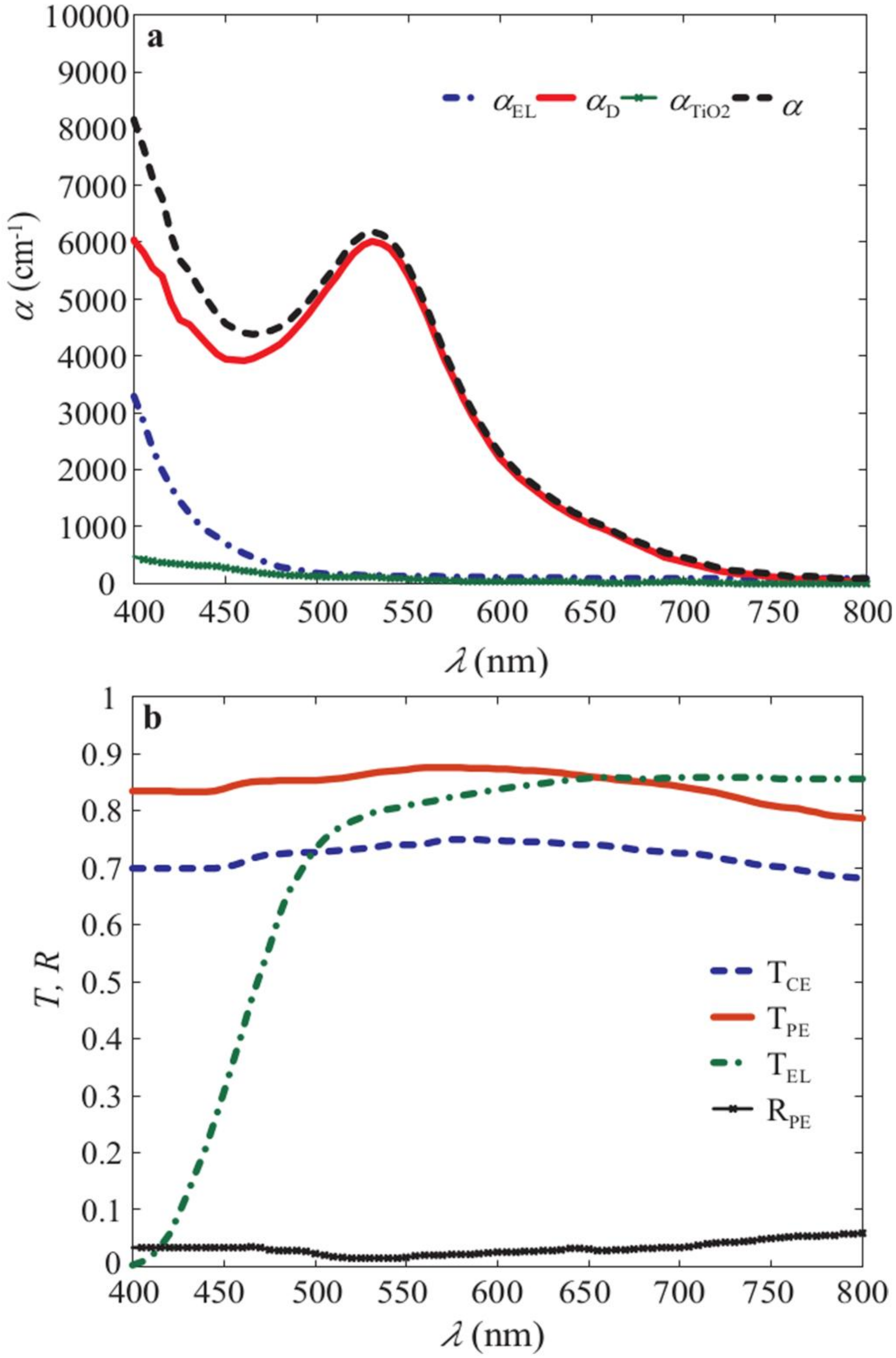

Fig. 6.43 Optical absorption spectra of the cell components exploited in the simulations (a). Spectral transmittance and reflectance of photoelectrode, counter electrode and electrolyte exploited in the simulations (b).

The Nyquist plot in Fig. 6.44 compares the measured and fitted impedance at different bias voltages, showing that R_{CE}, C_{CE} and R_s do not present any significant voltage dependence, thus allowing to neglect possible mass transport limitations from the electrolyte and the activation of an overpotential at the CE [52, 55, 56].

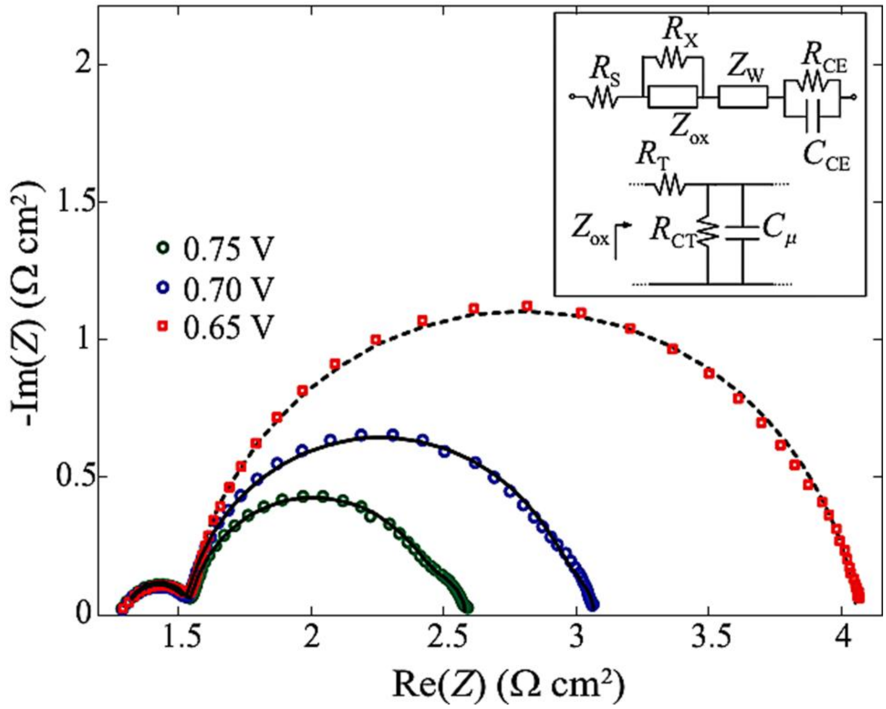

Fig. 6.44 Example of *EIS* fitting under 1 sun at different bias voltages. The inset shows the used equivalent circuit.

By exploiting Eqs. (6.19) - (6.21), the *EIS* equivalent circuit fitting also allows for a preliminary estimation of a few electronic parameters, namely α, N_T, D_0, to be refined then on the basis of the numerical simulations.

Literature data were used for the conduction band effective density of states $N_c = 3.24 \cdot 10^{20}$ cm^{-3} [57, 58], and the electrolyte redox potential at thermal equilibrium $E_c - E_{redox,0} =$ 0.93 eV [59], corresponding to a dark electron density (in the conduction band) $n_0 = 3.32 \cdot 10^4$ cm^{-3}.

Finally, the β exponent characterizing the electron density dependence of the recombination rate is estimated on the basis of the discrepancy between the short circuit current density measured at 1 sun and the one extrapolated from the *IPCE* spectra.

The electrical parameters values used in the following simulations, in good agreement with the typical ones reported in the literature, are summarized in Table 6.18, together with the estimation method exploited. All the model parameters, with the exception of T_{EL} and T_{CE}, were extracted from the experimental data under PE-side illumination.

Table 6.18 Electrical model parameters used in the simulations.

Parameter	**Value**	**Estimation method**
D_0	0.18 cm^2/s	*EIS*, optimized
β	0.72	*IPCE* and *I-V*, optimized
k_0	$5.35 \cdot 10^8$ cm$^{3\beta}$/s	*EIS* and *I-V*, optimized
α	0.32	*EIS*, optimized
N_T	$1.18 \cdot 10^{20}$ cm^{-3}	*EIS*, optimized
R_S	$1.3\ \Omega$ cm^2	*EIS*
R_{CE}	$0.25\ \Omega$ cm^2	*EIS*
C_{CE}	$1.20 \cdot 10^{-4}$ F/cm^2	*EIS*
R_W	$0.2\ \Omega$ cm^2	*EIS*
ω_W	3.0 rad/s	*EIS*
R_X	$1485\ \Omega$ cm^2	*EIS*

The measured and simulated *IPCE* spectra and *I-V* characteristics for both PE- and CE-side illumination are compared in Fig. 6.45a and Fig. 6.45b, respectively, with good agreement.

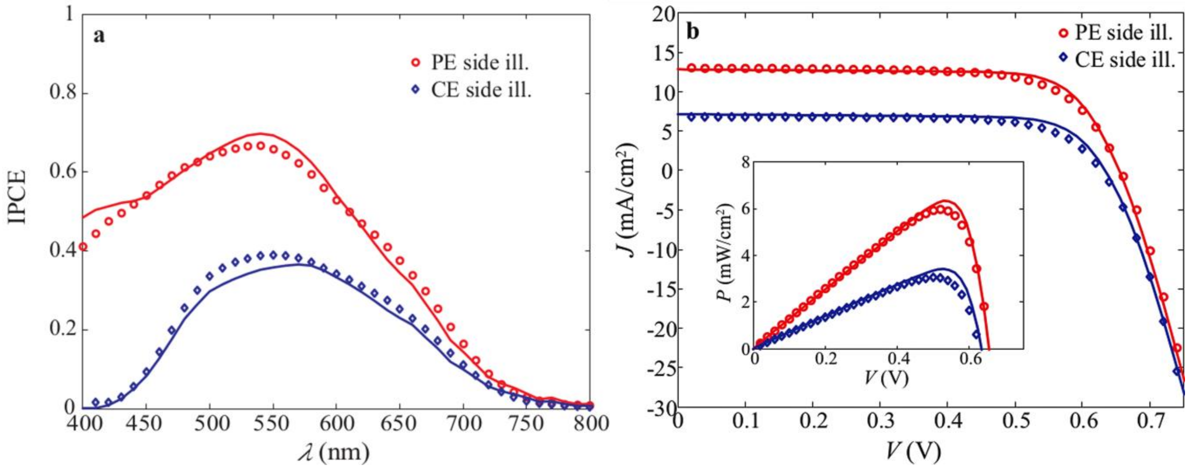

Fig. 6.45 Measured (symbols) and simulated (solid lines) *IPCE* for both the illumination sides (a). Measured (symbols) and simulated (solid lines) *I-V* characteristics under AM 1.5 G solar illumination. The inset compares the corresponding power density (*P*) *vs.* voltage curves (b).

The maximum deviation between measured and simulated *I-V* appears around the maximum power point, due to an overestimation of the cell Fill Factor (see the inset of Fig. 6.45b). A better fit could be obtained by increasing the series parasitic resistance (at the expense, however, of the fit at high forward bias) or by introducing an empirical ideality factor (*m*) in the conduction band electron Boltzmann statistics [55, 60]. Such a parameter would not affect neither the short circuit current density nor the *IPCE*, while it would affect the open circuit voltage and its dependence on the light intensity (I_x). In particular, based on a diode-like interpretation of the *I-V* characteristics, at a first approximation the slope of the V_{oc} *vs.* I_x curve will be proportional to the ratio m/β. On the other hand, for the analyzed cells, it was not possible to obtain a satisfactory match of the *IPCE/I-V* discrepancy and of the light intensity dependence of the V_{oc}, which for the cells considered here are fully described by the nonlinear recombination model. Thus, at the present stage the inclusion of this further empirical parameter, whose physical motivation is currently under study [61, 62, 63], was discarded. Finally, Fig. 6.46 reports the calculated light harvesting efficiency and collection efficiency, pointing out the significant effect of the assumed nonlinear recombination mechanism on η_{COLL}; in fact, η_{COLL} is almost ideal and wavelength independent at 1 sun, whereas it turns out to be comparable to η_{LH} and dependent on the wavelength and on the illumination side under weak light intensity (0.05 mW/cm^2).

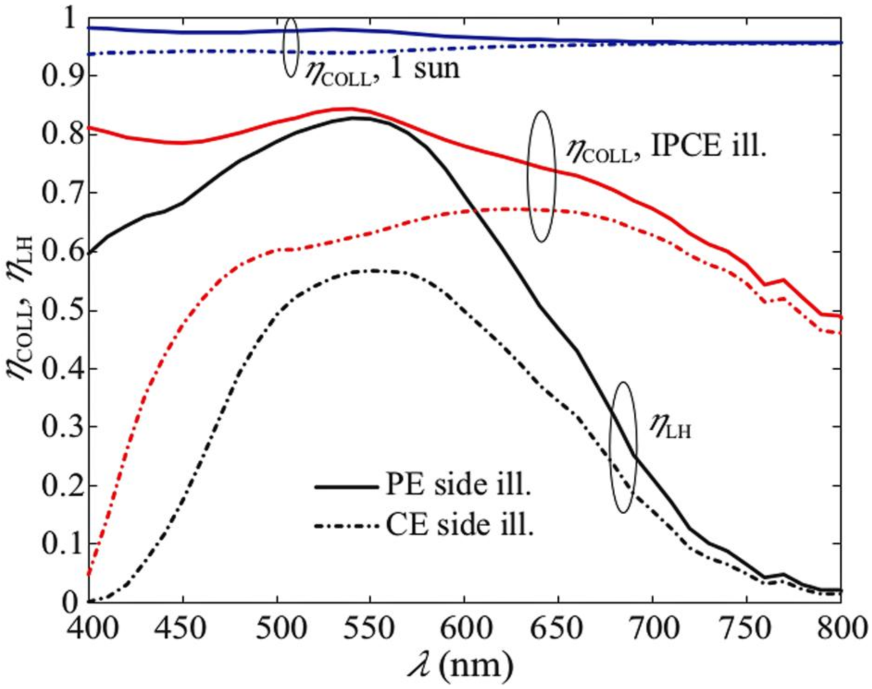

Fig. 6.46 Simulated η_{LH} and η_{COLL}, obtained through *I-V* (1 sun) and *IPCE* characterizations, for both the illumination sides.

While from the application standpoint the conventional *IPCE* characterization under bias light is the obvious choice for assessing the cell photovoltaic performances, unbiased *IPCE* measurements could be a useful tool to investigate more deeply the electron transport and recombination mechanisms, whose apparent density dependence still lacks a sound physical explanation.

6.4.1.2 DC and SS simulations under different light intensities

It may be asked whether the assumed nonlinear recombination mechanism is able to predict the impact of the different illumination intensities on the photovoltaic response of the analyzed DSCs. To this aim, a set of *I-V* and *EIS* measurements with incident light intensity ranging from 0.1 to 1 sun was implemented. Within this range of light intensity, the measured short circuit current density (J_{sc}) increases linearly with I_x and the open circuit voltage (V_{oc}) shows a logarithmic dependence from I_x, as expected according to a diode-like interpretation of the cell, with a non-ideal slope of about 40 mV. Fig. 6.47 shows the measured and simulated light intensity dependence of J_{sc} and V_{oc}, providing a validation of the model against measurements not used during the model parameter extraction.

The fact that, despite the assumed electron density dependence of the recombination rate, the predicted short circuit current density closely follows the measured linear behavior with respect to the light intensity, can be explained by analyzing the behavior of the collection efficiency. In particular, the behavior of the average collection efficiency in the wavelength range of interest $\Delta\lambda$

$$\bar{\eta}_{COLL} = \frac{1}{\Delta\lambda} \int_{\Delta\lambda} \eta_{COLL}(\lambda) d\lambda \,, \tag{6.22}$$

reported in Fig. 6.48 can be considered as a function of the incident light intensity. Within the 0.1 - 1 sun range, $\bar{\eta}_{COLL}$ exhibits a weak dependence on I_x, consistent with the linear behavior of J_{sc} *vs.* I_x in Fig. 6.47; in contrast, a significant dependence on I_x is observed at light intensities comparable to the one exploited under unbiased *IPCE* measurements.

Finally, numerical simulations under AC conditions, with the cell biased at open circuit voltage under varying light intensity, were performed. Fig. 6.49 compares the measured and simulated Nyquist plots, showing a very good agreement. Correspondingly, Fig. 6.50 shows the small-signal transport parameters as a function of the incident light intensity, as extracted from the measured and simulated *EIS* impedance according to Eqs. (6.19) - (6.21). Coherently with the previous analysis of $\bar{\eta}_{COLL}$, the extracted diffusion length results to be almost independent of the incident light flux.

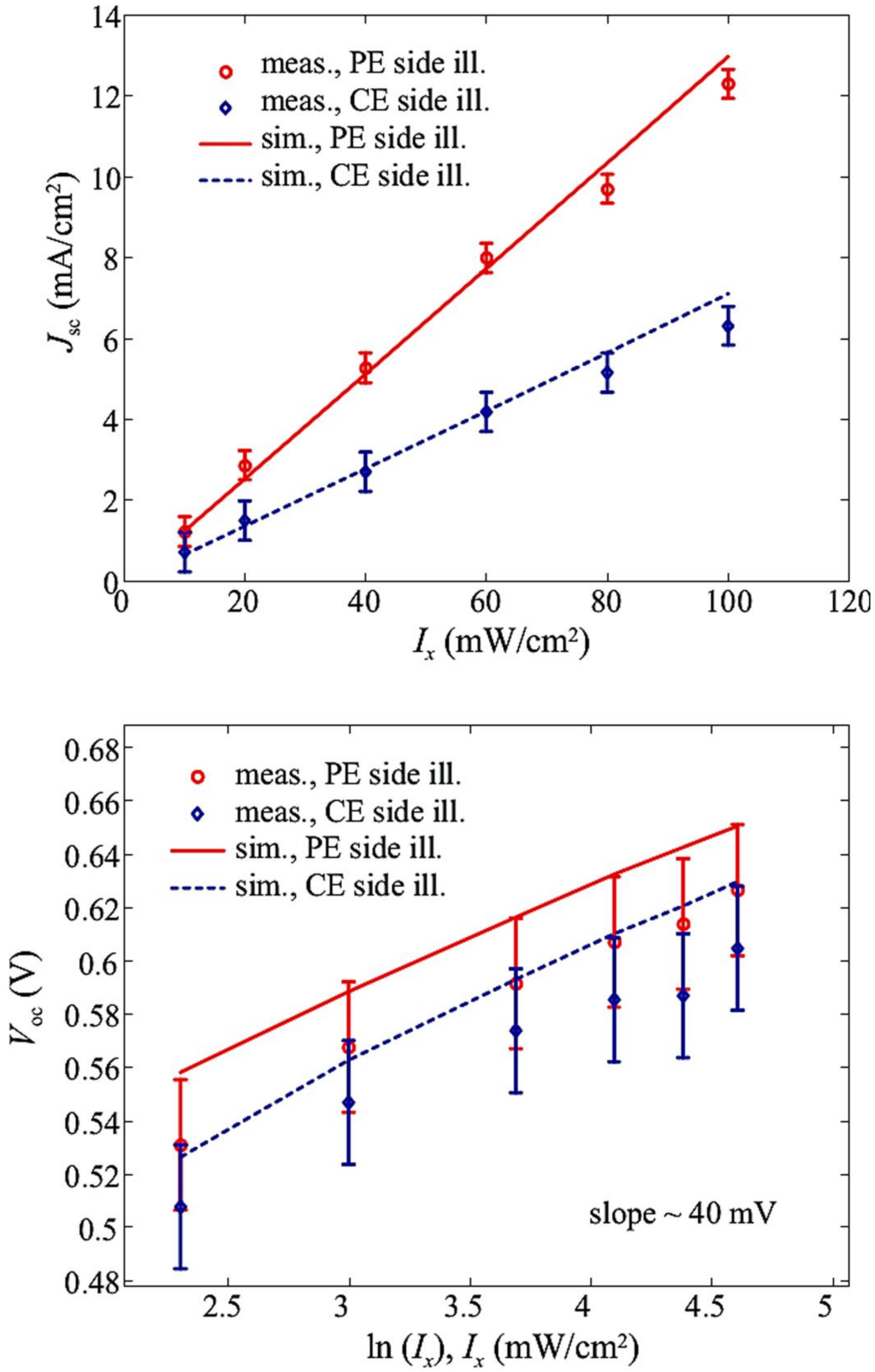

Fig. 6.47 Measured (symbols) and simulated (solid lines) J_{sc} (top) and V_{oc} (bottom) as function of the incident light intensity. Error bars indicate the fluctuations observed during the repeated measurements.

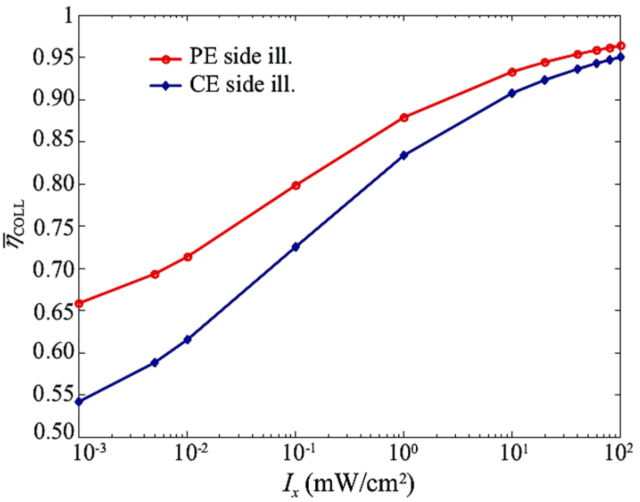

Fig. 6.48 Calculated dependence of the average collection efficiency $\bar{\eta}_{COLL}$ as a function of the incident light intensity. As a reference, the lamp power density during the *IPCE* measurement was around 0.05 mW/cm^2.

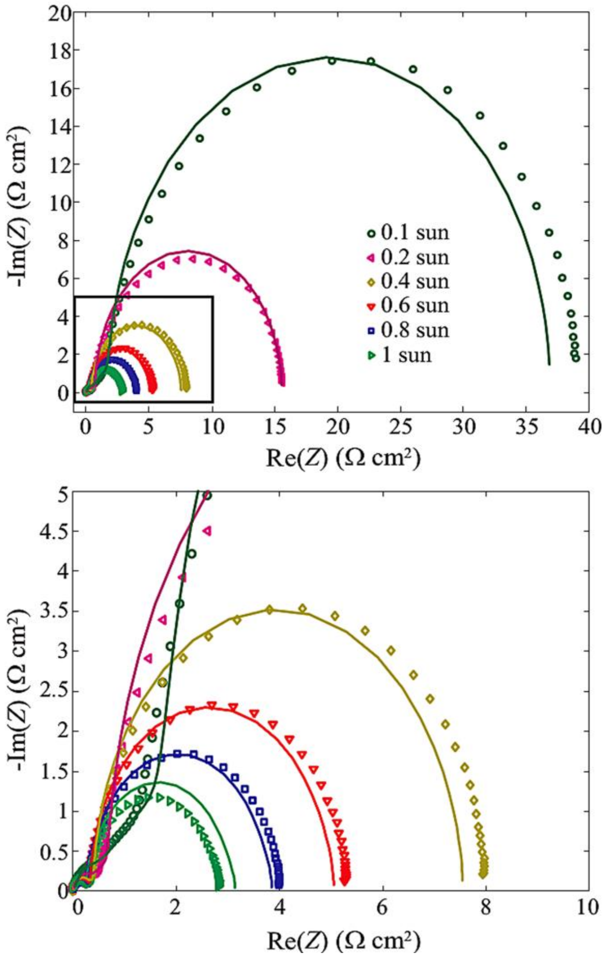

Fig. 6.49 Measured (symbols) and simulated (solid lines) *EIS* Nyquist plots under open circuit conditions and under different incident light intensities. The boxed range is zoomed out in the bottom figure.

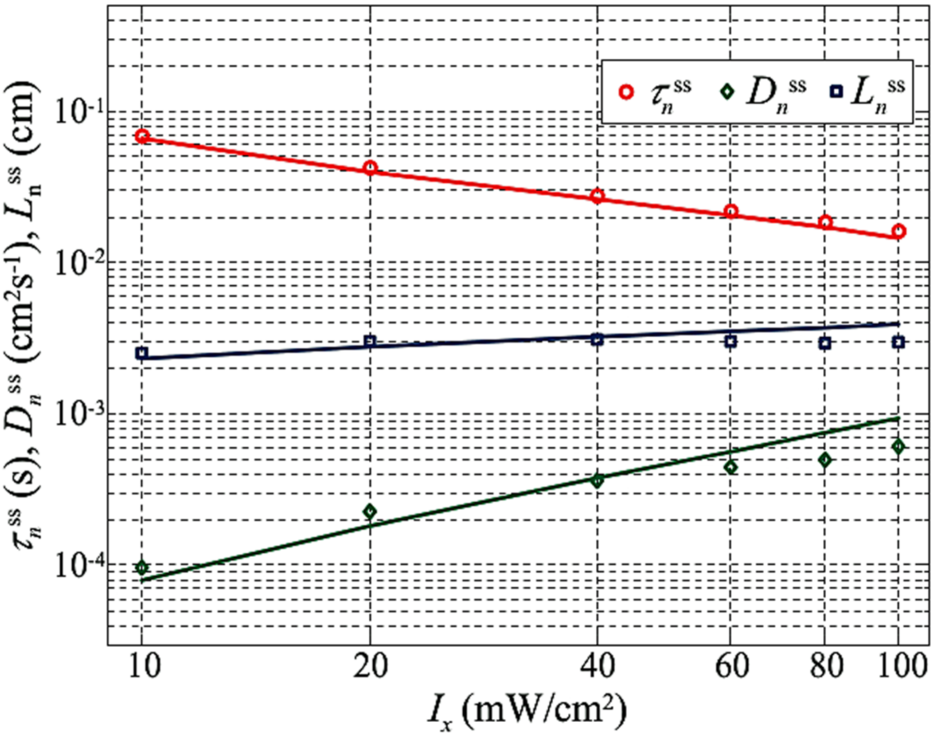

Fig. 6.50 Comparison between measured small-signal transport parameters *vs.* light intensity, as extracted from measured *EIS* (symbols) and from simulated *EIS* (solid lines).

To conclude, a mixed-mode physics-based and circuit-level model of the DSC able to consistently predict the device behavior under a wide range of experimental conditions was presented. The model couples in a self-consistent way an accurate description of electron photogeneration, transport and recombination across the nanocrystalline photoactive layer, with an equivalent compact circuit for the parasitic parts of the cell. Trap-limited dynamics and nonlinear recombination are included and their impact on the steady-state and small-signal dynamic behavior of the device is assessed, based on experimental data and numerical simulations. A unique and limited set of physical and electrical parameters is derived and verified on the basis of a suitable range of experimental data. The simulation results successfully reproduce the *I-V*, *IPCE* and *EIS* measurements under different operating conditions (light intensity, illumination direction, and applied voltage), allowing to clearly identify the optical and electrical losses across the cell and to gain insight into the collection efficiency dependence on the electron density.

References

[1] M. A. Baker, W. Gissler, S. Klose, M. Trampert, and F. Weber, *Surf. Coating Technol.* **125**, 207 (2000).

[2] A. F. Jankowski, and J. P. Hayes, *J. Vac. Sci. Technol. A* **21**, 422 (2003).

[3] K. Keis, E. Magnusson, H. Lindstrom, S.-E. Lindquist, and A. Hagfeldt, *Sol. Energy Mater. Sol. Cells* **73**, 51 (2002).

[4] I. Gonzalez-Valls, and M. Lira-Cantu, *Energy Environ. Sci.* **2**, 19 (2009).

[5] A. Lamberti, R. Gazia, A. Sacco, S. Bianco, M. Quaglio, A. Chiodoni, E. Tresso, and C. F. Pirri, *Prog. Photovoltaics Res. Appl.* **22**, 189 (2014).

[6] N. Memarian, I. Concina, A. Braga, S. M. Rozati, A. Vomiero, and G. Sberveglieri, *Angew. Chem. Int. Ed.* **123**, 12529 (2011).

[7] P. J. Cameron, and L. M. Peter, *J. Phys. Chem. B* **109**, 7392 (2005).

[8] Y. Liu, X. Sun, Q. Tai, H. Hu, B. Chen, N. Huang, B. Sebo, and X.-Z. Zhao, *J. Power Sources* **196**, 475 (2011).

[9] S. M. Waita, B. O. Aduda, J. M. Mwabora, C. G. Granqvist, S.-E. Lindquist, G. A. Niklasson, A. Hagfeldt, and G. Boschloo, *J. Electroanal. Chem.* **605**, 151 (2007).

[10] A. Sacco, A. Lamberti, I. Berardone, S. Bianco, R. Gazia, D. Pugliese, M. Quaglio, E. Tresso, and C. F. Pirri, *Acta Phys. Pol. A* **123**, 386 (2013).

[11] D. Pugliese, F. Bella, V. Cauda, A. Lamberti, A. Sacco, E. Tresso, and S. Bianco, *ACS Appl. Mater. Interfaces* **5**, 11288 (2013).

[12] K. Keis, J. Lindgren, S.-E. Lindquist, and A. Hagfeldt, *Langmuir* **16**, 4688 (2000).

[13] K. Keis, C. Bauer, G. Boschloo, A. Hagfeldt, K. Westermark, H. Rensmo, and H. Siegbahn, *J. Photochem. Photobiol., A* **148**, 57 (2002).

[14] Z. Yu, N. Vlachopoulos, M. Gorlov, and L. Kloo, *Dalton Trans.* **40**, 10289 (2011).

[15] M. Wang, C. Grätzel, S. M. Zakeeruddin, and M. Grätzel, *Energy Environ. Sci.* **5**, 9394 (2012).

[16] H. Yang, J. Liu, Y. Lin, J. Zhang, and X. Zhou, *Electrochim. Acta* **56**, 6271 (2011).

[17] F. Bella, E. D. Ozzello, A. Sacco, S. Bianco, and R. Bongiovanni, *Int. J. Hydrogen Energy* **39**, 3036 (2014).

[18] G. Cicero, G. Musso, A. Lamberti, B. Camino, S. Bianco, D. Pugliese, F. Risplendi, A. Sacco, N. Shahzad, A. M. Ferrari, B. Ballarin, C. Barolo, E. Tresso, and G. Caputo, *Phys. Chem. Chem. Phys.* **15**, 7198 (2013).

[19] A. Hagfeldt, G. Boschloo, L. Sun, L. Kloo, and H. Pettersson, *Chem. Rev.* **110**, 6595 (2010).

[20] J. Park, C. Barolo, F. Sauvage, N. Barbero, C. Benzi, P. Quagliotto, S. Coluccia, D. Di Censo, M. Grätzel, M. K. Nazeeruddin, and G. Viscardi, *Chem. Commun.* **48**, 2782 (2012).

[21] M. Matsui, H. Mase, J.-Y. Jin, K. Funabiki, T. Yoshida, and H. Minoura, *Dyes Pigm.* **70**, 48 (2006).

[22] M. Guo, P. Diao, Y.-J. Ren, F. Meng, H. Tian, and S.-M. Cai, *Sol. Energy Mater. Sol. Cells* **88**, 23 (2005).

[23] J. A. Mikroyannidis, P. Suresh, M. S. Roy, and G. D. Sharma, *Electrochim. Acta* **56**, 5616 (2011).

[24] T. Ono, T. Yamaguchi, and H. Arakawa, *Sol. Energy Mater. Sol. Cells* **93**, 831 (2009).

[25] D. Pugliese, N. Shahzad, A. Sacco, G. Musso, A. Lamberti, G. Caputo, E. Tresso, S. Bianco, and C. F. Pirri, *Int. J. Photoenergy* **2013**, 871526 (2013).

[26] G. Schlichthörl, S. Y. Huang, J. Sprague, and A. J. Frank, *J. Phys. Chem. B* **101**, 8141 (1997).

[27] G. Schlichthörl, N. G. Park, and A. J. Frank, *J. Phys. Chem. B* **103**, 782 (1999).

[28] R. Kern, R. Sastrawan, J. Ferber, R. Stangl, and J. Luther, *Electrochim. Acta* **47**, 4213 (2002).

[29] X. Yang, M. Yanagida, and L. Han, *Energy Environ. Sci.* **6**, 54 (2013).

[30] A. Ehret, L. Stuhl, and M. T. Spitler, *J. Phys. Chem. B* **105**, 9960 (2001).

[31] B. O'Regan, and J. R. Durrant, *Acc. Chem. Res.* **42**, 1799 (2009).

[32] D. Pugliese, N. Shahzad, A. Sacco, E. Tresso, and A. L. Alexe-Ionescu, *J. Appl. Phys.* **114**, 094901 (2013).

[33] S. Havriliak, and S. Negami, *Polymer* **8**, 161 (1967).

[34] A. L. Alexe-Ionescu, G. Barbero, C. F. Pirri, and E. Tresso, *J. Appl. Phys.* **112**, 024106 (2012).

[35] C. H. Yang, W. Y. Ho, H. H. Yang, and M. L. Hsueh, *J. Mater. Chem.* **20**, 6080 (2010).

[36] Z. Lan, J. Wu, D. Wang, S. Hao, J. Lin, and Y. Huang, *Sol. Energy* **80**, 1483 (2006).

[37] R. A. Robinson, and R. H. Stokes, *Angew. Chem. Int. Ed.* **72**, 426 (1960).

[38] Y. Yang, J. Zhang, C. Zhou, S. Wu, S. Xu, W. Liu, H. Han, B. Chen, and X. Z. Zhao, *J. Phys. Chem. B* **112**, 6594 (2008).

---

[39] R. Kawano, H. Matsui, C. Matsuyama, A. Sato, M. A. Bin Hasan Susan, N. Tanabe, and M. Watanabe, *J. Photochem. Photobiol., A* **164**, 87 (2004).

[40] J. R. Nair, C. Gerbaldi, G. Meligrana, R. Bongiovanni, S. Bodoardo, N. Penazzi, P. Reale, and V. Gentili, *J. Power Sources* **178**, 751 (2008).

[41] J. K. Gillham, *Polym. Eng. Sci.* **26**, 1429 (1986).

[42] L. W. Hill, *Prog. Org. Coat.* **31**, 235 (1997).

[43] S. C. Lai, K. N. P. Connor, and L. Ke, *J. Electrochem. Soc.* **158**, H1193 (2011).

[44] F. Bella, D. Pugliese, J. R. Nair, A. Sacco, S. Bianco, C. Gerbaldi, C. Barolo, and R. Bongiovanni, *Phys. Chem. Chem. Phys.* **15**, 3706 (2013).

[45] D. Qin, Y. Zhang, S. Huang, Y. Luo, D. Li, and Q. Meng, *Electrochim. Acta* **56**, 8680 (2011).

[46] H. S. Lee, C. H. Han, Y. M. Sung, S. S. Sekhon, and K. J. Kim, *Curr. Appl Phys.* **11**, S158 (2011).

[47] P. T. Nguyen, P. E. Hansen, and T. Lund, *Sol. Energy* **88**, 23 (2013).

[48] J. Halme, G. Boschloo, A. Hagfeldt, and P. Lund, *J. Phys. Chem. C* **112**, 5623 (2008).

[49] D. Gentilini, D. D’Ercole, A. Gagliardi, A. Brunetti, A. Reale, T. Brown, and A. Di Carlo, *Superlattices Microstruct.* **47**, 192 (2010).

[50] X. Guo, Y. Luo, C. Li, D. Qin, D. Li, and Q. Meng, *Curr. Appl. Phys.* **12**, e54 (2011).

[51] F. Cappelluti, S. Ma, D. Pugliese, A. Sacco, A. Lamberti, G. Ghione, and E. Tresso, *Phys. Chem. Chem. Phys.* **15**, 14634 (2013).

[52] J. Halme, P. Vahermaa, K. Miettunen, and P. Lund, *Adv. Mater.* **22**, E210 (2010).

[53] G. Boschloo, and A. Hagfeldt, *Inorg. Chim. Acta* **61**, 729 (2008).

[54] J. Bisquert, *J. Phys. Chem. B* **106**, 325 (2002).

[55] P. R. F. Barnes, A. Y. Anderson, J. R. Durrant, and B. O'Regan, *Phys. Chem. Chem. Phys.* **13**, 5798 (2011).

[56] J. Villanueva, J. A. Anta, E. Guillen, and G. Oskam, *J. Phys. Chem. C* **113**, 19722 (2009).

[57] A. Gagliardi, M. A. der Maur, D. Gentilini, and A. Di Carlo, *J. Comput. Electron.* **8**, 398 (2009).

[58] D. Fitzmaurice, *Sol. Energy Mater. Sol. Cells* **32**, 289 (1994).

[59] G. Smestad, *Sol. Energy Mater. Sol. Cells* **32**, 273 (1994).

[60] J. R. Jennings, A. Ghicov, L. M. Peter, P. Schmuki, and A. B. Walker, *J. Am. Chem. Soc.* **130**, 13364 (2008).

[61] J. R. Jennings, and Q. Wang, *J. Phys. Chem. C* **115**, 15109 (2011).

[62] S. Koops, B. O'Regan, P. F. Barnes, and J. R. Durrant, *J. Am. Chem. Soc.* **131**, 4808 (2009).

[63] J. Cai, N. Satoh, and L. Han, *J. Phys. Chem. C* **115**, 6033 (2011).

Chapter 7: Conclusions and future works

The objective of the thesis work was to develop and optimize innovative and low cost materials for Dye-sensitized Solar Cells application.

The DSC is an electrochemical solar cell, and its operation is closely related to the nanometer scale morphology of the TiO_2 electrode and to the molecular nature of the TiO_2+dye/electrolyte interface. The standard DSC technology is based on a sintered nanostructured TiO_2 electrode deposited by screen printing or tape casting of a colloidal TiO_2 solution onto FTO-covered glass, a Ru-based metal-organic dye, a liquid nitrile-based redox couple and a thermal platinum catalyst-based counter electrode.

These conventional materials, however, highlight some important drawbacks: in particular, TiO_2 presents the disadvantage of a reduced charge transport due to a long pathway for the electron diffusion within the semiconductor network; Ru-based sensitizers exhibit the important limits of expensive synthesis process, relatively low molar extinction coefficient in the visible region, limited availability of precursors and waste disposal troubles; finally, liquid solvent-based electrolytes are characterized by a limited long-term stability, difficulty in sealing and leakage, thus preventing the realization of devices having a high and constant-over-time efficiency.

With the goal of overcoming these issues, two different ZnO nanostructures, namely the sponge-like and the flower-like, were successfully employed as alternative photoanode materials, hemi-squaraine (CT1) organic dye molecule was exploited as promising TiO_2 sensitizer, and UV-crosslinked polymer membrane and cellulose-based gel were proposed as quasi-solid electrolytes.

Sponge-like ZnO was characterized in terms of photovoltaic and charge transport properties, in particular examining their dependence on the oxide thickness and on the soaking time. A noticeable photovoltaic conversion efficiency of 4.83% was evaluated, with a charge carrier lifetime at open circuit voltage equal to 48 ms, employing a 15 µm-thick photoanode and a sensitization time of 2 h.

Promising photovoltaic properties of ZnO flower-like microstructures, synthesized by a simple, reproducible and low cost hydrothermal process, were demonstrated. A chemometric approach was used with the purpose of establishing the best sensitization conditions, thus avoiding the long-term degradation to ZnO surface and the Zn^{2+}/dye complexes formation typically shown by ZnO photoanodes in presence of metal-organic dyes. A maximum photoconversion efficiency value of 3.16%, enhanced up to 3.59% when adding, as unprecedently reported in the presence of a ZnO photoanode, N-methylbenzimidazole into the liquid electrolyte, was achieved. This effect was attributed to the reduction of charge recombination and to the enhancement of the diffusion coefficient, as evidenced by the *EIS* analysis.

The effectiveness of the hemi-squaraine CT1 as a sensitizer for TiO_2 was proved by carrying out a combined experimental and theoretical investigation of the structural and electronic coupling between the hemi-squaraine and the anatase surface, focused on the role of its anchoring group. *Ab initio* simulations revealed that the squarate moiety of the dye strongly interacts with the anatase surface giving rise to an optimal alignment of the electronic molecular levels with respect to the oxide energy bands, thus favoring an adiabatic electron transfer from the excited molecule to the semiconductor. This resulted in an efficient electron injection with an observed maximum *IPCE* of 87% and a maximum photoconversion efficiency of 3.54% for a sensitization time of 5 h and a CDCA concentration of 10 mM. Subsequently an optimization of the photovoltaic performances of the CT1-based DSCs was carried out by studying the effect of the sensitization time of the TiO_2 photoelectrode in the dye solution and by investigating the addition of the chenodeoxycholic acid (CDCA) as co-adsorbent in the dye solution at different concentrations for reducing the dye aggregation. A maximum photoconversion efficiency of 1.75% for a sensitization time of only 30 minutes without co-adsorbent was obtained, and this value was enhanced up to 2.50% when adding CDCA at 1 mM in the dye solution and fixing the loading time to 1 h. The very fast kinetics in the dye adsorption, with optimal sensitization time intervals almost 15 times lower than conventional Ru-based sensitizers, confirms the theoretical predictions and indicates a strong interaction of the semisquaric acid group with the anatase surface. This result suggests that this small molecule can be a promising sensitizer even in a continuous industrial process.

A novel methacrylic-based crosslinked polymer electrolyte, obtained by a rapid, economic and environmentally friendly process of photo-curing, using low cost chemicals, was reported. Light-to-electricity conversion efficiency of the DSC assembled with this polymer electrolyte was admirably quite equal to that of the corresponding liquid cell, moreover a remarkably better long-term stability was obtained with BEMA:PEGMA membranes. The experimental conditions for the preparation of the polymer electrolyte were optimized by a design of experiments approach. An interesting correlation between the photoelectrochemical results and the structure of the polymeric network was presented, showing that tuning the polymer composition, and consequently the crosslinking density of the polymeric network, is a promising way to enhance the efficiency of the device.

A polymer gel electrolyte with the micro-cellulose as natural gelling agent was prepared and applied in Dye-sensitized Solar Cells. The volume percentage ratio between the two ionic liquids MPII and EMISC, the weight percentage of 4-TBP and micro-cellulose and the time and the temperature of the heating step necessary to improve the gel penetration into the TiO_2 layer, were successfully monitored. A maximum photoconversion efficiency of 2.71% was obtained by heating the cell at 60 °C for 1 h and by employing a gel prepared with 2 wt% of LiI, iodine (1/10th of the whole weight of iodide), 5 wt% of micro-cellulose, 10 wt% of 4-TBP and a MPII/EMISC volume percentage ratio of 50/50. An ageing test on the DSC photovoltaic performances was carried out and a good stability in severe conditions, namely more the 8 h of measurements performed in a lapse time longer than one month, was reached.

Two consistent physics-based models were also reported, with the aim of better understanding the complex mechanisms involved in the Dye-sensitized Solar Cells and supporting, at the same time, the obtained experimental results.

The first one, based on the hypothesis that organic dye molecules can aggregate on the electrode surface creating an adsorbed layer which prevents the charge transfer, thus worsening the electrical performances of the cell, was built to study the influence of the dye adsorption time on the electrical impedance of a CT1-based Dye-sensitized Solar Cell. Differently from the case of Ru-based solar cells, a non-monotonic behavior of the impedance of the cell was observed when varying the dye soaking time. The model fits well the experimental data if a correction is made regarding the difference between the illuminated area of the cell and the total area available in the electrical measurements.

The second model, which self-consistently couples a physics-based description of the nanoporous photoactive layer to a compact circuit-level description of the passive parts of the cell, was applied to build a consistent picture of the static and dynamic small-signal performances of nanocrystalline TiO_2-based DSCs under different incident illumination intensities and directions and under different applied voltages. Trap-limited dynamics and nonlinear recombination were included and their impact on the steady-state and small-signal dynamic behavior of the device was assessed, based on experimental data and numerical simulations. A unique and limited set of physical and electrical parameters was derived and verified on the basis of a suitable range of experimental data. The simulation results successfully reproduced the *I-V*, *IPCE* and *EIS* measurements under different operating conditions, allowing to clearly identify the optical and electrical losses across the cell and to gain insight into the collection efficiency dependence on the electron density.

The great and fascinating challenge for the future, instead, will be the realization of a flexible Dye-sensitized Solar Cell for space human robotics applications by employing the quasi-solid electrolytes presented in the thesis work and thin metal sheets or ITO-coated plastic materials as photoelectrode substrates. The sintering process at 450 - 500 °C employed in conventional DSC technology, essential to remove the organic additives contained in the TiO_2 paste and to achieve a better electrical connection between the nanoparticles, is no longer viable when replacing the glass substrates with flexible ones due to their thermal instability at such high temperatures. Within this framework, a lot of efforts will be needed to develop low temperature growth methods able to guarantee a complete necking between TiO_2 nanoparticles, thus maximizing the device performances.

Acknowledgements

At the end of these intense and exciting three years of PhD, I would like to thank everyone who have supported me.

First of all, I would like to thank especially Prof. Elena Tresso, my supervisor, for her inspiration, guidance and encouragement throughout the duration of this research work. Her ideas and advices have been decisive to improve this thesis.

I wish to express my warm thanks to Dr. Stefano Bianco and Dr. Marzia Quaglio, my co-supervisors in IIT, whose experience and kind support have been precious for me. Their explanations, ideas and constructive comments gave me important guidance during my PhD.

I would like to express my gratitude to Prof. Fabrizio Pirri for having given me the opportunity to work in his fantastic research group.

I would like to acknowledge Dr. Adriano Sacco and Dr. Andrea Lamberti for their teachings regarding the electrical characterization techniques and the assembly procedures of the DSCs, respectively.

I would like to extend my gratitude to the staff of Chilab Materials and Microsystems Laboratory in Chivasso, in particular to Dr. Denis Perrone and Dr. Simone Marasso, for making me feel at home since the first moment I have known the reality of their lab and for teaching me all the secrets of technological processes in clean room.

Special thanks go to my colleagues and friends Federico Bella, Matteo Gerosa and Nadia Shahzad, for sharing with me moments of deep scientific interaction, often resulted in good works, new ideas and suggestions, mixed to pleasant interludes of worldly life.

Heartfelt acknowledgements go to all people with whom I have profitably collaborated: Prof. Anca Ionescu, Dr. Federica Cappelluti, Dr. Shuai Ma, Dr. Giuseppe Caputo, Ms. Giorgia Musso, Dr. Claudia Barolo, Dr. Claudio Gerbaldi, Dr. Jijeesh Ravi Nair, Dr. Valentina Cauda, Dr. Giancarlo Cicero, Ms. Francesca Risplendi, Dr. Gian Paolo Salvador and Dr. Rossana Gazia.

Warm thanks go to my friends outside the labs: Andrea, Luca, Mario, Valentina, Nerea, Riccardo, Fabrizio, Davide, Marco, Simone, Irene for all the pleasant moments spent together.

Dulcis in fundo, heartfelt acknowledgements go to my parents and my sister for all their love, unconditional support, upbringing, guidance and teachings… for being by my side all days of my life.

List of publications

Articles published:

[1] A. Sacco, A. Lamberti, **D. Pugliese**, A. Chiodoni, N. Shahzad, S. Bianco, M. Quaglio, R. Gazia, E. Tresso, and C. F. Pirri, "Microfluidic housing system: a useful tool for the analysis of dye-sensitized solar cell components", *Appl. Phys. A - Mater. Sci. Process.* **109**, 377 (2012).

[2] F. Cappelluti, S. Ma, **D. Pugliese**, A. Sacco, A. Lamberti, G. Ghione, and E. Tresso, "Consistent static and small-signal physics-based modeling of dye-sensitized solar cells under different illumination conditions", *Phys. Chem. Chem. Phys.* **15**, 14634 (2013).

[3] A. Sacco, A. Lamberti, I. Berardone, S. Bianco, R. Gazia, **D. Pugliese**, M. Quaglio, E. Tresso, and C. F. Pirri, "Spongelike porous ZnO photoanodes for highly efficient Dye Sensitized Solar Cells", *Acta Phys. Pol. A* **123**, 386 (2013).

[4] F. Bella, **D. Pugliese**, J. R. Nair, A. Sacco, S. Bianco, C. Gerbaldi, C. Barolo, and R. Bongiovanni, "A UV-crosslinked polymer electrolyte membrane for quasi-solid dye-sensitized solar cells with excellent efficiency and durability", *Phys. Chem. Chem. Phys.* **15**, 3706 (2013).

[5] G. Cicero, G. Musso, A. Lamberti, B. Camino, S. Bianco, **D. Pugliese**, F. Risplendi, A. Sacco, N. Shahzad, A. M. Ferrari, B. Ballarin, C. Barolo, E. Tresso, and G. Caputo, "Combined experimental and theoretical investigation of the hemi-squaraine/TiO_2 interface for dye sensitized solar cells", *Phys. Chem. Chem. Phys.* **15**, 7198 (2013).

[6] F. Santamaria, G. Boffetta, M. Martins Afonso, A. Mazzino, M. Onorato, and **D. Pugliese**, "Stokes drift for inertial particles transported by water waves", *Europhys. Lett.* **102**, 1 (2013).

[7] M. I. Zaman, S. Ferrero, D. Perrone, L. Scaltrito, N. Shahzad, and **D. Pugliese**, "Fabrication of Ni/Ti/Al Schottky contact to n-type 4H-SiC under various annealing conditions", *Journal of Physics. Conference Series* **439**, 4 pages (2013).

[8] N. Shahzad, **D. Pugliese**, A. Lamberti, A. Sacco, A. Virga, R. Gazia, S. Bianco, M. I. Shahzad, E. Tresso, and C. F. Pirri, "Monitoring the dye impregnation time of nanostructured photoanodes for dye sensitized solar cells", *Journal of Physics. Conference Series* **439**, 12 pages (2013).

[9] **D. Pugliese**, N. Shahzad, A. Sacco, E. Tresso, and A. L. Alexe-Ionescu, "Modeling of the dye loading time influence on the electrical impedance of a dye-sensitized solar cell", *J. Appl. Phys.* **114**, 094901 (2013).

[10] **D. Pugliese**, N. Shahzad, A. Sacco, G. Musso, A. Lamberti, G. Caputo, E. Tresso, S. Bianco, and C. F. Pirri, "Fast TiO_2 sensitization using the semisquaric acid as anchoring group", *Int. J. Photoenergy* **2013**, 871526 (2013).

[11] N. Shahzad, F. Risplendi, **D. Pugliese**, S. Bianco, A. Sacco, A. Lamberti, R. Gazia, E. Tresso, and G. Cicero, "Comparison of Hemi-squaraine Sensitized TiO_2 and ZnO Photoanodes for DSSC Applications", *J. Phys. Chem. C* **117**, 22778 (2013).

[12] **D. Pugliese**, F. Bella, V. Cauda, A. Lamberti, A. Sacco, E. Tresso, and S. Bianco, "A Chemometric Approach for the Sensitization Procedure of ZnO Flowerlike Microstructures for Dye-sensitized Solar Cells", *ACS Appl. Mater. Interfaces* **5**, 11288 (2013).

[13] V. Cauda, **D. Pugliese**, N. Garino, A. Sacco, S. Bianco, F. Bella, A. Lamberti, and C. Gerbaldi, "Multi-functional energy conversion and storage electrodes using flower-like Zinc oxide nanostructures", *Energy* **65**, 639 (2014).

Article submitted:

[1] N. Shahzad, **D. Pugliese**, M. I. Shahzad, and E. Tresso, "Monitoring the dye uptake and the impregnation time in TiO_2 and ZnO photoanodes by means of different spectroscopic measurements", *J. Photochem. Photobiol., A.*